eman ta zabal zazu

Universidad del País Vasco

Euskal Herriko Unibertsitatea

TESIS DOCTORAL

Computational predictive modeling of integrated cerebral metabolism, electrophysiology and hemodynamics

Autor:

Gabriela CAPO RANGEL

Directores:

Prof. Luca GERARDO-GIORDA

Prof. Daniela CALVETTI

Bilbao, 2019

basque center for applied mathematics

EXCELENCIA SEVERO OCHOA

DOCTORAL THESIS

Computational predictive modeling of integrated cerebral metabolism, electrophysiology and hemodynamics

Author:
Gabriela CAPO RANGEL

Supervisors:
Prof. Luca GERARDO-GIORDA
Prof. Daniela CALVETTI

Bilbao, 2019

This research was carried out at the Basque Center for Applied Mathematics (BCAM) within the Mathematical Modelling in Biosciences (MMB) group and was supported by the Spanish Ministry of Economics and Competitiveness MINECO through the BCAM Severo Ochoa excellence accreditations SEV-2013-0323 and SEV-2017-0718 and the "Plan Estatal de Investigación. Desarollo e Innovación Orientada a los Retos de la Sociedad" under Grant BELEMET - Brain ELEctro-METabolic modeling and numerical approximation (MTM2015-69992-R). The support of MINECO and BERC Grants is acknowledged for the three months visit at Case Western Reserve University, Cleveland, USA.

Acknowledgments

This thesis concludes a four years journey during which I had the opportunity to be surrounded by amazing people, who had an effect not only on my career but also on my personal development.

First and foremost, I would like to thank my supervisor, Dr. Luca Gerardo-Giorda, for his guidance, patience and support during these four years. I will be forever grateful to my coadvisor, Dr. Daniela Calvetti and to Dr. Erkki Somersalo, whose immense passion and determination inspired me to read, to work and to understand more about the human brain. I owe them everything I know and they are both my biggest role models, not only scientifically but also on a personal level. I can only hope that some day I will be able to repay everything they have done for me, and I will treat and inspire my future students, in the same way that they inspired me. I am thankful to them for having me in Cleveland, for welcoming me into their house, for all the dinners and lunches, for all the late nights calibrating our models or writing articles and for all of their corrections.

I am very grateful to my entire team, the Mathematical Modeling in Biosciences (MMB) Group, for all the fruitful group talks, for all the BCAM lunches and dinners and simply for their company. In particular, Martina Conte and Argyrios Petras have both inspired me in so many ways and I don't know how I would have made it through the last months without their help. Regardless of where life will take me next, I know I gained two friends that I will always cherish. I thank Nicole Cusimano for her endless support and advice, her native leadership skills and for the way in which she took care of each and every one of us. Ich danke Julia Kroos für die Zeit, die wir zusammen innerhalb und außerhalb des BCAMs verbracht haben, und dafür, dass sie die beste Reisebegleiterin ist, die man sich wünschen kann. Ihre Entschlossenheit und Stärke sind eine Inspiration für mich.

I would also like to express my gratitude to all the people with whom I shared the lunch breaks at BCAM, most of whom I have already named in the pre-

vious paragraph. In particular, I thank Havva Yoldas and Sandeep Kumar for their amazing company, as they were not officially part of the MMB group, but somehow adopted by us!

Agradezco haber conocido a Mikel Aguirre, por ser la mejor compañía que alguien pudiera pedir y tener siempre una actitud positiva contagiosa sobre la vida. Estoy también muy feliz de haber conocido a Miren, aunque por muy corto tiempo, su personalidad tan agradable y abierta, y su manera de vivir la vida, me ha enseñado mucho. Eskerrik asko!

Muchas gracias a todos mis compañeros de oficina: con Josu hemos compartido la misma oficina por tres años, y le doy las gracias por haberme hecho reír cuando más lo necesitaba y eskerrik asko por sus clases de euskera. Le agradezco también a Daniel, Javier y Lore por el buen ambiente que nuestra oficina siempre ha tenido.

Me gustaría también dar las gracias a todo el equipo administrativo de BCAM. Muchas gracias a Miguel Benitez, por estar disponible siempre, a cualquier hora y en cualquier día, a todas mis preguntas confusas sobre cualquier aspecto burocrático. El me ha ayudado desde el momento en que apliqué a la beca de doctorado y él fue también el que me ayudó a preparar las formalidades para defender esta tesis, por lo cual le voy a estar siempre agradecida.

Finalmente, quiero agradecerle a Marco por apoyarme y ayudarme en cualquier momento lo necesitaba y por soportarme cada vez que he estado ocupada o estresada estos cuatro años. Multumesc intregii mele familii, pentru dragostea lor, pentru sprijinul si intelegerea pe care mi-au acordat-o intotdeauna. In special, ii multumesc mamei mele, cea mai puternica persoana pe care o cunosc, pentru ca intotdeauna m-a indrumat sa am curajul sa fac ceea ce imi place. Le sunt foarte recunoscutoare si prietenelor mele de o viata: Madalina, Alina, Eliza, Cristina, Irina si Ioana. Imi pare rau ca, fiind atat de departe de casa, nu va pot vedea mai des, imi este foarte dor de voi toate!

Abstract

Understanding the energetic requirement of brain cells during resting state and during high neuronal activity is a very active research area where mathematical models have contributed significantly by providing a context for the interpretation of the experimental results. In this thesis, we present three new computational predictive mathematical models to elucidate several dynamics in the brain, comprising electrophysiological activity, cellular metabolism and hemodynamic response. Many computational challenges had to be addressed, mostly due to the very different characteristic times at which the electrical, metabolic and hemodynamic events occur.

The first part of the thesis proposes a novel predictive mathematical electro-metabolic model connecting the electrophysiological activity and the metabolism through a double feedback mechanism based on energy demand and production. This model sheds light on the role of the glial potassium cleaning in brain energy metabolism by integrating a four compartment metabolic model with one describing in details the electrical activity. The results of computed experiments performed with this model for different protocols, namely awake resting state, transitions between resting state and neuronal activation and ischemic episodes are in agreement with experimental observations.

In the second part of the thesis, the electro-metabolic model is expanded to comprise the brain hemodynamic response. This is attained through a triple feedback mechanism between the electrophysiology, metabolism and a three compartment hemodynamic model tracking the changes of cerebral blood flow and cerebral blood volume through arteries, capillaries and veins. During neuronal activation, the increase in extracellular potassium concentration triggers an increase in the cerebral blood flow and concurrently vasodilation, ensuring the supply of nutrients necessary for the metabolic response to sustain the increased energy demand. The ensuing hemo-electro-metabolic model provides a better insight on the transitions between resting state and neuronal activation.

In the third and last part of the thesis, we propose a variant of the electro-

metabolic model that adequately describes the changes in the brain in connection with cortical spreading depression (CSD) waves. In addition the dynamics of sodium and potassium, the new model accounts for chloride dynamics, the glutamate-glutamine cycle, as well as neuronal swelling accompanied by shrinkage of extracellular space. As illustrated with computed experiments, with this model it is possible to follow simultaneously the changes in ionic homeostasis, the alterations in the volumes of the cellular compartments and of the extracellular space, and large modifications in brain metabolism during cortical spreading depression waves. The model predictions, in agreement with findings reported in the experimental literature, show a large decrease in glucose and oxygen concentration and a significant increase in lactate concentration during the passing of cortical spreading depression waves.

Contents

Resumen

A pesar de que el peso promedio del cerebro representa tan sólo el 2% del cuerpo humano, su elevado consumo energético ha cautivado el interés de diferentes comunidades científicas en las últimas décadas. Como resultado de muchos años de investigación, hoy en día está se suele atribuir la mayor parte de la energía consumida por el cerebro a las bombas ionicas, al mantenimiento del potencial de reposo y a la propagación los potenciales de acción [1, 2].

A pesar de que en un principio, la mayor parte del interés científico estaba enfocado al estudio de las neuronas, en los últimos años, la importancia del estudio de los astrocitos ha sido reconocida [3, 4, 5, 6, 7]. Más especificamente, los astrocitos son destacados por jugar un papel determinante a la hora de reducir la concentración extracelular del potasio durante la activación neuronal, isquemia o depresión cortical propagada. Asimismo, muy recientemente se ha propuesto que debido a la proximidad de los pies terminales de los astrocitos al capilar, estas céelulas pueden tener un rol significativo en la regulación de la respuesta del flujo sanguíneo cerebral [1].

Las técnicas de neuroimagen disponibles hoy en día permiten visualizar diferentes aspectos del cerebro por separado, por lo cual es difícil de elucidar cómo el cerebro coordina sus diferentes funciones. La actividad eléctrica del cerebro se puede observar mediante electroencefalografía (EEG), magnetoencefalografía (MEG) o electrocorticografía. Por otro lado, a través de la tomografía por emisión de positrones (PET) se puede visualizar cambios en el metabolismo, mientras que la respuesta del flujo sanguíneo se puede determinar a través de la imagen por resonancia magnética funcional (fMRI) y, en particular, mediante la Imagen de contraste dependiente del nivel de oxígeno en la sangre (BOLD). En los últimos 20 años, los modelos matemáticos se han convertido en una herramienta importante en el estudio de diversas condiciones adecuadas y patológicas del cerebro. En esta disertación se proponen tres modelos matemáticos que proporcionan una visión holística sobre los diferentes procesos que ocurren en el cerebro.

Una de las principales contribuciones de esta disertación se centra en el de-

sarrollo de un modelo Hemo-Electro-Metabólico integrado, que coordina y sincroniza tres funciones cerebrales diferentes pero conectadas. El modelo proporciona una comprensión más completa de cómo la actividad eléctrica cerebral, su metabolismo y su respuesta hemodinámica interactúan, como se regulan mutuamente y cómo el deterioro de uno de estos aspectos puede provocar una interrupción de los demás.

Es sabido que la actividad electrofisiológica del cerebro sólo se puede mantener si el conjunto de procesos bioquímicos, que tienen lugar en el metabolismo, es capaz de producir una cantidad adecuada de energía (ATP), que puede variar sustancialmente según el nivel de activación neuronal. Por otro lado, la cantidad de energía producida por el metabolismo depende de la disponibilidad de diferentes especies bioquímicas y, por lo tanto, también de la cantidad de flujo sanguíneo, ya que éste transporta glucosa y oxígeno.

El acoplamiento de la electrofisiología y el metabolismo se puede encontrar en varios artículos publicados en los últimos años, tanto en la literatura sobre el metabolismo cerebral [8, 9, 10] como en la literatura sobre la actividad electrofisiológica [11]. Por ejemplo, en [8], *Aubert et al.* incluyen en su modelo metabólico el costo de la bomba de sodio y potasio, mientras que en [9], *Cloutier et al.* agregan el costo del ciclo de glutamato-glutamina al modelo metabólico propuesto. Asimismo, varios modelos relacionados con la actividad electrofisiológica, tienen en cuenta, al menos parcialmente, la disponibilidad de algunos de los metabolitos. Por ejemplo, en el modelo propuesto por *Wei et al.* en [11], que capta la actividad electrofisiológica del cerebro durante diferentes patrones de disparo neuronal, la actividad de la bomba de sodio y potasio está expresada con respecto a la concentración disponible de oxígeno.

En este trabajo, proponemos un modelo de doble retroalimentación, que no sólo incluye el costo energético de la bomba de sodio y potasio en el metabolismo, sino también interpone la respuesta metabólica a este costo energético. Una de las principales dificultades en el desarrollo de dicho modelo acoplado se debe a que los distintos procesos característicos tienen diferentes órdenes de magnitud en las escalas de tiempo: mientras la actividad electrofisiológica del cerebro se ejecuta en milisegundos, la contraparte metabólica es mucho más lenta, con una dinámica del orden de minutos. Debido a que estas escalas de tiempo son tan drásticamente diferentes, se requiere una atención especial y un manejo computacional adecuado, por lo cual desarrollamos un algoritmo de integración de tiempo para resolver el sistema acoplado.

Esta disertación está estructurada en cinco capítulos: los dos primeros capítulos están dedicados a la descripción del modelo electrofisiológico y metabólico. El acoplamiento electro-metabólico se desarrolla en el Capítulo 3, donde abordamos

las dificultades matemáticas que surgen de las diferentes escalas de tiempo de los dos procesos. En el Capítulo 4 explicamos cómo enriquecer el modelo agregando una descripción detallada de la respuesta del flujo sanguneo cerebral durante la activación neuronal, acoplando nuestro modelo Electro-Metabólico a un modelo hemodinámico en el que los cambios en el flujo sanguíneo se rastrean a través de tres compartimentos diferentes: arterias, capilares y venas. Como la respuesta del flujo sanguíneo es más lenta que la respuesta electrofisiológica y metabólica, introducimos una escala de tiempo adicional en nuestro enfoque multiescalar. El último capítulo de esta tesis está dedicado a un nuevo modelo matemático electro-metabólico diseñado específicamente para investigar la depresión cortical propagada (CSD) y las grandes alteraciones que estas ondas producen en las concentraciones iónicas, en las concentraciones de metabolitos y la respuesta hemodinámica. Debido a los cambios masivos provocados por CSD, reemplazamos el modelo de actividad electrofisiológica descrito en el Capítulo 1 por un modelo más complejo específicamente diseñado para simular las ondas de depresión cortical propagada (CSD). Posteriormente, abordamos el acoplamiento de este modelo con el modelo metabólico presentado en el Capítulo 2, en el cual además consideramos los grandes cambios en las fracciones de volumen durante el paso de las ondas CSD.

El primer capítulo de esta tesis está dedicado a la descripción de la actividad electrofisiológica del cerebro. La primera sección consiste en una revisión de los modelos matemáticos que capturan la actividad eléctrica, a partir del modelo clásico de Hodgkin-Huxley, y continuando con el modelo de Fitzhugh-Nagumo, el modelo de Hindmarsh-Rose y el modelo de Izhikevich. El modelo electrofisiológico utilizado en los primeros cuatro capítulos de esta tesis está presentado en detalle en la segunda sección del primer capítulo. Este modelo, que fue propuesto originalmente por *Cressman et al.* [12, 13] ha sido modificado para obtener una concentración extracelular de potasio para el cerebro en reposo de aproximadamente 3 mM, como se sugiere en la literatura experimental más reciente [14]. Luego, calibramos este modelo de manera que pueda producir la frecuencia de 4 Hz característica de la neurona en reposo, y desarrollamos un mecanismo de activación neuronal mediante el aumento temporal de las conductancias de fuga de sodio y potasio. Los resultados obtenidos en estas simulaciones están analizados para tres frecuencias diferentes que caracterizan el estado de reposo alfa: 8 Hz, 10 Hz y 12 Hz. Los cambios a lo largo del tiempo en el potencial de la membrana, la concentración de potasio extracelular, la concentración del sodio intracelular y las variables de activación correspondientes se presentan en la sección de resultados del Capítulo 1.

El segundo capítulo, dedicado al metabolismo cerebral, inicia con una intro-

ducción a la modelación matemática asociada a los modelos metabólicos espacialmente agrupados en múltiples compartimentos; luego, hacemos una descripción matemática de las tasas de transporte y de los flujos de reacción, y proseguimos con una descripción de las principales reacciones bioquímicas consideradas. Adicionalmente, presentamos una breve reseña de dos modelos metabólicos muy reconocidos: el modelo de Aubert y Costalat [8] y el modelo de Cloutier [9], ambos incluyen parcialmente el costo energético de la bomba de sodio y potasio. En la cuarta sección del Capítulo 2 presentamos el modelo metabólico utilizado a lo largo de esta tesis; describimos la dinámica de las concentraciones de metabolitos en los cuatro compartimentos y presentamos la descripción matemática de los flujos de transporte entre los diferentes compartimentos y los flujos de reacción en los dos compartimentos celulares.

El modelo metabólico que consideramos está constituido por 26 ecuaciones diferenciales en las cuales se rastrean las especies bioquímicas en cuatro compartimentos: sangre, neurona, astrocito y espacio extracelular. El sistema resultante de ecuaciones diferenciales es muy rígido y, por lo tanto, requiere atención especial. En primer lugar, garantizamos la positividad de nuestras 26 especies bioquímicas expresándolas en forma exponencial y, posteriormente, desarrollamos el marco matemático para resolver numéricamente dicho sistema. En particular, utilizamos una familia de métodos implícitos conocidos como las fórmulas de diferenciación hacia atrás (BDF, por sus siglas en inglés), diseñadas específicamente para este tipo de sistemas. Posteriormente, calibramos nuestro modelo, eligiendo la energía necesaria para los procesos de mantenimiento de manera que el índice de oxígeno glucosa (OGI), definido como la división entre el flujo de oxígeno y el flujo de glucosa entre la sangre y el espacio extracelular, caiga en el rango sugerido en la literatura durante el estado de reposo alfa y durante la activación neuronal sostenida. A lo largo de las simulaciones realizadas en este capítulo, el costo energético proporcionado por la actividad electrofisiológica se mantiene constante y está determinado por el modelo descrito en el Captulo 1, para cuatro niveles diferentes de activación: 8 Hz, 10 Hz, 12 Hz y 90 Hz. A continuación, realizamos dos simulaciones en las cuales describimos la respuesta metabólica a la transición del sistema de un estado de reposo de 8 Hz a un período de tres minutos de activación neuronal correspondiente a una frecuencia de 90 Hz, seguido de otro perodo de disparo neuronal de 8Hz. En el primer caso, correspondiente a un experimento in vitro, el flujo sanguíneo se mantiene constante a lo largo de la simulación, mientras que durante el segundo experimento aumentamos el flujo sanguíneo un 30% durante el período de activación neuronal, protocolo que corresponde a un análisis in vivo. La última sección muestra los resultados obtenidos para los dos protocolos de manera comparativa y de acuerdo con la literatura

experimental.

El tercer capítulo describe el modelo electro-metabólico de doble retroalimentación. En este capítulo presentamos el método por el cual, según el consumo y la demanda de ATP, realizamos el acoplamiento entre el modelo de actividad electrofisiológica y el modelo metabólico. Las diferentes escalas de tiempo empleadas por los dos modelos requieren una consideración especial: en la tercera sección describimos el enfoque computacional multiescala que desarrollamos. Nuestro modelo ha sido probado en diferentes escenarios: primero consideramos activaciones neuronales consecutivas, separadas por diferentes períodos de recuperación y evaluamos cómo la duración del período de recuperación afecta la segunda activación neuronal. El segundo protocolo simula un episodio isquémico, durante el cual el flujo sanguíneo muestra una disminución del 90% durante un período de 90 segundos y en el tercero, un episodio isquémico es seguido por un período de activación neuronal. Para todos estos casos, mostramos los cursos de tiempo del potencial de la membrana, las concentraciones iónicas, las concentraciónes de los metabolitos principales y las tasas de transporte y reacción. Además, para comparar los resultados obtenidos con aquellos de la literatura, mostramos el curso temporal del índice de oxígeno-glucosa que hemos obtenido en cada caso.

La hemodinámica del cerebro es el tema del Capítulo 4, en cuya introducción describimos los mecanismos básicos de la imagen por resonancia magnética funcional (fMRI) y la imagen de contraste dependiente del nivel de oxígeno en la sangre (BOLD) destacando además algunos debates abiertos sobre el tema en la literatura. Para completar, ofrecemos una breve revisión de los modelos matemáticos del flujo sanguíneo cerebral, incluido el modelo de Buxton [15, 16, 17] y un modelo reciente de tres compartimentos de *Barrett et al.* [18]. Por otro lado, acoplamos una extensión del modelo de *Barret et al.*, que ha sido recientemente propuesta en [19, 20], a nuestro modelo electro-metabólico que hemos descrito en el Capiítulo 3 y expresamos el estímulo vasodilatador en términos de la concentración extracelular de potasio. Las predicciones calculadas por este modelo hemo-electro-metabólico con triple retroalimentación son presentadas en la última sección para dos protocolos: uno en el cual el estado de reposo es seguido por un periodo de activación neuronal y otro donde hay dos activaciones neuronales consecutivas. Nuestros resultados están en concordancia con la literatura más reciente.

En el Capítulo 5, se propone un nuevo modelo matemático para investigar los cambios en la actividad eléctrica y metabólica durante la depresión cortical propagada (CSD), donde las ondas de depolarización celular, que se propagan lentamente, están acompañadas del silenciamiento neuronal y de cambios radicales en la homeostasis iónica. Después de una breve introducción sobre las

ondas de depresión cortical propagada y de las alteraciones extremas que se producen en las concentraciones iónicas, la morfología celular, el metabolismo y la hemodinámica, presentamos una breve revisión de algunos modelos matemáticos que generan ondas de depresión cortical propagada. En particular, nos referimos al modelo de *Wei et al.* [11] y al modelo de *Huguet et al.* [21]. En la tercera sección de este capítulo, proponemos un nuevo modelo, basado en el trabajo de *Hubel et al.* en [22], específicamente diseñado para capturar la actividad electrofisiológica durante la CSD. Además, describimos cómo los parámetros del modelo son calibrados para lograr el disparo a las frecuencias deseadas y cómo se implementa el acoplamiento de este nuevo modelo electrofisiológico con el modelo metabólico descrito en el Capítulo 2. Para tener en cuenta los grandes cambios morfológicos que se producen durante el paso de las ondas de depresión cortical propagada, nuestro modelo electro-metabólico de CSD asume fracciones de volumen variables tanto en el modelo de actividad electrofisiológica como en el metabólico. Los resultados obtenidos, al simular las ondas de CSD con nuestro modelo electro-metabólico de CSD, capturan no sólo los grandes cambios en las concentraciones iónicas proporcionadas por aumentos masivos en la concentración extracelular de potasio y en la concentración intracelular de sodio, sino también la característica metabólica observada típicamente durante la CSD: una disminución significativa en la glucosa y un aumento masivo en la concentración de lactato. Nuestro modelo predice, de acuerdo con los hallazgos experimentales reportados en la literatura, una contracción pronunciada del espacio extracelular, debido a la expansión de los compartimentos celulares.

Summary

The sizable energetic consumption of human brain, when considering its relatively small weight of approximately 2% of an average human body, has captivated the interest of different scientific communities for the past few decades. As a result of many years of investigation on brain energetics, today it is generally agreed that most of the energy consumed by the brain goes on driving the ionic pumps, on maintaining the resting potential and on propagating action potentials [1, 2].

While most of the scientific interest at first was directed towards studying neurons, in the last years, the essential role of astrocytes in the brain has been acknowledged [3, 4, 5, 6, 7]. More specifically, astrocytes are credited with playing a crucial role in cleaning the large concentration of extracellular potassium in the wake of neuronal activation, ischemic events or cortical spreading depression. In addition, recently it was proposed that due to the proximity of the astrocytic endfeet to the capillary, they may have a very significant role on regulating the cerebral blood flow response [1].

The neuroimaging modalities currently available visualize different aspects of the brain separately, thus making it difficult to elucidate how the brain coordinates its different functions. Brain electrical activity is observed through electroencephalography (EEG), magnetoencephalography (MEG) or electrocorticography (ECOG). Positron emission tomography (PET) monitors metabolic events, while the blood flow response is determined via functional MRI and in particular through the blood oxygenation dependent signal (BOLD). In the last 20 years, mathematical models have become an important tool in studying various healthy and pathologic conditions in the brain. This thesis proposes three new mathematical models to provide a holistic view over the different processes occurring in the brain.

One of the main achievements of this thesis is an integrated **Hemo-Electro-Metabolic model**, that coordinates and synchronizes three different, yet connected brain functions. The model provides a more complete understanding of how brain electrical activity, its metabolism and its hemodynamic response in-

teract, how they are mutually regulated and how the impairment of one of these aspects can lead to a disruption of the other ones.

It is known that brain electrophysiological activity can only be sustained if the ensemble of biochemical processes taking place in the metabolism is able to produce an adequate quantity of energy (ATP), which can vary substantially depending on the level of neuronal activation. In turn, the amount of energy produced by metabolism depends on the availability of different biochemical species and therefore, also on the amount of blood flow, as it transports glucose and oxygen.

Coupling the electrophysiology and metabolism can be found in a number of articles published in recent years, both in the literature regarding brain metabolism [8, 9, 10] and the literature regarding electrophysiological activity [11]. For example, in [8], *Aubert et al.* include in their metabolic model the cost of the sodium potassium pump and in [9], *Cloutier et al.* add the cost of the glutamate-glutamine cycle to the metabolic model they developed. On the other hand, various models concerning the electrophysiological activity, take into account, at least in part, the availability of some of the metabolites. For example, in the model proposed by [11] in *Wei et al.*, able to capture brain electrophysiological activity and different firing patterns, the activity of the sodium potassium pump is expressed with respect to the available concentration of oxygen.

In this thesis we propose a **double-feedback model**, which not only accounts for the energetic cost of the sodium potassium pump in the metabolism, but also for the metabolic response to this energetic cost. A major difficulty in developing such a coupled model comes from the different orders of magnitude in the time scales of the characteristic processes: while brain electrophysiologic activity runs at milliseconds, the metabolic counterpart is much slower, with dynamics of the order of minutes. These dramatically different time scales require special attention and adequate computational handling, which we address by developing a time integration algorithm to solve the coupled system.

This thesis is structured in five main chapters: the first two chapters are devoted to the description of the electrophysiologic and the metabolic model. The Electro-Metabolic coupling is discussed in detail in Chapter 3, where we address the mathematical difficulties arising from the different time scales of the two processes. Chapter 4 describes how to enrich the model by adding a detailed description of the cerebral blood flow response during neuronal activation, by linking our Electro-Metabolic model to a hemodynamic model in which the changes in blood flow are tracked through three different compartments: arteries, capillaries and veins. As the blood flow response is slower than the electrophysiologic and metabolic response, one additional time scale is introduced in

our multiscale approach. The last chapter of this thesis is dedicated to a novel electro-metabolic mathematical model specifically designed to investigate cortical spreading depression (CSD) and the large changes which occur in the ionic concentrations, metabolites concentrations and hemodynamic response. Due to the massive alterations triggered by CSD, we replaced the electrophysiological activity model described in Chapter 1, with a more complex model, specifically taylored for simulating CSD. We then address the coupling of this model with the metabolic model presented in Chapter 2, in which we account also for the large changes in the volume fractions during the passing of CSD waves.

The first chapter of this thesis is devoted to describing the brain electrophysiological activity. The first section consists of a review of the mathematical models capturing electrical activity, starting from the classical Hodgkin-Huxley model, and continuing with Fitzhugh-Nagumo model, Hindmarsh-Rose model and Izhikevich model. The electrophysiologic model used in the first four chapters of this thesis is described in detail in the second section of the first chapter. This model, which was originally proposed by *Cressman et al.* [12, 13], was modified to match an extracellular potassium concentration for the brain at rest of approximately 3 mM, as suggested in the most recent experimental literature [14]. We calibrated this model so that it can produce the frequency of 4 Hz characteristic to the neuron at rest, and we developed a mechanism of inducing neuronal activation by temporarily increasing the leak conductances of sodium and potassium. The results obtained in these simulations are presented for three different frequencies characterizing the alpha awake resting state 8 Hz, 10 Hz and 12 Hz. The changes over time in the membrane potential, concentration of extracellular potassium, intracellular sodium and the corresponding gating variables are presented in the results section of Chapter 1.

The second chapter dedicated to brain metabolism, starts with an introduction of mathematical modeling of spatially lumped metabolic models featuring multiple compartments, the mathematical description of the transport rates and reaction fluxes, and continuing with a description of the main biochemical reactions we are considering. A short review of two well known metabolic models follows: the Aubert and Costalat model [8] and the Cloutier model [9], both of which partially include the energetic cost of the sodium potassium pump. In the fourth section of Chapter 2 we introduce the metabolic model [41] used throughout this thesis; we describe the dynamics of the metabolites concentrations in the four compartments and we present the mathematical description of the transport fluxes between the different compartments and the reaction fluxes in the two cellular compartments. In summary, the metabolic model we consider consists of 26 differential equations in which the biochemical species are tracked in four

different compartments: blood, neuron, astrocyte and extracellular space. The resulting system of differential equations is very stiff, and therefore requires special attention. Therefore, we first guarantee the positivity of our 26 biochemical species by expressing them in exponential form, and we develop the mathematical framework to numerically solve such a stiff system. We use a family of implicit methods known as the Backward Differentiation Formulae (BDF) methods, specifically designed for stiff systems. We then calibrate our model, by choosing the household energy such that the oxygen glucose index (OGI) index, defined as the ratio between the flux of oxygen and the flux of glucose between the blood and the extracellular space, falls in the range reported by the literature during alpha awake resting state and during sustained neuronal activation. Throughout the simulations performed in this chapter, the energetic cost provided by the electrophysiological activity was kept constant and was determined from the model described in Chapter 1, for four different levels of activation: 8 Hz, 10 Hz, 12 Hz and 90 Hz. We perform two computed experiments in which we describe the metabolic response to the system transitioning from an awake resting state of 8 Hz to a a period of three minutes of neuronal activation corresponding to a frequency of 90 Hz, followed by another period of 8Hz neuronal firing. In the first case we considered, the blood flow is kept constant throughout the experiment, corresponding to an in vitro experiment, while during the second experiment we increase the blood flow by 30% during the neuronal activation period, protocol which corresponds to an in vivo case. The last section shows the results obtained for the two protocols in a comparative manner and agree with the experimental literature.

The third chapter describes the double feedback Electro-Metabolic model. In this chapter we describe the manner in which, based on the ATP consumption and ATP demand, we perform the coupling between the electrophysiological activity model and the metabolic model. The different time scales employed by the two models, required special consideration: in the third section we describe the ad hoc multiscale computational approach we developed. Our model is tested in various situations: we first consider consecutive neuronal activations, separated by different recovery periods and we assess how the duration of the recovery period impacts the second neuronal activation. The second protocol simulates an ischemic episode, during which the blood flow exhibits a 90% decay for a period of 90 seconds and in the third one, an ischemic episode is followed by a neuronal activation period. For all these cases, we show the time courses of the membrane potential, the ionic concentrations, the concentration of the main metabolites, the transport rates and the reaction rates. In addition, for comparison with the experimental literature, we show the time course of the oxygen glucose index we

obtained in each case.

Brain hemodynamics is the topic of Chapter 4, where in the introduction section, we describe the basic mechanisms of functional Magnetic Resonance Imaging (fMRI) and Blood Oxygenation Level Dependent (BOLD) highlighting some open debates in the literature. For completeness, we provide a short review of mathematical models of cerebral blood flow response, including the Balloon Model [15, 16, 17] and a recent three compartment model by *Barrett et al.* [18]. We couple an extension of the latter recently proposed in [19, 20] to our Electro-Metabolic model introduced in Chapter 3 and we express the vasodilatory stimulus in terms of extracellular potassium concentration. The computed predictions of this three way feed-back Hemo-Electro-Metabolic model are presented in the last section for two protocols: one where resting state is followed by a period of neuronal activation and one where there are two consecutive neuronal activations. Our results and are in agreement with the most recent literature.

Chapter 5 proposes a new mathematical model for investigating the changes in electric and metabolic activity during cortical spreading depression (CSD), where slowly propagating waves of cellular depolarizations are accompanied by neuronal silencing and extreme changes in the ionic homeostasis. After a short introduction to CSD waves and the extreme alterations they produce in the ionic concentrations, cellular morphology, metabolism and hemodynamics, we present a brief review of some mathematical models generating cortical spreading depression waves. In particular, we refer to the Wei model [11] and Huguet model [21]. In the third section of this chapter we propose a new model, based on the work of *Hubel et al.* in [23], specifically designed for capturing the electrophysiological activity during CSD. In addition, we describe how we calibrated the model parameters to attain firing at the desired frequencies and how the coupling with the metabolic model described in Chapter 2 is implemented. To take into account the very large morphologic changes which occur during the passing of cortical spreading depression waves, our coupled CSD Electro-Metabolic model assumes variable volume fractions in both the electrophysiological activity model and in the metabolic one. The results obtained when simulating CSD waves with our coupled CSD Electro-Metabolic model capture not only the large changes in ionic concentrations given by massive increases in the concentration of extracellular potassium and intracellular sodium, but also the metabolic signature typically observed during CSD: a significant decrease in glucose and a massive increases in lactate concentration. Our model predicts, in agreement with experimental findings reported in the literature, a pronounced shrinkage of the extracellular space, due to the swelling of the cellular compartments.

Chapter 1

Electrophysiology

Brain electrophysiology is concerned with the study of the electrical activity of neurons. In the recent years, mathematical modelling and computer simulations have become an essential tool in uncovering fundamental mechanisms in neuroscience: numerous mathematical models have been developed for describing a wide range of phenomena: from characterizing the biophysical mechanisms of current flow through individual ion channels to modeling the activity of large populations of neurons [24]. This chapter provides an overview of mathematical models for describing the electrical activity of the brain and the differences in the ionic homeostasis during resting state and neuronal excitation periods. We begin with a short review of the mathematical models for the brain electrophysiological activity and we then concentrate on describing the electrophysiologic model we are going to use throughout this thesis.

1.1 Review of electrophysiological models

In this section we present a general overview of the mathematical models to describe electrical activity in the brain, starting with the pioneering work by Sir Alan Hodgkin and Sir Andrew Huxley for the ionic mechanisms underlying action potentials. The next subsection presents the Fitzhugh-Nagumo model, reducing the complexity of the Hodgkin-Huxley model while maintaining its essential characteristics. Modifications of this model include the Hindmarsh Rose model and the Izhikevich model, and we focus on their capacity of producing not only tonic spiking behavior but also various bursting patterns.

1.1.1 Hodgkin-Huxley model

The foundation of most of today's electrophysiological models is the work of Sir Alan Hodgkin and Sir Andrew Huxley [25, 26, 27], who in the middle of the twentieth century, performed experiments on the squid giant axon and subsequently provided a description of the behaviour of the macroscopic ionic currents with respect to changes in the sodium and potassium conductances in the axon membrane.

Their discoveries led to the formulation of the Hodgkin-Huxley model (HH), describing the dependency of the sodium and potassium conductances on voltage and time. Every ion channel consists of one or more gates that regulate the flow of ions through the channel [24]. In the squid axon there are three major currents: the persistent potassium current, I_{K}, with four activation gates, the transient sodium current I_{Na} with three activation gates and one inactivation gate and the Ohmic leak current, I_{leak}, carried mostly by chloride ions [28]. The ionic currents are proportional to the maximum conductance characteristic to each current (g_{Na}, g_{K}, g_{leak}), multiplied by the difference between the membrane voltage (V) and the equilibrium voltage (V_{K}, V_{Na}, V_{leak}):

$$I_{\mathrm{Na}} = g_{\mathrm{Na}}(V - V_{\mathrm{Na}}), \qquad I_{\mathrm{K}} = g_{\mathrm{K}}(V - V_{\mathrm{K}}), \qquad I_{\mathrm{leak}} = g_{\mathrm{leak}}(V - V_{\mathrm{leak}}).$$

Their sum represents the total ionic current I_{ion}:

$$I_{\mathrm{ion}} = g_{\mathrm{Na}}(V - V_{\mathrm{Na}}) + g_{\mathrm{K}}(V - V_{\mathrm{K}}) + g_{\mathrm{leak}}(V - V_{\mathrm{leak}}).$$

The empirical expressions found by Hodgkin and Huxley for the sodium and potassium channel conductances are:

$$g_{\mathrm{Na}} = \bar{g}_{\mathrm{Na}} m^3 h, \qquad g_{\mathrm{K}} = \bar{g}_{\mathrm{K}} n^4, \tag{1.1}$$

where n represents the open probability for the activation gate of potassium channel, m is the open probability for the activation gate of sodium and h is the inactivation gate for the sodium channel.

The Hodgkin-Huxley model consists of four differential equations, one de-

scribing the change in membrane voltage over time and the others describing the changes in the rate processes over time:

$$I = c_m \frac{dV}{dt} + I_{\text{ion}}, \tag{1.2}$$

$$\frac{dn}{dt} = \alpha_n(V)(1-n) - \beta_n(V)n, \tag{1.3}$$

$$\frac{dm}{dt} = \alpha_m(V)(1-m) - \beta_m(V)m, \tag{1.4}$$

$$\frac{dh}{dt} = \alpha_h(V)(1-h) - \beta_h(V)h, \tag{1.5}$$

where $\alpha_i,\ \beta_i$ for $i = \{n, m, h\}$ are dimensionless rate constants corresponding to each of the gates; their expressions are listed in Table 1.1.

w	m	h	n
$\alpha_w(V)$	$0.1\dfrac{25-V}{\exp((25-V)/10)-1}$	$0.07\exp(-(V/20)$	$0.01\dfrac{10-V}{\exp((10-V)/10)-1}$
$\beta_w(V)$	$4\exp(-V/18)$	$\dfrac{1}{1+\exp((30-V)/10)}$	$0.125\exp(-V/80)$

Table 1.1: Gating variables: voltage-dependent saturation functions for Hodgkin-Huxley model.

In the original work by Hodgkin and Huxley [25, 26, 27], the parameters of the model (see Table 1.2) were chosen such that the resting potential is approximately 0, and hence the membrane potential was shifted by 65 mV.

Name	Symbol	Value	Units
Membrane capacitance	c_m	1	$\mu\text{F/cm}^2$
Applied current	I_{ion}	0	$\mu\text{A/cm}^2$
Sodium Nernst equilibrium potential	V_{Na}	120	mV
Potassium Nernst equilibrium potential	V_{K}	-12	mV
Leak Nernst equilibrium potential	V_{leak}	10.6	mV
Sodium maximal conductance	$\bar{g}_{\text{Na}}$	120	mS/cm^2
Potassium maximal conductance	$\bar{g}_{\text{K}}$	36	mS/cm^2
Leak maximal conductance	g_{leak}	0.3	mS/cm^2

Table 1.2: Parameters values in HH model.

Figure 1.1 shows the resulting action potential and the gating variables for the choice of parameters given in Table 1.2. In this simulation, the stimulus

$I = 2.5\ \mu\text{A/cm}^2$ was applied at time $t = 5$ milliseconds and had a duration of 5 milliseconds. These initial conditions were obtained by setting $V = 0$, yielding $n(0) = 0.318$, $h(0) = 0.5963$ and $m(0) = 0.053$. For this simulation, we solved the system of differential equations (1.2) using the Matlab built-in function ode15s. The right panel of Figure 1.1 shows the time course of the conductances defined in equation (1.1). Notice that the amplitude of the injected current I is sufficiently large to induce an increase in the sodium conductance and the peak of the action potential coincides with the peak of the sodium conductance.

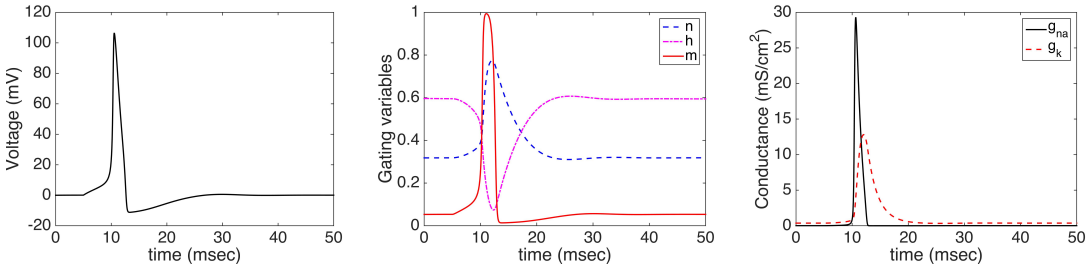

Figure 1.1: Voltage (left), gating variables (middle) and conductances (right) in the Hodgkin Huxley model.

1.1.2 Fitzhugh-Nagumo model

The complexity of the Hodgkin-Huxley model was reduced in 1961 by Fitzhugh [29], who observed that the time scale of the activation gate for the sodium channel m is much faster than the other gates (see Figure 1.1), justifying the assumption that the activation gate m reaches its value immediately, thus, its value can be determined by simply setting $\frac{dm}{dt} = 0$ while keeping h constant. This consideration reduces (1.2)-(1.5) to the following system containing only two differential equations.

$$\begin{aligned} c_m \frac{dV}{dt} &= I - g_{\text{Na}}(0.8 - n)(V - V_{\text{Na}}) - g_{\text{K}}(V - V_K) - g_{\text{leak}}(V - V_{\text{leak}}), \\ \frac{dn}{dt} &= \alpha_n(V)(1 - n) - \beta_n(V)n. \end{aligned} \tag{1.6}$$

Using the fact that the V nullcline has the shape of a cubic function and could be approximated by a straight line, Fitzhugh reduced the complexity of

the model (1.6) even further, by proposing a polynomial model of the form:

$$\begin{aligned} \frac{dx}{dt} &= x - \frac{x^3}{3} - y + I, \\ \frac{dy}{dt} &= \frac{1}{\gamma}(x - by + a). \end{aligned} \tag{1.7}$$

The action potential generated with this model is shown in Figure 1.2 together with the time course for the gating variable y. For this simulation we used the built-in Matlab solver ode15s, with the choice of parameters: $a = 0.8$, $b = 0.7$ and $\gamma = 13$. At $t = 5$ milliseconds, we consider a stimulus $I = 0.4$ having a duration of 3 milliseconds.

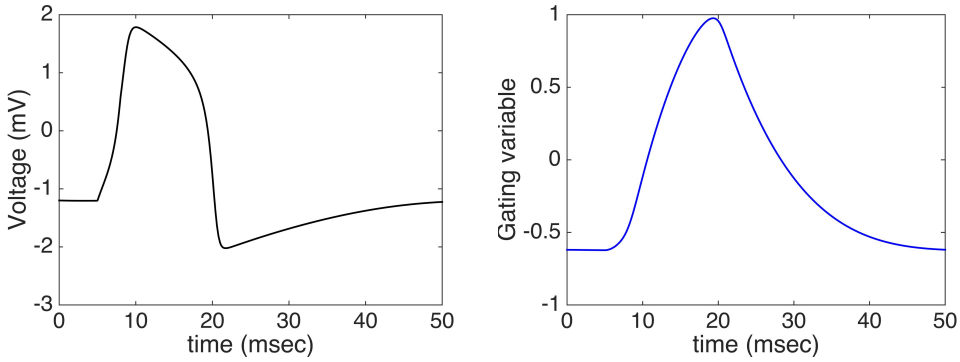

Figure 1.2: Voltage (left) and the gating variable y (right) in the Fitzhugh-Nagumo model.

1.1.3 Hindmarsh-Rose model

The Hindmarsh-Rose model is a modification of the FitzHugh-Nagumo model. An adaptation variable z was added to control the termination of the firing by lowering the effective current when the neuron is firing, and by returning to zero when the membrane potential has reached its resting value. In this manner, the neuron does not fire indefinitely and it is capable of generating oscillations which exhibit long intervals between the spikes [30, 31].

The model consists of three nonlinear differential equations (1.8) where x is

the membrane voltage, y is the recovery current and z is the bursting variable.

$$\begin{aligned} \frac{dx}{dt} &= -x^3 + 3x^2 + y - z + I, \\ \frac{dy}{dt} &= -5x^2 - y + 1, \\ \frac{dz}{dt} &= \mu(4(x + h) - z). \end{aligned} \tag{1.8}$$

An essential feature of the Hindmarsh model is its capacity to generate two of the most common signals: the tonic spiking, characterized by the continuous firing of the action potentials, and the bursting behaviour, in which oscillations appear. Numerous articles [30, 31, 32, 33] study in detail the transitions between these states.

The time courses obtained for solving equations (1.8) with $h = 1.6$ and $I = 2$ are showed in Figure 1.3. The parameter μ represents the ratio of time scales between fast and slow fluxes in the membrane. We performed experiments with various values of μ: the first row of Figure 1.3 illustrates the bursting behavior obtained for $\mu = 0.002$, while in the bottom row we show the tonic firing corresponding to $\mu = 0.02$.

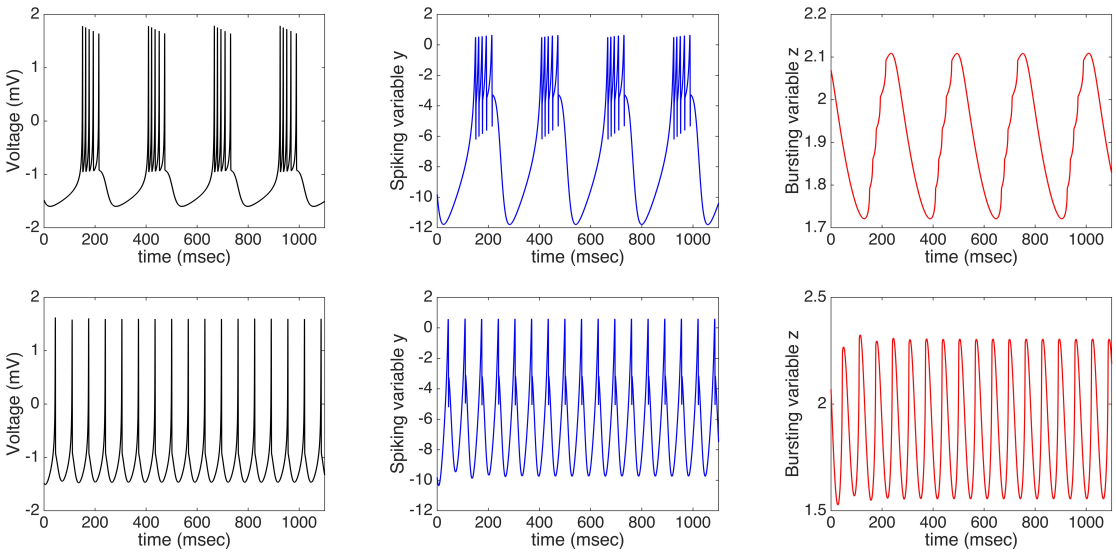

Figure 1.3: Simulation results of the Hindmarsh-Rose model with $h = 1.6$ and $I = 2$ in two cases: $\mu = 0.002$ (top row) and $\mu = 0.02$ (bottom row)

1.1.4 Izhikevich model

The Izhikevich model, like the Hindmarsh-Rose model, is able to reproduce both spiking and bursting behaviour [34] and consists of two differential equations:

$$\begin{aligned} C\frac{dv}{dt} &= k(v - v_{\text{rest}})(v - v_{\text{thresh}}) - u + I, \\ \frac{du}{dt} &= a[b(v - v_{\text{rest}}) - u], \end{aligned} \tag{1.9}$$

coupled with the following after-spike resetting:

$$\text{if } v \geq v_{\text{peak}} \text{ then } \begin{cases} v = c, \\ u = u + d. \end{cases} \tag{1.10}$$

Here v is the membrane potential, u the recovery current, C is the membrane capacitance, a the recovery time constant, c the value to which the voltage resets after having reached the peak value v_{peak}; the threshold potential is denoted by v_{thresh}. Whenever the depolarization exceeds v_{thresh} the resting membrane potential v_{rest}, a spike response is induced. The parameter d accounts for the difference between the outward and the inward currents activated during the spike, affecting the behavior after the spike. The parameters k and b can be determined using the information about the membrane excitability, i.e. the rheobase and the input resistance of the neuron [28]. As discussed in detailed in [28, 34], various classes of firing patterns corresponding to various neuron types can be observed by varying these parameters. In Table 1.3 we present the parameter values corresponding to three situations: a tonic neuronal firing, a fast rythmic bursting, also known as chattering, and an intrinsically bursting behavior.

In Figure 1.4 we show simulations obtained with model (1.9), using an explicit forward Euler method,

$$\begin{aligned} Cv(t + \Delta t) &= v(t) + \Delta t \left[k(v(t) - v_{\text{rest}})(v(t) - v_{\text{thres}}) - u(t) + I(t)\right], \\ u(t + \Delta t) &= u(t) + a[b(v(t) - v_{\text{rest}}) - u(t)], \end{aligned}$$

with time step $\Delta t = 0.5$ msec; the parameters corresponding to the three different firing patterns are given in Table 1.3.

Parameter	Tonic firing	Fast rythmic bursting	Intrinsically bursting	Unit measure
V_{rest}	-60	-60	-75	mV
V_{thresh}	-40	-40	-45	mV
V_{peak}	30	25	50	mV
C	100	50	150	pF
k	0.7	1.5	1.2	-
a	0.03	0.03	0.01	-
b	-2	1	5	-
c	-50	-40	-56	-
d	100	150	130	-
I	70	400	500	pA

Table 1.3: Parameter values in Izhikevich model for different neuronal firing patterns.

In addition to the continuous firing showed in the left column of Figure 1.4, in the center we observe high frequency bursts of spikes characterized by a very short interburst period. On the other hand, in the right column of Figure 1.4 we see that multiple spikes are being generated at the beginning of a sufficiently strong pulse, while further on, a regular firing pattern is formed.

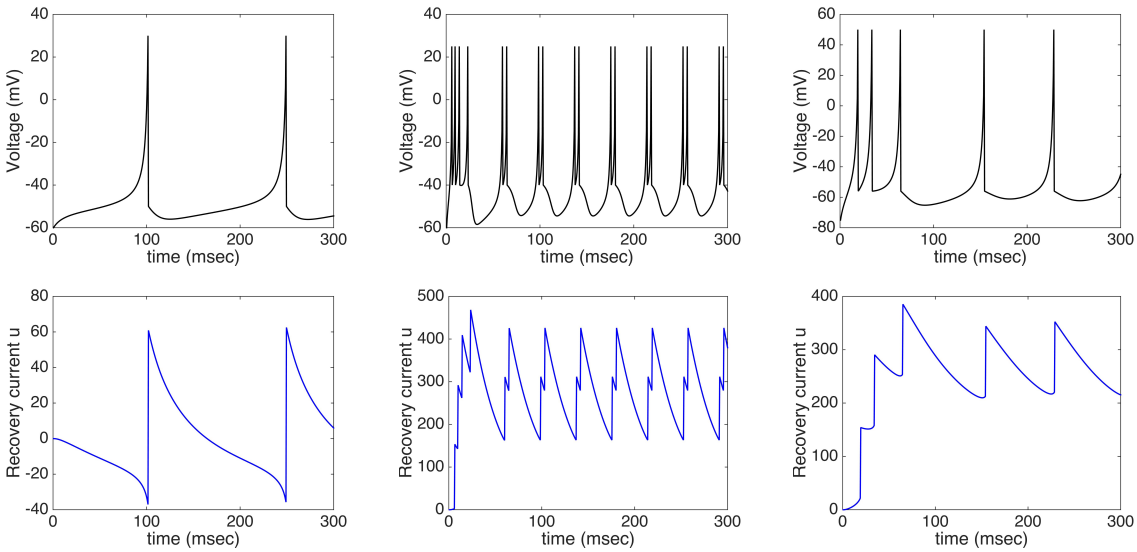

Figure 1.4: Simulation of the Izhikevich model [28, 34] using parameters defined in Table 1.3 corresponding to tonic firing (left), fast rythmic bursting (middle) and intrinsically bursting neurons (right).

1.2 The proposed electrophysiological model

In this section we provide a detailed description of the electrophysiologic model we used throughout this thesis. Based on Hodgkin-Huxley model, Cressman et al. [12, 13] features important additions as they include an ionic current for the sodium potassium pump, an ionic current for the glial uptake and a diffusion current of potassium outside the neighborhood. This section contains various modifications we brought to the original model [12, 13], based on physiological considerations. One of most important changes we have done was to adjust the extracellular potassium concentration to approximately 3mM during resting state. This is significantly lower than the value initially proposed by Cressman [12] and Barreto [13] but it represents the currently accepted value for the concentration of extracellular potassium for the brain during resting state [14].

1.2.1 Description

The model for the electrophysiological activity portion of this thesis follows the one developed by *Cressman et al.* in [12, 13]. Starting from the classical Hodgkin-Huxley model for the neuron membrane potential described in Section 1.1.1, the Cressman model introduces various essential features, including sodium and potassium dynamics and accounts for the ionic currents induced by the sodium potassium pump, glial potassium cleaning and potassium diffusion.

Following the Hodgkin-Huxley paradigm, the membrane potential and the gating variables n, m and h are governed by the differential equations:

$$c_m \frac{dV}{dt} = -I_{\mathrm{Na}^+} - I_{\mathrm{K}^+} - I_{\mathrm{leak}}, \tag{1.11}$$

$$\frac{dw}{dt} = \varphi(\alpha_w(V)(1-w) - \beta_w(V)w), \quad w \in \{n, m, h\}, \tag{1.12}$$

where c_m is the membrane capacitance, φ the time constant of the gating variables and the saturating functions α_w and β_w corresponding for each gating variable $w \in \{n, m, h\}$, are specified in Table 1.4.

As in the Fitzhugh-Nagumo model, Cressman and Barreto [12, 13] assume that the activation gate for sodium $m = m(V)$ is much faster than the other gates,

w	m	h	n
$\alpha_w(V)$	$0.1\dfrac{V+30}{1-\exp(-(V+30)/10)}$	$0.07\exp(-(V+44)/20)$	$0.01\dfrac{V+34}{1-\exp(-(V+34)/10)}$
$\beta_w(V)$	$4\exp(-(V+55)/18)$	$\dfrac{1}{1+\exp(-(V+4)/10)}$	$0.125\exp(-(V+44)/80)$

Table 1.4: Gating variables: voltage-dependent saturation functions.

reaching equilibrium sufficiently fast to justify the steady state approximation:

$$m = m(V) = \frac{\alpha_m(V)}{\alpha_m(V) + \beta_m(V)}.$$

The equations governing the ionic currents [13] corresponding to sodium, potassium and chloride are:

$$I_{\mathrm{Na}^+} = g_{\mathrm{Na}^+} m^3 h (V - V_{\mathrm{Na}^+}) + g_{\mathrm{Na}^+,\mathrm{leak}} (V - V_{\mathrm{Na}^+}), \tag{1.13}$$

$$I_{\mathrm{K}^+} = g_{\mathrm{K}^+} (V - V_{\mathrm{K}^+}) + g_{\mathrm{K}^+,\mathrm{leak}} (V - V_{\mathrm{K}^+}), \tag{1.14}$$

$$I_{\mathrm{leak,Cl}^-} = g_{\mathrm{Cl}^-} (V - V_{\mathrm{Cl}^-}), \tag{1.15}$$

where g_{Na^+}, $g_{\mathrm{Na}^+,\mathrm{leak}}$, g_{K^+} and $g_{\mathrm{K}^+,\mathrm{leak}}$ are the conductances and the leak conductances of sodium and potassium, and g_{Cl^-} is the leak conductance of chloride; their values are listed in Table 1.5. The total leak current is the sum of the leak currents of sodium, potassium and chloride:

$$I_{\mathrm{leak}} = g_{\mathrm{Na}^+,\mathrm{leak}} (V - V_{\mathrm{Na}^+}) + g_{\mathrm{K}^+,\mathrm{leak}} (V - V_{\mathrm{K}^+}) + g_{\mathrm{Cl}^-} (V - V_{\mathrm{Cl}^-}).$$

The reversal potentials V_{Na^+}, V_{K^+} and V_{Cl^-} are expressed in terms of the ionic concentrations inside and outside the membrane, and are obtained via the Nernst equations,

$$V_{\mathrm{X}} = 26.64 \ln\left(\frac{[\mathrm{X}]_{\mathrm{ecs}}}{[\mathrm{X}]_{\mathrm{i}}}\right), \quad \mathrm{X} \in \{\mathrm{Na}^+, \mathrm{K}^+, \mathrm{Cl}^-\}. \tag{1.16}$$

As the model does not include chloride dynamics, the concentrations of chloride inside and outside the cell are kept constant: $[\mathrm{Cl}^-]_{\mathrm{ecs}}$=6 mM and $[\mathrm{Cl}^-]_{\mathrm{i}}$=130 mM, yielding a reversal potential of chloride of -81.93mV.

Name	Symbol	Value	Units
Capacitance	c_m	1	μF/cm^2
Time constant	φ	3	1/msec
Sodium conductance	g_{Na^+}	46	mS/cm^2
Potasium conductance	g_{K^+}	16.25	mS/cm^2
Sodium leak conductance	$g_{\mathrm{Na}^+,\mathrm{leak}}$	0.0175	mS/cm^2
Potassium leak conductance	$g_{\mathrm{K}^+,\mathrm{leak}}$	0.02	mS/cm^2
Chloride conductance	g_{Cl}	0.05	mS/cm^2

Table 1.5: Parameter values for the Cressman model

In the Cressman model, the total concentration of sodium is assumed to be conserved, while the intracellular concentration of sodium is compensated by the potassium concentration outside the cell:

$$[\mathrm{Na}^+]_{\mathrm{ecs}} = 144\,\mathrm{mM} - \beta([\mathrm{Na}^+]_{\mathrm{i}} - 10.5\,\mathrm{mM}), \tag{1.17}$$

$$[\mathrm{K}^+]_{\mathrm{i}} = 140\,\mathrm{mM} + (10.5\,\mathrm{mM} - [\mathrm{Na}^+]_{\mathrm{i}}), \tag{1.18}$$

where 10.5 mM and 140 mM are the concentrations at rest of sodium and potassium inside the neuron, and 144 mM is the resting concentration of extracellular sodium.

The differential equations governing the intracellular concentration of sodium and the extracellular concentration of potassium are:

$$\tau\frac{d[\mathrm{Na}^+]_{\mathrm{i}}}{dt} = -\gamma\frac{I_{\mathrm{Na}^+}}{\beta} - 3J_{\mathrm{pump},\mathrm{Na}^+}, \tag{1.19}$$

$$\tau\frac{d[\mathrm{K}^+]_{\mathrm{ecs}}}{dt} = \gamma I_{\mathrm{K}^+} - 2\beta J_{\mathrm{pump},\mathrm{Na}^+} - J_{\mathrm{glia},\mathrm{K}^+} - J_{\mathrm{diff},\mathrm{K}^+}, \tag{1.20}$$

where $\tau = 1000$ is a conversion factor from seconds to milliseconds, the parameter $\gamma = 0.33$ mM cm$^2/\mu$C converts the electric current to mass flux [12] and $\beta = \eta_{\mathrm{n}}/\eta_{\mathrm{ECS}}$ is the ratio between the intracellular and extracellular volume of the cell, which in our case is $\beta = 1.33$.

In the model, $J_{\mathrm{pump},\mathrm{Na}^+}$ represents the ion current induced by the sodium potassium pump, $J_{\mathrm{glia},\mathrm{K}^+}$ is the ion current induced by the astrocytic potassium cleaning and $J_{\mathrm{diff},\mathrm{K}^+}$ accounts for the diffusion of potassium. These ion mass

currents are defined through the equations:

$$J_{\text{pump,Na}^+} = \left(\frac{\rho}{1+\exp(25-[\text{Na}^+]_\text{i})/3)}\right) \times \left(\frac{1}{1+\exp(2.2-[\text{K}^+]_\text{ecs})}\right), \quad (1.21)$$

$$J_{\text{glia,K}^+} = \frac{G_\text{glia}}{1+\exp((14.7-[\text{K}^+]_\text{ecs})/25)}, \quad (1.22)$$

$$J_{\text{diff,K}^+} = \varepsilon([\text{K}^+]_\text{ecs} - k_\infty), \quad (1.23)$$

where ρ is the strength of the sodium potassium pump, G_glia the strength of the glial uptake, ε is the diffusion coefficient and k_∞ is the potassium bath concentration.

1.2.2 Neuronal activation

In this section we provide a detailed description of the mechanism underlying neuronal activation in our model and describing the different metabolic response to various levels of synaptic activity.

Rather than driving neuronal activation by explicitly modelling the glutamate-glutamine cycle as done in [9], here we rely on the fact that during the neuronal activation the glutamate secreted by the presynaptic neuron is sensed by the postsynaptic glutamate receptors and there is an increase of the influx of sodium and potassium ions [35].

Mathematically, this physiological observation translates into a temporary increase of the leak conductances of sodium and potassium for the period of neuronal excitation:

$$g_{\text{Na}^+,\text{leak}}(t) = (1+\xi(t))g^0_{\text{Na}^+,\text{leak}} \quad (1.24)$$

$$g_{\text{K}^+,\text{leak}}(t) = (1+\xi(t))g^0_{\text{K}^+,\text{leak}} \quad (1.25)$$

where $g^0_{\text{Na}^+,\text{leak}}$ and $g^0_{\text{K}^+,\text{leak}}$ are the constant resting values of the leak conductances, and $\xi = \xi(t)$ is the time dependent *activation function* that models the effect of glutamate. The effect of this function on the neuronal firing frequency is discussed in Section 1.2.4.

To summarize, our electrophysiological model consists of 5 differential equa-

tions (1.11), (1.12), (1.19) and (1.20) and can be expressed as:

$$\frac{du}{dt} = f(u, \xi), \tag{1.26}$$

where u is a vector containing the unknows:

$$u = \begin{bmatrix} V \\ [\mathrm{Na}^+]_{\mathrm{i}} \\ [\mathrm{K}^+]_{\mathrm{ecs}} \\ n \\ h \end{bmatrix}, \tag{1.27}$$

while ξ is an activation function controlling the level of neuronal firing (see Figure 1.7).

1.2.3 Calibration

In light of the in-vitro experiments confirming that the excitability of the neuron depends strongly on the concentration of potassium in the extracellular space [36], the firing pattern of the electrophysiological model depends on the parameters that control the extracellular potassium concentration, which in Cressman model are k_∞, $\varepsilon_{\mathrm{ecs}}$, G_{glia}, and ρ. In [12] the authors performed a bifurcation analysis for these parameters, by considering a reduced model consisting of equations (1.17)-(1.20), in which the fast scale effects of the complete model were ignored. In this manner they were able to distinguish between regions characterized by high-frequency firing bursts and regions of continuous firing.

In our case, rather than controlling the potassium level itself, we induce the firing mechanism by controlling the input function ξ. Firstly, we performed a manual calibration of the electrophysiological model such that the choice of the four parameters mentioned above results in a 4 Hz background firing. With respect to the original model proposed by Cressman [12], we neglected the calcium dynamics, as it was done by the same author in a more recent publication [13]. Also, in order to be in agreement with the recent experimental literature [14] on the concentration of extracellular potassium during resting state for a human

brain, we downgraded the potassium bath concentration k_∞ to 3 mM. The partitioning of the total potassium cleaning power $T_p = G_{\text{glia}} + \rho$ was done such that 60% of the total cleaning power was attributed to the glia and 40% to the neuron. The parameter values chosen in order to obtain a firing frequency of 4Hz, characteristic for the neuron at rest, are given in Table 1.6, while the initial conditions are showed in Table 1.7.

Name	Symbol	Value	Units
Potassium bath concentration	k_∞	3	mM
Diffusion coefficient	ε	9.33	s^{-1}
Glial uptake strength	G_{glia}	20.75	mM/s
Neuronal pump strength	ρ	13.83	mM/s

Table 1.6: Parameter values in the electrophysiological model corresponding to a 4Hz background firing rate.

V (mV)	n	h	$[K^+]_{ecs}$ (mM)	$[Na^+]_i$ (mM)
-57.3351	0.1417	0.9177	2.9871	10.0039

Table 1.7: Initial conditions of membrane potential, ionic concentrations and gating variables for the Cressman model.

1.2.4 Simulation results

In this section we show various results obtained from simulating our modification of the Cressman model by using the ode15s built in Matlab solver.

In Figure 1.5 we see the membrane potential, the intracellular sodium concentration, the extracellular potassium concentration and the two gates of activation, respectively inactivation for sodium and potassium, for the parameter choice summarized in Table 1.6 with the initial conditions given in Table 1.7. Setting the activation function to $\xi = 0$, produces the characteristic response for the neuron at rest: a neuronal frequency of 4 spikes within one second, a concentration of intracellular sodium of approximatively $[Na]_i \approx 10$ mM and an extracellular potassium concentration of $[K]_{ecs} \approx 3$ mM.

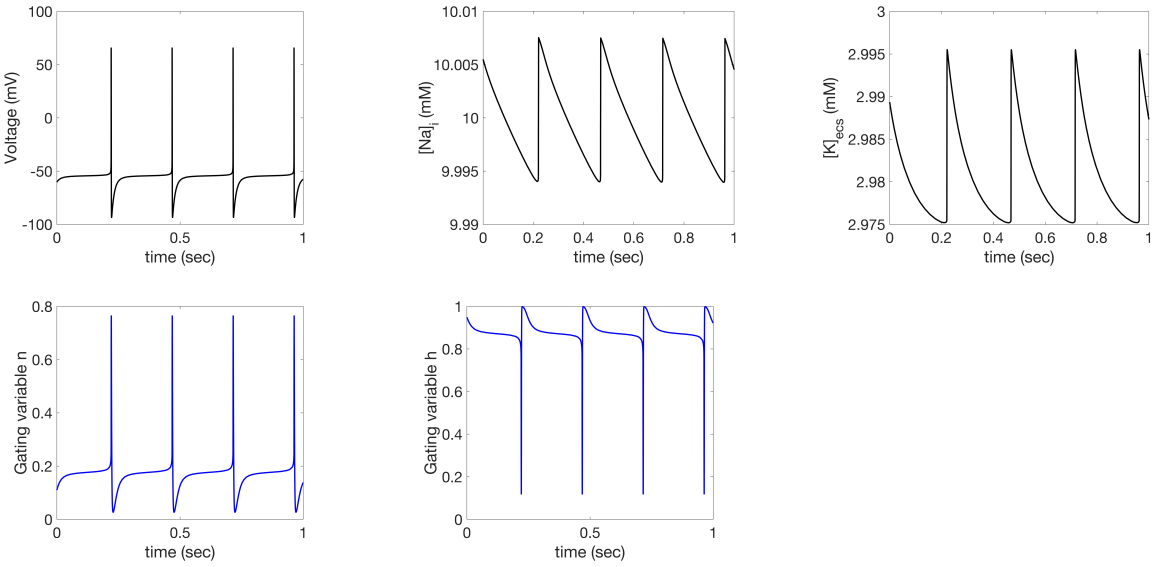

Figure 1.5: Simulation of the Cressman model corresponding to a 4Hz background firing obtained for $\xi = 0$ and the parameter values defined in Table 1.6.

In the experiments above, the parameter k_∞ was tuned to obtain the 4Hz background firing. Multiple simulations to study the dependency between k_∞ and the firing frequency suggest that increasing the value of the potassium bath concentration leads to an increase in the firing frequency as shown in Figure 1.6.

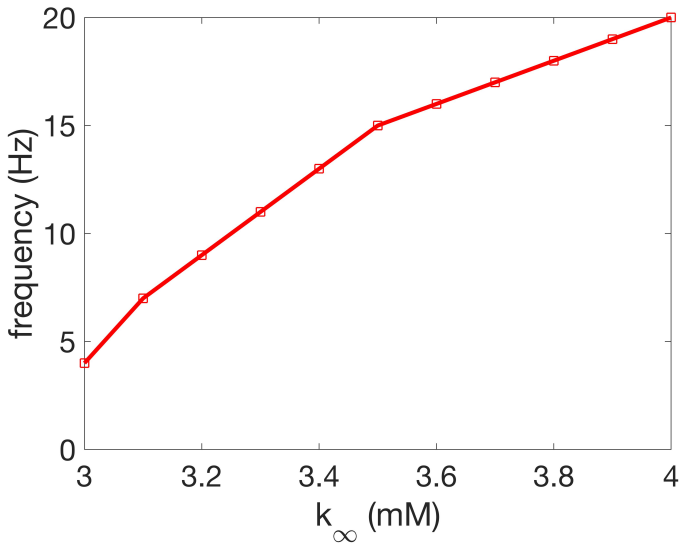

Figure 1.6: Frequency dependence of the k_∞ parameter. Increasing the bath concentration of potassium produces an increase in the frequency.

As described in Section 1.2.2, the neuronal activation is modeled through a temporary increase in the sodium and potassium leak conductances, in turn regulated by the time dependent activation function ξ. As expected, increasing

the function ξ leads to an increase in the firing frequency. Figure 1.7 shows the effect of ξ on the firing frequency. In these experiments we used the parameters as defined in Table 1.6 and we varied $\xi \in [0, 10]$.

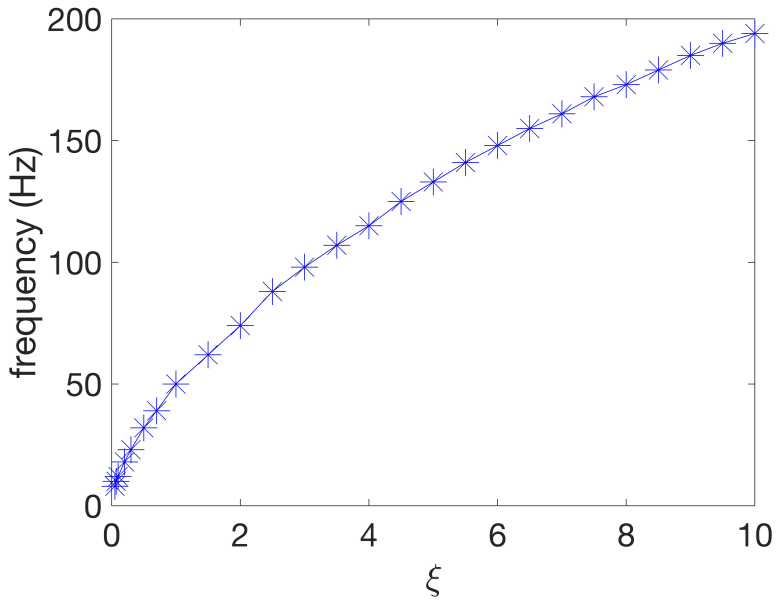

Figure 1.7: Dependence of frequency on the activation parameter ξ.

The frequency band characterized by a firing frequency between 8 and 13 Hz, known as the alpha state, occurs during awake resting state. When simulating the alpha state we considered three different values of the activation function: $\xi = 0.05$ corresponding to 8 Hz, $\xi = 0.07$ corresponding to 10 Hz and $\xi = 0.1$ corresponding to 12Hz. In Figure 1.8 we show the time courses of membrane potential, ionic concentrations of intracellular sodium and extracellular potassium and gating variables n and h for these three cases. Note the change in the intracellular sodium concentration from the first column, where it settles around $[\text{Na}]_\text{i} = 10.5$ mM for a 8Hz firing to the last column where $[\text{Na}]_\text{i} = 11.3$ mM corresponds to a firing of 12 Hz.

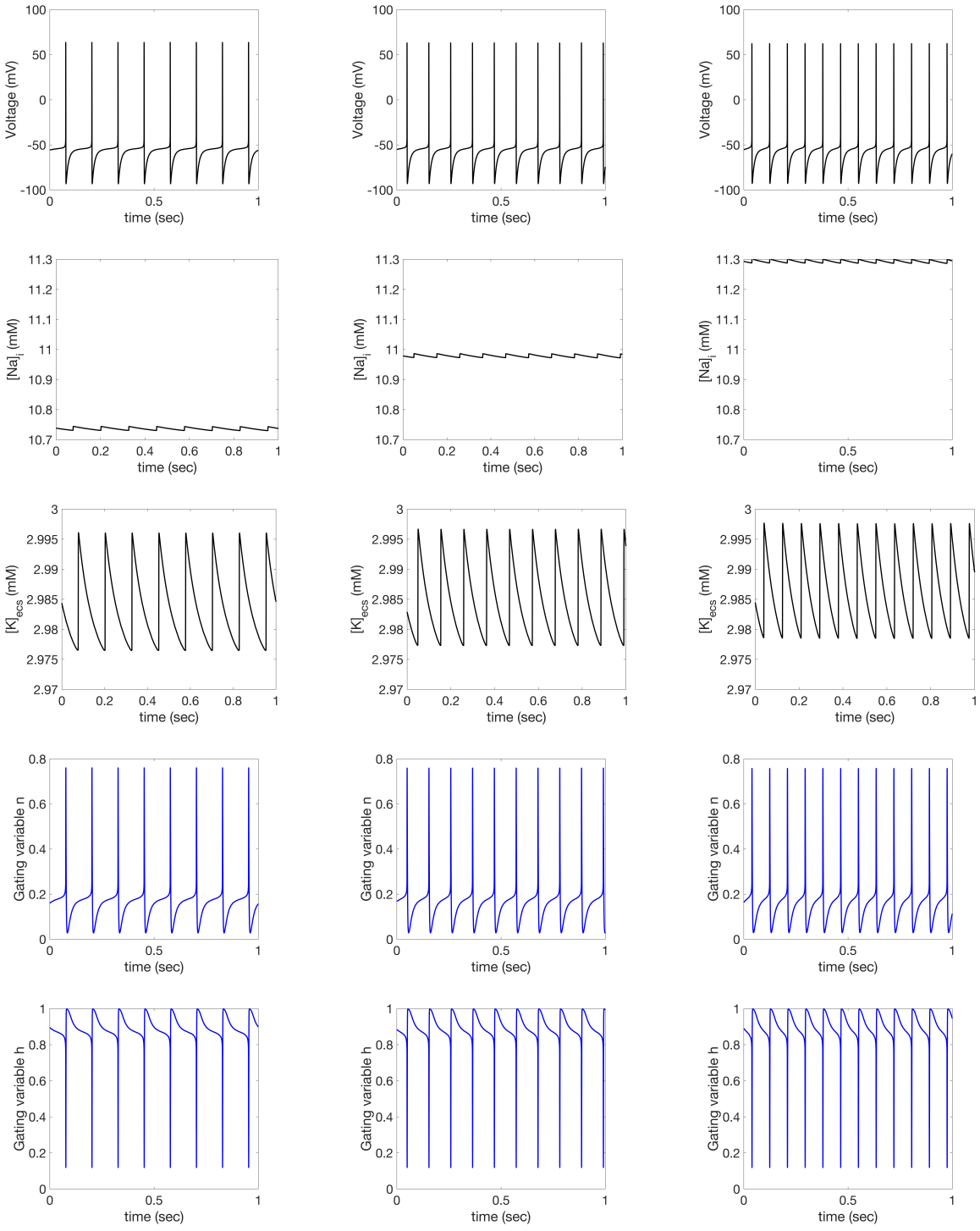

Figure 1.8: Results obtained for simulating the Cressman model for $\xi = 0.05$ (8Hz, left column), $\xi = 0.07$ (10Hz, middle column) and $\xi = 0.1$ (12Hz, right column).

Figure 1.9 shows the ionic currents related to sodium potassium pump and glial potassium cleaning for the three frequencies that we consider in alpha awake resting state. These quantities will play a role in the next chapter, where we discuss the metabolic response during different levels of neuronal activity.

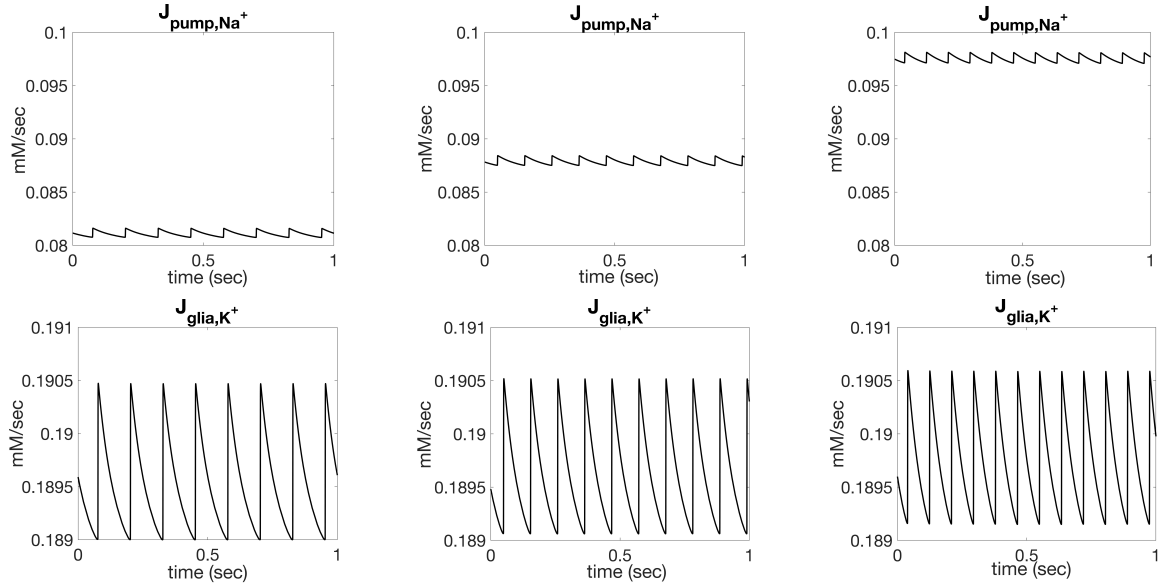

Figure 1.9: Time course of the ionic current corresponding to the sodium potassium pump (upper row) and the glial uptake (bottom row) for an alpha firing frequency of 8Hz (left column), 10Hz (middle column) and 12Hz (right column).

The Cressman model, like the Izhikevich and Hindmarsh models discussed in Section 1.1.4 and Section 1.1.3, can produce other firing patterns: the five bursts that can be observed in Figure 1.10 were obtained with a modified Cressman model where the diffusion coefficient ε is reduced to a third of its baseline value.

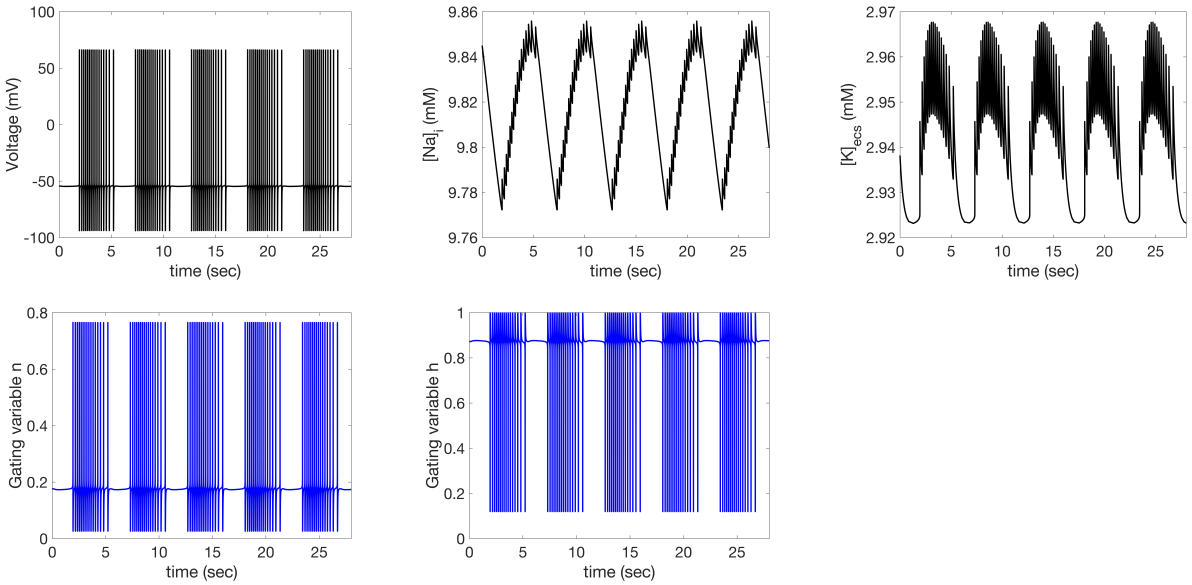

Figure 1.10: Bursting pattern obtained by simulating the modified Cressman model with the parameters defined in Table 1.6 but reducing the diffusion coefficient to a third of its normal value.

Chapter 2

Brain Metabolism

Brain energetics plays an important role in neuronal activity because the latter can be sustained only if the metabolic processes can produce enough energy to restore the difference in the transmembrane potential.

2.1 Introduction

Spatially lumped metabolic models comprise separate compartments, established according to physiological considerations to be investigated. Each compartment is, in turn, characterized by its biochemical species and corresponding biochemical reactions. The communication between compartments occurs through exchange of biochemical species. Mathematically, spatially lumped dynamic metabolic models are governed by systems of ordinary differential equations. Each reaction occurring in a compartment has a corresponding reaction flux denoted by ψ; similarly, for each exchange between compartments, there is a related transport rate J. The aggregate of biochemical species, reaction fluxes and transport rates for all compartments are the constituents of the metabolic network.

The mathematical description of the reaction rates depends on the type of enzyme and the expression level [37]. The classic Michaelis-Menten form assumes that an enzyme e interacts with a substrate S to form an enzyme-substrate eS which is then decomposed into the enzime e and a product P:

$$\psi : \ e + S \longrightarrow eS \longrightarrow e + P.$$

The corresponding reaction flux ψ can be can written as:

$$\psi = V_{\max} \frac{[S]}{K_{\max} + [S]},$$

where $V_{\max}$ is the maximum reaction velocity, $K_{\max}$ is the affinity constant and $[S]$ the concentration of the substrate S.

On the other hand, the transport fluxes of biochemical species can take place either via passive diffusion, as is usually the case for gases and lipids, or with the help of a transporter. In the passive diffusion case, the transport rates can be expressed as:

$$J = \lambda \left([S]_x - [S]_y \right),$$

where $[S]_x$ and $[S]_y$ are the concentration of the species in compartment x and y respectively. Many molecules however, are too large or too charged to pass through the cell membrane and require carrier proteins to facilitate their cross-membrane transport. Carrier facilitated transfers can be seen as enzymatic reactions in which the role of enzyme is played by a membrane bound protein X [37]:

$$J: \ S_x + X \longrightarrow SX \longrightarrow X + S_y,$$

and the corresponding transfer rate can be written as:

$$J = T_{\max} \frac{[S]_x}{M + [S]_x},$$

where M is the affinity and $T_{\max}$ is the maximum transport rate. When the carrier acts isotropically, the bidirectional transport flux can be written as:

$$J = T_{\max} \left(\frac{[S]_x}{M + [S]_x} - \frac{[S]_y}{M + [S]_y} \right).$$

2.2 Main biochemical reactions

Glycolysis refers to a chain of chemical reactions taking place in the cytosol of the cell that convert one molecule of glucose (Glc) into two molecules of pyruvate

(Pyr),

$$\mathrm{Glc} + 2\mathrm{NAD}^+ + 2\mathrm{ADP} + 4\mathrm{P}_i \longrightarrow 2\mathrm{Pyr} + 2\mathrm{NADH} + 2\mathrm{ATP}.$$

The first step of the glycolysis reaction adds one phosphate group to the sixth carbon of the glucose molecule, producing a molecule of glucose 6-phosphate (G6P). This process is catalyzed by the enzyme hexokinase and consumes one molecule of ATP. In the second step, the enzyme phosphoglucose isomerase (pfg) transforms the G6P molecule into fructose 6-phosphate (F6P), which is later changed into fructose 1,6-phosphate (FBP) with the help of phosphofructokinase (pfk). In this third step, one molecule of ATP is consumed.

Further on, the aldolase enzyme separates FBP into two individual molecules consisting of three carbon atoms each: glyceraldehyde-3-phosphate (GAP) and hydroxyacetone phosphate (DHAP), which is transformed through the enzyme triphosphate isomerase (tim) into GAP; as a result, at the end of the fifth step, two molecules of GAP have been produced. So far in the process two molecules of ATP have been consumed. GAP is then transformed into 1,3 biphosphoglycerate (BPG), with the action of the glyceraldehyde phosphate dehydrogenase (gapdh) enzyme, in a process where one NAD^+ molecule is consumed. In the seventh step, one phosphate group is cleaned from BPG through the enzyme phosphoglycerate kinase (PK) forming 3-phosphate glycerate (3PG), in a reaction where two molecules of ATP are being produced. Subsequently, the enzyme phosphoglyceromutase shifts one phosphate group from the third carbon to the second one, therefore producing one molecule of 2-phosphoglycerate (2PG). In the next step, through the enolase enzyme, 2PG loses one molecule of H_2O and becomes phosphoenolpyruvic acid (PEP). The last step of glycolysis consists of the conversion of PEP into pyruvate, which occurs with the aid of pyruvate kinase and generates two ATP molecules.

In Figure 2.1 we present a schematic overview of this process. The initial and the end product of the glycolysis reaction (Glc, respectively Pyr) are coloured in green while the intermediary products are given in blue. The enzyme corresponding to each reaction is indicated on top of the arrow; additionally, we specify the steps in which ATP is consumed in red and the steps in which ATP is produced

in blue.

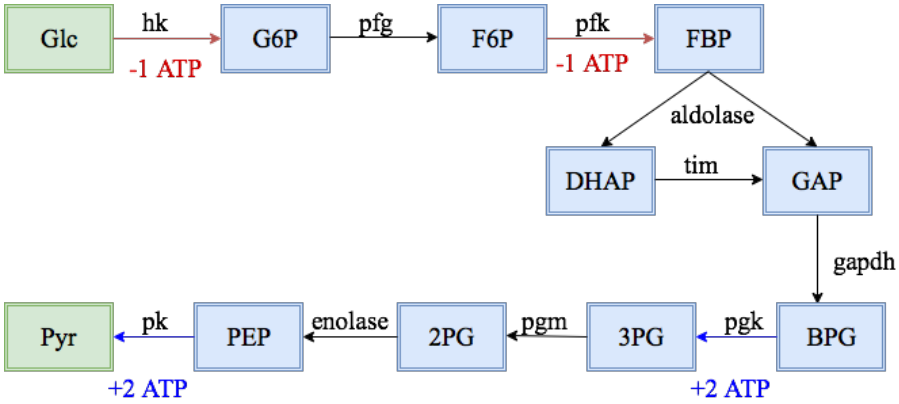

Figure 2.1: Glycolysis reaction: intermediate steps

Some metabolic models [9, 38] include, in addition to glucose and pyruvate, various intermediary products. For example, in [38], the glycolysis reaction consists of the following steps: the hexokinase-phosphofructokinase system (HK-PFK), phosphoglycerate kinase (PGK) and pyruvate kinase (PK), and additionally the intermediary products PEP and GAP are modelled through differential equations. On the other hand, the glycolysis model used in [9] follows hexokinase, phosphoglucose isomerase, phosphofructokinase and phosphoglycerate kinase, and the dynamic behavior of G6P, F6P, GAP and PEP is being studied.

A portion of the pyruvate produced in the glycolysis reaction enters mitochondria and participates in the **tricarboxylic acid cycle (TCA)**, also known as the **Krebs cycle**, where it is transformed into three carbon dioxide molecules in a process where one ATP and five NADH are produced:

$$\mathrm{Pyr} + \mathrm{ADP} + 5\mathrm{NAD}^{+} \longrightarrow 3\mathrm{CO}_2 + \mathrm{ATP} + 5\mathrm{NADH}.$$

Oxidative phosphorylation is the last stage of cellular respiration, and it comprises two steps: the electron transport chain and chemiosmosis. In the electron transport chain, electrons pass from one molecule to another through a series of redox reactions. The energy released in these reactions is then used to produce ATP in the process called chemiosmosis. In the oxidative phosphorylation the NADH produced in the two reactions described above pass their electrons to oxygen, with the help of some intermediary species that are embedded in the membrane. The energy released in this process pumps H^{+} ions, causing them to

move into the intermembrane space and later on, with the help of the enzyme ATPsynthase ATP is being produced:

$$O_2 + 2NADH + 5ADP \longrightarrow 2NAD^+ + 5ATP + H_2O.$$

Creatine phosphorylation is a reversible reaction in which one phosphate group is transferred from phosphocreatine to ADP to form ATP:

$$PCr + ADP \longleftrightarrow Cr + ATP.$$

During intense activity, phosphocreatine can be used as a buffer of ATP concentration.

Some of the concentrations of the species mentioned above can be measured through **nuclear magnetic resonance spectroscopy** (**NMR**) or (**MRS**), a noninvasive diagnostic test that analyzes molecules such as hydrogen protons and uses this information in order to determine the concentration of various brain metabolites [39].

The oxygenation status and the brain hemodynamics can be assessed through **near infrared spectroscopy (NIRS)**, which is a noninvasive optical image technique in which blood flow changes associated with brain activity can be measured by using low levels of light. NIRS relies on two main tissue characteristics: the relative transparency of tissue to light in the near infrared range, and the oxygenation dependent light that absorbs hemoglobin features. Through this procedure any changes in oxyhemoglobin, deoxyhemoglobin or total hemoglobin can be detected.

2.3 Review of metabolic models

2.3.1 Aubert and Costalat models

In 2002, Aubert and Costalat [38] proposed a mathematical model to follow the behaviour of the main metabolites during neuronal activation. The model consists of two compartments, tissue and capillaries, and comprises of fifteen state variables including glucose (intracellular and capillary), lactate (intracellular and

capillary), oxygen (intracellular and capillary), pyruvate, phosphocreatine, ATP, NADH, glyceraldehyde-3-phosphate, phosphoenolpyruvate, intracellular sodium concentration, venous volume and deoxyhemoglobin.

Neuronal activation is attained by increasing intracellular sodium concentration, which leads to an increase in the blood flow and eventually an increase in venous blood volume. The two input functions consist of a stimulus $\xi(t)$ which establishes the energetic need depending on different levels of neuronal activation and the function $F_{in}(t)$ controlling the increase in the blood flow level that occurs during activation. The oxygen in the capillaries is used as an input for the balloon model [15, 16, 17], while the BOLD signal obtained from the balloon model and the metabolite concentrations represent the outputs. Figure 2.2 contains a schematic representation of this model.

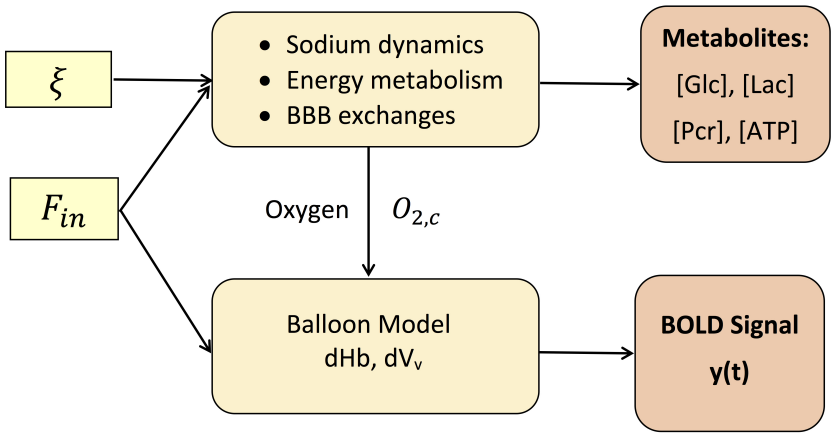

Figure 2.2: Schematic overview the Aubert and Costalat model.

The stimulus enters in the equation for intracellular concentration of sodium:

$$\frac{d[\mathrm{Na}^+]_i}{dt} = I_{\mathrm{Na,leak}} - 3J_{\mathrm{pump,Na^+}} + \xi(t), \tag{2.1}$$

where $I_{\mathrm{Na,leak}}$ is the sodium leak current modelled in [38] through the Hodgkin-Horowicz equation:

$$I_{\mathrm{leak,Na}} = \frac{S_m}{V_i} \frac{g_{\mathrm{Na^+}}}{\mathrm{F}} \left(\frac{\mathrm{RT}}{\mathrm{F}} \ln \frac{[\mathrm{Na}^+]_{\mathrm{ecs}}}{[\mathrm{Na}^+]_i} - V \right), \tag{2.2}$$

$J_{\mathrm{pump,Na^+}}$ represents the rate of the sodium potassium pump and depends on the

availability of ATP and on the intracellular sodium concentration:

$$J_{\text{pump,Na}^+} = \frac{S_m}{V_i} k_{\text{pump}} [\text{ATP}][\text{Na}^+]_i \left(1 + \frac{[\text{ATP}]}{K_{\text{m,pump}}}\right)^{-1}, \tag{2.3}$$

and

$$\xi(t) = \nu_1 + \frac{\nu_2}{\tau_{\text{stim}}} \exp\left(\frac{-t}{\tau_{\text{stim}}}\right) \text{ for } 0 \leq t \leq t_{\text{end}}, \tag{2.4}$$

drives the energetic need. The description and values of the parameters used in equations (2.2) and (2.3) are given in Table 2.1

Description	Parameter	Value	Unit
Membrane potential	V	-70	mV
Sodium conductance	g_{Na^+}	0.0039	mS/cm^2
Faraday constant	F	$9.65 \cdot 10^4$	C/mol
Product between the universal rate constant and temperature divided by the Faraday constant	RT/F	26.73	mV
Ratio of membrane area and intracellular volume	S_m/V_i	$9 \cdot 10^4$	1/cm
Extracellular concentration of sodium	$[\text{Na}^+]_{\text{ecs}}$	150	mM
Intracellular resting concentration of sodium	$[\text{Na}^+]_i^0$	15	mM
Transport rate constant	k_{pump}	$0.29 \cdot 10^{-6}$	$\frac{\text{cm}}{\text{mM·s}}$
Affinity constant for the sodium potassium pump	$K_{\text{m,pump}}$	0.5	mM

Table 2.1: Parameters used for describing the intracellular concentration of sodium in Aubert and Costalat model [38].

The model tracks the changes in the concentration of the biochemical species, $X = \{\text{Glc, Lac, O}_2, \text{Pyr, GAP, PEP, PCr, NADH, ATP}\}$, accounting separately when they belong to different compartments. More specifically, the concentrations of glucose, lactate and oxygen are tracked separately in tissue and in capillaries. To distinguish the compartment where they belong, by $[X]_i$ we denote the intracellular concentrations and by $[X]_c$ the concentrations in the capillaries. The steady state values of the metabolites and intermediate concentrations are listed in Table 2.2.

	[Glc]	[O_2]	[Lac]	[Pyr]	[PCr]	[GAP]	[PEP]	[NADH]	[ATP]
c	4.56	7.01	0.35						
i	1.2	0.026	1	0.16	5	0.0057	0.02	0.026	2.2

Table 2.2: **Metabolites:** List of metabolites in the two compartments (capillary (c), intracellular (i)) and their resting concentrations (in mM).

The dynamics of the metabolites inside the tissue is modeled through the following differential equations [38].

$$\begin{aligned}
\frac{d[\mathrm{Glc}]_i}{dt} &= j_{\mathrm{Glc}} - \psi_{\text{HK-PFK}},\\
\frac{d[\mathrm{Lac}]_i}{dt} &= \psi_{\mathrm{LDH}} - j_{\mathrm{Lac}},\\
\frac{d[\mathrm{O_2}]_i}{dt} &= j_{\mathrm{O_2}} - n_{\mathrm{aero}} j_{\mathrm{mit}},\\
\frac{d[\mathrm{Pyr}]}{dt} &= \psi_{\mathrm{PK}} - \psi_{\mathrm{LDH}} - \psi_{\mathrm{mit}},\\
\frac{d[\mathrm{GAP}]}{dt} &= 2\psi_{\text{HK-PFK}} - \psi_{\mathrm{PGK}},\\
\frac{d[\mathrm{PEP}]}{dt} &= \psi_{\mathrm{PGK}} - \psi_{\mathrm{PK}},\\
\frac{d[\mathrm{PCr}]}{dt} &= -\psi_{\mathrm{CK}},\\
\frac{d[\mathrm{NADH}]}{dt} &= \psi_{\mathrm{PGK}} - \psi_{\mathrm{LDH}} - \psi_{\mathrm{mit}},\\
\frac{d[\mathrm{ATP}]}{dt} &= \left(\psi_{\mathrm{PGK}} - 2\psi_{\text{HK-PFK}} + \psi_{\mathrm{PK}} - \psi_{\mathrm{ATPase}} - J_{\mathrm{pump,Na^+}} + n_{\mathrm{op}}\psi_{\mathrm{mit}} + \psi_{\mathrm{CK}}\right)\zeta,
\end{aligned} \tag{2.5}$$

where:

$$\zeta = \left(1 - \frac{d[\mathrm{AMP}]}{d[\mathrm{ATP}]}\right)^{-1},$$

where j_C denotes the transport rate of metabolite $C = \{[\mathrm{Glc}], [\mathrm{Lac}], [\mathrm{O_2}]\}$ across the BBB where the mathematical expressions follow (2.8) and (2.9), $\psi_{\text{HK-PFK}}$, ψ_{PK} and ψ_{PGK} are the reaction rates corresponding to hexokinase-phosphofructokinase, pyruvate kinase and phosphoglycerate kinase, respectively and ψ_{CK} represents the rate of the creatine kinase. The ATPase flux ψ_{ATPase} set to 0.149 mM/s accounts for the energetic need required for processes other than the sodium potassium pump. The equations for the reaction rates and the relevant parameters are listed in Table 2.11.

The dynamics of the capillary glucose, lactate and oxygen concentrations are:

$$\begin{aligned}
\frac{d[\mathrm{Glc}]_c}{dt} &= J_{\mathrm{Glc}} - \frac{1}{r_c} j_{\mathrm{Glc}},\\
\frac{d[\mathrm{Lac}]_c}{dt} &= J_{\mathrm{Lac}} + \frac{1}{r_c} j_{\mathrm{Lac}},\\
\frac{d[\mathrm{O_2}]_c}{dt} &= J_{\mathrm{O_2}} - \frac{1}{r_c} j_{\mathrm{O_2}},
\end{aligned} \tag{2.6}$$

where r_c is the ratio between capillary volume (V_c) and intracellular volume (V_i)

and J_C for $C = \{\mathrm{Glc}, \mathrm{Lac}, \mathrm{O_2}\}$ denotes the contribution from the blood flow, governed by equations (2.10). In [38] the concentration of oxygen in capillaries is expressed as the average of the arterial concentration and the concentration at the end of the capillaries:

$$[\mathrm{O_2}]_c = \frac{[\mathrm{O_2}]_a + [\mathrm{O_2}]_{\bar{c}}}{2}. \tag{2.7}$$

Rate equations	**Parameter**	**Value**	**Unit**
Hexokinase phosphofructokinase ($\psi_{\text{HK-PFK}}$)	$k_{\text{HK-PFK}}$	0.12	s^{-1}
	$K_{1,\text{ATP}}$	1	mM
$k_{\text{HK-PFK}}[\text{ATP}]\left[1+\left(\frac{[\text{ATP}]}{\mathrm{K}_{1,\text{ATP}}}\right)^{n_H}\right]^{-1}\frac{[\text{Glc}]_i}{[\text{Glc}]_i+\mathrm{K}_g}$	n_H	4	-
	K_g	0.05	mM
Pyruvate kinase (ψ_{PK})	k_{PK}	86.7	$\mathrm{mM}^{-1}\mathrm{s}^{-1}$
$k_{\text{PK}}[\text{PEP}][\text{ADP}]$			
Lactate dehydrogenase (ψ_{LDH})	k^+_{LDH}	2000	$\mathrm{mM}^{-1}\mathrm{s}^{-1}$
$k^+_{\text{LDH}}[\text{Pyr}][\text{NADH}] - k^-_{\text{LDH}}[\text{Lac}]_i[\text{NAD}^+]$	k^-_{ldh}	44.8	$\mathrm{mM}^{-1}s^{-1}$
Creatine kinase (ψ_{CK})			
$k^+_{\text{CK}}[\text{PCr}][\text{ADP}] - k^-_{\text{CK}}[\text{Cr}][\text{ATP}]$	k^+_{CK}	3666	$\mathrm{mM}^{-1}\mathrm{s}^{-1}$
	k^-_{CK}	20	$\mathrm{mM}^{-1}s^{-1}$
where $[\text{PCr}]+[\text{Cr}] = \mathrm{P}_{\text{tot}}$	P_{tot}	10	mM
Phosphoglycerate kinase (ψ_{PGK})			
$k'_{\text{PGK}}[\text{GAP}][\text{ADP}]\frac{[\text{NAD}^+]}{[\text{NADH}]}$	k'_{PGK}	42.6	$\mathrm{mM}^{-1}s^{-1}$
where $[\text{NADH}]+[\text{NAD}^+] = \mathrm{N}$	N	0.212	mM

Table 2.3: Rate equations and their corresponding parameters in Aubert and Costalat model [38].

The transport rates of glucose and lactate across the Blood-Brain-Barrier are described following a classical Michaelis Menten formalism:

$$\begin{aligned} j_{\text{Glc}} &= T_{\text{max,Glc}}\left[\frac{[\text{Glc}]_c}{[\text{Glc}]_c + K_{\text{t,Glc}}} - \frac{[\text{Glc}]_i}{[\text{Glc}]_i + K_{\text{t,Glc}}}\right], \\ j_{\text{Lac}} &= T_{\text{max,Lac}}\left[\frac{[\text{Lac}]_i}{[\text{Lac}]_i + K_{\text{t,Lac}}} - \frac{[\text{Lac}]_c}{[\text{Lac}]_c + K_{\text{t,Glc}}}\right], \end{aligned} \tag{2.8}$$

where $\mathrm{T}_{\text{max,Glc}}$ and $\mathrm{T}_{\text{max,Lac}}$ are the maximum transport rates for glucose and lactate and $\mathrm{K}_{\text{t,Glc}}$ and $\mathrm{K}_{\text{t,Lac}}$ are affinity constants, whose values are listed in Table 2.4.

The oxygen transport rate depends on the intracellular concentration of oxy-

gen ($[O_2]_i$), the capillary concentration of oxygen ($[O_2]_c$), the permeability of the Blood-Brain-Barrier (P), the surface S_c, the intracellular volume (V_i), hemoglobin (Hb) and its oxiphoric power (OP) defined as the maximum number of oxygen molecules carried by one mole of hemoglobin, as well as on the affinity constant for oxygen K_{O_2}:

$$j_{O_2} = \frac{PS_c}{V_i}\left(K_{O_2}\left(\frac{Hb \cdot OP}{[O_2]_c} - [O_2]_i\right)\right). \tag{2.9}$$

The blood flow related contributions to the variations of glucose, lactate and oxygen concentrations are described by:

$$\begin{aligned} J_{Glc} &= \frac{2F_{in}(t)}{V_c}\left(C_{art,Glc} - [Glc]_c\right), \\ J_{Lac} &= \frac{2F_{in}(t)}{V_c}\left(C_{art,Lac} - [Lac]_c\right), \\ J_{O_2} &= \frac{2F_{in}(t)}{V_c}\left(C_{art,O_2} - [O_2]_c\right), \end{aligned} \tag{2.10}$$

where $F_{in}(t)$ is the input function controlling the blood flow defined in equation (2.19), V_c is the volume of the capillaries, $C_{art,Glc}$, $C_{art,Lac}$ and C_{art,O_2} are the arterial concentrations of glucose, lactate and oxygen, which are assumed to remain constant, and $[Glc]_c$, $[Lac]_c$ and $[O_2]_c$ the capillary concentrations.

The values of the arterial concentrations and of the other parameters in the description of the blood flow can be found in Table 2.5.

Transport flux	Parameter	Value	Unit
Glucose	$T_{max,Glc}$	0.0476	mM/s
	$K_{t,Glc}$	9	mM
Lactate	$T_{max,Lac}$	0.00628	mM/s
	$K_{t,Lac}$	0.5	mM
Oxygen	K_{O_2}	0.0261	mM
	$Hb \cdot OP$	8.6	mM
	n_H	2.73	–
	PS_{cap}/V_i	1.6	s^{-1}

Table 2.4: Parameters corresponding to the transport fluxes in Aubert and Costalat model [38].

Blood Flow parameters			Arterial concentrations		
Parameter	Value	Units	Parameter	Value	Units
F_0	0.012	s^{-1}	$C_{\text{art,Glc}}$	4.8	mM
α	0.5	-	$C_{\text{art,Lac}}$	0.313	mM
$V_{v,0}$	0.0237	-	$C_{\text{art,O}_2}$	8.34	mM
τ_v	35	s			

Table 2.5: Blood related parameters and arterial concentrations

In light of the fact that a molecule of adenosine triphosphate (ATP) and adenosine monophosphate (AMP) produces two molecules of adenosine diphosphate (ADP) in a reversible reaction ATP + AMP $\longleftrightarrow$ 2ADP, known to be nearly at equilibrium in the brain [38], the authors express the concentration of ADP and AMP as a function of ATP

$$[\text{ADP}] = \frac{[\text{ATP}]}{2}\left(-q_{\text{AK}} + \sqrt{q_{\text{AK}}^2 + 4q_{\text{AK}}\left(\frac{\text{A}}{[\text{ATP}]} - 1\right)}\right), \tag{2.11}$$

$$[\text{AMP}] = \text{A} - [\text{ATP}] - [\text{ADP}], \tag{2.12}$$

where q_{AK} is the equilibrium constant of adenylate kinase and A is the total adenine nucleotide concentration. Furthermore, the ATP is also produced or consumed at the rate ψ_{CK} in the reversible reaction between phosphocreatine (PCr) and adenosine diphosphate (ADP), PCr + ADP $\longleftrightarrow$ Cr + ATP, where $[\text{PCr}] + [\text{Cr}] = \text{P}_{\text{tot}}$.

The total amount of ATP produced through the mitochondrial respiration is the product between ψ_{mit} and n_{op} where ψ_{mit} is the number of pyruvate moles per unit cell volume and time which are being oxidized by the mitochondria and n_{op} the number of ATP moles that are being produced per each mole of pyruvate. One of the novelties of this model is that it allows variations in the intracellular concentration of oxygen and it account for both exchanges through the blood brain barrier and consumption of oxygen by the mitochondria. For example, the right hand side of the differential equation of intracellular oxygen concentration (2.5) contains the term $n_{\text{aero}}\psi_{\text{mit}}$ accounting for the cerebral metabolic rate of oxygen; here n_{aero} is just a stoichiometric coefficient, while four different scenarios are tested for ψ_{mit}.

In the first one, the number of pyruvate moles oxidized by the mithocondria

(ψ_{mit}) is kept constant during neuronal stimulation $\psi_{\mathrm{mit}} = \psi^0_{\mathrm{mit}}$, while in the second, it increases according to:

$$\begin{aligned} \psi_{\mathrm{mit}}(t) &= (1+\alpha_{\mathrm{mit}})\psi^0_{\mathrm{mit}} \qquad \text{for } t_1 \le t \le t_{\mathrm{f}}, \\ \psi_{\mathrm{mit}}(t) &= \psi^0_{\mathrm{mit}} \qquad \text{for } t = 0 \text{ or } t \ge t_{\mathrm{f}} + t_1, \end{aligned} \tag{2.13}$$

where α_{mit} represents the rate at which the cerebral metabolic rate of oxygen increases during activation.

The third and the fourth scenarios rely on the dependency of ψ_{mit} on pyruvate, intracellular oxygen, ATP and ADP. The equation used in the third case is of the form

$$\psi_{\mathrm{mit}} = V_{\mathrm{max,mit}} \frac{[\mathrm{Pyr}]}{[\mathrm{Pyr}] + K_{\mathrm{m,mit}}} \frac{1}{1 + \left(\dfrac{[\mathrm{ATP}]}{[\mathrm{ADP}] \cdot K_{1,\mathrm{mit}}} \right)^{n_H}} \frac{[\mathrm{O_2}]_i}{\mathrm{K}_{\mathrm{O}_{2,i}} + [\mathrm{O_2}]_i}, \tag{2.14}$$

where $V_{\mathrm{max,mit}}$ is the maximal rate of mitochondrial activity, $K_{\mathrm{m,mit}}$ is the affinity constant of pyruvate, $K_{\mathrm{O}_{2,i}}$ is the Michaelis constant for oxygen, $K_{1,\mathrm{mit}}$ is an inhibition coefficient and n_H is the Hill coefficient.

In the fourth case, an additional input function $f(t)$ is added to the expression used in (2.14) in order to account for the potential messengers action on the Krebs cycle or the respiratory chain [38]:

$$\psi_{\mathrm{m}it} = V_{\mathrm{max,mit}} \frac{[\mathrm{Pyr}]}{[\mathrm{Pyr}] + K_{\mathrm{m,mit}}} \frac{1}{1 + \left(\dfrac{[\mathrm{ATP}]}{[\mathrm{ADP}] \cdot \mathrm{K}_{1,\mathrm{mit}}} \right)^{n_H}} \frac{[\mathrm{O_2}]_i}{\mathrm{K}_{\mathrm{O}_{2,i}} + [\mathrm{O_2}]_i} f(t). \tag{2.15}$$

The quantity $f(t)$ increases during stimulation:

$$f(t) = 1 + a_J \frac{\tanh(b_J(t - t_J)) + 1}{2}, \text{ for } t \le t_f, \tag{2.16}$$

and decreases exponentially after the end of the activation:

$$f(t) = 1 + a'_J \exp\left(\frac{t_f - t}{t_d} \right), \text{ for } t \ge t_f, \tag{2.17}$$

where a_J is the maximum increase fraction of the cerebral metabolic rate of oxygen, b_J is the slope, t_j the characteristic time of the increase and α'_J has been

calculated to guarantee the continuity of the function at $t = t_f$. The description of the blood flow follows the Buxton's Balloon model [15, 16], a hemodynamical model to be discussed in more detail in Chapter 4. In this model, the venous compartment is seen as a balloon, with inflow the cerebral blood flow F_{in} and whose outflow, F_{out}, depends on the balloon's volume. The time course of the venous volume satisfies the differential equation:

$$\frac{dV_v}{dt} = F_{in}(t) - F_{out}, \tag{2.18}$$

where

$$F_{in}(t) = \begin{cases} (1+\alpha_F)F_0 & \text{for} \quad t_1 \leq t \leq t_\text{f} \\ F_0 & \text{for} \quad t = 0 \text{ or } t \geq t_\text{f} + t_1 \end{cases}, \tag{2.19}$$

and

$$F_{out} = F_0 \left(\left(\frac{V_v}{V_v^0} \right)^{\frac{1}{\alpha}} + \frac{\tau_v}{V_v^0} \left(\frac{V_v}{V_v^0} \right)^{-\frac{1}{2}} \frac{dV_v}{dt} \right). \tag{2.20}$$

Here F_0 is the value of the blood flow during rest, α_F is the increase of the blood flow during neuronal activation and t_1 marks the time at which the activation is started and t_f the final time of the activation, τ_v is the viscosity parameter and V_v^0 is the value of the venous volume at rest. The steady state values of the relevant parameters are listed in Table 2.5.

The changes in deoxyhemoglobin (dHb) content per unit tissue are governed by

$$\frac{d\text{dHb}}{dt} = F_{in}(t) \cdot \left(C_{\text{a,O}_2} - [\text{O}_2]_{\bar{c}} \right) - F_{out} \frac{\text{dHb}}{V_v}, \tag{2.21}$$

where $C_{\text{a,O}_2}$ is the arterial oxygen concentration and $[\text{O}_2]_{\bar{c}}$ is the concentration of oxygen at the end of the capillaries.

The blood oxygen-level dependent (BOLD) signal is expressed in terms of

deoxyhemoglobin and venous volume, normalized to their resting value, i.e.

$$y(t) = V_v^0 \left(k_1 \left(1 - \frac{\mathrm{dHb}}{\mathrm{dHb}^0} \right) + k_2 \left(1 - \frac{\frac{\mathrm{dHb}}{\mathrm{dHb}^0}}{\frac{V_v}{V_v^0}} \right) \right) + k_3 \left(1 - \frac{V_v}{V_v^0} \right), \quad (2.22)$$

where $k_1 = 7E_0$, $k_2 = 2$, $k_3 = 2E_0 - 0.2$, dHb^0 is the resting deoxyhemoglobin content and V_v^0 is the resting volume, whose values can be found in Table 2.5.

The model predictions corresponding to four different protocols reported in [38] agree with the experimental results reported in the literature in some but not all cases.

2.3.2 Cloutier model

The model proposed by *Cloutier et al.* [9], comprising of separate compartments for neuron, astrocyte, capillaries and extracellular space, extends the work in [38, 40] by adding glycogen dynamics in the astrocyte compartment and by extending the glycolysis model from three intermediary steps (as in [38]) to five intermediary steps: hexokinase (HK), phosphoglucose isomerase (PFG), phosphofructokinase (PFK), phosphoglycerate kinase (PGK) and pyruvate kinase (PK) (see Figure 2.1). Glycogen acts as a buffer in the transition between resting state and neuronal activation. The kinetic parameters in the reaction rates are calibrated according to in vivo neurochemical measurements.

The Cloutier model subdivides the tissue compartment into neurons and astrocytes, and follows the time course of the intracellular concentration of sodium in each of compartment separately, while keeping extracellular sodium concentration ($[\mathrm{Na}^+]_{\mathrm{ecs}}$) constant. The governing equations for intracellular sodium is similar to equation (2.1)

$$\frac{d[\mathrm{Na}^+]_i}{dt} = I^i_{\mathrm{leak,Na}} - 3J^i_{\mathrm{pump,Na}^+} + \xi^i(t), \quad (2.23)$$

for the index i specifying the neuron ($i = n$) or astrocyte ($i = a$). The sodium leak currents $I^n_{\mathrm{leak,Na}}$ and $I^a_{\mathrm{leak,Na}}$ in neuron and astrocyte are modeled as in [38]:

$$I^i_{\mathrm{leak,Na}} = \frac{S_m}{V_i} \frac{g^i_{\mathrm{Na}}}{\mathrm{F}} \left(\frac{\mathrm{RT}}{\mathrm{F}} \ln \frac{[\mathrm{Na}^+]_{\mathrm{ecs}}}{[\mathrm{Na}^+]_i} - V \right), \quad (2.24)$$

where g^i_{Na} are the sodium conductances, V_i the corresponding volumes, F the Faraday constant, R the perfect gas constant and T the temperature. The values of these parameters are given in Table 2.7. The sodium potassium pump $J_{\mathrm{pump,Na^+}}$ depends on the availability of the energy supply

$$J^i_{\mathrm{pump,Na^+}} = \frac{S_m}{\eta_i} k_{\mathrm{pump}} [\mathrm{ATP}]_i [\mathrm{Na^+}]_i \left(1 + \frac{[\mathrm{ATP}]_i}{K_{\mathrm{m,pump}}}\right)^{-1}, \tag{2.25}$$

as in [38]. The mathematical expressions for sodium inflow due to stimulation in the neuron $\xi^n(t)$ and astrocyte $\xi^a(t)$ are of the form

$$\begin{aligned} &\xi^i(t) = \nu_i^1 + \left(\nu_i^2 \frac{t}{t_{\mathrm{st}}} \mathrm{e}^{-\frac{t}{t_{\mathrm{st}}}}\right) && \text{for } 0 \le t \le t_{\mathrm{f}} \\ &\xi^i(t) = 0 && \text{for } t > t_{\mathrm{f}}, \end{aligned} \tag{2.26}$$

where t_{f} is the final time of the stimulation.

Following the activation triggered by the sodium inflow ξ^n, neuron releases glutamate which is then taken up by astrocyte and transformed into glutamine. This process, showed schematically in Figure 2.3, known as the glutamate cycling, requires two ATP molecules to process one molecule of glutamate, one for pumping sodium and another one for the conversion of glutamate to glutamine and makes it possible to account for the activation of the ATPase in astrocyte at the end of neuronal activation. The governing equations of glutamate cycling are of the form

$$\begin{aligned} \frac{d[\mathrm{Glu}]_n}{dt} &= I^{a\to n}_{\mathrm{Glu}} - R_{\text{Na-Glu}} \xi^n, \\ \frac{d[\mathrm{Glu}]_a}{dt} &= I^{\mathrm{ecs}\to a}_{\mathrm{Glu}} - I^{a\to n}_{\mathrm{Glu}}, \\ \frac{d[\mathrm{Glu}]_{\mathrm{ecs}}}{dt} &= R_{\text{n-ecs}} R_{\text{Na-Glu}} \xi^n - \xi^n, \end{aligned} \tag{2.27}$$

with glutamate release rate, glutamate uptake and glutamate transfer to neurons

rates given by:

$$
\begin{aligned}
I_{\text{Glu}}^{n\to\text{ecs}} &= \xi^n R_{\text{Na-Glu}}, \\
I_{\text{Glu}}^{\text{ecs}\to a} &= I_{\text{max,Glu}}^{\text{ecs}\to a} \frac{[\text{Glu}]_{\text{ecs}}}{[\text{Glu}]_{\text{ecs}} + K_{\text{m,Glu}}}, \\
I_{\text{Glu}}^{a\to n} &= I_{\text{max,Glu}}^{a\to n} \frac{[\text{Glu}]_a}{[\text{Glu}]_a + K_{\text{m,Glu}}} \frac{[\text{ATP}]_a}{[\text{ATP}]_a + K_{\text{m,ATP}}}.
\end{aligned}
\tag{2.28}
$$

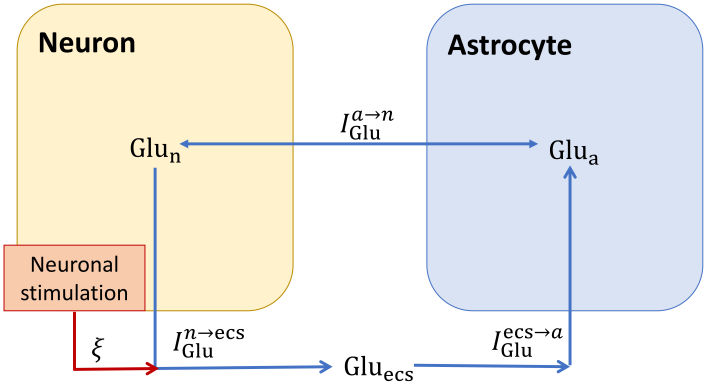

Figure 2.3: Schematic view over the glutamate cycling.

Compartment	Sodium	Glutamate
neuron	15	3
astrocyte	15	1e-6
extracellular space	150	1e-6

Table 2.6: Steady state values for the sodium and glutamate dynamics.

Description	Parameter	Value	Unit
Membrane potential	V	-70	mV
Sodium conductance in the neuron	g_{Na}^n	0.0039	mS/cm^2
Sodium conductance in the astrocyte	g_{Na}^a	0.0039	mS/cm^2
Faraday constant	F	$9.65 \cdot 10^4$	C/mol
Perfect gas constant and temperature kPa	RT	2577340	L/ mmol
Characteristic sodium length in the neuron	S_m^n	40500	1/cm
Characteristic sodium length in the astrocyte	S_m^a	10500	1/cm
Extracellular concentration of sodium	$[\text{Na}^+]_{\text{ecs}}$	150	mM
Transport rate constant	k_{pump}	$3.17 \cdot 10^{-7}$	cm/(mM $\cdot$ s)
Affinity constant for the sodium potassium pump	$K_{\text{m,pump}}$	0.4243	mM
Sodium glutamate ratio	$R_{\text{Na-Glu}}$	0.075	-

Table 2.7: Parameters in the description of the intracellular concentration of sodium and the glutamate cycling in *Cloutier et al.* model [9].

The blood flow is described using the balloon model with the venous volume changing according to

$$\frac{dV_v}{dt} = F_{in}(t) - F_{out}(t), \tag{2.29}$$

where

$$F_{in}(t) = F_0 + f_{\mathrm{CBF}}(t), \tag{2.30}$$

$$F_{out}(t) = F_0 \left[\left(\frac{V_v}{V_v^0} \right)^{1/x} + \tau_v \left(\frac{V_v}{V_v^0} \right)^{-1/2} \frac{1}{V_v^0} \frac{dV}{dt} \right], \tag{2.31}$$

and

$$f_{\mathrm{CBF}}(t) = 1 + \Delta_F \left[f(t, 2, 25) - f(t, 2 + t_{\mathrm{f}}, 25) \right],$$

where t is the post stimulation time and t_{f} is the duration of the stimulation.The switch function $f(t, \delta, \alpha)$ describes the changes in the cerebral blood during stimulation

$$f(t, \delta, \alpha) = \frac{1}{1 + \mathrm{e}^{-\alpha(t-\delta)}}. \tag{2.32}$$

Note that in (2.32) t is the time, δ is the time at which the stimulation starts and α indicates the slope during the stimulation. The description and values of the parameters in the description of the dynamics of the blood flow are given in Table 2.8.

Description	Parameter	Value	Unit
Baseline venous volume fraction	V_v^0	0.0237	-
Characteristic time for venous volume dynamics	τ_v	35	s
CBF fractional increase during activation	Δ_F	0.42	-
Stimulation duration	t_{f}	300	s

Table 2.8: Parameters used for describing the blood flow [9].

Since in *Cloutier et al.* glycolysis is described in five steps, additional metabolites and intermediates are considered, namely glucose 6-phosphate (G6P), fructose 6-phosphate (F6P), glyceraldehyde 3-phosphate (GAP) and phosphoenolpyruvic acid (PEP). The list of the metabolites and their resting values in four compartments is presented in Table 2.9.

[M]	n	a	ecs	c	[M]	n	a	ecs	c
[Glc]	0.43	0.16	0.47	4.64	[GAP]	0.05	0.05	-	-
[Lac]	0.28	0.89	0.37	0.33	[PEP]	0.025	0.025	-	-
[O_2]	0.102	0.102	-	7.46	[Pyr]	0.12	0.12	-	-
[CO_2]	-	-	-	0.98	[PCr]	2.5	1.5	-	-
[G6P]	0.75	0.75	-	-	[NADH]	0.04	0.04	-	-
[F6P]	0.2	0.2	-	-	[ATP]	2.25	2.2	-	-

Table 2.9: **Steady state values for the metabolites.** List of the metabolites $M = \{\mathrm{Glc}, \mathrm{Lac}, \mathrm{O_2}, \mathrm{CO_2}, \mathrm{G6P}, \mathrm{F6P}, \mathrm{GAP}, \mathrm{PEP}, \mathrm{Pyr}, \mathrm{PCr}, \mathrm{NADH}, \mathrm{ATP}\}$ in the four compartments (neuron (n), astrocyte (a), extracellular space (ecs) and capillary (c)) and their resting concentrations (in mM).

We denote the rates $r = \{\mathrm{HK}, \mathrm{PG1}, \mathrm{PGK}, \mathrm{PPP}, \mathrm{LDH}\}$ corresponding to the 5 steps of the glycolysis reaction: hexokinase, phosphoglucose isomerase, phosphofructokinase, phosphoglycerate kinase respectively lactate dehydrogenase by ψ_r, and let ψ_{mit} denote the rate of the mitochondrial pyruvate oxidation, ψ_{CK} the creatine kinase rate, ψ_{PK} the pyruvate kinase rate, and ψ_{ATPase} the ATP turnover. The kinetic equations and the values of the corresponding parameters are given in Table 2.11. The ATP requirement during neuronal stimulation is accounted for through the sodium potassium pump rate $J_{\mathrm{pump,Na^+}}$, whose expression is given in equation (2.25).

We use superscripts, e.g. $j_m^{\mathrm{ecs}\to n}$, to indicate the reaction flux or the transport direction of the metabolite m from the extracellular space to the neuron. By $j_m^{c\to n}$ we refer to the flux from the capillary to the neuron.

The changes in metabolites concentrations inside the neuron compartment

are modeled through the following differential equations:

$$
\begin{aligned}
\frac{d[\mathrm{Glc}]_n}{dt} &= j_{\mathrm{Glc}}^{\mathrm{ecs}\to n} - \psi_{\mathrm{HK}}^n, \\
\frac{d[\mathrm{G6P}]_n}{dt} &= \psi_{\mathrm{HK}}^n - \psi_{\mathrm{PG1}}^n - \psi_{\mathrm{G6PDH}}^n, \\
\frac{d[\mathrm{F6P}]_n}{dt} &= \psi_{\mathrm{PG1}}^n - \psi_{\mathrm{PFK}}^n - \psi_{\mathrm{PPP}}^n, \\
\frac{d[\mathrm{GAP}]_n}{dt} &= 2\psi_{\mathrm{PFK}}^n - \psi_{\mathrm{PGK}}^n - \psi_{\mathrm{PPP}}^n, \\
\frac{d[\mathrm{PEP}]_n}{dt} &= \psi_{\mathrm{PGK}}^n - \psi_{PK}^n, \\
\frac{d[\mathrm{Lac}]_n}{dt} &= \psi_{\mathrm{LDH}}^n - j_{\mathrm{Lac}}^{\mathrm{ecs}\to n}, \\
\frac{d[\mathrm{PCr}]_n}{dt} &= -\psi_{\mathrm{CK}}^n, \\
\frac{d[\mathrm{Pyr}]_n}{dt} &= \psi_{\mathrm{PK}}^n - \psi_{\mathrm{LDH}}^n - \psi_{\mathrm{mit}}^n, \\
\frac{d[\mathrm{NADH}]_n}{dt} &= \psi_{\mathrm{PGK}}^n - \psi_{\mathrm{LDH}}^n - \psi_{\mathrm{mit}}^n, \\
\frac{d[\mathrm{ATP}]_n}{dt} &= (-\psi_{\mathrm{HK}}^n - \psi_{\mathrm{PFK}}^n + \psi_{\mathrm{PGK}}^n + \psi_{\mathrm{PK}}^n + \psi_s^n + \psi_{\mathrm{CK}}^n)\left(1 - \frac{d[\mathrm{AMP}]_n}{d[\mathrm{ATP}]_n}\right)^{-1}, \\
\frac{d[\mathrm{O_2}]_n}{dt} &= j_{\mathrm{O_2}}^{\mathrm{c}\to n} - 3\psi_{\mathrm{mit}}^n,
\end{aligned}
\tag{2.33}
$$

where $\psi_{\mathrm{s}}^n = 15\psi_{\mathrm{mit}}^n - J_{\mathrm{pump,Na^+}}^n - \psi_{\mathrm{ATPase}}^n$.

Similarly, in the astrocyte compartment, the time course of the metabolites is described through the following differential equations:

$$
\begin{aligned}
\frac{d[\mathrm{Glc}]_a}{dt} &= j_{Glc}^{\mathrm{ecs}\to a} + j_{\mathrm{Glc}}^{\mathrm{c}\to a} - \psi_{\mathrm{HK}}^a,\\
\frac{d[\mathrm{G6P}]_a}{dt} &= \psi_{\mathrm{HK}}^a + \psi_{\mathrm{PG1}}^a - \psi_{\mathrm{GLYS}}^a + \psi_{\mathrm{GLYP}}^a,\\
\frac{d[\mathrm{F6P}]_a}{dt} &= \psi_{\mathrm{PG1}}^a - \psi_{\mathrm{PFK}}^a,\\
\frac{d[\mathrm{GAP}]_a}{dt} &= 2\psi_{\mathrm{PFK}}^a - \psi_{\mathrm{PGK}}^a,\\
\frac{d[\mathrm{PEP}]_a}{dt} &= \psi_{\mathrm{PGK}}^a - \psi_{\mathrm{PK}}^a,\\
\frac{d[\mathrm{Lac}]_a}{dt} &= \psi_{\mathrm{LDH}}^a + j_{\mathrm{Lac}}^{\mathrm{ecs}\to a} - j_{\mathrm{Lac}}^{\mathrm{a}\to c},\\
\frac{d[\mathrm{PCr}]_a}{dt} &= -\psi_{\mathrm{CK}^a},\\
\frac{d[\mathrm{Pyr}]_a}{dt} &= \psi_{\mathrm{PK}}^a - \psi_{\mathrm{LDH}}^a - \psi_{\mathrm{mit}}^a,\\
\frac{d[\mathrm{NADH}]_a}{dt} &= \psi_{\mathrm{PGK}}^a + \psi_{\mathrm{LDH}}^a - \psi_{\mathrm{mit}}^a,\\
\frac{d[\mathrm{ATP}]_a}{dt} &= (-\psi_{\mathrm{HK}}^a - \psi_{\mathrm{PFK}}^a + \psi_{\mathrm{PGK}}^a + \psi_{\mathrm{PK}}^a + \psi_s^a + \psi_{\mathrm{CK}}^a)\left(1 - \frac{\mathrm{d}[\mathrm{AMP}]_a}{\mathrm{d}[\mathrm{ATP}]_a}\right)^{-1},\\
\frac{d[\mathrm{O_2}]_a}{dt} &= j_{\mathrm{O_2}}^{\mathrm{c}\to a} - 3\psi_{\mathrm{mit}}^a,
\end{aligned}
\tag{2.34}
$$

where $\psi_{\mathrm{s}}^a = 15\psi_{\mathrm{mit}}^a - J_{\mathrm{pump,Na^+}}^a - \psi_{\mathrm{ATPase}}^a$.

In the astrocyte, the contribution of glycogen to the energy metabolism is mediated through G6P. The authors argue that it is important to consider this contribution because the glycogen pool in astrocyte could sustain cerebral activity for a couple of minutes [9].

The time course of glycogen in the astrocyte is:

$$
\frac{d[\mathrm{GLY}]_a}{dt} = \psi_{\mathrm{GLYS}}^a - \psi_{\mathrm{GLYP}}^a, \tag{2.35}
$$

where ψ_{GLYS}^a and ψ_{GLYP} are the reaction rates for the the glycogen synthase and phosphorylase given by:

$$
\begin{aligned}
\psi_{\mathrm{GLYS}}^a &= V_{\mathrm{max,GLYS}}^a \left(\frac{[\mathrm{G6P}]_a}{[\mathrm{G6P}]_a + K_{\mathrm{m,G6P}}}\right)(1 - f([\mathrm{GLY}]_a, 4.2, 20)),\\
\psi_{\mathrm{GLYP}}^a &= V_{\mathrm{max,GLYP}}^a \left(\frac{[\mathrm{G6P}]_a}{[\mathrm{G6P}]_a + K_{\mathrm{m,G6P}}}\right)(1 + f_{\mathrm{GLY}}),
\end{aligned}
\tag{2.36}
$$

with

$$f_{\mathrm{GLY}} = \Delta_{\mathrm{GLY}} \left[f(t, t_{0,\mathrm{GLY}}, 4) - f(t, t_{0,\mathrm{GLY}} + t_{\mathrm{f,GLY}}, 4) \right].$$

The maximum reaction rates for synthase of glycogen from G6P, and glycogen breakdown, denoted by $V^a_{\mathrm{max,GLYP}}$ and $V^a_{\mathrm{max,GLYS}}$, are specified in Table 2.10. The function f is the switch function used for describing the changes in the blood flow during neuronal stimulation and was given in equation (2.32).

Description	Parameter	Value	Unit
Maximum reaction rate for glycogen synthase	$V_{\mathrm{max,GLYS}}$	$1.53\mathrm{e}^{-4}$	mM/s
Maximum reaction rate for glycogen phosphorylase	$V_{\mathrm{max,GLYP}}$	$4.92\mathrm{e}^{-5}$	mM/s
Glycogen breakdown fractional increase during stimulation	Δ_{GLY}	62	-
Delay before glycogen breakdown	$t_{0,\mathrm{GLY}}$	71	s
Duration of glycogen breakdown	$t_{\mathrm{f,GLY}}$	403	s

Table 2.10: Parameters used for describing the glycogen dynamics in *Cloutier et al.* model [9].

The model assumes that the sum of the energetic shuttles, denoted by ANP, remains constant at the value given in Table 2.12:

$$[\mathrm{ATP}] + [\mathrm{ADP}] + [\mathrm{AMP}] = [\mathrm{ANP}].$$

In light of adenylate kinase equilibrium, adenosine diphosphate concentration can be expressed in terms of adenosine triphosphate:

$$[\mathrm{ADP}] = \frac{[\mathrm{ATP}]}{2} \left(-q_{\mathrm{AK}} + \sqrt{u} \right),$$

and the derivative of adenosine monophosphate can be expressed as

$$\frac{d[\mathrm{AMP}]}{d[\mathrm{ATP}]} = -1 + \frac{q_{\mathrm{AK}}}{2} - 0.5\sqrt{u} + q_{\mathrm{AK}} \frac{[\mathrm{ANP}]}{[\mathrm{ATP}]\sqrt{u}},$$

where $u = q^2_{\mathrm{AK}} + 4q_{\mathrm{AK}} \left(\frac{[\mathrm{ANP}]}{[\mathrm{ATP}]-1} \right)$ and q_{AK} is the equilibrium constant for adenylate kinase reaction, listed in Table 2.12.

Similarly, it is assumed that the sum of the concentrations of NADH and NAD^+ is constant:

$$[\mathrm{NADH}] + [\mathrm{NAD}^+] = \mathrm{N}^{\mathrm{tot}},$$

as is the sum of the concentrations of phosphocreatine and creatine:

$$[\mathrm{PCr}] + [\mathrm{Cr}] = \mathrm{P_{tot}}.$$

The values of $\mathrm{N^{tot}}$ and $\mathrm{P_{tot}}$ assumed by the Cloutier model are given in Table 2.12.

Kinetic equations for the neuron and the astrocyte	Parameter	Value	Unit
Hexokinase (ψ^i_{HK})			
$k^i_{\mathrm{HK}}[\mathrm{ATP}]_i \left(\frac{[\mathrm{Glc}]_i}{[\mathrm{Glc}]_i + \mathrm{K_{m,Glc}}}\right)(1 - f([\mathrm{G6P}]_i, 0.6, 20))$	k^n_{HK}	0.051	mM/s
	k^a_{HK}	0.050	mM/s
	$K_{\mathrm{m,Glc}}$	0.105	mM
Phosphoglucose isomerase (ψ^i_{PG1})	$\psi^{n,\mathrm{f}}_{\mathrm{m,PG1}}$	0.502	mM/s
$\psi^{i,\mathrm{f}}_{\mathrm{m,PG1}} \left(\frac{[\mathrm{G6P}]_i}{[\mathrm{G6P}]_i + \mathrm{K_{m,G6P}}}\right) - \psi^{i,\mathrm{r}}_{\mathrm{m,PG1}} \left(\frac{[\mathrm{F6P}]_i}{[\mathrm{F6P}]_i + \mathrm{K_{m,F6P}}}\right)$	$\psi^{a,\mathrm{f}}_{\mathrm{m,PG1}}$	0.483	mM/s
	$\psi^{n,\mathrm{r}}_{\mathrm{m,PG1}}$	0.503	mM/s
	$\psi^{a,\mathrm{r}}_{\mathrm{m,PG1}}$	0.451	mM/s
	$K_{\mathrm{m,F6P}}$	0.06	mM
	$K_{\mathrm{m,G6P}}$	0.50	mM
Phosphofructokinase (ψ^i_{PFK})	k^n_{PFK}	0.558	$\mathrm{mM^{-1}s^{-1}}$
$k^i_{\mathrm{PFK}}[\mathrm{ATP}]_i \left(1 + \left(\frac{[\mathrm{ATP}]_i}{\mathrm{K_{1,ATP}}}\right)^{n_H}\right)^{-1} \left(\frac{[\mathrm{F6P}]_i}{[\mathrm{F6P}]_i + \mathrm{K_{m,F6P}}}\right)$	k^a_{PFK}	0.403	$\mathrm{mM^{-1}s^{-1}}$
	$K_{\mathrm{m,F6P}}$	0.06	mM
	$K_{\mathrm{1,ATP}}$	0.7595	mM
	n_H	4	-
Phosphoglycerate kinase (ψ^i_{PGK})			
$k^i_{\mathrm{PGK}}[\mathrm{GAP}]_i[\mathrm{ADP}]_i \frac{[\mathrm{NAD^+}]_i}{[\mathrm{NADH}]_i}$	k^n_{PGK}	0.429	$\mathrm{mM^{-1}s^{-1}}$
	k^a_{PGK}	0.251	$\mathrm{mM^{-1}s^{-1}}$
Mitochondrial pyruvate oxidation (ψ^i_{mit})	$\psi^n_{\mathrm{max,mit}}$	0.0556	mM/s
	$\psi^a_{\mathrm{max,mit}}$	0.0084	mM/s
$\psi^n_{\mathrm{max,mit}} \left(\frac{[\mathrm{Pyr}]_i}{[\mathrm{Pyr}]_i + \mathrm{K_{m,Pyr}}}\right) \left(\frac{[\mathrm{ADP}]_i}{[\mathrm{ADP}]_i + \mathrm{K_{m,ADP}}}\right) f_m$	$K_{\mathrm{m,Pyr}}$	0.063	mM
	$K_{\mathrm{m,ADP}}$	0.00107	mM
where $f_{\mathrm{m}} = [1 - f(\frac{[\mathrm{ATP}]_i}{[\mathrm{ADP}]_i}, 20, 5)] \left(\frac{[\mathrm{O_2}]_i}{[\mathrm{O_2}]_i + \mathrm{K_{m,O_2}}}\right)$	$K_{\mathrm{m,O_2}}$	0.00297	mM
Pyruvate kinase (ψ^i_{PK})	k^n_{PK}	8.61	$\mathrm{mM^{-1}s^{-1}}$
$k^i_{\mathrm{PK}}[\mathrm{PEP}]_i[\mathrm{ADP}]_i$	k^a_{PK}	2.73	$\mathrm{mM^{-1}s^{-1}}$
Lactate dehydrogenase (ψ^i_{LDH})	$k^n_{\mathrm{LDH,f}}$	5.30	$\mathrm{mM^{-1}s^{-1}}$
$k^i_{\mathrm{LDH,f}} + [\mathrm{Pyr}]_i[\mathrm{NADH}]_i - k^i_{\mathrm{LDH,r}}[\mathrm{Lac}]_i[\mathrm{NAD^+}]_i$	$k^a_{\mathrm{LDH,f}}$	6.26	$\mathrm{mM^{-1}s^{-1}}$
	$k^n_{\mathrm{LDH,r}}$	0.105	$\mathrm{mM^{-1}s^{-1}}$
	$k^a_{\mathrm{LDH,r}}$	0.547	$\mathrm{mM^{-1}s^{-1}}$
Creatine kinase (ψ^i_{CK})	$k^n_{\mathrm{CK,f}}$	0.0524	$\mathrm{mM^{-1}s^{-1}}$
$k^i_{\mathrm{CK,f}}[\mathrm{PCr}]_i[\mathrm{ADP}]_i - k^i_{\mathrm{CK,r}}[\mathrm{Cr}]_i[\mathrm{ATP}]_i$	$k^a_{\mathrm{CK,f}}$	0.0243	$\mathrm{mM^{-1}s^{-1}}$
	$k^{n,\mathrm{r}}_{\mathrm{CK}}$	0.0152	$\mathrm{mM^{-1}s^{-1}}$
	$k^{a,\mathrm{r}}_{\mathrm{CK}}$	0.0207	$\mathrm{mM^{-1}s^{-1}}$
ATPase (excluding the Na-K pump cost) (ψ^i_{ATPase})	$K_{\mathrm{m,ATP}}$	0.0153	mM
$V^i_{\mathrm{m,ATPase}} \left(\frac{[\mathrm{ATP}]_i}{[\mathrm{ATP}]_i + K_{\mathrm{m,ATP}}}\right)$	$V^n_{\mathrm{m,ATPase}}$	0.0489	mM/s
	$V^a_{\mathrm{m,ATPase}}$	0.0357	mM/s

Table 2.11: Rate equations and their corresponding parameters in *Cloutier et al.* model [9].

Description	Parameter	Value	Unit
Total concentration of NADH and NAD^+	N_{tot}	0.22	mM
Total concentration of PCr and Cr	P_{tot}	5	mM
Total energy shuttles	[ANP]	2.38	mM
Equilibrium constant for adenylate kinase reaction	q_{AK}	0.92	-

Table 2.12: Physical constants and known values for the reaction fluxes [9].

The changes in glucose and lactate concentration in extracellular space follow the differential equations

$$\begin{aligned} \frac{d[\text{Glc}]_{\text{ecs}}}{dt} &= j_{\text{Glc}}^{c\to\text{ecs}} + R_{n\to\text{ecs}} j_{\text{Glc}}^{\text{ecs}\to n} - R_{a\to\text{ecs}} j_{\text{Glc}}^{\text{ecs}\to a}, \\ \frac{d[\text{Lac}]_{\text{ecs}}}{dt} &= j_{\text{Lac}}^{n\to\text{ecs}} R_{\text{ecs}\to n} + R_{\text{ecs}\to a} j_{\text{Lac}}^{a\to\text{ecs}} - j_{\text{Lac}}^{\text{ecs}\to c}, \end{aligned} \tag{2.37}$$

where the transport fluxes $j_{\text{Glc}}^{c\to\text{ecs}}$, $j_{\text{Glc}}^{\text{ecs}\to n}$ and $j_{\text{Glc}}^{\text{ecs}\to a}$ obey equations (2.39).

Volume fractions		**Volumetric ratios**	
Parameter	Value	Parameter	Value
η_n	0.45	$R_{\text{ecs}\to n}$	4/9
η_a	0.25	$R_{\text{ecs}\to a}$	0.8
η_{ecs}	0.2	$R_{c\to\text{ecs}}$	0.0275
η_c	0.0055	$R_{c\to a}$	0.022
		$R_{c\to n}$	0.01222

Table 2.13: Volume fractions and volumetric ratios in the *Cloutier et al.* model.

The time courses of the four metabolites in the capillary compartment are governed by the system of differential equations

$$\begin{aligned} \frac{d[\text{Glc}]_c}{dt} &= j_{\text{Glc}}^{c} - R_{\text{ecs}\to c} j_{Glc}^{c\to\text{ecs}} - R_{a\to c} j_{\text{Glc}}^{c\to a}, \\ \frac{d[\text{Lac}]_c}{dt} &= j_{\text{Lac}}^{c} - R_{\text{ecs}\to c} j_{Glc}^{c\to\text{ecs}} - R_{a\to c} j_{\text{Lac}}^{c\to a}, \\ \frac{d[\text{O}_2]_c}{dt} &= j_{\text{O}_2}^{c} - R_{c\to a} j_{\text{O}_2}^{c\to a} + R_{c\to n} j_{\text{O}_2}^{c\to n}, \\ \frac{d[\text{CO}_2]_c}{dt} &= j_{\text{CO}_2}^{c} - R_{c\to a} j_{\text{CO}_2}^{c\to a} + R_{c\to n} j_{\text{CO}_2}^{c\to n}. \end{aligned} \tag{2.38}$$

The glucose and lactate transport rates across the Blood-Brain-Barrier follow

classical Michaelis Menten form:

$$
\begin{aligned}
j_{\text{Glc}}^{c\to\text{ecs}} &= V_{\text{max,Glc}}^{c\to\text{ecs}} \left[\frac{[\text{Glc}]_c}{[\text{Glc}]_c + K_{\text{t,Glc}}^{c\to\text{ecs}}} - \frac{[\text{Glc}]_{\text{ecs}}}{[\text{Glc}]_{\text{ecs}} + K_{\text{t,Glc}}^{c\to\text{ecs}}} \right], \\
j_{\text{Glc}}^{c\to a} &= V_{\text{max,Glc}}^{c\to a} \left[\frac{[\text{Glc}]_c}{[\text{Glc}]_c + K_{\text{t,Glc}}^{c\to a}} - \frac{[\text{Glc}]_a}{[\text{Glc}]_a + K_{\text{t,Glc}}^{c\to a}} \right], \\
j_{\text{Glc}}^{\text{ecs}\to n} &= V_{\text{max,Glc}}^{\text{ecs}\to n} \left[\frac{[\text{Glc}]_{\text{ecs}}}{[\text{Glc}]_{\text{ecs}} + K_{\text{t,Glc}}^{\text{ecs}\to n}} - \frac{[\text{Glc}]_n}{[\text{Glc}]_n + K_{\text{t,Glc}}^{\text{ecs}\to n}} \right], \\
j_{\text{Glc}}^{\text{ecs}\to a} &= V_{\text{max,Glc}}^{\text{ecs}\to a} \left[\frac{[\text{Glc}]_{\text{ecs}}}{[\text{Glc}]_{\text{ecs}} + K_{\text{t,Glc}}^{\text{ecs}\to a}} - \frac{[\text{Glc}]_a}{[\text{Glc}]_a + K_{t,Glc}^{\text{ecs}\to a}} \right], \\
j_{\text{Lac}}^{\text{ecs}\to c} &= V_{\text{max,Lac}}^{\text{ecs}\to c} \left[\frac{[\text{Lac}]_{\text{ecs}}}{[\text{Lac}]_{\text{ecs}} + K_{\text{t,Lac}}^{\text{ecs}\to c}} - \frac{[\text{Lac}]_c}{[\text{Lac}]_c + K_{t,Lac}^{\text{ecs}\to c}} \right], \\
j_{\text{Lac}}^{n\to\text{ecs}} &= V_{\text{max,Lac}}^{n\to\text{ecs}} \left[\frac{[\text{Lac}]_n}{[\text{Lac}]_n + K_{\text{t,Lac}}^{n\to\text{ecs}}} - \frac{[\text{Lac}]_{\text{ecs}}}{[\text{Lac}]_{\text{ecs}} + K_{\text{t,Lac}}^{n\to\text{ecs}}} \right], \\
j_{\text{Lac}}^{a\to c} &= V_{\text{max,Lac}}^{a\to c} \left[\frac{[\text{Lac}]_a}{[\text{Lac}]_a + K_{\text{t,Lac}}^{a\to c}} - \frac{[\text{Lac}]_c}{[\text{Lac}]_c + K_{\text{t,Lac}}^{a\to c}} \right], \\
j_{\text{Lac}}^{a\to\text{ecs}} &= V_{\text{max,Lac}}^{a\to\text{ecs}} \left[\frac{[\text{Lac}]_a}{[\text{Lac}]_a + K_{\text{t,Lac}}^{a\to\text{ecs}}} - \frac{[\text{Lac}]_{\text{ecs}}}{[\text{Lac}]_{\text{ecs}} + K_{\text{t,Lac}}^{a\to\text{ecs}}} \right],
\end{aligned}
\tag{2.39}
$$

where $V_{\text{max,Glc}}$, $V_{\text{max,Lac}}$ are the maximum transport rate and $K_{\text{t,Glc}}$, $K_{\text{t,Lac}}$ are affinity constants for glucose and lactate. The values of these parameters are given in Table 2.14.

Transport Flux	**Glucose**			**Lactate**		
	Parameter	Value	Units	Parameter	Value	Units
Capillary ↔ ecs	$V_{\text{max,Glc}}^{c\to\text{ecs}}$	0.0496	mM/s	$V_{\text{max,Lac}}^{\text{ecs}\to c}$	0.0325	mM/s
	$K_{\text{t,Glc}}^{c\to\text{ecs}}$	8.45	mM	$K_{\text{t,Lac}}^{\text{ecs}\to c}$	0.764	mM
Capillary ↔ Astrocyte	$V_{\text{max,Glc}}^{c\to a}$	0.010	mM/s	$V_{\text{max,Lac}}^{a\to c}$	0.0002	mM/s
	$K_{\text{t,Glc}}^{c\to a}$	9.92	mM	$K_{\text{t,Lac}}^{a\to c}$	0.128	mM
ecs ↔ Neuron	$V_{\text{max,Glc}}^{\text{ecs}\to n}$	0.504	mM/s	$V_{\text{max,Lac}}^{n\to\text{ecs}}$	0.1978	mM/s
	$K_{\text{t,Glc}}^{\text{ecs}\to n}$	5.32	mM	$K_{\text{t,Lac}}^{n\to\text{ecs}}$	0.093	mM
ecs ↔ Astrocyte	$V_{\text{max,Lac}}^{\text{ecs}\to a}$	0.038	mM/s	$V_{\text{max,Lac}}^{a\to\text{ecs}}$	0.0861	mM/s
	$K_{\text{t,Glc}}^{\text{ecs}\to a}$	3.52	mM	$K_{\text{t,Lac}}^{a\to\text{ecs}}$	0.221	mM

Table 2.14: Parameters corresponding to the transport fluxes *Cloutier et al.* model [9].

The exchange rate of oxygen between the capillaries and neurons or astrocytes is expressed in terms of the permeability (P) of the blood brain barrier, capillary surface S_c, cellular compartment volume (V_n, V_a), hemoglobin (Hb) and oxiphoric

power (OP):

$$j_{\mathrm{O}_2}^{c\to n} = \frac{\mathrm{P}S_c^n}{\eta_n}\left(K_{\mathrm{O}_2}\left(\frac{\mathrm{Hb}\cdot\mathrm{OP}}{[\mathrm{O}_2]_c}-1\right)^{-1/n_h} - [\mathrm{O}_2]_n\right), \tag{2.40}$$

$$j_{\mathrm{O}_2}^{c\to a} = \frac{\mathrm{P}S_c^a}{\eta_a}\left(K_{\mathrm{O}_2}\left(\frac{\mathrm{Hb}\cdot\mathrm{OP}}{[\mathrm{O}_2]_c}-1\right)^{-1/n_h} - [\mathrm{O}_2]_a\right), \tag{2.41}$$

where K_{O_2} is the oxygen transport constant. The values of the relevant parameters are given in Table 2.15.

The blood flow contributions to the variations of glucose, lactate and oxygen are [38]:

$$\begin{aligned} j_{\mathrm{Glc}}^c &= \frac{2F_{in}(t)}{\eta_c}\left(C_{\mathrm{art,Glc}} - [\mathrm{Glc}]_c\right), \\ j_{\mathrm{Lac}}^c &= \frac{2F_{in}(t)}{\eta_c}\left(C_{\mathrm{art,Lac}} - [\mathrm{Lac}]_c\right), \\ j_{\mathrm{O}_2}^c &= \frac{2F_{in}(t)}{\eta_c}\left(C_{\mathrm{art,O_2}} - [\mathrm{O}_2]_c\right), \end{aligned} \tag{2.42}$$

where $F_{in}(t)$ is the input function controlling the blood flow in equation (2.19), V_c the volume of the capillaries, $C_{\mathrm{art,Glc}}$, $C_{\mathrm{art,Lac}}$ and $C_{\mathrm{art,O_2}}$ the arterial concentrations of glucose, lactate and oxygen and $[\mathrm{Glc}]_c$, $[\mathrm{Lac}]_c$ and $[\mathrm{O}_2]_c$ their capillary concentration.

Blood Flow parameters			Arterial concentrations		
Parameter	Value	Units	Parameter	Value	Units
nOP	15		$C_{\mathrm{art,Glc}}$	4.8	mM
HbOP	8.6	mM	$C_{\mathrm{art,Lac}}$	0.313	mM
$\mathrm{N_{aero}}$	3		$C_{\mathrm{art,O_2}}$	8.34	mM
$\mathrm{CBF_0}$	0.012	$\mathrm{s^{-1}}$	$C_{\mathrm{art,CO_2}}$	27.5	mM
PS_c^n	0.220	$\mathrm{s^{-1}}$			
PS_c^a	0.245	$\mathrm{s^{-1}}$			
K_{O_2}	0.0897	mM			
n_h	2.7				

Table 2.15: Blood related parameters and arterial concentrations in the *Cloutier et al.* model.

2.4 Metabolic model

The metabolic model used in this thesis is based on that proposed by *Calvetti et al.* in [41, 42], which comprises separate compartments for neuron, astrocyte, extracellular space surrounding them and blood. Both neuron and astrocyte are equipped with their own metabolic network and interact biochemically through extracellular space. The latter interfaces with the blood compartment by exchanging some metabolites through the permeable Blood-Brain-Barrier (BBB). Each compartment $X = \{\text{b, ecs, n, a}\}$ is assumed a volume fraction, denoted by η_X, listed in Table 2.16.

This metabolic model does not explicitly describe the glutamate - glutamine cycling between the cellular compartments (see Figure 2.3), which was included in previous models to account for the energetic cost of activation. In our case, this is no longer necessary due to the fact that the energetic link is done in a more physiological manner, being directly correlated to the changes in the ionic concentrations which depend on the level of activation [43].

2.4.1 Blood compartment

In the blood compartment, our model follows the concentration of three substances: glucose (Glc), lactate (Lac) and oxygen (O_2). We denote the metabolite by m, where $m = \{\text{Glc, Lac, } O_2\}$. To indicate the concentration in blood and the arterial concentration of the metabolite m, we use the notation $[m]_\text{b}$, respectively $C_{\text{art,m}}$. The arterial concentrations are assumed to be constant and their values are given in Table 2.16. The blood flow is a function of time $q = q(t)$ and the mixing ratio between the arterial and the venous blood is denoted by F, where $F \in (0, 1)$.

The concentrations of the three metabolites in blood are modeled through the differential equations:

$$\eta_b \frac{d[\text{Glc}]_\text{b}}{dt} = \frac{q}{F}(C_{\text{art,Glc}} - [\text{Glc}]_\text{b}) - J_{\text{Glc}}, \tag{2.43}$$

$$\eta_b \frac{d[\text{Lac}]_\text{b}}{dt} = \frac{q}{F}(C_{\text{art,Lac}} - [\text{Lac}]_\text{b}) - J_{\text{Lac}}, \tag{2.44}$$

$$\eta_b \frac{d[\text{O}_2]_\text{b}}{dt} = \frac{q}{F}(C_{\text{art,O}_2} - [\text{O}_2]_\text{b}) - J_{\text{O}_2}, \tag{2.45}$$

where the transport rates of glucose, lactate and oxygen between blood and extracellular space J_{Glc}, J_{Lac} and $J_{\mathrm{O_2}}$ are expressed in terms of the metabolite concentrations in the two compartments, by using symmetric Michaelis-Menten expressions

$$J_{\mathrm{Glc}} = T_{\mathrm{b,Glc}} \left(\frac{[\mathrm{Glc}]_{\mathrm{b}}}{M_{\mathrm{b,Glc}} + [\mathrm{Glc}]_{\mathrm{b}}} - \frac{[\mathrm{Glc}]_{\mathrm{ecs}}}{M_{\mathrm{ecs,Glc}} + [\mathrm{Glc}]_{\mathrm{ecs}}} \right), \tag{2.46}$$

$$J_{\mathrm{Lac}} = T_{\mathrm{b,Lac}} \left(\frac{[\mathrm{Lac}]_{\mathrm{b}}}{M_{\mathrm{b,Lac}} + [\mathrm{Lac}]_{\mathrm{b}}} - \frac{[\mathrm{Lac}]_{\mathrm{ecs}}}{M_{\mathrm{ecs,Lac}} + [\mathrm{Lac}]_{\mathrm{ecs}}} \right). \tag{2.47}$$

Here $T_{\mathrm{b,Glc}}$, $T_{\mathrm{b,Lac}}$ are the maximum transport rates, and $M_{\mathrm{b},m}$, $M_{\mathrm{ecs},m}$ the affinity constants of the metabolites in blood compartment and extracellular space, given in Table 2.17.

The oxygen in the blood can be either freely dissolved in plasma or bound to hemoglobin. The total oxygen concentration can be written with respect to the free oxygen concentration $[\mathrm{O_2}]_{b,\mathrm{free}}$ according to Hill's equation [44]:

$$[\mathrm{O_2}]_{\mathrm{b}} = [\mathrm{O_2}]_{\mathrm{b,free}} + 4\,\mathrm{Hct}\,[\mathrm{Hb}] \frac{[\mathrm{O_2}]^n_{\mathrm{b,free}}}{K^n_{\mathrm{H}} + [\mathrm{O_2}]^n_{\mathrm{b,free}}} = H\big([\mathrm{O_2}]_{\mathrm{b,free}}\big),$$

where [Hb] is the hemoglobin concentration in plasma, Hct the hematocrit, K_{H} the affinity constant and Hill's constant is set to $n = 2.5$.

The transport flux of oxygen follows a modified Fick's law:

$$J_{\mathrm{O_2}} = \lambda_{\mathrm{b,O_2}} \big([\mathrm{O_2}]_{\mathrm{b,free}} - [\mathrm{O_2}]_{\mathrm{ecs}}\big)^{\kappa} = \lambda_{\mathrm{b,O_2}} \big(H^{-1}([\mathrm{O_2}]_{\mathrm{b}}) - [\mathrm{O_2}]_{\mathrm{ecs}}\big)^{\kappa}, \tag{2.48}$$

where λ_{b,O_2} is the membrane's permeability to oxygen and κ was set to 0.1.

For notational convenience, we collect the concentrations of metabolites in blood compartment in the vector

$$C_{\mathrm{b}}(t) = \begin{bmatrix} [\mathrm{Glc}]_{\mathrm{b}}(t) \\ [\mathrm{Lac}]_{\mathrm{b}}(t) \\ [\mathrm{O_2}]_{\mathrm{b}}(t) \end{bmatrix}. \tag{2.49}$$

Volume fractions		Blood Flow parameters			Arterial concentrations		
Parameter	Value	Parameter	Value	Units	Parameter	Value	Units
η_{n}	0.4	Hct	0.45		$C_{\mathrm{art,Glc}}$	5	mM
η_{a}	0.3	Hb	5.18		$C_{\mathrm{art,Lac}}$	1.1	mM
η_{ecs}	0.3	K_H	$36.4 \cdot 10^{-3}$	mM	$C_{\mathrm{art,O_2}}$	9.14	mM
η_{b}	0.04	q	0.40	mL/min			

Table 2.16: **Volume fractions and blood related parameters:** List of the volume fractions of the four compartments (left), values of the parameters in the expression for blood flow (center) and arterial concentrations of glucose, lactate and oxygen (right).

2.4.2 Extracellular space

Changes in concentrations of glucose, lactate and oxygen depend only on exchanges with other compartments, hence

$$\eta_{\mathrm{ecs}} \frac{d[\mathrm{Glc}]_{\mathrm{ecs}}}{dt} = J_{\mathrm{Glc}} - j^{\mathrm{n}}_{\mathrm{Glc}} - j^{\mathrm{a}}_{\mathrm{Glc}}, \tag{2.50}$$

$$\eta_{\mathrm{ecs}} \frac{d[\mathrm{Lac}]_{\mathrm{ecs}}}{dt} = J_{\mathrm{Lac}} - j^{\mathrm{n}}_{\mathrm{Lac}} - j^{\mathrm{a}}_{\mathrm{Lac}}, \tag{2.51}$$

$$\eta_{\mathrm{ecs}} \frac{d[\mathrm{O_2}]_{\mathrm{ecs}}}{dt} = J_{\mathrm{O_2}} - j^{\mathrm{n}}_{\mathrm{O_2}} - j^{\mathrm{a}}_{\mathrm{O_2}}, \tag{2.52}$$

where J_{Glc}, J_{Lac} and $J_{\mathrm{O_2}}$ are the fluxes from the blood to the extracellular space, defined in (2.46), (2.47) and (2.48), and $j^{\mathrm{n/a}}_{\mathrm{Glc}}$, $j^{\mathrm{n/a}}_{\mathrm{Lac}}$ and $j^{\mathrm{n/a}}_{\mathrm{O_2}}$ are the transport rates of glucose, lactate and oxygen from the extracellular space to the neuron or astrocyte, with the convention that positive fluxes are directed away from the extracellular space.

The transport of glucose and lactate into the cellular compartments occurs with the facilitation of glucose (GLUT) and monocarboxylate (MCT) transporters, whose rates are expressed in Michaelis-Menten form:

$$j^{\mathrm{n}}_{\mathrm{Glc}} = T_{\mathrm{n,Glc}} \left(\frac{[\mathrm{Glc}]_{\mathrm{ecs}}}{M_{\mathrm{n,Glc}} + [\mathrm{Glc}]_{\mathrm{ecs}}} - \frac{[\mathrm{Glc}]_{\mathrm{n}}}{M_{\mathrm{n,Glc}} + [\mathrm{Glc}]_{\mathrm{n}}} \right), \tag{2.53}$$

$$j^{\mathrm{n}}_{\mathrm{Lac}} = T_{\mathrm{n,Lac}} \left(\frac{[\mathrm{Lac}]_{\mathrm{ecs}}}{M_{\mathrm{n,Lac}} + [\mathrm{Lac}]_{\mathrm{ecs}}} - \frac{[\mathrm{Lac}]_{\mathrm{n}}}{M_{\mathrm{n,Lac}} + [\mathrm{Lac}]_{\mathrm{n}}} \right), \tag{2.54}$$

$$j^{\mathrm{a}}_{\mathrm{Glc}} = T_{\mathrm{a,Glc}} \left(\frac{[\mathrm{Glc}]_{\mathrm{ecs}}}{M_{\mathrm{a,Glc}} + [\mathrm{Glc}]_{\mathrm{ecs}}} - \frac{[\mathrm{Glc}]_{\mathrm{a}}}{M_{\mathrm{a,Glc}} + [\mathrm{Glc}]_{\mathrm{a}}} \right), \tag{2.55}$$

$$j^{\mathrm{a}}_{\mathrm{Lac}} = T_{\mathrm{a,Lac}} \left(\frac{[\mathrm{Lac}]_{\mathrm{ecs}}}{M_{\mathrm{a,Lac}} + [\mathrm{Lac}]_{\mathrm{ecs}}} - \frac{[\mathrm{Lac}]_{\mathrm{a}}}{M_{\mathrm{a,Lac}} + [\mathrm{Lac}]_{\mathrm{a}}} \right), \tag{2.56}$$

where $T_{\mathrm{n,Glc}}$, $T_{\mathrm{a,Glc}}$, $T_{\mathrm{n,Lac}}$ and $T_{\mathrm{a,Lac}}$ are the maximum transport rates and $M_{\mathrm{n,Glc}}$, $M_{\mathrm{a,Glc}}$, $M_{\mathrm{n,Lac}}$ and $M_{\mathrm{a,Lac}}$ are the affinity constants, whose values are listed in Table 2.17.

Oxygen transport into neuron and astrocyte obeys Fick's law with constant permeabilities,

$$j^{\mathrm{n}}_{\mathrm{O_2}} = \lambda_{\mathrm{n,O_2}}\big([\mathrm{O_2}]_{\mathrm{ecs}} - [\mathrm{O_2}]_{\mathrm{n}}\big), \tag{2.57}$$

$$j^{\mathrm{a}}_{\mathrm{O_2}} = \lambda_{\mathrm{a,O_2}}\big([\mathrm{O_2}]_{\mathrm{ecs}} - [\mathrm{O_2}]_{\mathrm{a}}\big). \tag{2.58}$$

We collect the concentrations of metabolites in extracellular space in the vector

$$C_{\mathrm{ecs}}(t) = \begin{bmatrix} [\mathrm{Glc}]_{\mathrm{ecs}}(t) \\ [\mathrm{Lac}]_{\mathrm{ecs}}(t) \\ [\mathrm{O_2}]_{\mathrm{ecs}}(t) \end{bmatrix}. \tag{2.59}$$

Flux	Blood ↔ Ecs			Ecs ↔ Neuron			Ecs ↔ Astrocyte		
	Param	Value	Units	Param	Value	Units	Param	Value	Units
[Glc]	$T_{\mathrm{b,Glc}}$	0.02	mM/s	$T_{\mathrm{n,Glc}}$	83.33	mM/s	$T_{\mathrm{a,Glc}}$	83.33	mM/s
	$M_{\mathrm{b,Glc}}$	4.60	mM	$M_{\mathrm{n,Glc}}$	5.00	mM	$M_{\mathrm{a,Glc}}$	12500.00	mM
[Lac]	$T_{\mathrm{b,Lac}}$	0.17	mM/s	$T_{\mathrm{n,Lac}}$	66.67	mM/s	$T_{\mathrm{a,Lac}}$	66.67	mM/s
	$M_{\mathrm{b,Lac}}$	5.00	mM	$M_{\mathrm{n,Lac}}$	0.40	mM	$M_{\mathrm{a,Lac}}$	0.40	mM
$[\mathrm{O}]_2$	$\lambda_{\mathrm{b,O_2}}$	0.04	1/s	$\lambda_{\mathrm{n,O_2}}$	0.94	1/s	$\lambda_{\mathrm{a,O_2}}$	0.68	1/s

Table 2.17: **Transports:** List of parameters in the expression of the transport rates and their corresponding values. By $T_{c,m}$ we denote the maximum transport rate, while by $M_{c,m}$ we denote the affinity constant in the Michaelis-Menten expressions describing the transport rate of the metabolite $m = \{\mathrm{Glc, Lac}\}$ from compartment c, where $c = \{\mathrm{blood, neuron, astrocyte\ or\ ecs}\}$. $\lambda_{c,\mathrm{O_2}}$ is the parameter in Fick's law describing the diffusion of oxygen from compartment c.

2.4.3 Neuron and astrocyte

In the two cellular compartments, we follow the time course of the concentrations of glucose, lactate, oxygen, pyruvate (Pyr), creatine (Cr), phosphocreatine (Pcr), adenosine triphosphate (ATP), adenosine diphosphate (ADP) and the oxidized and reduced forms of nicotinamide adenine dinucleotide ($\mathrm{NAD^+}$, respectively NADH). These ten metabolites, whose resting concentrations are listed in Table 2.18, participate in the chemical reactions in Table 2.19.

	[Glc]	[O_2]	[Lac]	[Pyr]	[PCr]	[Cr]	[ATP]	[ADP]	[NADH]	[NAD]
b	4.51	6.67	1.24							
ecs	1.19	0.04	1.30							
n	1.19	0.03	1.30	0.38	10.33	3.0e-4	2.18	6.3e-3	1.2e-3	0.03
a	0.65	0.03	1.30	0.35	10.32	1.1e-3	2.17	0.03	1.2e-3	0.03

Table 2.18: **Metabolites:** List of metabolites in the 4 compartments (blood (b), extracellular space (ecs), neuron (n) and astrocyte (a)) and their corresponding resting concentrations expressed in mM.

Name	Symbol	Reaction
Gcl	$\psi_{\text{Gcl,n/a}}$	$\text{Glc} + 2\,\text{NAD}^+ + 2\,\text{ADP} \longrightarrow 2\,\text{Pyr} + 2\,\text{NADH} + 2\,\text{ATP}$
LDH1	$\psi_{\text{LDH1,n/a}}$	$\text{Pyr} + \text{NADH} \longrightarrow \text{Lac} + \text{NAD}^+$
LDH2	$\psi_{\text{LDH2,n/a}}$	$\text{Lac} + \text{NAD}^+ \longrightarrow \text{Pyr} + \text{NADH}$
TCA	$\psi_{\text{TCA,n/a}}$	$\text{Pyr} + \text{ADP} + 5\,\text{NAD}^+ \longrightarrow 3\,\text{CO}_2 + \text{ATP} + 5\,\text{NADH}$
OxPhos	$\psi_{\text{OxPhos,n/a}}$	$\text{O}_2 + 2\text{NADH} + 5\text{ADP} \longrightarrow 2\,\text{NAD}^+ + 5\,\text{ATP} + 2\ \text{H}_2\text{O}$
PCr	$\psi_{\text{PCr,n/a}}$	$\text{PCr} + \text{ADP} \longrightarrow \text{Cr} + \text{ATP}$
Cr	$\psi_{\text{Cr,n/a}}$	$\text{Cr} + \text{ATP} \longrightarrow \text{PCr} + \text{ADP}$
ATPase	$\psi_{\text{ATPase,n/a}}$	$\text{ATP} \rightarrow \text{ADP}$

Table 2.19: **Reactions:** List of the lumped reactions included in the model. Abbreviations for the reaction names: Gcl = Glycolysis, LDH = Lactate dehydrogenase, reversible reaction, TCA = Tricarbocylic acid cycle, OxPhos = Oxidative phospohorylation, PCr = Phosphocreatine dephosphorylation, Cr = Creatine phosphorylation, ATPase = ATP dephosphorylation, mostly accounting for the Na^+/K^+ ATPase. Observe that the glutamate/glutamine cycling is not included in the dynamic system, as they are used as a coupling between the electrophysiology and metabolism.

The mass balance of the ten species in the two cellular compartments, is

expressed by the set of equations:

$$\begin{aligned}
\eta_j \frac{d[\mathrm{Glc}]_\mathrm{c}}{dt} &= j^\mathrm{c}_\mathrm{Glc} - \psi^\mathrm{c}_\mathrm{Gcl},\\
\eta_j \frac{d[\mathrm{Lac}]_\mathrm{c}}{dt} &= j^\mathrm{c}_\mathrm{Lac} + \psi^\mathrm{c}_\mathrm{LDH1} - \psi^\mathrm{c}_\mathrm{LDH2},\\
\eta_j \frac{d[\mathrm{O_2}]_\mathrm{c}}{dt} &= j^\mathrm{c}_{\mathrm{O}_2} - \psi^\mathrm{c}_\mathrm{OxPhos},\\
\eta_j \frac{d[\mathrm{Pyr}]_\mathrm{c}}{dt} &= 2\psi^\mathrm{c}_\mathrm{Gcl} - \psi^\mathrm{c}_\mathrm{LDH1} + \psi^\mathrm{c}_\mathrm{LDH2} - \psi^\mathrm{c}_\mathrm{TCA},\\
\eta_j \frac{d[\mathrm{PCr}]_\mathrm{c}}{dt} &= -\psi^\mathrm{c}_\mathrm{PCr} + \psi^\mathrm{c}_\mathrm{Cr},\\
\eta_j \frac{d[\mathrm{Cr}]_\mathrm{c}}{dt} &= \psi^\mathrm{c}_\mathrm{PCr} - \psi^\mathrm{c}_\mathrm{Cr},\\
\eta_j \frac{d[\mathrm{ATP}]_\mathrm{c}}{dt} &= 2\psi^\mathrm{c}_\mathrm{Gcl} + \psi^\mathrm{c}_\mathrm{TCA} + 5\psi^\mathrm{c}_\mathrm{Oxphos} + \psi^\mathrm{c}_\mathrm{PCr} - \psi^\mathrm{c}_\mathrm{Cr} - \psi^\mathrm{c}_\mathrm{ATPase},\\
\eta_j \frac{d[\mathrm{ADP}]_\mathrm{c}}{dt} &= -2\psi^\mathrm{c}_\mathrm{Gcl} - \psi^\mathrm{c}_\mathrm{TCA} - 5\psi^\mathrm{c}_\mathrm{Oxphos} - \psi^\mathrm{c}_\mathrm{PCr} + \psi^\mathrm{c}_\mathrm{Cr} + \psi^\mathrm{c}_\mathrm{ATPase},\\
\eta_j \frac{d[\mathrm{NADH}]_\mathrm{c}}{dt} &= 2\psi^\mathrm{c}_\mathrm{Gcl} - \psi^\mathrm{c}_\mathrm{LDH1} + \psi^\mathrm{c}_\mathrm{LDH2} + 5\psi^\mathrm{c}_\mathrm{TCA} - 2\psi^\mathrm{c}_\mathrm{OxPhos},\\
\eta_j \frac{d[\mathrm{NAD^+}]_\mathrm{c}}{dt} &= -2\psi^\mathrm{c}_\mathrm{Gcl} + \psi^\mathrm{c}_\mathrm{LDH1} - \psi^\mathrm{c}_\mathrm{LDH2} - 5\psi^\mathrm{c}_\mathrm{TCA} + 2\psi^\mathrm{c}_\mathrm{OxPhos},
\end{aligned} \tag{2.60}$$

where c = {n,a}, $j^\mathrm{c}_\mathrm{Glc}$, $j^\mathrm{c}_\mathrm{Lac}$ and $j^\mathrm{c}_{\mathrm{O}_2}$ are the transport rates from the extracellular space defined in equations (2.53)-(2.58). By ψ we indicate the rate corresponding to each reaction occurring in the neuron and the astrocyte, they are concentration dependent and their mathematical expressions are given in Table 2.20.

We define the phosphorylation state as the ratio between the ATP concentration and the ADP concentration in the two compartments:

$$p_\mathrm{n} = \frac{[\mathrm{ATP}]_\mathrm{n}}{[\mathrm{ADP}]_\mathrm{n}}, \quad p_\mathrm{a} = \frac{[\mathrm{ATP}]_\mathrm{a}}{[\mathrm{ADP}]_\mathrm{a}}, \tag{2.61}$$

and the redox state, as the ratio between the concentration of NADH and $\mathrm{NAD^+}$:

$$r_\mathrm{n} = \frac{[\mathrm{NADH}]_\mathrm{n}}{[\mathrm{NAD^+}]_\mathrm{n}}, \quad r_\mathrm{a} = \frac{[\mathrm{NADH}]_\mathrm{a}}{[\mathrm{NAD^+}]_\mathrm{a}}. \tag{2.62}$$

Reaction	Parameter	Units	Neuron	Astrocyte
Glycolysis (ψ_{Gcl})	V_{Gcl}	mM/s	0.26	0.25
	K_{Gcl}	mM	4.60	3.10
$V_{\mathrm{Gcl}}\frac{1/p}{\mu_{\mathrm{Gcl}}+1/p}\frac{1/r}{\psi_{\mathrm{Gcl}}+1/r}\frac{[\mathrm{Glc}]}{[\mathrm{Glc}]+K_{\mathrm{Gcl}}}$,	μ_{Gcl}		0.09	0.09
	ψ_{Gcl}		10.00	10.00
Lactate dehydrogenase (ψ_{LDH1})	V_{LDH1}	mM/s	1436.00	4160.00
$V_{\mathrm{LDH1}}\frac{r}{\psi_{\mathrm{LDH1}}+r}\frac{[\mathrm{Pyr}]}{[\mathrm{Pyr}]+K_{\mathrm{LDH1}}}$	K_{LDH1}	mM	2.15	6.24
	ψ_{LDH1}		0.10	0.10
Lactate dehydrogenase (ψ_{LDH2})	V_{LDH2}	mM/s	1579.83	3245.00
$V_{\mathrm{LDH2}}\frac{1/r}{\psi_{\mathrm{LDH2}}+1/r}\frac{[\mathrm{Lac}]}{[\mathrm{Lac}]+K_{\mathrm{LDH2}}}$	K_{LDH2}	mM	23.70	48.66
	ψ_{LDH2}		10.00	10.00
TCA cycle (ψ_{TCA})	V_{TCA}	mM/s	0.03	0.01
$V_{\mathrm{TCA}}\frac{1/p}{\mu_{\mathrm{TCA}}+1/p}\frac{1/r}{\psi_{\mathrm{TCA}}+1/r}\frac{[\mathrm{Pyr}]}{[\mathrm{Pyr}]+K_{\mathrm{TCA}}}$	K_{TCA}	mM	0.01	0.01
	μ_{TCA}		0.01	0.01
	ψ_{TCA}		10.00	10.00
Oxidative phosphorylation (ψ_{OxPhos})	V_{OxPhos}	mM/s	8.18	2.55
	K_{OxPhos}	mM	1.00	1.00
$V_{\mathrm{OxPhos}}\frac{1/p}{\mu_{\mathrm{OxPhos}}+1/p}\frac{r}{\psi_{\mathrm{OxPhos}}+r}\frac{[\mathrm{O_2}]}{[\mathrm{O_2}]+K_{\mathrm{OxPhos}}}$	μ_{LDH1}		0.01	0.01
	ψ_{LDH1}		0.10	0.10
Creatine phosphorylation (ψ_{Cr})	V_{Cr}	mM/s	16666.67	16666.67
$V_{\mathrm{Cr}}\frac{p}{\mu_{\mathrm{Cr}}+p}\frac{[\mathrm{Cr}]}{[\mathrm{Cr}]+K_{\mathrm{Cr}}}$	K_{Cr}	mM	495.00	495.00
	μ_{Cr}		0.01	0.01
Creatine dephosphorylation (ψ_{PCr})	V_{PCr}	mM/s	16666.67	16666.67
$V_{\mathrm{PCr}}\frac{1/p}{\mu_{\mathrm{PCr}}+1/p}\frac{[\mathrm{PCr}]}{[\mathrm{PCr}]+K_{\mathrm{PCr}}}$	K_{PCr}	mM	528.00	528.00
	μ_{PCr}		100.00	100.00
ATP dephosphorylation (ψ_{ATPase})	$J_{\mathrm{pump,base}}$	mM/s	0.0811	-
$H_{1/2}+E_s^{1/2}$	$J_{\mathrm{glia,base}}$	mM/s	-	0.1897
	$J_{\mathrm{pump,act}}$	mM/s	0.4444	-
	$J_{\mathrm{glia,act}}$	mM/s	-	0.1933

Table 2.20: **Reactions rates:** Michaelis-Menten type expressions for the reaction fluxes in neuron and astrocyte and the values of the respective parameters.

The concentrations of all the metabolites in neuron and astrocyte are collected

into the vectors $C_{\mathrm{n}}(t)$ and $C_{\mathrm{a}}(t) \in \mathbb{R}^{10}$.

$$C_{\mathrm{n/a}}(t) = \begin{bmatrix} [\mathrm{Glc}]_{\mathrm{n/a}}(t) \\ [\mathrm{Lac}]_{\mathrm{n/a}}(t) \\ [\mathrm{O_2}]_{\mathrm{n/a}}(t) \\ [\mathrm{Pyr}]_{\mathrm{n/a}}(t) \\ [\mathrm{PCr}]_{\mathrm{n/a}}(t) \\ [\mathrm{Cr}]_{\mathrm{n/a}}(t) \\ [\mathrm{ATP}]_{\mathrm{n/a}}(t) \\ [\mathrm{ADP}]_{\mathrm{n/a}}(t) \\ [\mathrm{NADH}]_{\mathrm{n/a}}(t) \\ [\mathrm{NAD^+}]_{\mathrm{n/a}}(t) \end{bmatrix}. \tag{2.63}$$

The expression for ATP dephosphorylation reaction (see Table 2.19), not expressed in terms of metabolite concentrations, will be discussed in more detail in the following chapter, where the coupling between the electrophysiological and metabolic model is addressed. We define ψ_{ATPase} as the sum of the energetic cost towards housekeeping tasks H, and the energetic cost for signaling E_s

$$\psi^n_{\mathrm{ATPase}} = H_1 + E^1_s, \quad \psi^a_{\mathrm{ATPase}} = H_2 + E^2_s. \tag{2.64}$$

In this chapter, the signaling costs E^1_s and E^2_s are assumed to be constant and their values depend on the activation level. On the other hand, quantifying the household energy continues to be topic debated in recent literature [45, 2]. We will revisit these energetic costs in Section 2.4.5.

2.4.4 Mathematical considerations

After collecting the concentrations of the metabolites in the four compartments in a vector

$$C(t) = \begin{bmatrix} C_{\mathrm{b}}(t) \\ C_{\mathrm{ecs}}(t) \\ C_{\mathrm{n}}(t) \\ C_{\mathrm{a}}(t) \end{bmatrix} \in \mathbb{R}^{26}, \tag{2.65}$$

we can write the differential equations of the metabolic model compactly in the form

$$\frac{dC}{dt} = f(C). \tag{2.66}$$

For simplicity, equation (2.66) deals with the metabolites concentrations. This aspect will be revisited in the next chapter where we will address the roles of blood flow and ATP dephosphorylation.

To guarantee the positivity of the concentrations, we make the change of variable:

$$C_j = C_0 \mathrm{e}^{U_j}, \qquad 1 \leq j \leq n. \tag{2.67}$$

Writing

$$C = h(U), \text{ where } X = \begin{bmatrix} U_1 \\ \vdots \\ U_n \end{bmatrix}, \tag{2.68}$$

and applying the chain rule, it follows that

$$\frac{dC_j}{dt} = \frac{dh_j(U)}{dt} = \sum_{k=1}^{n} \frac{\partial h_j}{\partial U_k} \frac{dU_k}{dt}, \tag{2.69}$$

which can be written in shorthand notation as

$$\frac{dC}{dt} = \frac{d}{dt}(h(U)) = \frac{\partial h}{\partial U} \frac{dU}{dt}. \tag{2.70}$$

Differentiating (2.68) with respect to the variable X, we obtain:

$$\frac{\partial h_j}{\partial U_k} = h_j \delta_{j,k},$$

which, in our case, becomes

$$\frac{\partial h}{\partial U} = \mathrm{diag}(h(U)) = \Lambda(U), \tag{2.71}$$

and we can write our initial system (2.66) with respect to the variable X as

$$\frac{dU}{dt} = \Lambda(U)^{-1} f(h(U)), \tag{2.72}$$

$$H(U) = \Lambda(U)^{-1} f(h(U)), \tag{2.73}$$

the system (2.66) becomes:

$$\begin{cases} \dfrac{dU}{dt} = H(U) \\ U(t_0) = U_0 \end{cases} . \tag{2.74}$$

Due to the different characteristic time scales of the metabolic processes, the system (2.74) is stiff: special care must therefore be given to its numerical solution. Backward Differentiation Formulae (BDF), a family of implicit methods, are well suited for this purpose. The BDF linear multistep methods are characterized by the following formulas:

a) **BDF1**

$$U_{n+1} - U_n = \mathrm{dt} H(t_{n+1}, U_{n+1}), \tag{2.75}$$

b) **BDF2**

$$U_{n+2} - \frac{4}{3}U_{n+1} + \frac{1}{3}U_n = \frac{2}{3}\mathrm{dt} H(t_{n+2}, U_{n+2}), \tag{2.76}$$

c) **BDF3**

$$U_{n+3} - \frac{18}{11}U_{n+2} + \frac{9}{11}U_{n+1} - \frac{2}{11}U_n = \frac{6}{11}\mathrm{dt} H(t_{n+3}, U_{n+3}), \tag{2.77}$$

d) **BDF4**

$$U_{n+4} - \frac{48}{25}U_{n+3} + \frac{36}{25}U_{n+2} - \frac{16}{25}U_{n+1} + \frac{3}{25}U_n = \frac{12}{25}\mathrm{dt} H(t_{n+4}, U_{n+4}), \tag{2.78}$$

where dt represents the step size: $t_n = t_0 + n\mathrm{dt}$.

Introduce the vector $H^{\mathrm{v}} = [H_1^{\mathrm{v}}\ H_2^{\mathrm{v}}\ H_3^{\mathrm{v}}\ H_4^{\mathrm{v}}]^t$ which contains the right hand

side of each of the equations (2.75)-(2.78), we can write

$$H_1^{\mathrm{v}} = U_{n+1} - U_n - \mathrm{dt}H(t_{n+1}, U_{n+1}), \tag{2.79}$$

$$H_2^{\mathrm{v}} = 3U_{n+2} - 4U_{n+1} + U_n - 2\mathrm{dt}H(t_{n+2}, U_{n+2}), \tag{2.80}$$

$$H_3^{\mathrm{v}} = 11U_{n+3} - 18U_{n+2} + 9U_{n+1} - 2U_n - 6\mathrm{dt}H(t_{n+3}, U_{n+3}), \tag{2.81}$$

$$H_4^{\mathrm{v}} = 25U_{n+4} - 48U_{n+3} + 36U_{n+2} - 16U_{n+1} + 3U_n - 12\mathrm{dt}H(t_{n+4}, U_{n+4}). \tag{2.82}$$

The nonlinear equations (2.79)-(2.82), are solved by Newton's Method, hence the value of U at $t = n + 1$ is:

$$U^{n+1} = U^n - J_{H_{\mathrm{v}}}^{-1} \cdot H_{val}, \tag{2.83}$$

where we can write the Jacobian $J_{H_{\mathrm{v}}}$ formally as

$$J_{H_v} = \begin{bmatrix} \text{-dt} \\ -2\mathrm{dt} \\ -6\mathrm{dt} \\ -12\mathrm{dt} \end{bmatrix} \frac{\partial H}{\partial U}.$$

The (j, k) element of the Jacobian matrix of the function H:

$$\frac{\partial H}{\partial U} = \begin{bmatrix} \frac{\partial H_1}{\partial U_1} & \cdots & \frac{\partial H_1}{\partial U_n} \\ \vdots & & \vdots \\ \frac{\partial H_n}{\partial U_1} & \cdots & \frac{\partial H_n}{\partial U_n} \end{bmatrix},$$

is

$$\begin{aligned} \left(\frac{\partial H}{\partial U}\right)_{j,k} &= \frac{\partial H_j}{\partial U_k} = \frac{\partial}{\partial U_k}\left(\frac{1}{h_j(U)} f_j(U)\right) \\ &= -\frac{1}{h_j(U)^2}\frac{\partial h_j}{\partial U_k} f_j(U) + \frac{1}{h_j(U)}\frac{\partial f_j}{\partial U_k}(U). \end{aligned}$$

From (2.71), we have

$$\frac{1}{g_j(U)^2}\frac{\partial h_j}{\partial U_k} f_j(U) = \delta_{j,k}\frac{1}{h_j} f_j(U) = \delta_{j,k} H_j(U),$$

hence,

$$\frac{\partial H}{\partial U} = -\mathrm{diag}(H) + \Lambda^{-1}\frac{\partial f}{\partial U}.$$

We calculate the partial derivative of f with respect to U by an application of the chain rule:

$$\frac{\partial f_j}{\partial U_k} = \sum_{\ell=1}^{n} \frac{\partial f_j}{\partial C_\ell}\frac{\partial h_\ell}{\partial U_k} = \sum_{\ell=1}^{n} \frac{\partial f_j}{\partial C_\ell} h_\ell \delta_{\ell,k} = \frac{\partial f_j}{\partial C_k} h_k,$$

and write it in matrix notation as

$$\frac{\partial f}{\partial U} = \frac{\partial f}{\partial C}\Lambda.$$

In summary,

$$\frac{\partial H}{\partial U} = -\mathrm{diag}(H) + \Lambda^{-1}\frac{\partial f}{\partial C}\Lambda.$$

Given the stoichiometric matrix $\mathsf{S} \in \mathbb{R}^{26\times 26}$ and the vector $\Psi(C) \in \mathbb{R}^{26}$ collecting the convection terms in blood, the transport rates and the reaction fluxes:

$$\Psi = \begin{bmatrix} B \\ \mathbf{J} \\ \mathbf{j}^{\mathrm{n}} \\ \mathbf{j}^{\mathrm{a}} \\ \psi^{\mathrm{n}} \\ \psi^{\mathrm{a}} \end{bmatrix}, \tag{2.84}$$

we can express f as

$$f(C) = \mathsf{S}\Psi(C). \tag{2.85}$$

More specifically, the stoichiometric matrix $S \in \mathbb{R}^{26\times 26}$ is of the form

$$S = \begin{bmatrix} \mathbb{I}_{3\times 3} & -\mathbb{I}_{3\times 3} & & & & \\ & \mathbb{I}_{3\times 3} & -\mathbb{I}_{3\times 3} & -\mathbb{I}_{3\times 3} & & \\ & & & S_1 & \mathbb{O}_{10\times 3} & S_2 \\ & & & & S_1 \quad \mathbb{O}_{10\times 7} & S_2 \end{bmatrix}, \tag{2.86}$$

where $\mathbb{I}$ is the identity matrix, $\mathbb{O}$ the null matrix, $S_1 \in \mathbb{R}^{10\times 3}$ and $S_2 \in \mathbb{R}^{10\times 7}$

$$S1 = \begin{bmatrix} 1 & 0 & 0 \\ 0 & 0 & 0 \\ 0 & 1 & 0 \\ 0 & 0 & 1 \\ 0 & 0 & 0 \\ 0 & 0 & 0 \\ 0 & 0 & 0 \\ 0 & 0 & 0 \\ 0 & 0 & 0 \\ 0 & 0 & 0 \end{bmatrix}, \quad S_2 = \begin{bmatrix} -1 & 0 & 0 & 0 & 0 & 0 & 0 \\ 2 & -1 & 1 & -1 & 0 & 0 & 0 \\ 0 & 1 & -1 & 0 & 0 & 0 & 0 \\ 0 & 0 & 0 & 0 & -1 & 0 & 0 \\ 0 & 0 & 0 & 0 & 0 & -1 & 1 \\ 0 & 0 & 0 & 0 & 0 & 1 & -1 \\ 2 & 0 & 0 & 1 & 5 & 1 & -1 \\ -2 & 0 & 0 & -1 & -5 & -1 & 1 \\ 2 & -1 & 1 & 5 & -2 & 0 & 0 \\ -2 & 1 & -1 & -5 & 2 & 0 & 0 \end{bmatrix}.$$

The vector B in (2.84) contains the first term of the right hand side of each equation (2.43)-(2.45):

$$B = \begin{bmatrix} \frac{q}{F}(C_{\text{art,Glc}} - [\text{Glc}]_{\text{b}}) \\ \frac{q}{F}(C_{\text{art,Lac}} - [\text{Lac}]_{\text{b}}) \\ \frac{q}{F}(C_{\text{art,O}_2} - [\text{O}_2]_{\text{b}}) \end{bmatrix},$$

while $\mathbf{J}$ is the vector of the fluxes from blood to extracellular space defined in equations (2.46)-(2.48). The vectors $\mathbf{j}^{\text{c}}$, $c = \{n, a\}$, contain the transport fluxes from extracellular space to neuron and astrocyte, whose mathematical expressions were given in (2.53)-(2.58), while the reaction rates given in Table 2.20 are collected into the vector ψ^{c}.

$$\mathbf{J} = \begin{bmatrix} J_{\mathrm{Glc}} \\ J_{\mathrm{Lac}} \\ J_{\mathrm{O_2}} \end{bmatrix}, \quad \mathbf{j}^{\mathrm{c}} = \begin{bmatrix} j^{\mathrm{c}}_{\mathrm{Glc}} \\ j^{\mathrm{c}}_{\mathrm{Lac}} \\ j^{\mathrm{c}}_{\mathrm{O_2}} \end{bmatrix}, \quad \psi^{\mathrm{c}} = \begin{bmatrix} \psi_{\mathrm{Gcl,c}} \\ \psi_{\mathrm{LDH1,c}} \\ \psi_{\mathrm{LDH2,c}} \\ \psi_{\mathrm{TCA,c}} \\ \psi_{\mathrm{Oxphos,c}} \\ \psi_{\mathrm{PCr.c}} \\ \psi_{\mathrm{Cr,c}} \end{bmatrix}, \text{ where } \mathrm{c} = \{\mathrm{n}, a\}.$$

2.4.5 Calibration

The recent literature on brain energetics [45, 2] emphasizes the fact that most of the energy consumed by the brain goes toward activating the sodium potassium pump, maintaining the ion gradients and restoring the membrane potentials. Other energy needs go towards other processes including neurotransmitter packing into vesicles and neurotransmitter recycling. The energy required for these secondary processes is referred to as household energy, while the signaling energy refers to the energetic cost of the sodium potassium pump $J_{\mathrm{pump,Na^+}}$ and glial uptake $J_{\mathrm{glia,K^+}}$

$$E_s^1 = s\eta_n J_{\mathrm{pump,Na^+}}, \tag{2.87}$$

$$E_s^2 = s\frac{\eta_{\mathrm{ecs}}}{2} J_{\mathrm{glia,K^+}}, \tag{2.88}$$

where η_{n} and η_{ecs} are the volume fractions of neuron and extracellular space and s is a parameter introduced to compensate for considering different total volumes.

In this chapter, the energetic cost of the sodium potassium pump and glial uptake are treated as inputs obtained from the electrophysiological model and are dependent on the level of neuronal activation.

To properly calibrate our model, we set the household energy (H_1 and H_2) and the parameter weighting the energetic need (s) so that the Oxygen Glucose Index (OGI) is in agreement with values reported in literature. The OGI is defined [46, 47] as:

$$\mathrm{OGI} = \frac{J_{\mathrm{O_2}}}{J_{\mathrm{Glc}}}, \tag{2.89}$$

where J_{Glc} and J_{O_2} are the fluxes of glucose and oxygen from the blood to the extracellular space; see equations (2.46) and (2.48). We consider OGI during four different levels of neuronal activity: 8 Hz, 10 Hz, 12 Hz and 90 Hz. The first three frequencies correspond to the alpha resting state [48, 49, 50], while the last one corresponds to a neuronal activation period. In our simulations, we used the input of the energetic cost of the sodium potassium pump and the glial potassium cleaning which were obtained from the electrophysiological model. The 8 Hz frequency corresponds to activation factor $\xi = 0.05$, the 10 Hz frequency to a $\xi = 0.07$, the 12 Hz frequency to $\xi = 0.1$ and the 90 Hz to $\xi = 2.5$. Each case carries a different signaling cost (E_s^1 and E_s^2), and we vary the household energy H_1 and the parameter s, while maintaining constant the ratio between the household energy of the neuron and astrocyte:

$$H_2 = 0.833 H_1.$$

Figure 2.4 shows the corresponding OGI values: the three frequencies in the alpha state range are rendered through colour maps, while the OGI during neuronal activation (90 Hz frequency) is shown in the form of red curves. Our results are in agreement with OGI values reported in literature: ranging from 4 to 4.5 during neuronal activation and 5 to 5.5 during resting state [51, 46, 52, 47, 53].

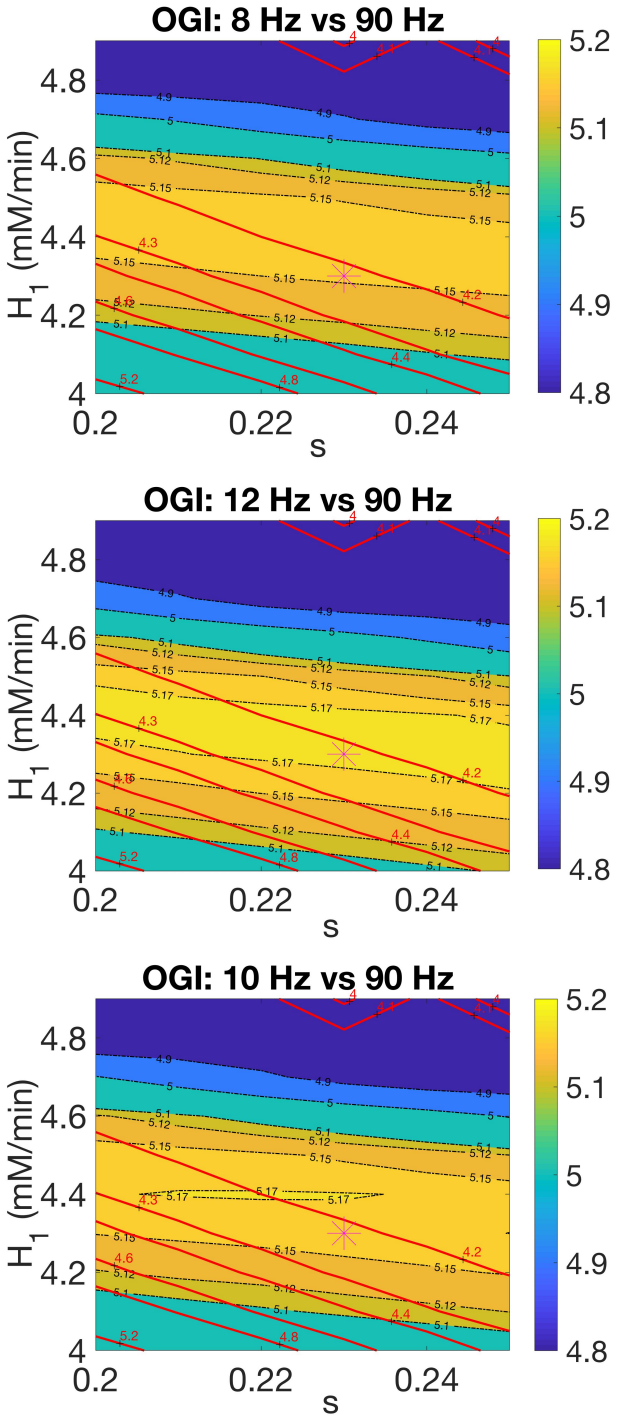

Figure 2.4: OGI analysis: cross scales parameter s versus household energy H_1. OGI values for three frequencies characterizing the awake resting state: 8 Hz (top row), 10 Hz (middle row) and 12 Hz (bottom row). The colour map shows OGI regions as the cross scaling parameter s ranges from 0.2 to 0.25 and the household energy H_1 ranges from 4 to 4.9 mM/min. The OGI values corresponding to the neuronal activation are shown using the red curves.

In light of these results, in the remainder of this thesis we set a household energy $H_1 = 4.3$ mM/min and the proportionality parameter $s = 0.23$, so as

to have an OGI index of approximately 5.2 during resting state and 4.2 during neuronal activation, values which are in agreement with recent experimental literature [46, 52, 47, 53].

2.4.6 Results

In this section we show the response of the metabolic model described in the previous sections to neuronal activation. We consider a total simulation time of 30 minutes, during which we induce a three minutes neuronal activation, while the remainder 27 minutes are spent in awake resting state with firing frequency of 8 Hz. The transition between resting state and activation is attained through the different ATP requirements dictated by the two states:

$$\psi_{\text{ATPase,n}} = \begin{cases} H_1 + s\eta_n J_{\text{pump,act}} & \text{if } t \in [2,5] \\ H_1 + s\eta_n J_{\text{pump,base}} & \text{elsewhere} \end{cases}, \tag{2.90}$$

$$\psi_{\text{ATPase,a}} = \begin{cases} H_2 + s\frac{\eta_{\text{ecs}}}{2} J_{\text{glia,act}} & \text{if } t \in [2,5] \\ H_2 + s\frac{\eta_{\text{ecs}}}{2} J_{\text{glia,base}} & \text{elsewhere} \end{cases} \tag{2.91}$$

where $J_{\text{pump,act}}$, $J_{\text{glia,act}}$, $J_{\text{pump,base}}$, $J_{\text{glia,base}}$ are the values of the sodium potassium pump, respectively for the glial potassium cleaning corresponding to the two levels of activation.

We consider the following two protocols, which differ on the blood flow response during neuronal activation

A: The blood flow is constant throughout the neuronal activation (in vitro).

B: The blood flow increases by approximatively 30% during the sustained activation (in vivo).

According to hemodynamic experimental literature [54], the blood flow response to neuronal activation is slightly delayed at the start and the end of the neuronal stimulation. We model this physiological response by using a piecewise model $q(t) = A(t)q_0$, where A(t) is described in Table 2.21, with a delay of $d_{\text{i}} = 2$ seconds at the beginning of the stimulation and $d_{\text{f}} = 5$ seconds at the end of the neuronal activation. If we denote the initial time of activation by t_i, then the

blood flow increase starts at $t_i + d_i$ and it reaches 130% of its resting state value at $t_i + d_i + r_i$, where $r_i = 10$ seconds represents the ramping time response to the start of the neuronal activation. Similarly, once the activation has ended, we consider a ramping time response of $r_\mathrm{f} = 20$ seconds.

Time	$[t_0, t_\mathrm{i} + d_\mathrm{i})$	$[t_\mathrm{i} + d_\mathrm{i}, t_\mathrm{i} + d_\mathrm{i} + r_\mathrm{i})$	$[t_\mathrm{i} + d_\mathrm{i} + r_\mathrm{i}, t_\mathrm{f} + d_\mathrm{f})$	$[t_\mathrm{f} + d_\mathrm{f}, t_\mathrm{f} + d_\mathrm{f} + r_\mathrm{f})$	$[t_\mathrm{f} + d_\mathrm{f} + r_\mathrm{f}, T)$
$A(t)$	1	$1 + \delta \dfrac{t - t_\mathrm{i} - d_\mathrm{i}}{r_\mathrm{i}}$	$1 + \delta$	$e^{-\alpha(t - t_\mathrm{f} - d_\mathrm{f})}\, a + b$	1

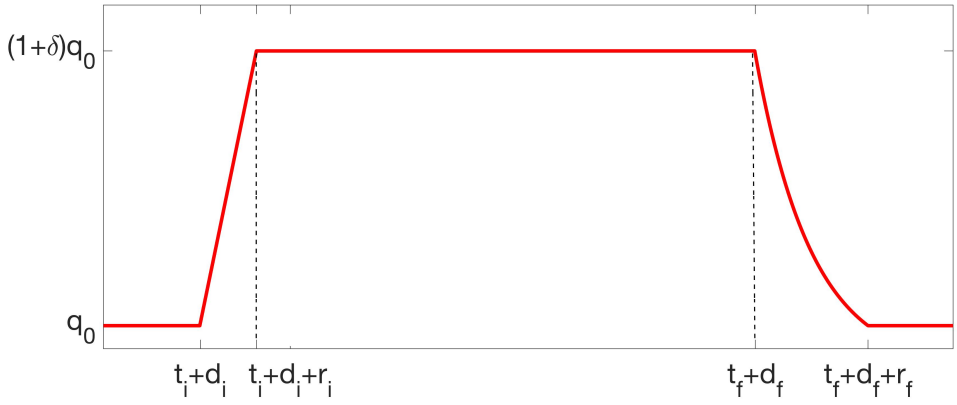

Table 2.21: **Blood flow regulation during sustained neuronal activation (Protocol B)**. The definition of the activation function A(t) can be seen in the table above, where the first row shows the periods in time at which the function is defined according to its corresponding cell on the bottom row. The graph underneath the table shows the resulting blood flow course where q_0 represents the baseline blood flow, δ gives the increase of blood during neuronal activation, t_i and t_f are the initial respectively final time of the activation, d_i and d_f are delays in the blood flow response and r_i and r_f are the ramping time response to the beginning and the end of the stimulus. The values and the units of all these parameters are given in Table 2.22. The parameters α, a and b are chosen such that the continuity of the blood flow function is ensured throughout the experiment: $\alpha = 0.1$, $a = 0.35$, and $b = 0.95$.

Param	Value	Description	Unit
q_0	0.4	Baseline blood flow	mL/min
δ	0.3	Blood flow increment during neuronal activation	-
r_i	10	Ramping time response to the start of the activation	s
r_f	20	Ramping time response to the end of the activation	s
d_i	2	Delay time in response to the start of the activation	s
d_f	5	Delay time in response to the end of the activation	s

Table 2.22: Parameters corresponding to the activation function A(t) defined in Table 2.21.

Using the blood flow protocols defined above, we run two simulations: one with protocol A and another with protocol B. Both protocols induce a three minutes neuronal activation starting at t = 2 minutes. The results are presented in a comparative manner in Figures 2.5-2.10. In all figures blue dashed lines refer to Protocol A while red lines refer to Protocol B. In these tests we can observe the behavior of the brain metabolites during neuronal activation when blood supply is constant (in vitro) or increased (in vivo).

Figure 2.5 shows the time course of the concentrations of glucose, lactate and oxygen in the four compartments. As expected, the activation period $t \in [2, 5]$ is characterized by high consumption of glucose and oxygen, accompanied by high production of lactate. More specifically, the decrease in glucose concentration in neuron and extracellular space is of approximately 65% under protocol A and 63% under protocol B, both compared to its value during the awake resting state. The consumption of glucose is much higher in the astrocyte compartment, where we record a decay to 89% in the case of protocol B and 88% in the case of protocol A of its value during the resting state. In neuron, astrocyte and extracellular space, the concentration of lactate exhibits a big increase from its baseline value: 65% under protocol A and 75% under protocol B. In the case of oxygen, we note a decay of 90% in the neuron, 76% in the astrocyte and 50% in the extracellular space.

As expected, we see very different behaviors under the two protocols in the blood compartment. Under protocol A, we observe an immediate decrease of 4% of glucose concentration below resting value, while under protocol B, we see an initial increase of 2% followed by a slow decrease. The same response also holds for the level of oxygen in blood: if the blood level is kept constant throughout the neuronal stimulation, we notice a decay of 5% in the case of oxygen, while under the increased blood flow protocol, the oxygen shows an increase of 4% compared to its baseline value and is followed by a dip at the end of the activation. Both protocols show a significant lactate production during neuronal activation, slightly bigger under protocol A.

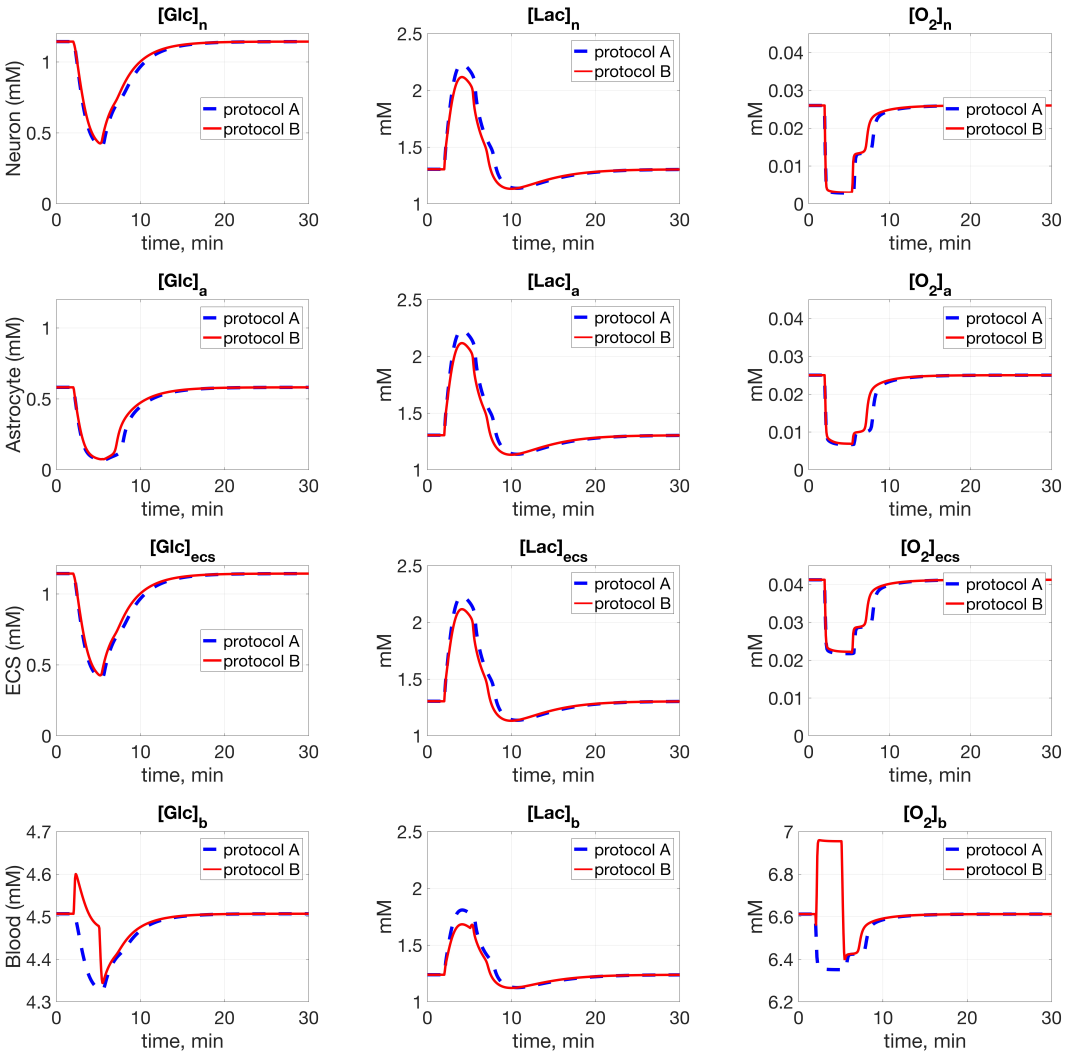

Figure 2.5: **Neuronal activation: in vivo and in vitro.** Time course of metabolite concentrations in the neuron (top row), astrocyte (second row), extracellular space (third row) and blood compartment (bottom row). In blue we see the concentrations when the blood flow is kept constant throughout the neuronal activation (protocol A), while the continuous red line shows the metabolites under protocol B, in which the blood flow exhibits an increase of 30% during the three minutes neuronal stimulation as described in Table 2.21.

Figure 2.6 shows the transport rates of glucose, lactate and oxygen from blood compartment to the extracellular space, with a higher increase in the cerebral metabolic rate of oxygen under protocol B (15% over its baseline value) than under protocol A (13% above baseline). This shows that due to the higher amount of blood flow available, the transfer of oxygen from the blood to the extracellular space is higher than before. The same holds for glucose flux from the blood compartment to the extracellular space, which has an increase of 40% under protocol B and 38% under protocol A, both calculated with respect to the value

of this flux during awake resting state. These flux values are used to calculate from (2.89) the OGI index, whose time course under the two protocols is showed on the bottom right corner of Figure 2.6. At the beginning of the activation, there is a spike in OGI for both protocols, followed by an 18% decrease below the resting state value.

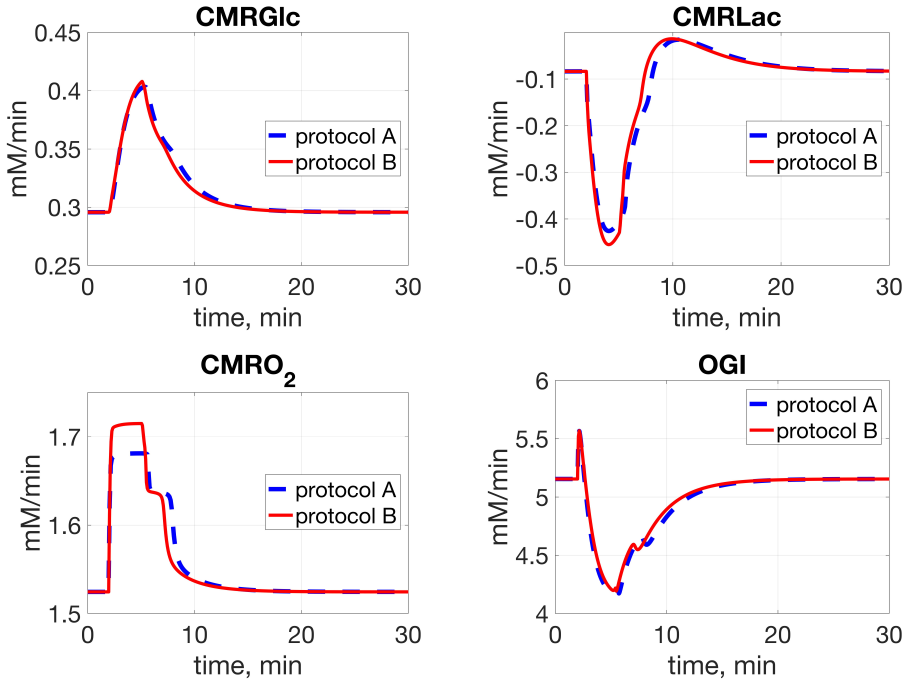

Figure 2.6: **Neuronal activation: in vivo and in vitro.** First row: Cerebral metabolic rate of glucose (left) and lactate (right). Bottom row: Cerebral metabolic rate of oxygen (left) and the resulting Oxygen-Glucose Index (right).

Figure 2.7 shows a depletion of pyruvate during the three minutes of the activation period: the concentration decreases by 84% in the neuron and by 59% in the astrocyte. As expected, the phosphorylation rates in neuron and astrocyte dramatically decrease during the activation period, due to the larger requirement of ATP during activation than during awake resting state. In both neuron and astrocyte, phosphorylation rate exhibits a decrease of approximatively 98.5% during the increased blood flow protocol B, and a 99.5% decrease when considering the blood flow constant. On the other hand, during activation, redox state increases 8 fold in the neuron and 4 fold in the astrocyte.

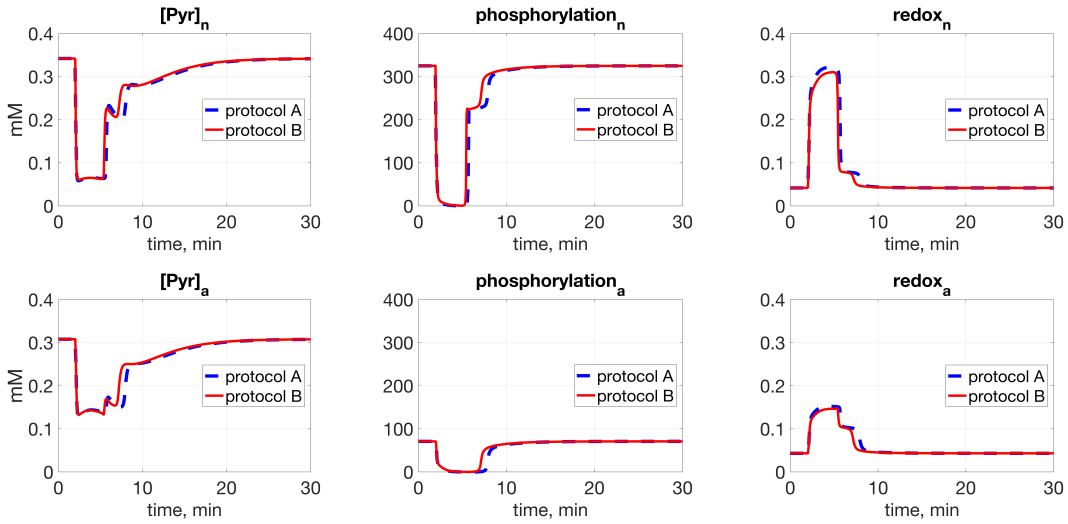

Figure 2.7: **Neuronal activation: in vivo and in vitro.** Time course of pyruvate, phosphorylation states and redox states in the neuron (top row) and astrocyte (bottom row).

Figure 2.8 illustrates the rates at which metabolites are transported from the extracellular space to the cellular compartments; glucose and oxygen transport rates substantially increase in the neuron during the activation period, while decaying in the astrocyte. On the other hand, the lactate flux dramatically decreases during activation to a negative value, and indicating that there is lactate exiting from the neuron to the extracellular space during the activation. Similarly, the lactate flux in the astrocyte is negative during baseline and increases slightly during activation.

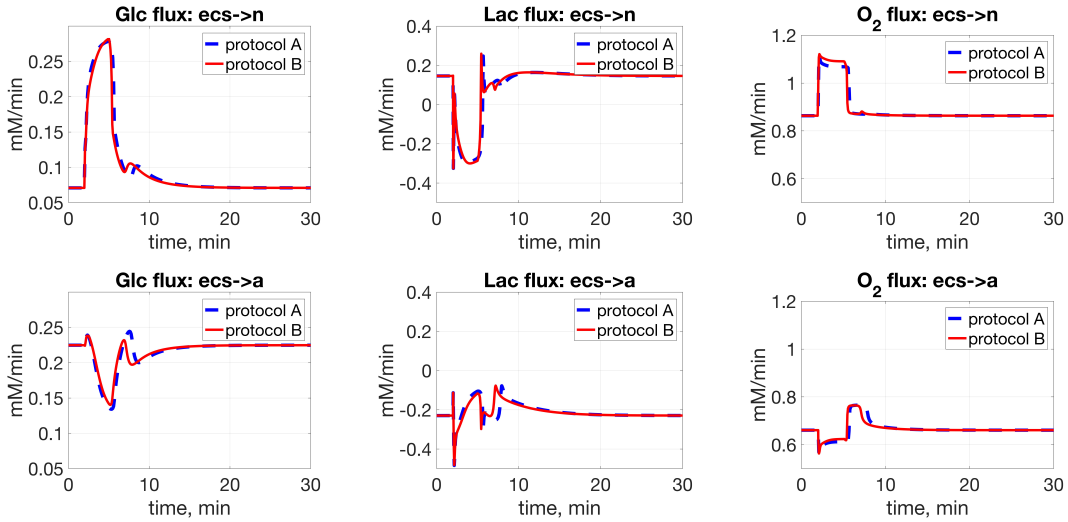

Figure 2.8: **Neuronal activation: in vivo and in vitro.** Metabolic fluxes between the extracellular space and the neuron (top row) and between the extracellular space and the astrocyte (bottom row).

The reaction fluxes in the two cellular compartments are shown in Figures 2.9 and Figure 2.10. The rate of glycolysis increases during activation in neuron, while dropping in astrocyte after an initial peak. Similar patterns are observed for the flux of the TCA cycle and oxidative phosphorylation fluxes, as well as for lactate dehydrogenase net flux.

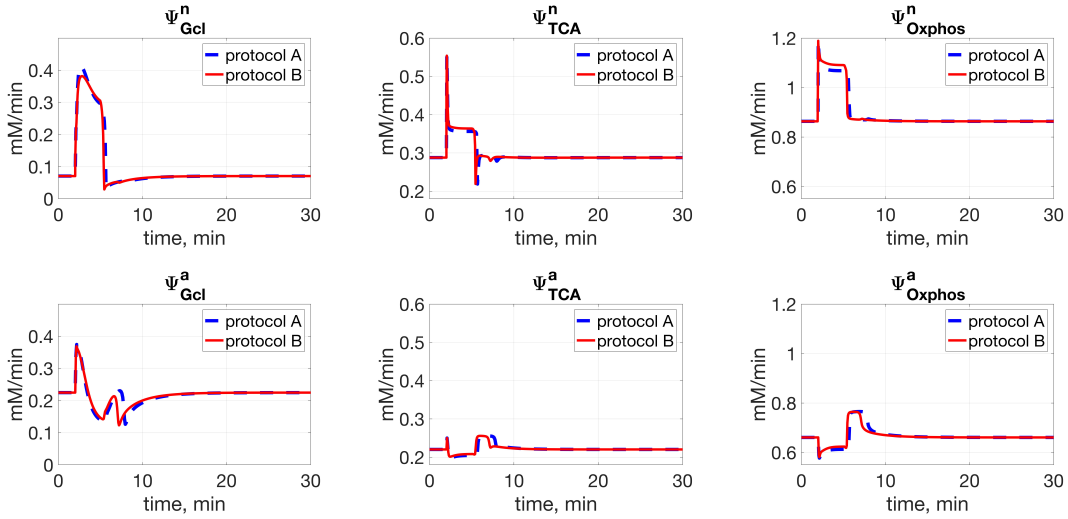

Figure 2.9: **Neuronal activation: in vivo and in vitro.** Reaction fluxes in the neuron (top row) and astrocyte compartments: glycolysis (left), TCA (middle) and oxidative phosphorylation (right).

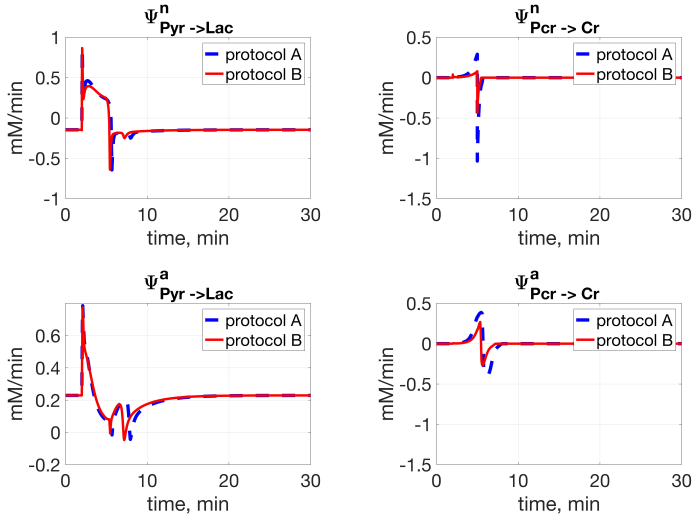

Figure 2.10: **Neuronal activation: in vivo and in vitro.** Reaction fluxes in the neuron (top row) and astrocyte compartments: lactate dehydrogenase balance flux (left) and creatine phosphorylation balance flux (right).

Chapter 3

Electro-Metabolic model

3.1 Introduction

In the previous two chapters we described two important aspects of brain dynamics: electrophysiology and metabolism. Despite their strong interconnection, these two aspects have been long studied in a separate manner by two scientific communities: one concerned with the study of the electrical properties of the brain cells and the other with the study of the main biochemical reactions occurring in the brain. In this chapter, we couple the two perspectives on the basis of their energetic production and consumption. On one hand, electrophysiological activity requires a sufficient amount of ATP, produced through the complex biochemical reactions occurring in the brain. On the other hand, the amount of energy produced depends on the availability of the different metabolites, and is dictated by the electrophysiology. This process is sketched in Figure 3.1.

In this chapter we describe a double feedback Electro-Metabolic model and propose an algorithm to deal with the dramatically different time scales of the processes: milliseconds for the electrophysiology and minutes for the metabolism. In the numerical results section we report simulations of awake resting state, consecutive neuronal activations and ischemic episodes.

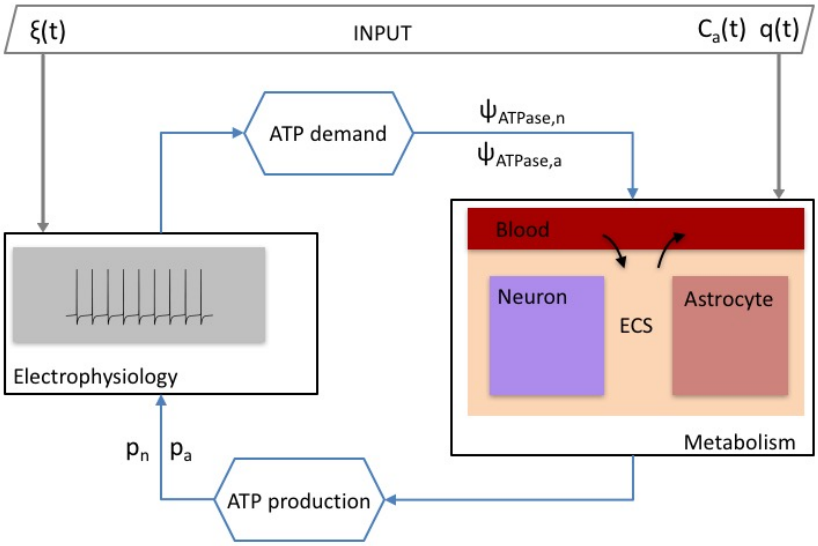

Figure 3.1: Schematic representation of the Electro-Metabolic model emphasizing the two dynamics through the ATP supply and demand [43]. p_n and p_a are the phosphorylation states of neuron, respectively astrocyte, $\psi_{\mathrm{ATPase,n}}$ and $\psi_{\mathrm{ATPase,a}}$ are the ATP dephosphorylation fluxes in neuron and in astrocyte, while $\xi(t)$ is the stimulus which induces neuronal activation and it is an input for the electrophysiology subunit. $q(t)$ is the blood flow while $C_{\mathrm{art,X}}(t)$ are the arterial concentrations of glucose, lactate and oxygen, all of which represent external inputs for the metabolic subunit.

3.2 Double-Feedback Model

A partial coupling of brain electrophysiology and metabolism was proposed by *Aubert et al.* in [38], where the energetic cost of the sodium potassium pump is added to the metabolic model, as described in Section 2.3; however, its major limitation is that their uni-directional approach does not account for how metabolic response affects electropysiological activities.

The double feedback mechanism described in this chapter includes the energetic cost of the electrophysiological activity in the metabolism and accounts for the metabolic response in the electrophysiological activity. This coupling of the electrophysiology and metabolism is based on the ATP supply and demand, rather than explicit modeling of the glutamate cycles as in [9].

3.2.1 Metabolism to Electrophysiology

To account for the metabolic response to the energetic cost demanded by the electrophysiology, we modify the expressions of the sodium potassium pump and the glial uptake given in Chapter 1, in equations (1.21) and (1.22) into (see [43]):

$$J_{\text{pump,Na}^+} = \frac{p_n}{\mu_\text{p} + p_n}\left(\frac{\rho}{1+\exp(25-[\text{Na}^+]_\text{i})/3)}\right)\left(\frac{1}{1+\exp(2.2-[\text{K}^+]_\text{ecs})}\right) \quad (3.1)$$

$$J_{\text{glia,K}^+} = \frac{p_a}{\mu_\text{g} + p_a}\frac{G_\text{glia}}{1+\exp((14.7-[\text{K}^+]_\text{ecs})/25)}, \quad (3.2)$$

where $p_n = p_n(t)$, $p_a = p_a(t)$ are the phosphorylation states in the neuron and astrocyte, and $\mu_\text{p} = 0.1$, $\mu_\text{g} = 0.1$ are affinity constants.

The modified pump activity model is such that, if the phosphorylation states determined by the metabolism are not sufficiently large, the sodium and potassium ion fluxes slow down, leading to an imbalance in ionic concentrations. We remark that the astrocytic potassium flux $J_{\text{glia,K}^+}$ is not directly dependent on ATP, but takes into account a metabolic cost to account for potassium cleaning by the astrocyte [55]. After the addition of the metabolic feedback, the electrophysiological model (1.26) becomes

$$\frac{du}{dt} = f(u, \xi, p_n, p_a), \quad (3.3)$$

where ξ is the stimulus controlling the activation, as explained in Section 1.2.2.

3.2.2 Electrophysiology to Metabolism

The electrophysiological feedback is encoded into the metabolic model through the energetic cost of the ion pump action [43]. The ATP dephosphorylation reaction: ATP $\rightarrow$ ADP releases a binding energy of $\Delta E = 30.5$ kJ/mol which can be used to maintain the pump actions. It is also well known that one ATPase is required for the exchange of three sodium ions for two potassium ions, therefore, the following stoichiometric relation holds for both cells:

$$\text{ATP} + 3\text{Na}^+_\text{i} + 2\text{K}^+_\text{ecs} \rightarrow \text{ADP} + 3\text{Na}^+_\text{ecs} + 2\text{K}^+_\text{i}.$$

The mass balance equations for intracellular sodium and extracellular potassium defined in (1.17) and (1.18) can be written with respect to the ATPase fluxes as:

$$\begin{aligned}\eta_n \frac{d[\mathrm{Na}^+]_i}{dt} &= -\gamma\eta_n I^+_{\mathrm{Na}} - 3\psi_{\mathrm{ATPase,n}},\\ \eta_{\mathrm{ecs}} \frac{d[\mathrm{K}^+]_{\mathrm{ecs}}}{dt} &= \gamma\eta_n I^+_{\mathrm{K}} - 2\psi_{\mathrm{ATPase,n}} - 2\psi_{\mathrm{ATPase,a}} - \varepsilon_{\mathrm{ecs}}([\mathrm{K}^+]_{\mathrm{ecs}} - k_\infty).\end{aligned}$$

If we denote by $I_{\mathrm{Na}^+,\mathrm{leak}}$ the leak sodium current induced by the increase of membrane permeability given by the function ξ:

$$I_{\mathrm{Na}^+,\mathrm{leak}} = g_{\mathrm{Na}^+,\mathrm{leak}}(t)(V - V_{\mathrm{Na}^+}),$$

and by $\mathrm{I}^0_{\mathrm{Na}^+,\mathrm{leak}}$ the average sodium leak current obtained during resting state, we can model the sodium current that acts alongside the neurotransmitter activity as:

$$I_{\mathrm{Na}^+,\mathrm{act}}(t) = \begin{cases} I_{\mathrm{Na}^+,\mathrm{leak}}(t) - I^0_{\mathrm{Na}^+,\mathrm{leak}} & \text{if } \xi(t) > 0 \\ 0 & \text{if } \xi(t) = 0 \end{cases}. \tag{3.4}$$

In light of the relation above between glutamate release and sodium ion currents, we assume a glutamate-glutamine flux relation of the form:

$$J_{\mathrm{glu}} = \frac{\gamma}{\sigma} I_{\mathrm{Na}^+,\mathrm{act}}, \tag{3.5}$$

where σ accounts for the energetic cost of the glutamate-glutamine cycling during synaptic activity. The value of σ was established in [43] according to the following considerations [45]:

1. The cost of each molecule of glutamate taken up by astrocyte and transformed into glutamine is of approximately 2.33 ATP, of which 1.33 ATP go towards glutamate uptake and the other 1 ATP is spent on glutamate conversion to glutamine.

2. A vesicle contains 4000 glutamate molecules. The energetic cost in neuron for vesicle packing is of 0.33 ATP per glutamate molecule.

3. When the glutamate molecules located inside a vesicle are released into the

synaptic cleft, 15-200 non-NMDA dependent sodium channels open with mean opening time in the range of 0.6-1.4 milliseconds. The release of each glutamate vesicle causes the entrance of 200.000 sodium ions in the postsynaptic neuron.

4. The presence of glutamate in the synaptic cleft opens the NMDA dependent channels for approximately 50 milliseconds, which allows the entrance of 180.000 sodium and 10.000 calcium ions per vesicle. The removal of the extra calcium requires the activation of the calcium-sodium pump, whose 1:3 calcium to sodium ratio means that in order to extrude 10.000 ions of calcium, 30.000 ions of sodium enter.

In summary, for each vesicle containing 4000 glutamate molecules there are 410.000 sodium ions entering postsynaptic neuron. Consequently, we assume that the number σ of sodium ions entering the neuron for each molecule of glutamate released in the synaptic clef is approximately 103. In Chapter 2, the ATP dephosphorylation fluxes in neuron and astrocyte were expressed as the sum of the household energy H and signaling energy E_s. We add to this sum the energetic cost of glutamate recycling, arriving at the following expression for ATPase fluxes:

$$\psi_{\text{ATPase,n}} = H_1 + s\left(\eta_n J_{\text{pump,Na}^+} + 0.33\frac{\gamma}{\sigma} I_{\text{Na}^+,\text{act}}\right), \tag{3.6}$$

$$\psi_{\text{ATPase,a}} = H_2 + s\left(\frac{\eta_{\text{ecs}}}{2} J_{\text{glia,K}^+} + 2.33\frac{\gamma}{\sigma} I_{\text{Na}^+,\text{act}}\right), \tag{3.7}$$

where γ is a conversion factor for transforming the electric current into a mass flux that depends on the cell geometry as discussed in Chapter 1.

We indicate explicitly the dependence of the metabolic system (2.66) on the dephosphorylation fluxes $\psi_{\text{ATPase,n}}$ and $\psi_{\text{ATPase,a}}$, on the blood flow q and on the arterial concentrations C_{art} by writing:

$$\Lambda\frac{dC}{dt} = g(C, C_{\text{art}}, \psi_{\text{ATPase,n}}, \psi_{\text{ATPase,a}}, q), \tag{3.8}$$

where the ATPase fluxes are, in turn, functions of the electrophysiological activ-

ity:

$$(\psi_{\text{ATPase,n}}, \psi_{\text{ATPase,a}}) = \Theta(u).$$

Conversely, in the equation for the electrophysiological system, we indicate explicitly the dependence on the phosphorylations states in the neuron (p_n) and astrocyte (p_a) and write:

$$\frac{du}{dt} = f(u, p_{\text{n}}, p_{\text{a}}, \xi). \tag{3.9}$$

where the phosphorylation states depend on the metabolite concentrations:

$$(p_{\text{n}}, p_{\text{a}}) = \theta(C).$$

To summarize, the governing differential equations of our Electro-Metabolic model [43] are given by (3.8) and (3.9).

3.3 Multiscale computational approach

The Electro-Metabolic model that we proposed in [43] couples two different models with dramatically different typical time scales; the milliseconds range of the electrophysiological model proposed in Chapter 1 and the minute range for the metabolic model discussed in Chapter 2. This difference in the orders of magnitude of the time scales makes the computation of the Electro-Metabolic model predictions very challenging. Therefore, we dedicate this section of the thesis to address the multiscale nature of our coupled model from a computational point of view. The electrophysiological propagation is carried out with a finer discretization than the metabolic one, and at the end of each slow step, we synchronize the coupling quantities [43]. Throughout this thesis, we denote by Δt the coarser time scale of the metabolism and by $\Delta\tau$ the finer time scale of the electrophysiology.

In Chapter 2, where we described how to compute the predictions of the metabolic system (2.66) and we introduced a change of variable (2.67) that guarantees the non-negativity of the solutions, we advocated using a BDF solver to address the stiffness of the system.

In the simulations of the Electro-Metabolic model, we proceed in a similar

manner: starting from equation (3.8), we make the change of variable:

$$C_j = h(U_j) = C_0 \exp(U_j),$$

and we obtain the ordinary differential equation system:

$$\begin{aligned} \frac{du}{dt} &= \Lambda(U)^{-1} g(h(U), \psi_{\text{ATPase,n}}, \psi_{\text{ATPase,a}}, q) && (3.10) \\ &= \Phi(h(U), \psi_{\text{ATPase,n}}, \psi_{\text{ATPase,a}}, q), && (3.11) \end{aligned}$$

that we solve by with a time numerical integrator based on the BDF solver. More specifically, letting

$$t_j = j\Delta t, \qquad j = 0, 1, ..J_{\max}, \qquad J_{\max} = \frac{T}{\Delta t} - 1,$$

and

$$\begin{aligned} U_j &= U(t_j), && (3.12) \\ \Phi_j &= \Phi\big(U_j, \psi_{\text{ATPase,n}}(t_j), \psi_{\text{ATPase,a}}(t_j), q(t_j)\big). && (3.13) \end{aligned}$$

The BDF time integrator of order r estimates U_j from the value $U_{j-\ell}$, $1 \leq \ell \leq r$ at r previous time instances and some scalars α_j and β by solving an equation of the form

$$\sum_{\ell=0}^{r} \alpha_\ell U_{j-\ell} = \Delta_t \beta \Phi_j,$$

with a few steps of the Newton method. Denoting the r-step BDF-based integrator symbolically as $\mathcal{B}_r$, we can write

$$U_j = \mathcal{B}_r(\Phi_j, U_{j-1}).$$

We see from (3.13) that Φ_j is a function of the ATP dephosphorylation fluxes in neuron and astrocyte $(\psi_{\text{ATPase,n}}(t_j), \psi_{\text{ATPase,a}}(t_j))$, which are in turn obtained by numerically integrating the electrophysiology model over the interval $(j\Delta t, (j+1)\Delta t)$. The time step $\Delta\tau$ used for the numerical time integration in the electrophysiology model is much smaller than the Δt used for the metabolic one. Moreover, the electrophysiology system is independent of the time at which

is updated at the metabolic time scale and can be computed on the interval $[0,\ \Delta t]$. To update the electrophysiologic portion we employ a built-in Matlab ode15s stiff integrator, which uses an adaptive $\Delta\tau$. Given the interpolation grid $\tau = [\tau_m]_{m=0,\dots,M_j}$ of the electrophysiology in $(0, \Delta t)$, we compute the values of $J_{\text{pump,Na}^+}(\tau_m)$, $J_{\text{glia,K}^+}(\tau_m)$ and $I_{\text{Na}^+,\text{act}}(\tau_m)$ at each time instant τ_m. These values are then inserted into equation (3.6) and (3.7) which returns the value of the ATPase dephosphorylation fluxes in neuron and astrocyte $\psi_{\text{ATPase,n/a}}(\tau_m)$ at each electrophysiologic time instant. To input this value into the metabolism model, we first need to compute the energetic cost between two successive updates of the metabolism, which is achieved by averaging $\psi_{\text{ATPase,n/a}}$ over the interval $(0, \Delta t)$ through a quadrature rule.

Additionally, to insert the metabolic cost into the electrophysiology through the phosphorylation states p_n and p_a, we proposed in [43] the following predictor-corrector iteration scheme. At first, the values of the phosphorylation states are those computed at the last metabolic state, then they are updated by interpolating their previous values and the newly computed ones. Algorithmically, for $j = 0, 1, \dots, J_{\max}$ define a time grid $\tau_0, \tau_1, \dots \tau_{M_j}$ of the time interval $[0, \Delta t]$ and let:

$$\tau = \begin{bmatrix} \tau_0 \\ \tau_1 \\ \vdots \\ \tau_{M_j} \end{bmatrix}, \mathbf{u}^{j,\tau} = \begin{bmatrix} \mathbf{u}^{j,0} \\ \mathbf{u}^{j,1} \\ \vdots \\ \mathbf{u}^{j,M_j} \end{bmatrix}, \mathbf{u}^j = \mathbf{u}^{j,0}, \mathbf{u}^{j,M_j} = \mathbf{u}^{j+1,0},$$

The predictor-corrector sequence is performed twice with the midpoint quadrature rule to compute the ATPase fluxes [43]. The implementation details are explained in Algorithm 1.

Algorithm 1 Multiscale Metabolic Update

1. Given: the metabolite concentrations $\{U_0, U_{-1}, \dots U_{-r+1}\}$ at the previous r time instances

2. For $j = 0, \dots, J_{\max}$

   Calculate p_n^j and p_a^j from (2.61).

   Set $p_n^{j+1} = p_n^j, \quad p_a^{j+1} = p_a^j$

   Predictor Step:

   Define

   $f_n(\tau) = p_n^j \left(1 - \frac{\tau}{\Delta t}\right) + p_n^{j+1} \frac{\tau}{\Delta t}$
   $f_a(\tau) = p_a^j \left(1 - \frac{\tau}{\Delta t}\right) + p_a^{j+1} \frac{\tau}{\Delta t}$

   Step 1: Compute $\mathbf{u}^{j+1,\boldsymbol{\tau}}$ from $f_n(\tau)$, $f_a(\tau)$ and $\mathbf{u}^j$ using a time integrator based on BDF;

   Approximate $f_n(\tau)$ and $f_a(\tau)$ in $\boldsymbol{\tau}$ by computing

   $p_{\mathrm{n}}^{j,m} = \left(1 - \frac{\tau_m}{\Delta t}\right) p_{\mathrm{n}}^{j,0} + \frac{\tau_m}{\Delta t} p_{\mathrm{n}}^{j,M_j}$
   $p_{\mathrm{a}}^{j,m} = \left(1 - \frac{\tau_m}{\Delta t}\right) p_{\mathrm{a}}^{j,0} + \frac{\tau_m}{\Delta t} p_{\mathrm{a}}^{j,M_j}$

   Evaluate $J^{j,m}_{\mathrm{pump,Na^+}}$, $J^{j,m}_{\mathrm{glia,\ K^+}}$ and $I^{j,m}_{\mathrm{Na^+,act}}$ at the fine scale from (3.1), (3.2) and (3.4).

   Evaluate the ATPase fluxes in the fine scale from (3.6) and (3.7).

   Update the ATPase fluxes in the coarse scale model:

   $$\psi_{\mathrm{ATPase,n}}((j+1)\Delta t) = \frac{1}{2\Delta t} \sum_{m=0}^{M_j - 1} \psi^{j,m}_{\mathrm{ATPase,n}} (\tau_{m+1} - \tau_{m-1})$$

   $$\psi_{\mathrm{ATPase,a}}((j+1)\Delta t) = \frac{1}{2\Delta t} \sum_{m=0}^{M_j - 1} \psi^{j,m}_{\mathrm{ATPase,a}} (\tau_{m+1} - \tau_{m-1})$$

   Step 2: Compute U_{j+1} by integrating numerically Φ_{j+1} from (3.13) with a time integrator based on BDF

   $$U_{j+1} = \mathcal{B}_r(\Phi_{j+1}, U_j).$$

   Corrector Step: Update p_n^{j+1} and p_a^{j+1} via (2.61) using the most recent value of U_{j+1}

   Repeat from Predictor Step

   End j

3.4 Results

In this section we present the computed predictions of the coupled Electro-Metabolic model. All results were computed using a self-developed Matlab code. In the first example we consider two consecutive neuronal activations accompanied by an increase in the blood supply as explained in Chapter 2, Protocol B, Figure 2.21. In the second example, we simulate a short ischemic event during which the blood supply is reduced by 90 percent and we analyze the behaviour of the main metabolites and ionic concentrations during such a drastic reduction of blood. The third example simulates an ischemic event followed by a neuronal activation.

3.4.1 Consecutive neuronal activations

In the first experiment we consider two brief consecutive neuronal activations, each lasting 3 minutes, separated by a resting period. The awake resting state characterized by a frequency of 8Hz is obtained by setting the stimulus ξ to 0.05, while for the neuronal activations, characterized by a frequency of 90Hz, the stimulus ξ is set to 2.5.

As the system transitions from the awake resting state to neuronal activation, we closely follow the electrophysiologic and metabolic changes. The blood flow protocol used in this example increases by 30% during each neuronal stimulation, as shown in Table 2.21.

According to the model prediction, neuronal activation is accompanied by a big increase in intracellular sodium concentration and extracellular potassium concentration, a large consumption of glucose and oxygen and a massive production of lactate, in agreement with recent experimental work [56, 57, 35]. However, the neuronal response depends on the resting time between two consecutive activations. We further investigate how recovery time changes the system's behavior in the second activation in the following subsections, where we consider two cases: one where the resting period is 5 minutes and another one where the period is 10 minutes.

In both situations, the neuronal frequency does not immediately return from 90Hz to the 8Hz alpha awake resting state. As a matter of fact, at the end of

each activation, our model is able to capture a very short gap in the firing known in the literature as the **slow after-hyperpolarization effect (sAHP)**. This effect has generated a lot of interest over the last years in the literature [58, 59, 60] as many authors are interested in determining the mechanisms that greatly influence sAHP. In [58], *Gulledge et al.* observe how trains of action potentials produce a 20 seconds after-hyperpolarization effect, which is mainly mediated by the sodium-potassium pump. On the other hand, *Shah et al.* investigate in [60] the role of the calcium channels in generating the sAHP effect, while in [61], *Turner et al.* assess the role of the IKCa channels in producing the sAHP in hippocampal pyramidal cells. In our numerical experiments, the slow after-hyperpolarization effect lasts approximately 16 seconds and it coincides with a drop in the extracellular potassium concentration under the baseline value.

Resting time: 5 minutes

The action potential and corresponding frequency are shown in Figure 3.2 together with the intracellular sodium and extracellular potassium concentrations. In this simulation, we allowed a resting time of five minutes between the neuronal activations. Intracellular sodium concentration increases from 10.5 mM during the awake resting state to 16 mM during the two neuronal activation periods, while extracellular potassium concentration increases from 3 mM to 3.05mM. During the neuronal stimulation periods, the model predicts a reduction of the amplitude of the action potential, in agreement with the literature [35].

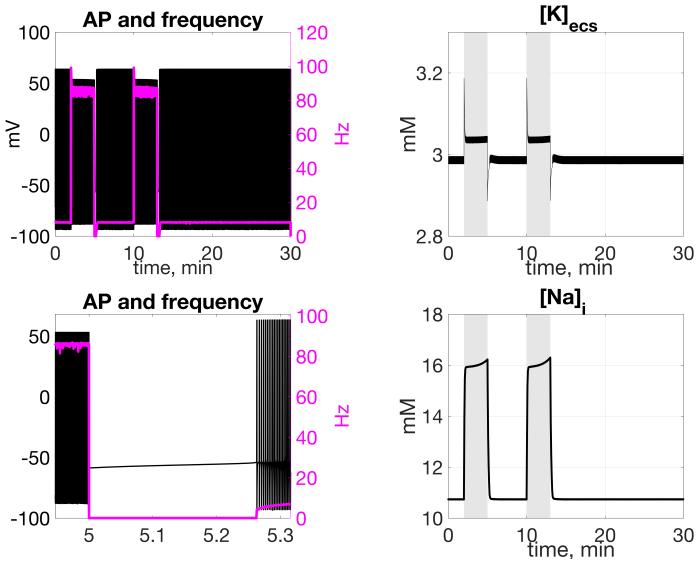

Figure 3.2: **Consecutive activations with a 5 minutes interval between.** Upper row. Left: action potential (black) and corresponding firing frequency (magenta). Right: time course of extracellular potassium concentration. Bottom row: Detail of the action potential and frequency around the time $t = 5$ min when the first activation is stopped. Right: time course of intracellular sodium concentration.

Time courses of the concentrations of the main metabolites in the blood compartment are showed in Figure 3.3 together with the corresponding transport fluxes of glucose, lactate and oxygen from the blood to the extracellular space and from the extracellular space to the two cellular compartments. At the beginning of the first neuronal activation, the concentration of glucose increases by 2%, followed by a sudden decrease of 4%. By the start of the second activation, the glucose concentration in blood had recovered to 99% of its baseline value, before showing a similar behavior to that during the first activation, except for a slightly lower initial increase of 1.5% above baseline. Lactate concentration in the blood compartment increases, during the first activation, by 37% with respect to the resting state value and is followed by a decrease to a lower value. At the beginning of the second activation, lactate concentration had only recovered to 91% of its resting value, and exhibits a smaller increase to 30% above its baseline value during the second neuronal activation event. Oxygen concentration in the blood compartment exhibits a modest increase of 4.3% above baseline during neuronal activation, followed by a decrease at the end of the activation, and then by a fast return to 99% of baseline value, after 5 minutes. The transport fluxes between

blood and the extracellular space increase by 38% above baseline for glucose, 15% for oxygen, while the lactate flux decreases 6 fold from its resting state value.

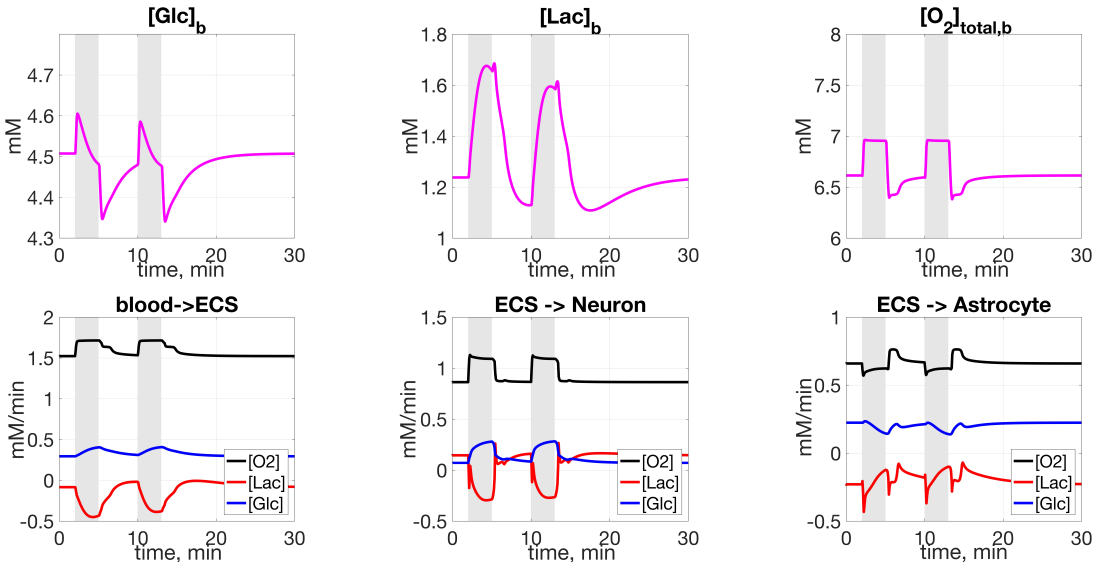

Figure 3.3: **Consecutive sustained activations with a 5 minutes interval between.** Time course of metabolite concentrations in the blood (top row): glucose (left), lactate (middle), and oxygen (right). Metabolic fluxes between compartments (bottom row): oxygen (black), lactate (red), and glucose (blue) between blood and extracellular space (left), between extracellular space and neuron (middle), and between extracellular space and astrocyte (right).

The first row of Figure 3.4 shows the time course of the concentrations of glucose, lactate and oxygen in neuron, astrocyte and extracellular space, while the second row captures the behavior of pyruvate, the phosphorylation and redox states in the two cellular compartments. During activation, glucose concentration decays by 64% of its resting state value in the neuron and extracellular space, and even more in the astrocyte, where it falls 87% below baseline. At the end of the 5 minutes resting period, glucose returns to 89% of its initial value in the neuron and extracellular space, and just 85% in astrocyte. In the second neuronal activation period, which starts with a lower glucose concentration, the decay is slightly larger in the astrocyte, where glucose concentration drops by 88% of baseline, while in neuron and extracellular space the decay is of 64%. Concurrently, lactate concentration shows a large increase of 65% over baseline value during the neuronal activation, at the end of which it starts decreasing. Once the 5 minutes resting period has ended, lactate concentration is 88% of baseline value. During the second neuronal activation, the increase in lactate concentration is slightly

smaller, topping at 53% above the resting state value. While oxygen consumption varies in the different compartments, with its concentration decreasing by 90% in neuron, 75% in astrocyte and 50% in extracellular space, its recovery time is much shorter than for glucose and lactate. At the end of the 5 minutes resting period, oxygen concentrations recover to 97% of their baseline value in all three compartments.

Figure 3.4 shows a significant consumption of pyruvate in both cellular compartments during neuronal activation, more pronounced in neuron, where the concentration drops 83% below its baseline value, while in astrocyte, it drops 60% below the resting state. In both compartments the recovery tops at 84% of its baseline value by the start of the second neuronal activation. The decrease in pyruvate during the second activation is larger than before, reaching a 84.5% decay in neuron and a 63% decay in astrocyte.

The effect of energetic requirement during the neuronal activations on the system can be clearly observed in Figure 3.4, where we see that during the 3 minutes neuronal stimulations, the phosphorylation states in the cellular compartments are almost entirely depleted: 99.8% below baseline value in the neuron and 97.7% in astrocyte, with an almost full recovery, up to 98% in neuron and 95% in astrocyte of initial baseline values. The redox states, which exhibit a massive increase during activation, 8 fold in the neuron and 4 fold in astrocyte, have fully recovered at the end of the 5 minutes resting period.

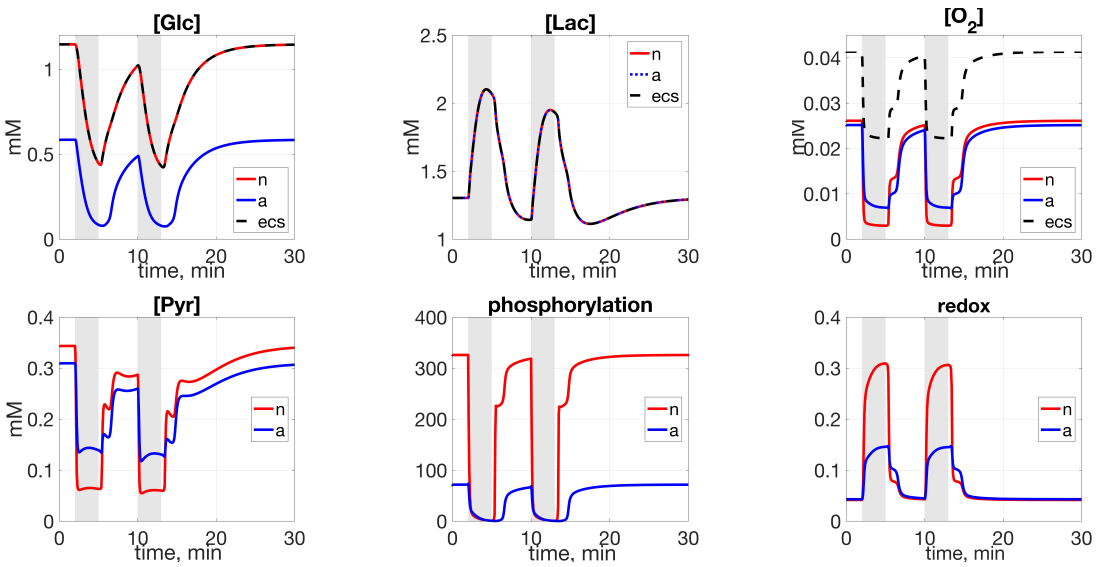

Figure 3.4: **Consecutive sustained activations with a 5 minutes interval between.** Time course of metabolite concentrations in the neuron (in red), astrocyte (blue) and extracellular space (black): glucose (top left), lactate (top middle), oxygen (top right), and pyruvate (bottom left). Time course of phosphorylation (bottom middle) and redox (bottom right) states.

Figure 3.5 shows the time course of the main reaction fluxes. The panel on the top row shows that the fluxes of glycolysis, tricarboxylic acid cycle and oxidative phosphorylation exhibit a significant increase during the activation periods in neuron, and an initial increase followed by a slight decrease in astrocyte. All fluxes return to their initial pre-activation value by the start of the second activation. The lactate dehydrogenase flux shows a large increase during neuronal stimulation in neuron, while in astrocyte, an initial increase is followed by a significant decay. Phosphocreatine fluxes in neuron and astrocyte show a slight increase during activation, and a large decrease at the end.

The OGI index calculated according to (2.89) is shown in Figure 3.5. Within the first seconds of the first neuronal activation, the OGI increases by 10% with respect to the baseline value of 5.15, after which it slowly decreases until it reaches the value 4.25 at the end of the neuronal activation. The five minutes recovery time are sufficient for the index to reach 95% of its initial value. During the second neuronal activation, the initial spike is lower than before: 5% above the resting state value, while the minimum value of 4.20 recorded at the end of the activation is slightly lower than the minimum during the previous activation.

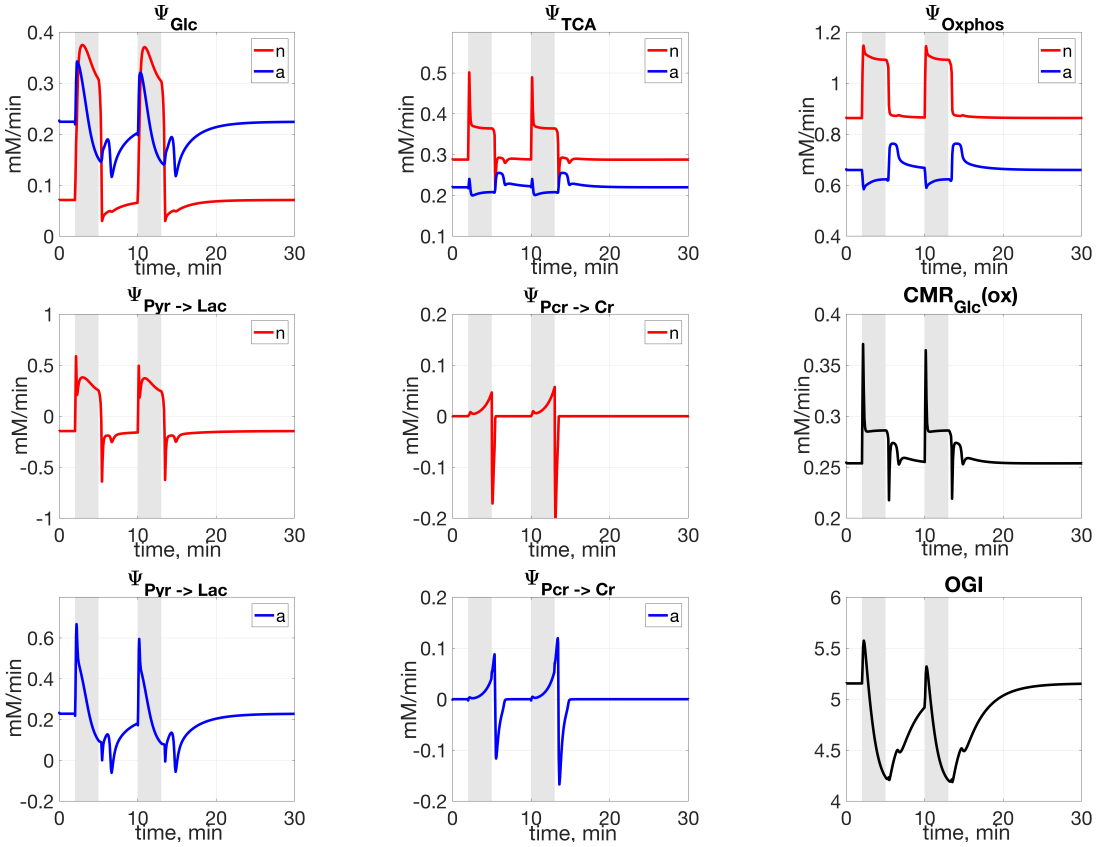

Figure 3.5: **Consecutive sustained activations with a 5 minutes interval between.** Reaction fluxes. Top row: glycolysis (left), TCA (middle) and oxidative phosphorylation (right) in neuron (red) and astrocyte (blue). Middle row: lactate dehydrogenase balance flux ($\Psi_{\mathrm{LDH1}} - \Psi_{\mathrm{LDH2}}$, left), and creatine phosphorylation balance flux ($\Psi_{\mathrm{PCr}} - \Psi_{\mathrm{Cr}}$, middle) in the neuron; time course of the cerebral metabolic oxygen rate of glucose (right). Bottom row: lactate dehydrogenase balance flux ($\Psi_{\mathrm{LDH1}} - \Psi_{\mathrm{LDH2}}$, left), and creatine phosphorylation balance flux ($\Psi_{\mathrm{PCr}} - \Psi_{\mathrm{Cr}}$, middle) in astrocyte; time course of the OGI index (right).

Resting time: 10 minutes

The results of the previous section show that the metabolites do not return to their initial resting state value at the same speed. In the first protocol, while some metabolites, like oxygen, recover very fast, others are significantly slower, like glucose, lactate and pyruvate.

Here, we considered two neuronal activation periods of 3 minutes each, but we extended the in between resting period to 10 minutes. In Figure 3.6 we visualize the action potential, the intracellular concentration of sodium and the extracellular concentration of potassium. We observe that the different period allowed between activations is not of relevance in this case and therefore, we obtain identical results to the one seen in Figure 3.2, probably because the electrophysiology

time scale is much faster than the time scale of the metabolism.

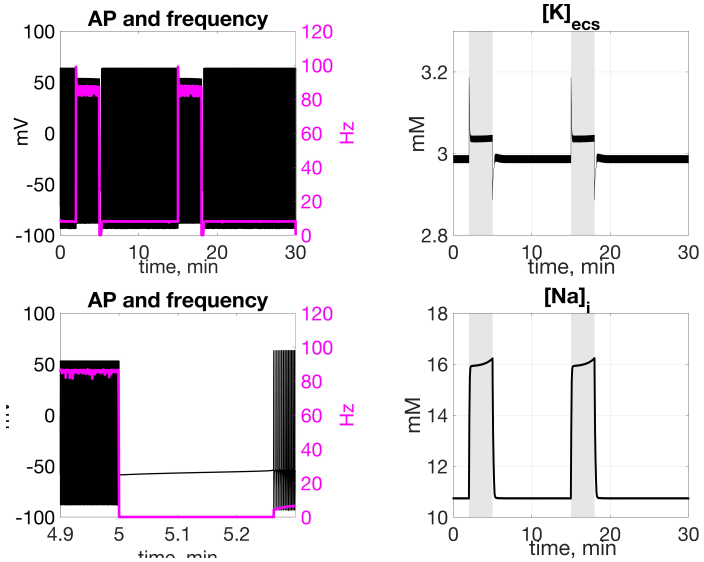

Figure 3.6: **Consecutive activations with a 10 minutes interval between.** Upper row. Left: action potential (black) and corresponding firing frequency (magenta). Right: time course of extracellular potassium concentration. Bottom row: Detail of the action potential and frequency around the time $t = 5$ min when the first activation is stopped. Right: time course of intracellular sodium concentration.

Figure 3.7 displays the time course of the metabolites in the blood compartment. In this case, the differences between the time courses of the metabolites during the first and the second activation are minimal, because the larger resting period in between the activations has allowed the metabolites to fully return to their initial resting state values prior to the second activation. More specifically, by the start of the second activation period, glucose and oxygen concentrations returned to their initial values, while lactate is 96% of it.

Similar observations are in order for the concentrations in extracellular space, in neuron and astrocyte, where the recovery is up to 98% for glucose, 100% for oxygen, 95% for lactate and 94% for pyruvate. The phosphorylation states are almost entirely replenished by the start of the second activation: 98.9% in astrocyte and 99.7% in neuron.

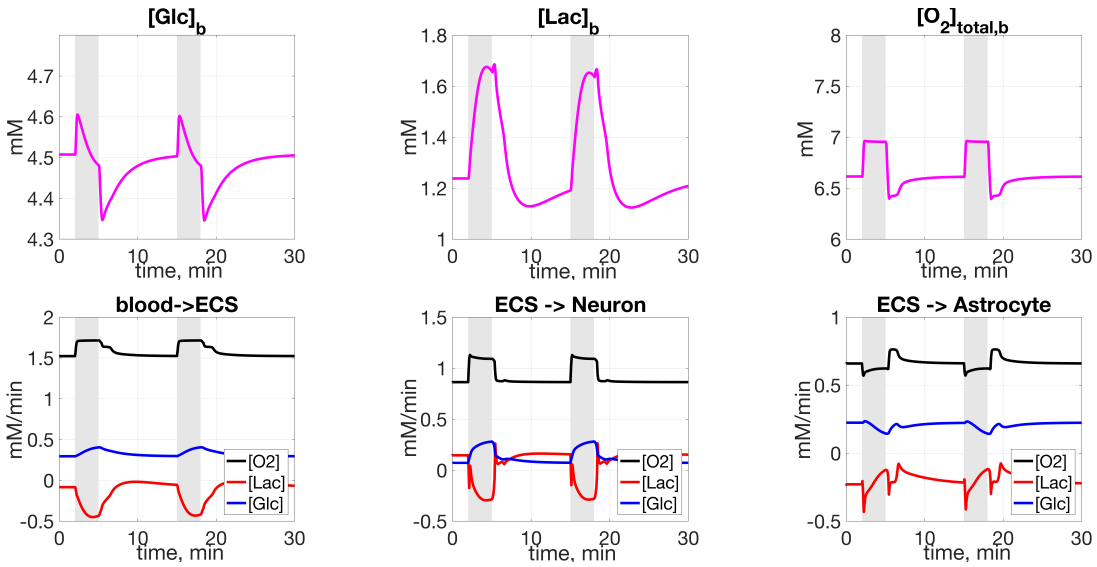

Figure 3.7: **Consecutive sustained activations with a 10 minutes interval between.** Time course of metabolite concentrations in the blood (top row): glucose (left), lactate (middle), and oxygen (right). Metabolic fluxes between compartments (bottom row): oxygen (black), lactate (red), and glucose (blue) between blood and extracellular space (left), between extracellular space and neuron (middle), and between extracellular space and astrocyte (right).

The reaction fluxes, showed in Figure 3.9, have fully reestablished their initial values at the end of the ten minute resting state period, as did the OGI index.

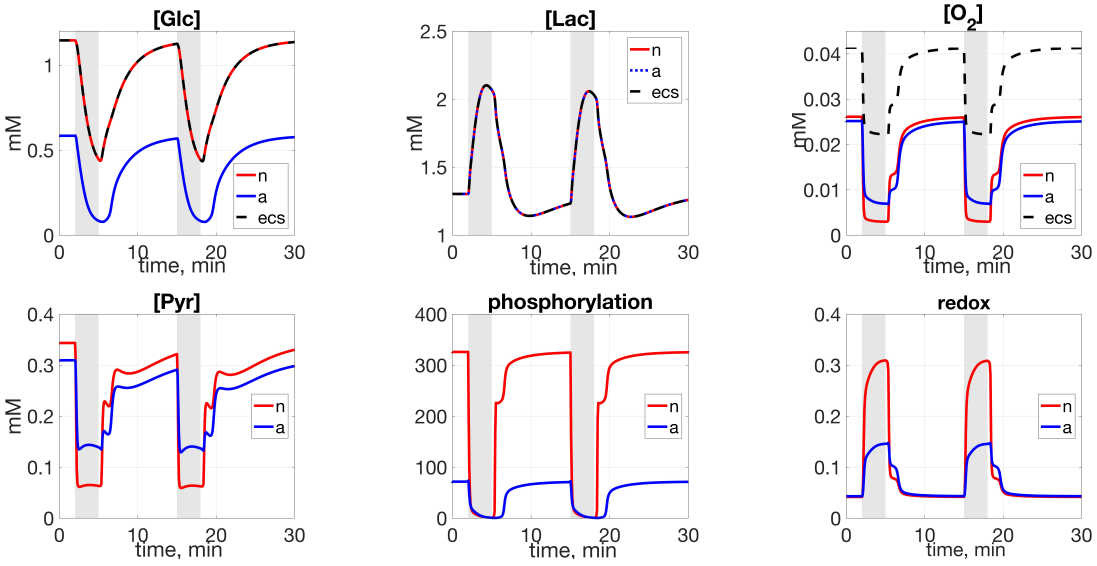

Figure 3.8: **Consecutive sustained activations with a 10 minutes interval between.** Time course of metabolite concentrations in the neuron (in red), astrocyte (blue) and extracellular space (black): glucose (top left), lactate (top middle), oxygen (top right), and pyruvate (bottom left). Time course of phosphorylation (bottom middle) and redox (bottom right) states.

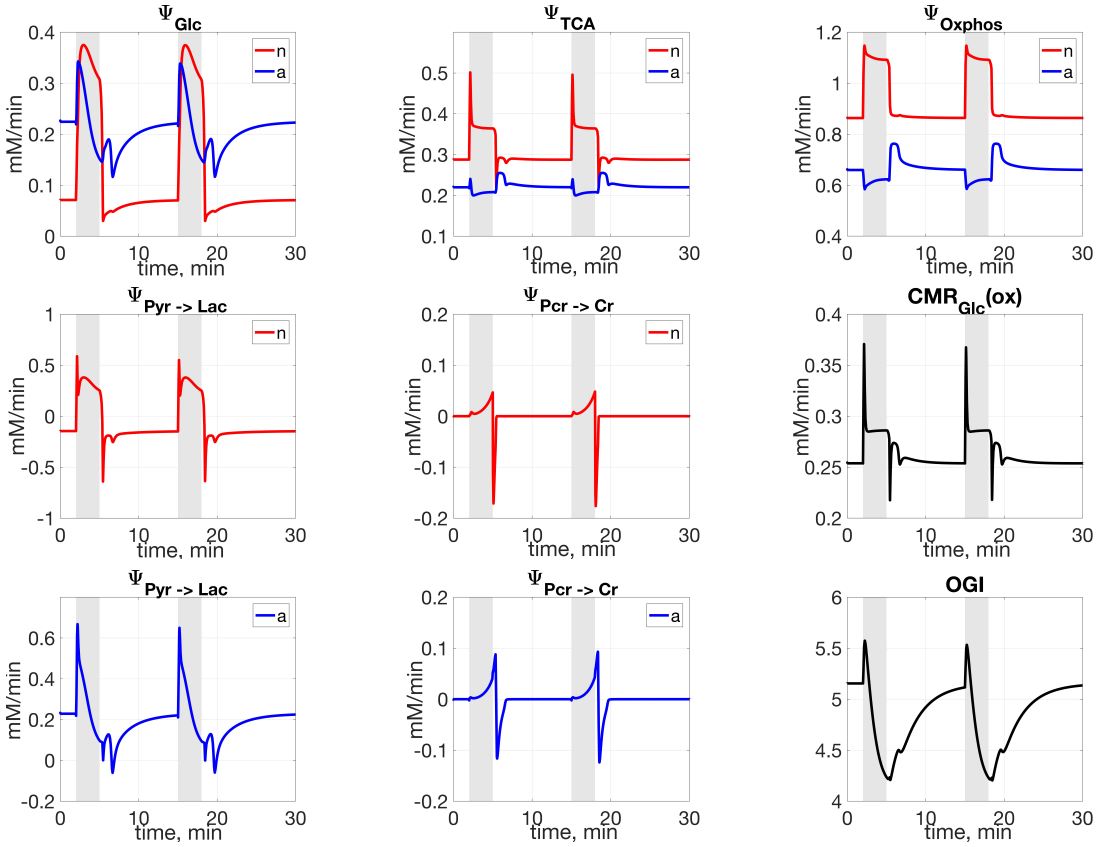

Figure 3.9: **Consecutive sustained activations with a 10 minutes interval between.** Reaction fluxes. Top row: glycolysis (left), TCA (middle) and oxidative phosphorylation (right) in neuron (red) and astrocyte (blue). Middle row: lactate dehydrogenase balance flux ($\Psi_{\mathrm{LDH1}} - \Psi_{\mathrm{LDH2}}$, left), and creatine phosphorylation balance flux ($\Psi_{\mathrm{PCr}} - \Psi_{\mathrm{Cr}}$, middle) in the neuron; time course of the cerebral metabolic oxygen rate of glucose (right). Bottom row: lactate dehydrogenase balance flux ($\Psi_{\mathrm{LDH1}} - \Psi_{\mathrm{LDH2}}$, left), and creatine phosphorylation balance flux ($\Psi_{\mathrm{PCr}} - \Psi_{\mathrm{Cr}}$, middle) in astrocyte; time course of the OGI index (right).

3.4.2 Metabolite recovery dependence on the period of time between activations

In the previous section we investigated the general electro-metabolic behavior during two consecutive activations when the length of the resting time in between is either 5 or 10 minutes. To study how the length of the resting state between the activation affects the recovery of the main metabolites, we performed various experiments where we varied the time interval between 2 and 20 minutes. The results are summarized in Figure 3.10, where we show in percentages, the recovery of glucose and lactate, with respect to the corresponding baseline value. We observe that the concentration of glucose requires a larger time in order to recover

its initial value than the concentration of lactate. However, in the case of both of these metabolites, a 20 minutes recovery period was sufficient for them to reach their baseline values.

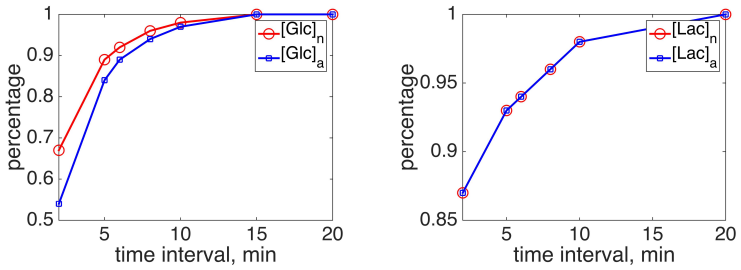

Figure 3.10: **Return to initial conditions vs length of time interval between consecutive activations** Relative recovery of glucose (left) and lactate (right) concentration in neuron (red) and astrocyte (blue) at the start of the second activation as a function of the interval between consecutive activations.

3.4.3 Ischemia

The third protocol that we consider simulates a brief ischemic event, during which the blood flow is reduced by 90%, starting at $t = 2$ minutes and lasting $T_d = 1.5$ minutes. This dramatic decrease starts within $r_1 = 5$ seconds from the onset of the ischemia and once the ischemic episode has ended, the blood flow increases gradually and returns to its resting state value over a period of $r_2 = 2$ minutes. This physiological behavior is modeled mathematically by expressing the blood flow via the piecewise linear function defined in Table 3.1.

The significant reduction of blood flow is expected to impact differently neurons and astrocytes, because of their different functions in maintaining neuronal firing. More precisely, we anticipate a rise in the extracellular potassium concentration, due to the decreased glial metabolic activity. The high potassium concentration increases the excitability of the neuron, but due to the very low supply of oxygen, the pump action can not be sustained.

Time	$[t_0, t_1)$	$[t_1, t_1 + r_1)$	$[t_1 + r_1, t_2)$	$[t_2, t_2 + r_2)$	$[t_2 + r_2, T)$
$A(t)$	1	$1 - \delta \frac{t - t_1}{r_1}$	$1 - \delta$	$1 - \delta \left(1 - \delta \frac{t - t_2}{r_2}\right)$	1

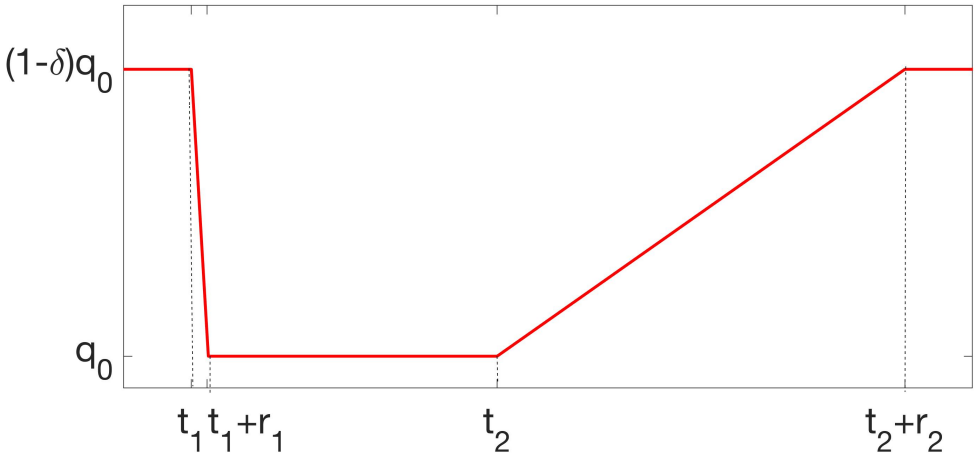

Table 3.1: **Blood flow regulation during transient ischemia.** The blood flow activation function used to simulate one ischemic episode. In the top row of the table are indicated the time intervals where the function is defined as described in the corresponding cell in the bottom row. The resulting blood flow time course is plotted in the graph underneath the table. Here q_0 is the blood flow baseline, δ denotes the blood flow reduction from its baseline value, t_1 and t_2 are the initial and final moment of the ischemic episode.

Figure 3.11 shows the effect of such a drastic reduction of the blood flow on the action potential and the ionic concentrations. As expected, during the ischemic event we see a large increase of intracellular sodium and extracellular potassium concentration, while the neuronal firing ceases within the first seconds of ischemia, returning to its baseline state once the normal blood flow is reestablished. The frequency, showed as a magenta curve in Figure 3.11, shows that the system transitions from a firing rate of 8Hz to 0Hz, and then back to 8Hz.

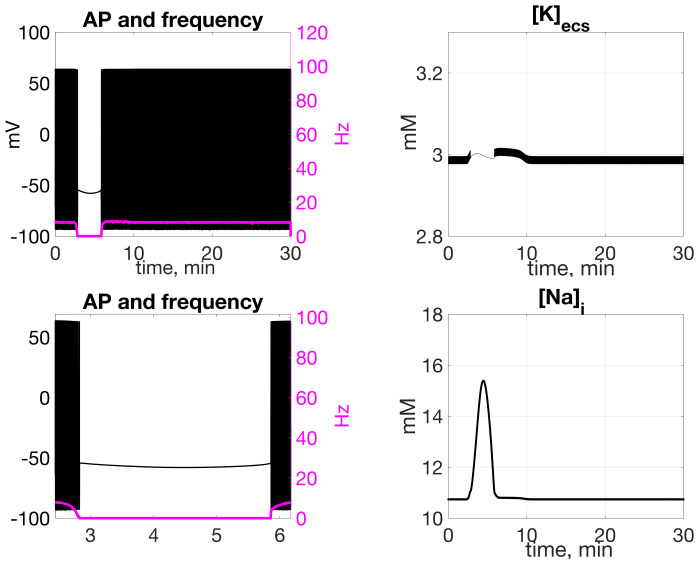

Figure 3.11: **Transient ischemia: electrophysiology**. Upper row: action potential (black) and corresponding firing frequency (magenta) in the left panel; and time course of extracellular potassium concentration in the right one. Bottom row: Detail of the action potential around the time of the ischemic event in the left panel, and the time course of intracellular sodium concentration in the right one.

The metabolism responds to the ischemic episode, as shown in Figures 3.12 and 3.13; we observe a very large consumption of glucose and oxygen and a large production of lactate in all the four compartments. The decay in glucose concentration is more significant in astrocyte, where it falls by 90% of its initial value, compared to neuron and extracellular space, which exhibit a 60% decay, and the blood compartment, where it decays by 50%. The oxygen supply is almost entirely depleted in the blood compartment and in the two cellular compartments, while in the extracellular space, oxygen concentration decreases by 85% of its normal value. The anaerobic metabolism, causes a significant production of lactate, which increases 3 fold over resting state in neuron, astrocyte and the extracellular space and approximately 2 fold in the blood compartment.

The transport fluxes of glucose, oxygen and lactate between blood and extracellular space and between the extracellular space and the two cellular compartments are displayed in the bottom row of Figure 3.12. In particular, the flux of oxygen from blood to the extracellular space shows a decrease of approximately 64% during ischemia, while at the end of the ischemic episode, increases by 13% over the baseline value. Similarly, the glucose flux from blood to extracellular

space decreases by 38% of its baseline level during ischemia, while at the end of the episode it shows a 40% increase. On the other hand, the lactate flux from the blood to the extracellular space has a 7 fold decrease.

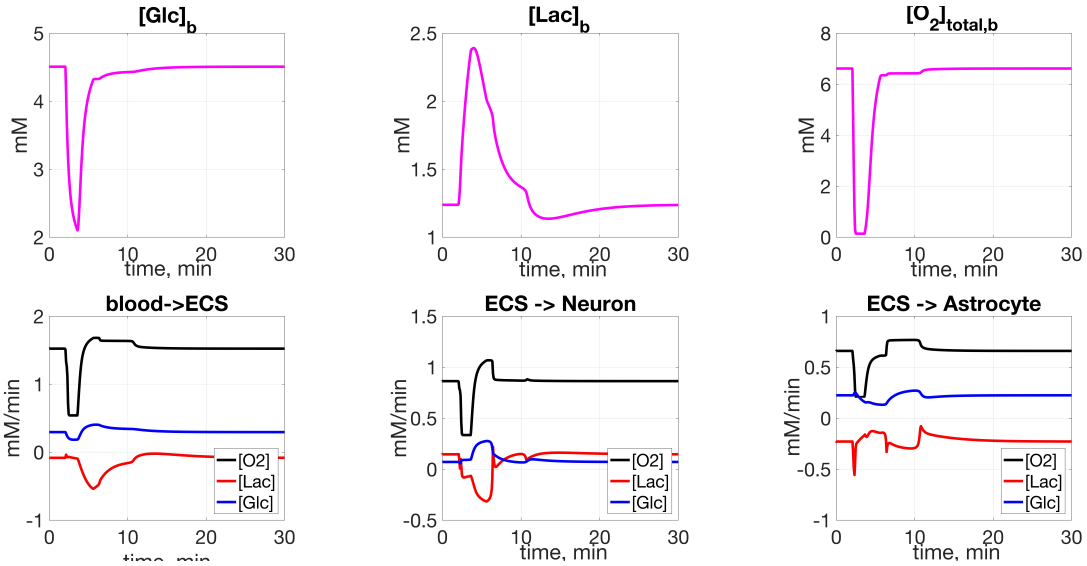

Figure 3.12: **Transient ischemia: blood concentrations and transport rates.** Time course of metabolite concentrations in blood (top row): glucose (left), lactate (middle), and oxygen (right). Transport rates fluxes between compartments (bottom row): oxygen (in black), lactate (red), and glucose (blue) between blood and extracellular space (left), between extracellular space and neuron (middle), and between extracellular space and astrocyte (right).

The left panel in the bottom row of Figure 3.13 shows a large decay in pyruvate concentration in neuron and astrocyte during the ischemic episode, all the way to 95% of baseline value in neuron and 90% in astrocyte. As expected, due to the very low supply of blood and therefore reduced glucose and oxygen availability, the phosphorylation states, shown in the middle panel of the bottom row, drop to 0 immediately as it starts. Concomitantly, as shown in the right panel of Figure 3.13, there is a surge in redox state, whose peak is approximately double in neuron than in astrocyte.

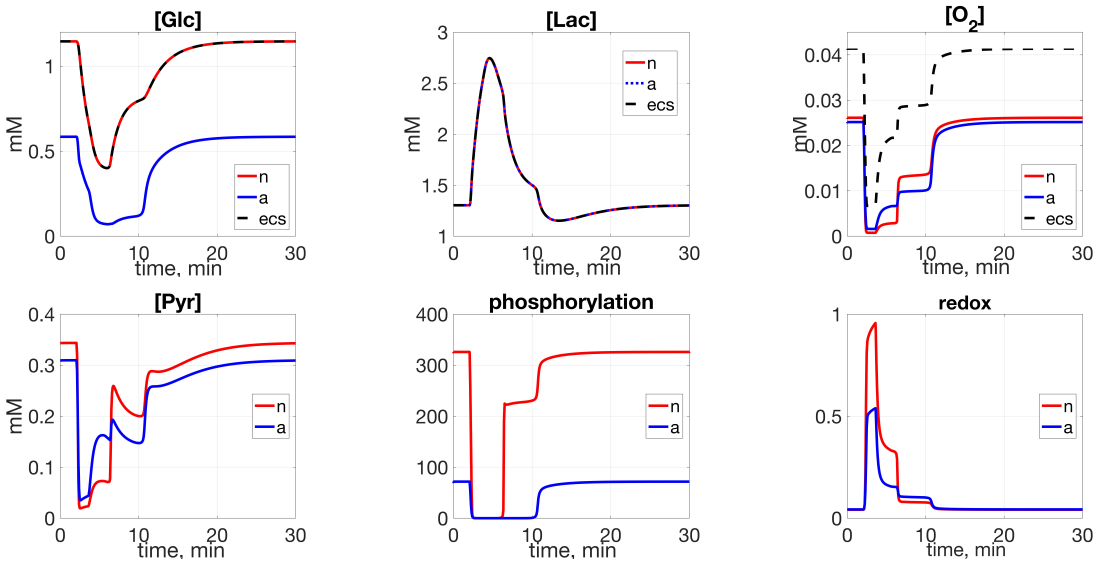

Figure 3.13: **Transient ischemia: metabolite concentrations.** Time course of metabolite concentrations in neuron (red), astrocyte (blue) and extracellular space (black): glucose (top left), lactate (top middle), oxygen (top right), and pyruvate (in neuron and astrocyte, bottom left). Time course of phosphorylation (bottom middle) and redox (bottom right) states in neuron and astrocyte.

Figure 3.14 displays the time course of the reaction fluxes. During the 90 seconds ischemic event, there is a sharp increase in the rate of glycolysis, concomitantly with a significant decrease in the TCA and oxidative phosphorylation fluxes, which reach values above the baseline once the blood flow is reestablished. The inhibition of oxidative metabolism occurs simultaneously with a surge in the anaerobic metabolism, as indicated by the large production of lactate from pyruvate and the very high rate of phosphocreatine kinase shown in the first two panels on the bottom row of Figure 3.14. The oxygen glucose index, shown in the last panel of Figure 3.14 exhibits a significant 50% decrease during ischemia and requires approximately 20 minutes to return to its initial baseline value.

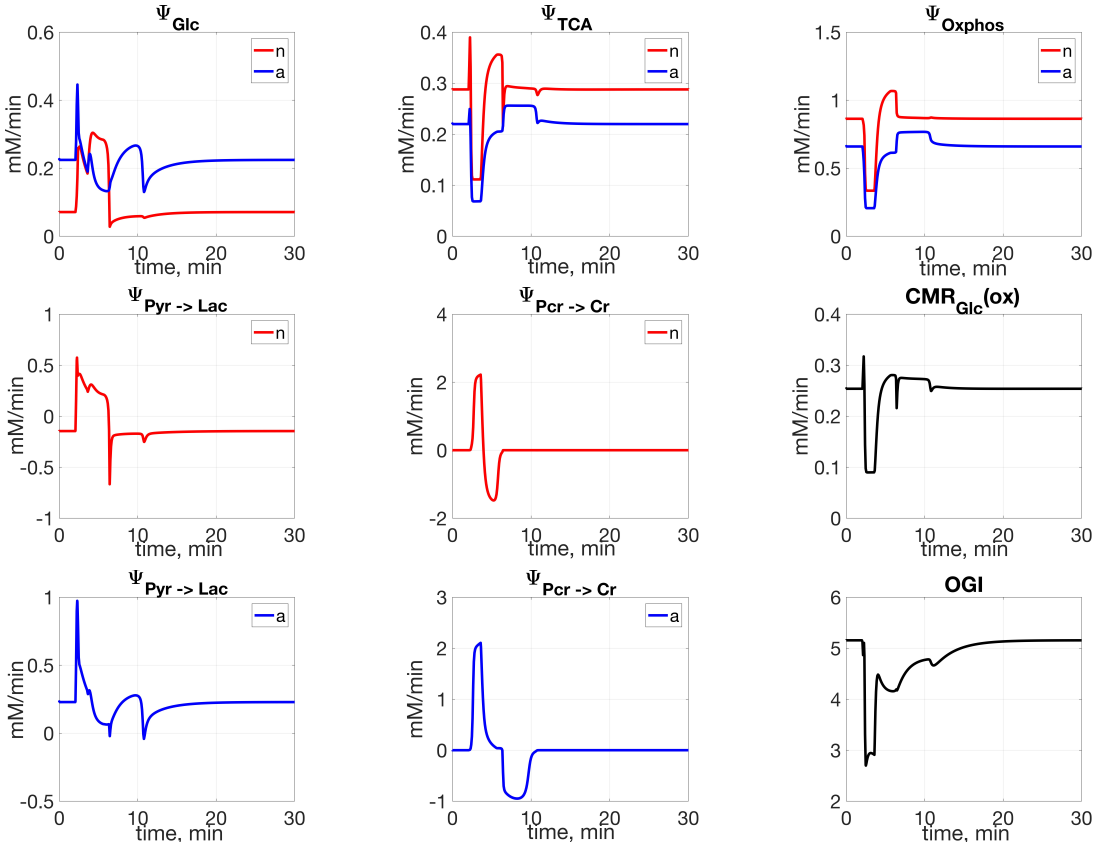

Figure 3.14: **Transient ischemia: reaction fluxes.** Reaction fluxes. Top row: glycolysis (left), TCA cycle (middle) and oxidative phosphorylation (right) in neuron (red) and astrocyte (blue). Middle row: lactate dehydrogenase balance flux, with positive direction indicating lactate production (left), creatine phosphorylation balance flux (middle) in neuron and oxidative cerebral metabolic rate of glucose (right). Bottom row: lactate dehydrogenase balance flux, with positive direction indicating lactate production (left), creatine phosphorylation balance flux (middle) in astrocyte and time course of the OGI index (right).

3.4.4 Ischemia followed by neuronal activation

The numerical experiment presented in this section is a combination of the two previous protocols, a transient ischemic event followed by resting state and a neuronal activation. The ischemic event starts at $t_i = 2$ minutes into the simulation, and has a duration of 1 minute and 30 seconds, followed by a 10 minute awake resting state period, at the end of which, there is a three minutes neuronal activation, starting at time $t_i = 13.5$ minutes and ending at $t_f = 16.5$ minutes. The blood flow protocol used in this experiment, showed schematically in Figure 3.15, combines the two previous protocols. As in the previous cases, in agreement with experimental literature, during an ischemic event and during neuronal ac-

tivation, there is some delay in the blood flow response. For the ischemic event, we consider a very small ramping time $r_1 = 5$ seconds during which the blood flow drops fast to 10% of its normal value, while at the end of the ischemic event, the blood requires a much longer time to reach its baseline value which we set in agreement with experimental work to $r_2 = 2$ minutes. In the case of neuronal activation, we account for the delay attributed to the response of the blood flow to the stimulus ξ, chosen as in Section 3.4.1 and Section 2.4.6 to be $\xi = 2.5$ for $t \in [13.5, 16.5]$, yielding a frequency of 90Hz. These delay times and the corresponding parameters were discussed in detail in Section 2.4.6; see also Table 2.21.

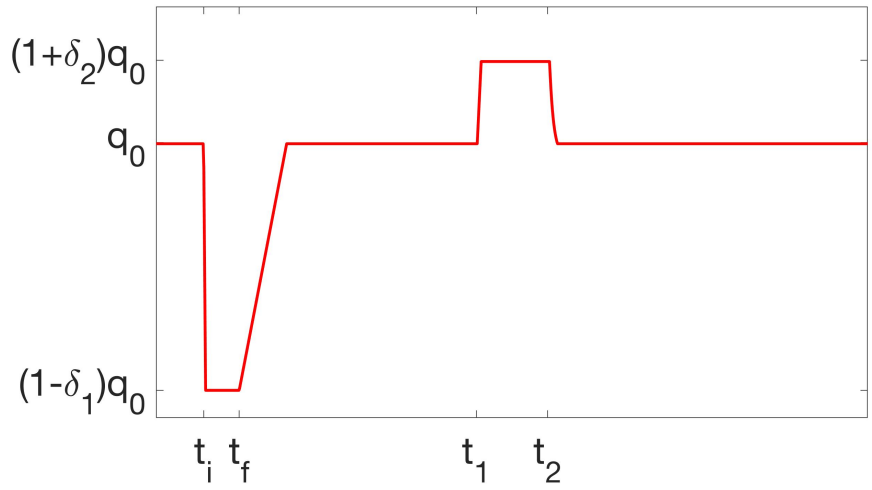

Figure 3.15: Blood flow regulation during transient ischemia followed by neuronal activation. The blood flow function used to simulate a transient ischemic event, followed by a 10 minute awake resting state and a three minutes neuronal activation. The initial time of the ischemic event is $t_i = 2$ minutes, while its final time is $t_f = 3.5$ minutes. The neuronal activation starts at $t_1 = 13.5$ and it ends at $t_2 = 16.5$ minutes.

In Figure 3.16 we show predictions of action potential, its corresponding frequency and time course of the ionic concentrations. In the first panel we see how the neuronal firing stops during the ischemic event, recovers to the awake resting state corresponding to an 8Hz frequency and it sustains a 90Hz frequency for a three minute period, after which we see a return to the awake resting state, preceded first by a slow after-hyperpolarization effect.

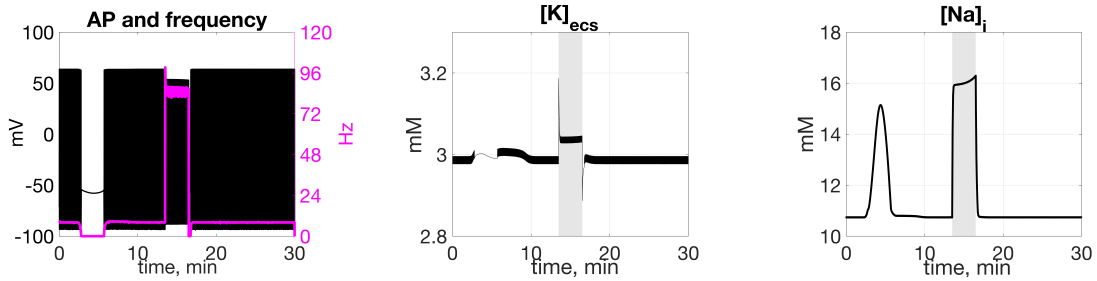

Figure 3.16: **Transient ischemia followed by activation.** Left: action potential (black) and corresponding firing frequency (magenta). Middle: time course of the extracellular potassium concentration. Right: time course of intracellular sodium concentration.

Figure 3.17 and Figure 3.18 display the metabolic response in the ischemia-activation protocol. Notice that while for some metabolites the response is very similar under ischemia and under neuronal activation, like for glucose, lactate and oxygen in neuron, astrocyte and extracellular space, for others the behavior is opposite, like glucose in the blood compartment drastically decreases during ischemia but it slightly increases during activation. In both situations, lactate exhibits an increase but, as expected, this increase is more significant during ischemia than during activation.

Despite the very large decrease in glucose and oxygen, and the very large increase in lactate during the ischemic event, their concentrations return to their initial values in the ten minutes after the ischemic event ends, and therefore, the system is able to sustain the neuronal activation. The same holds for the metabolites whose concentrations are shown in Figure 3.18; even though each metabolite has its own recovery time, most have reached 80% of their awake resting state value when the activation starts, which leads to a sufficient production of ATP, ensuring the energetic demand is met.

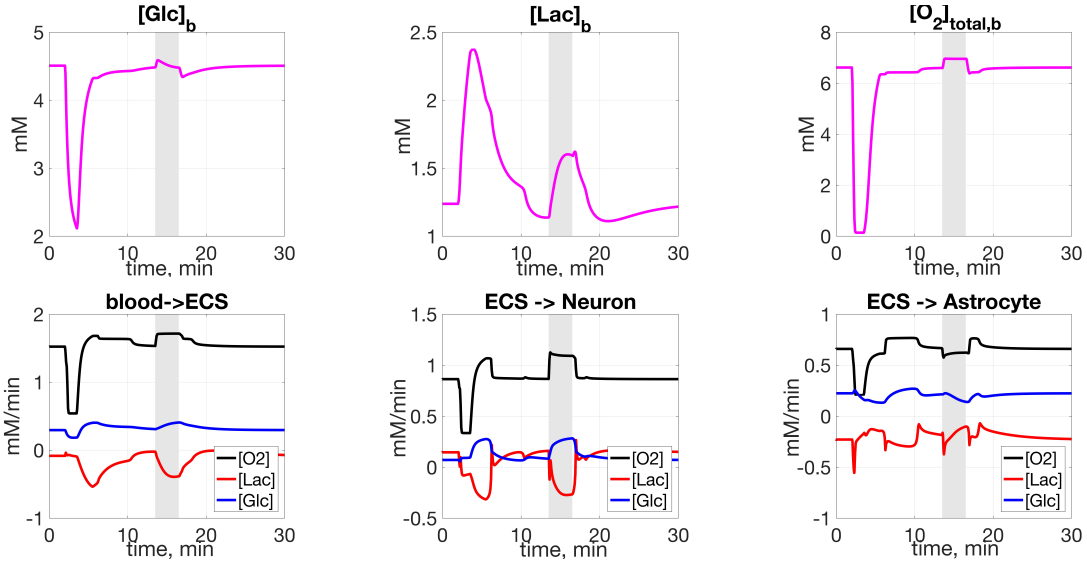

Figure 3.17: **Transient ischemia followed by activation** Time course of metabolite concentrations in blood (top row): glucose (left), lactate (middle), and oxygen (right). Transport rates between compartments (bottom row): oxygen (in black), lactate (in red), and glucose (in blue) between blood and extracellular space (left), between extracellular space and neuron (middle), and between extracellular space and astrocyte (right).

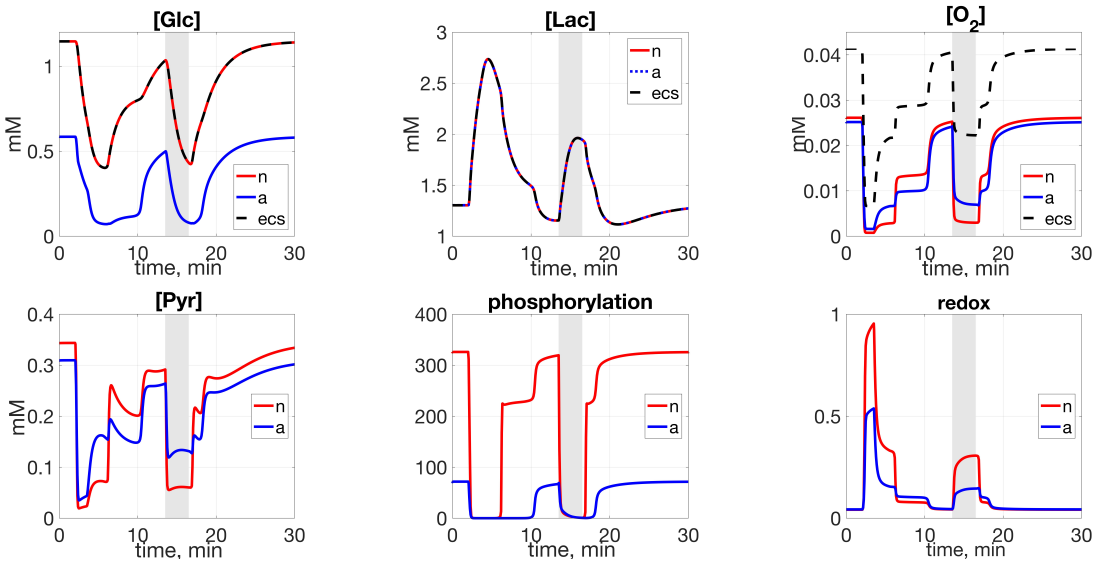

Figure 3.18: **Transient ischemia followed by activation.** Time course of metabolite concentrations in neuron (in red), astrocyte (in blue) and extracellular space (in black): glucose (top left), lactate (top middle), oxygen (top right), and pyruvate (bottom left). Time course of phosphorylation (bottom middle) and redox (bottom right) states in neuron and astrocyte.

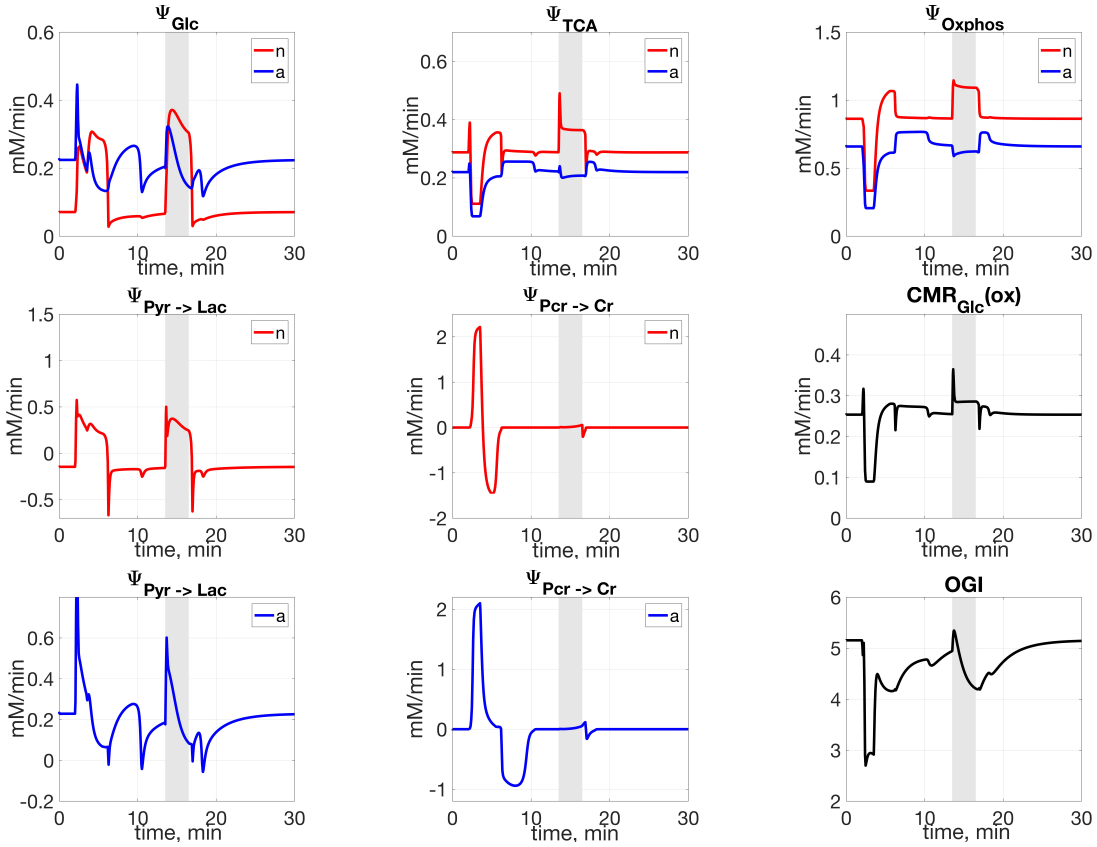

Figure 3.19: **Transient ischemia followed by activation.** Reaction fluxes. Top row: glycolysis (left), TCA cycle (middle) and oxidative phosphorylation (right) in neuron (red) and astrocyte (blue). Middle row: lactate dehydrogenase balance flux $\Psi_{LDH1} - \Psi_{LDH2}$ in neuron (left), creatine phosphorylation balance flux $\Psi_{PCr} - \Psi_{Cr}$ in neuron (middle); cerebral metabolic oxygen rate of glucose (right). Bottom row: lactate dehydrogenase balance flux $\Psi_{LDH1} - \Psi_{LDH2}$ in astrocyte (left); creatine phosphorylation balance flux $\Psi_{PCr} - \Psi_{Cr}$ in astrocyte (middle); OGI index (right).

3.5 Dependency of the firing rate on blood flow

Throughout this chapter we studied cases in which the blood flow was either increased, e.g. during the neuronal activations in Section 3.4.1, or decreased, e.g. during the ischemic episode described in Section 3.4.3. In the first situation, we observed that an increase of 30% in the blood flow is sufficient for maintaining a frequency of approximately 90Hz for a period of 3 minutes. On the other hand, in the ischemic event, during which the blood flow was reduced by 90%, the neuronal firing ceased within the first seconds. In this section we study for how long the neuron-astrocyte unit can sustain a specific frequency for a given steady blood flow.

To this end, we performed multiple simulations using three different blood flow values: the baseline cerebral blood flow value q_0, a 30% increase in the blood flow ($q = 1.3q_0$) and a 70% decrease in the baseline blood flow $q = 0.3q_0$. For each of these situations, we simulated different levels of neuronal firing, corresponding to frequencies between 4Hz and 100Hz. For each of the these frequencies and for each blood flow value we recorded the maximum amount of time that the neuron-astrocyte unit is able to sustain the firing. We noticed that while a 70Hz frequency can be sustained for one hour under the increased 30% blood protocol, for the baseline protocol $q = q_0$, the same frequency can be sustained for only 10 minutes, while for the decreased blood flow $q = 0.3q_0$ the frequency can only be maintained a couple of seconds.

The right panel of Figure 3.20 shows the OGI obtained for each frequency under the three blood flow protocols: $q = q_0$, $q = 0.3q_0$ and $q = 1.3q_0$. For normal and increased blood flows we observe a phase transition from aerobic metabolism (OGI > 5) to anaerobic metabolism (OGI ≈ 4), while in the case $q = 0.3q_0$, as expected, due to the insufficient oxygen supply, the OGI is very low for all levels of activation.

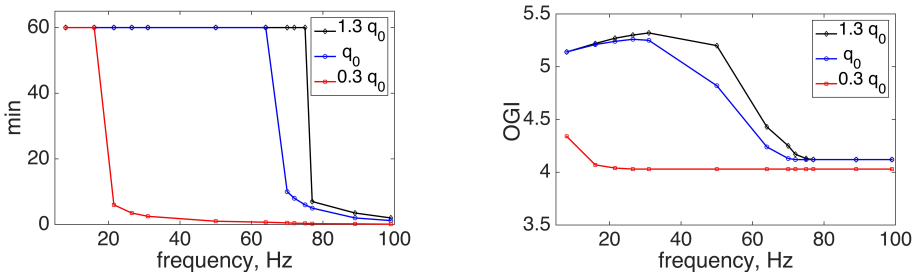

Figure 3.20: Left: maximum time interval during which the system can sustain firing at a given frequency as a function of the cerebral blood flow. Right: Dependency of the OGI on the firing frequency and the blood flow. The phase transition from high to low OGI marks the switch from aerobic to anaerobic metabolism.

3.6 Energetic cost

Figure 3.21 shows the energetic cost attributed to signaling processes in each of the protocols considered in this chapter: consecutive neuronal activations, ischemia and ischemia followed by neuronal activation. The periods corresponding to neuronal activation are indicated by a gray shadow in the left and right panels

of Figure 3.21. As expected, during the activation period, most of the energetic cost attributed to signaling occurs in neuron rather than in astrocyte; during activation, the ATP turnover shows a 6.5 fold increase with respect to baseline in neuron, while in astrocyte there is a very modest increase of 3% over the resting state value. During ischemia, we see a rapid drop in the energy levels in both cells. In neuron, however, ATP turnover rapidly recovers to baseline once the normal blood flow is reestablished, while in astrocyte because of the energy expenditure associated with potassium clearing, an additional four minutes are needed in order to recover to baseline values, suggesting that the signaling functions of the astrocyte are more affected by the ischemia.

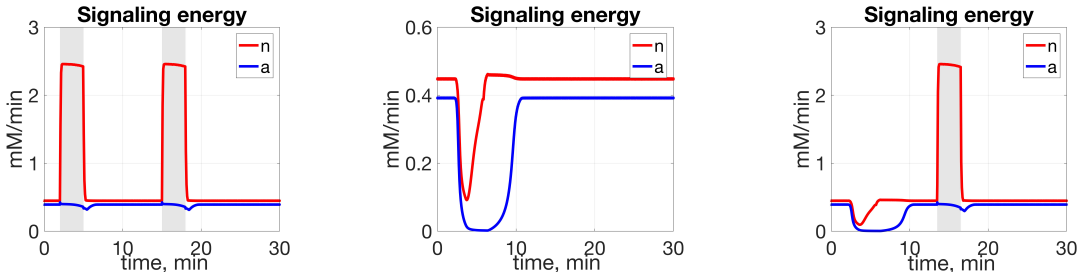

Figure 3.21: **ATP turnover from the signaling activity:** Protocol 1 (left): two consecutive activation events; Protocol 2 (middle): a transient ischemia episode; Protocol 3 (right) a transient ischemia followed by an activation event.

Chapter 4

Hemodynamics response

Most of the recently developed noninvasive neuro-imaging techniques rely on the strong coupling between the cerebral blood flow, neuronal activity and energy requirements [54]. In this chapter we focus on the behavior of the cerebral blood flow and how it relates to metabolism and neuronal activity. As previously seen, an insufficient amount of blood translates into an inadequate supply of glucose and oxygen that could lead to impairment of the neuronal activity (see Chapter 3, Section 3.4.3).

It is well known [62, 15, 63, 64] that an increase in the neuronal activity is followed by a rapid increase in both the cerebral blood flow (CBF) and cerebral blood volume (CBV), referred to as functional hyperemia; although this phenomenon has been extensively observed, its purpose and its detailed mechanisms remain a very active research topic [18, 65]. Through functional Magnetic Resonance Imaging (fMRI) it can be seen that even a very brief stimulus (2 seconds finger tapping) can induce a change in the cerebral blood flow level, which translates into a weak blood-oxygen-level dependent (BOLD) signal change [63].

In the previous chapters, we modeled the blood flow as a piecewise continuous function with a 30% increase in connection with a neuronal activation period. In this chapter, instead, we model the hemodynamic response by proposing a three compartment blood model which accounts separately for arteries, capillaries and veins.

We begin by making a short introduction with respect to the basic mechanisms of fMRI and BOLD, we comment on the current debates in this hemodynamic community and we give a brief review of the existing mathematical hemodynamical models. We start by reviewing the classical Balloon (Buxton)

Model [15, 16, 17], and continue with Barrett's three compartment model [18] and an alternative derivation and extension [19, 20] which we solve for the cerebral blood flow, used as input to our Electro-Metabolic model. Subsequently, we explain how we couple the electro-metabolic and hemodynamic models and propose an algorithm to address the multiple time scales. We conclude the chapter with numerical simulations of the three way feed-back Hemo-Electro-Metabolic model.

4.1 Introduction

In the regulation of cerebral hemodynamics, carbon dioxide plays a very important role because of its vasodilatory properties. When this gas is present in a big concentration, it triggers a condition known as hypercapnia, that leads to vasodilatation, while when the amount of carbon dioxide is too low, a condition referred to as hypocapnia, it induces vasoconstriction [66].

The Blood Oxygenation Level Depend (BOLD) contrast signal in functional MRI (fMRI) studies is sensitive to the change in the magnetic field that depends on the oxygenation state of hemoglobin [67]. The BOLD signal was discovered by *Ogawa et al.* [68] while performing experiments on rats, anesthetized and exposed to a gas mixture containing 10 percent of carbon dioxide and 90 percent of oxygen. The authors noticed that the MRI-contrast was susceptible to the blood oxygenation level and can be determined by the correlation between the blood flow and the oxygen extraction factor. BOLD fMRI quickly became an alternative approach to positron emission tomography (PET), with the great advantage of relying on an intrinsec contrast agent, rather than on exogenous contrasts agents needed for the latter [68, 64]. This noninvasive nature of BOLD fMRI removes the limitation with respect to the the number of measurements that can be taken on one research subject and it provides temporal information regarding the onset and the offset of the hemodynamic change.

Motivated by the initial results obtained on rodent brains, two years later, *Ogawa et al.* performed a similar analysis on human volunteers under normoxic physiological conditions [64] and validated the assumption that the BOLD contrast can be used to track the changes occurring in the oxygenation level during

neuronal activation in the human brain. In the original experiments, the neuronal activation was in response to visual stimulation [64]. Further research on the topic linked the BOLD contrast to changes in cerebral blood flow and cerebral blood volume [54].

The BOLD contrast has transformed fMRI into an essential neuro-imaging tool for studying the brain, whose advantages include its non-invasive nature, the relative low cost, general availability and good spatial resolution [67]. Alternative brain imaging modalities include Positron Emission Tomography (PET), MagnetoEncephalography (MEG), ElectroEncephalography (EEG) and Near Infrared Spectroscopy (NIRS) [67].

Despite the intensive research and the great advances made in BOLD imaging, the question as to what BOLD is really measuring remains open. During neuronal stimulation, arterioles in the nearby region dilate, providing a bigger supply of blood, and implicitly nutrients and oxygen. In the case of the venous compartment, the results derived from using MRI measurements and the results obtained when examining a single vein (via two-photon microscopy) are not in full agreement. On one hand, the authors using MRI to investigate the effects of hypercapnia and hypocapnia on the CBF and on the venous cerebral blood volume reported big changes in both these values [69].

During hypercapnia, an elevation of both CBF and venous cerebral blood volume (vCBV) was observed, although the change in the CBF was much greater, while during hypocapnia, a significant reduction in CBF and vCBV was recorded. In [69, 66], Chen and Pike prove that the BOLD signals obtained during hypocapnia are identical to those obtained during neuronal activation.

Two-photon microscopy technique allowed in vivo visualization of vessels in the brain, on rats [70] and mice [65] during neuronal activation, but these experiments show very little or no venous ballooning [65, 70], contradicting previous results and the classical mathematical models. It can be argued that these discrepancies can result from methodological differences including the species considered, the length of the stimulation or the type of anesthesia [18]. For example, in [65], the authors report a delayed increase in venous cerebral blood volume that can be observed only when the duration of the stimulation is greater than or equal to 20 seconds, thus explaining why it would not have been noticed in

[70], due to the shorter duration of stimulus (4 seconds).

Another essential factor when considering animal experiments is the type of anesthetic used. Isoflurane, the anesthetic used in [70], is vasodilative and may affect the vascular response [66]. For a review of the possible effects that the different anesthetic agents have on the general physiology, on how they interfere with the cortical neuronal processing and the way in which they can suppress the vascular cell activity we refer the reader to [71].

4.2 Review of hemodynamical models

In the recent years, great progress has been made with respect to studying the hemodynamics of the brain and in particular, with the development of neuroimaging techniques like PET or fMRI, which allow to map brain activation patterns [15]. However, in order to interpret the big amount of data resulting from all these measurements and to provide a better understanding of the effects of the neuronal activation on the blood flow, mathematical models are needed.

While the cerebral blood flow increases during neuronal activation by 20-60% of its resting state value, only a rather modest increase of 10-20% has been experimentally observed in the cerebral metabolic rate of oxygen [48, 52, 51, 72]: this uncoupling has been intensively studied in the last decade, [73, 74] but is not yet completely understood. To provide a description of this phenomenon, *Buxton et al.* developed a mathematical model of a vein as an expandable balloon with the ability of expanding or contracting, depending on the blood flow changes during neuronal activation [16, 15, 17, 75]. Recently, a more complex hemodynamic model consisting of three compartments has been proposed by *Barrett et al.* [18] to track the cerebral blood flow and volume in arteries, capillaries and veins. A main difference between the Buxton model [16] and this model is that *Barrett et al.* consider the ballooning in the arterial compartment, rather than in the venous one, while assuming that all compartments are able to dilate.

The balloon model [15, 16, 17] is a bio-mechanical model that describes the changes in the blood volume during activation. Its name originates from the fact that the venous compartment is modeled as an expandable balloon, with inflow the cerebral blood flow f_{in} and whose outflow is an increasing function

f_{out} of the balloon volume. The two dynamical variables tracked are the total deoxyhemoglobin (dHb) and the volume of the balloon $V_v(t)$.

The time course of the venous volume v is governed by the equation:

$$\frac{dv}{dt} = \frac{1}{\tau_0}\left(f_{in}(t) - f_{out}(v)\right). \tag{4.1}$$

Under the assumption that there is no capillary contribution and that all the deoxyhemoglobin is located in the venous compartment [15], the deoxyhemoglobin content per unit tissue volume, denoted by dHb satisfies the differential equation:

$$\frac{d}{dt}\mathrm{dHb} = \frac{1}{\tau_0}\left(f_{in}(t)\frac{E(t)}{E_0} - f_{out}(v)\frac{\mathrm{dHb}(t)}{v(t)}\right), \tag{4.2}$$

where the first term is the rate at which deoxyhemoglobin enters the venous compartment, while the second one represents the clearance rate from the tissue. Moreover, E is the oxygen extraction fraction and E_0 is the oxygen extraction factor at rest, which is usually set to 0.4 [16, 17]. τ_0 is the mean transit time through the venous compartment at rest $\tau_0 = \frac{v_0}{f_0}$ where f_0 is the resting flow and v_0 is the resting blood volume fraction. The oxygen extraction fraction is modeled as:

$$E = 1 - (1 - E_0)^{f_{in}},$$

where the inflow of blood f_{in} is a trapezoidal function with rise time between 4 and 6 seconds and variable duration [15, 16].

In the original description of the balloon model [15], the outflow function f_{out} was set so that different effects could be illustrated. The same authors have later proposed an expression for the outflow function which accounts for the viscoelastic properties of the blood vessels [16]:

$$f_{out}(v) = v^{\frac{1}{\alpha}} + v^{-\frac{1}{2}}\tau_v\frac{dv}{dt}, \tag{4.3}$$

where τ_v is a viscosity parameter and $\alpha = 0.5$.

From equations (4.1) and (4.3) we obtain the following expression for the

outflow:

$$f_{out}(v) = \frac{1}{1 + \frac{\tau_0}{\tau_v}\sqrt{v}} \left(f_{in}(t) + \frac{\tau_0}{\tau_v}\sqrt{v}v^{1/\alpha} \right), \tag{4.4}$$

whereas the BOLD signal is calculated in [15, 16, 38] as:

$$y(t) = v_0 \left(k_1(1 - \mathrm{dHb}) + k_2 \left(1 - \frac{\mathrm{dHb}}{v} \right) + k_3 \left(1 - v \right) \right), \tag{4.5}$$

where $k_1 = 7E_0$, $k_2 = 2$ and $k_3 = 2E_0 - 0.2$.

Figure 4.1 illustrates time course of the venous volume and the deoxyhemoglobin obtained from simulating the balloon model for the choice of paramters: $\alpha = 0.5$, $\tau_0 = 2$ and $\tau_v = 5$.

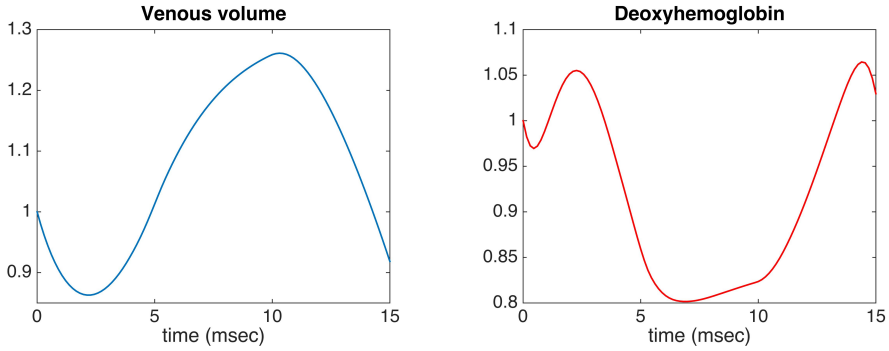

Figure 4.1: Simulation with the balloon model for $\alpha = 0.5$, $\tau_0 = 2$ and $\tau_v = 5$

4.3 Blood flow model

Recently, *Barrett et al.* [18] proposed a more complex model with separate compartments: arteries, capillaries and veins, which allows tracking blood flow and blood volume in the different vascular components. The main idea behind the Barrett model resides in the correspondences between hemodynamics and electrical circuits, with blood playing the role of electric current, and blood pressure that of voltage. Based on these observations, the classical Ohm's law could be rewritten as the product of blood flow and resistance. In addition, vascular compliance, intended as capacity of a vessel to dilate, can be interpreted as capacitance, defined as the ability of a conductor to store electric charge.

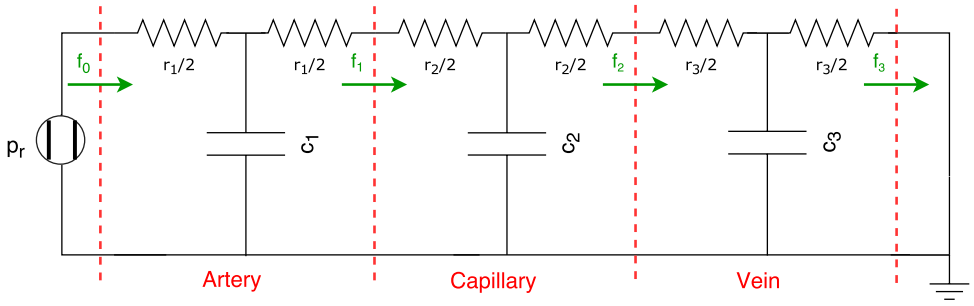

Figure 4.2: Electrical circuit representation of the model designed by *Barrett et al.* in [18].

Let us first denote the blood volume by v, the flow by f and the resistance by r and introduce indeces $j = \{1, 2, 3\}$ to account for the three vascular compartments. Then, the time course of the cerebral blood volume of a compartment with respect to time can be written in terms of the flow inside and outside the compartments,

$$\frac{dv_j}{dt} = f_{j-1}(t) - f_j(t), \text{ where } j = \{1, 2, 3\}. \tag{4.6}$$

The pressure at the entrance of the compartment is given by:

$$p_j(t) = \frac{1}{2} r_j(t) f_{j-1}(t) + \frac{v_j(t)}{c_j(t)}, \text{ where } j = \{1, 2, 3\}, \tag{4.7}$$

where the viscous resistance r_j can be expressed in terms of the length of the compartment l_j and the blood volume v_j

$$r_j(t) = \frac{l_j^3}{v_j(t)^2}, \tag{4.8}$$

while c_j represents the compliance and it measures the ability of the vessel to dilate. In the model of vascular compliance proposed by *Barrett et al.* [18], steady state is characterized by a linear relationship between the compliance and the blood volume, dynamic viscoelastic effects and changes in the compliance for

the active smooth muscle dilation or contraction [18]:

$$\frac{c_j(t)}{c_j^*} = \frac{\kappa_j - \frac{v_j(t)}{v_j^*}}{\kappa_j - 1} - \nu_j \frac{dv_j(t)}{dt} + s_j(t), \text{ where } j = \{1, 2, 3\}, \tag{4.9}$$

where by κ_j we denote the stiffness coefficient, ν_j is a viscoelastic coefficient, s the vasodilatory stimulus, while by c_j^* and v_j^* we denote the baseline value of the compliance, and blood volume, respectively.

The vasodilatory stimulus in [18] is built on observations of the behavior of the CBF during neuronal application, namely a rapid increase shortly after the onset of the stimulation, an initial overshoot followed by a plateau and once the stimulation is over, a decay back to the baseline value. Mathematically, this is expressed as:

$$s_1(t) = \begin{cases} s_{\text{up}}(t), & t < t_{\max} \\ s_{\text{decay}}(t), & t_{\max} \leq t \leq t_{\text{end}} \\ s_{\text{down}}(t), & t > t_{\text{end}} \end{cases}, \tag{4.10}$$

where $t_{\max}$ is the time at which the maximum stimulus $s_{\max}$ is reached, while $s_{\text{up}}(t)$, $s_{\text{decay}}(t)$ and $s_{\text{down}}(t)$ are defined as

$$s_{\text{up}}(t) = \frac{1}{2} s_{\max} \left[1 + \text{erf}\left(\frac{t - (t_0 + \frac{\tau_{\text{up}}}{2})}{32^{-1/2} \tau_{\text{up}}} \right) \right], \tag{4.11}$$

$$s_{\text{decay}}(t) = (s_{\max} - s^*) \exp\left(\frac{t_{\max} - t}{\tau_{\text{decay}}} \right), \tag{4.12}$$

$$s_{\text{down}}(t) = s_{\text{end}} \exp\left(\frac{t_{\text{end}} - t}{\tau_{\text{down}}} \right), \tag{4.13}$$

where erf is the error function, t_0 and t_{end} are the initial time and respectively, final time of the simulation. s^* represents the baseline value of the stimulus and τ_{up}, τ_{decay} and τ_{down} are time constants. Lastly, s_{end} is the value of the stimulus at t_{end}.

In [18] the vasodilatory stimulus is applied only to the arterial compartment, while the stimulus functions for the capillaries and the venous compartments are set to 0

$$s_2(t) = 0, s_3(t) = 0. \tag{4.14}$$

This choice was based on the experimental data by *Drew et al.* [65] obtained by applying two photon microscopy on anesthetized mice, suggesting that the changes in the venous and capillary compartment during neuronal activation are not significant unless the stimulus considered has a longer duration.

The total pressure p_r is the sum of the pressure drops over each compartment:

$$\Delta p_r = \sum_{j=1}^{3} \Delta p_j(t), \text{ where } j = \{1, 2, 3\}. \tag{4.15}$$

Equations (4.6), (4.7), (4.8) and (4.15), for $j = \{1, 2, 3\}$, yield a system of seven differential algebraic equations.

Parameter	Description	Artery	Capillary	Vein
v^*	Baseline volume fraction	0.29	0.44	0.27
r^*	Baseline resistance	0.74	0.08	0.18
l^*	Length	0.39	0.25	0.23
c^*	Baseline compliance	0.46	2.02	2.97
ν	Viscoelastic coefficient	31	163	122
κ	Stiffness coefficient	1.29	1.51	∞

Table 4.1: Baseline values and corresponding parameters to the three compartments: arteries, capillaries and veins as considered by Barrett et al. in [18]

In order to compare the model predictions with experimental results in [65, 70], the authors of [18] consider stimuli of different durations (1 second, 6 seconds and 30 seconds). Their results show that the onset of the stimulation is characterized by a great increase in the CBF, followed by a slower increase, reaching a peak of 53% above baseline for the 6 seconds stimulus and 65% for the 30 seconds stimulation. Similarly, the CBV increases during stimulation, up to 11% above baseline for the short stimulus and to 16% for the 30 seconds stimulus. It was observed that during the longer stimulation, the rise for the CBV was steeper than for the CBF and that in all cases CBF recovered to its baseline level faster that the CBV.

In this model, the dilation in the arteries accounts for 88% of the total increase in volume, with the remaining 12% partitioned between capillaries and veins. Similar to the behavior described in [65], increasing the stimulation time from 6 to 30 seconds, produced additional dilation in the capillaries and veins, which now

account for 15% and 21% respectively, while the arterial contribution is decreased to 64% of the total volume change.

In summary, Barrett's results suggest that during neuronal activation, the arteries account for most of the change in CBV and CBF, while the veins and the capillaries become an essential part only when the stimulus duration is large enough.

One drawback of the model proposed by *Barrett et al.* is the assumption that the vasodilatory stimulus is known and is expressed in the parametric form (4.10). One very active topic of debate in the literature regards the compartment on which the stimulus acts upon. In [18], the authors assume that the stimulus acts only on the arterial compartment, in conflict with various experimental reports [69, 66] and the classical Balloon Model [15, 16, 17]. These aspects are discussed in detail in [19].

In [19, 20], the authors formulate an inverse problem of the hemodynamic response with the objective of estimating the stimulus in each hemodynamic compartments, rather than only in the arterial one, as in [18], or the venous one, as in [15, 16, 17]. In this way, the stimulus, and implicitly the compliance in each compartment can be deduced, based on data obtained directly from measurements of the cerebral blood flow.

The presence of the derivative of the volume in (4.9) transforms the system formed by the equations (4.6), (4.7), (4.8) and (4.15) into a system of differential algebraic equations (DAEs), whose solution requires special consideration, as discussed in detail in [20], where an efficient solution has been found.

Having the solution of the system above, the blood flow can be computed by averaging the flows between the three compartments [76]:

$$\mathrm{CBF}(t) = \frac{\sum_{j=1}^{3} v_j(t)\,[f_{j-1}(t) + f_j(t)]}{\sum_{j=1}^{3} v_j(t)}. \tag{4.16}$$

4.4 Hemo-Electro-Metabolic coupling

In this section we describe how the hemodynamic model discussed in the previous section is coupled to the Electro-Metabolic model presented in Chapter 3. One of the basic feedback mechanisms affecting the coupling is the fact that the output

of the hemodynamic model provided by equation (4.16) becomes an input for the Electro-Metabolic model. Another important modification is that the arterial stimulus function $s_1(t)$, defined in (4.10), is given with respect to the extracellular potassium concentration $[K^+]_{ecs}(t)$ provided by the Electro-Metabolic model. As in [18], the stimulus in the other two compartments (venous and capillary) is set to 0. The fundamental feedback mechanisms underlying the Hemo-Electro-Metabolic coupling are showed schematically in Figure 4.3.

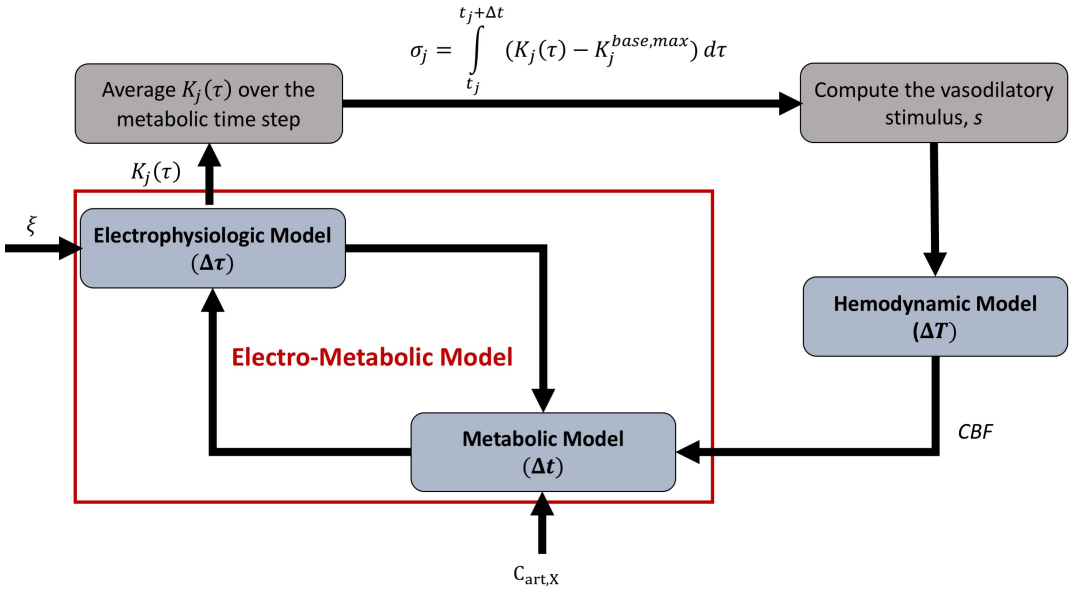

Figure 4.3: **Schematic representation of the three-way feedback loop.** The output of the Electro-Metabolic Model over the time interval $[t_j, t_j + \Delta t]$ comprises the extracellular potassium profile K_j, leading to the integrated potassium signal σ_j and, through integration over the interval $[T_i, T_i + \Delta T]$, to the hemodynamic stimulus s_i that serves as an input for the hemodynamic model. The hemodynamic model determines the cerebral blood flow profile that regulates the metabolic model through nutrient supply. The only external inputs are the arterial concentrations of glucose, oxygen and lactate ($C_{\text{art,X}}$), and the neuronal activation function describing an electrophysiological signal ξ arriving from outside the unit through the presynaptic axon.

Following [77], we assume that the high concentration of extracellular potassium triggers a calcium wave in the nearby astrocytes, that reaches the arterioles through the end feet, and therefore provokes an increase in the arterial compliances as modelled in equation (4.9). On the other hand, high compliance causes an increase in the arterial volume and a decrease in the resistance (4.8). The latter leads to an increased downstream pressure which causes an increase in the capillary and venous volumes. In Figure 4.4 we illustrate the interaction between

the electrophysiology, metabolism and hemodynamic response in two cases: in the left part, we consider the system at resting state, while on the right we illustrate the neuronal activation [76].

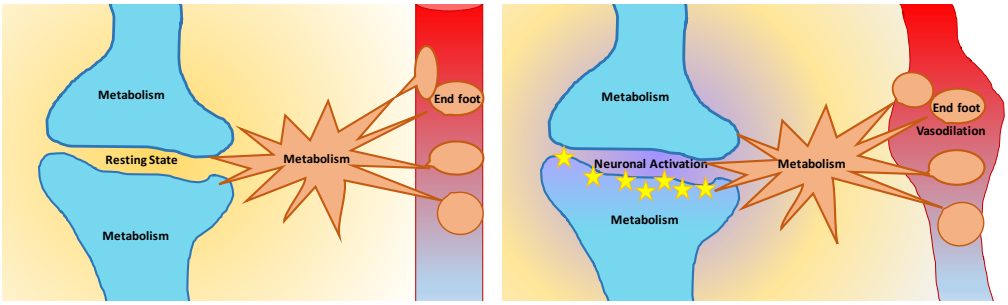

Figure 4.4: **Schematics of the integrated Hemo-Electro-Metabolic model**. The neuron (blue) and astrocyte (salmon) compartments are assigned separate compartments, but there is no division between the pre- and post-synaptic neuron, nor between the soma and end feed of astrocytes. A separate compartment is reserved for blood, separately accounting for arterial, capillaries and venous components in the hemodynamic module. In line with current understanding, we assume that the extra blood volume rushing to the activation site in response to a vasodilation stimulus in the arterioles triggered by the neuronal activation via increased potassium concentration in extracellular space (ecs) is accommodated by a change in the volume of the blood vessels. The uniform yellow background in the left panel indicates the higher sodium concentration in the extracellular space at rest: in the right panel the lilac cloud illustrates the temporary increase in extracellular potassium concentration during the repolarization phase due to the sodium potassium pump activation, also responsible for the increase in energy demand, symbolically denoted by yellow starts.

As shown in Figure 3.1, the external inputs to the Electro-Metabolic model are the activation function $\xi(t)$ which controls the level of neuronal activity, the arterial concentration $C_{\text{art,X}}$, $\text{X} = \{\text{Glc}, \text{Lac}, \text{O}_2\}$ and the blood flow q(t). The only input needed by the blood flow model is the vasodilatory extracellular potassium dependent stimulus. The concentration of extracellular potassium, an output of the Electro-Metabolic model, can be used to model the vasodilatory stimulus s(t):

$$\begin{aligned} s(t) &= \left([\text{K}^+]_{\text{ecs}}(\tau) - K^{\text{base,max}}\right) * w, \\ &= \int_0^t \left([\text{K}^+]_{\text{ecs}} - K^{\text{base,max}}\right) w(t-\tau) d\tau, \end{aligned} \tag{4.17}$$

where $K^{\text{base,max}}$ is the maximum extracellular potassium concentration corre-

sponding to the awake resting state, and w is a weight function of the form

$$w(t) = \exp\left(-\frac{t}{\chi}\right), \chi = 0.6514 \text{ sec.} \tag{4.18}$$

The kernel w captures the fading off of the vasodilatory stimulus after the astrocytes and the diffusion have cleared the potassium in excess from the extracellular space. The integral (4.17) is computed over an interval of three seconds, the time constant χ was chosen so that after a three seconds period, the kernel had decreased to only 1% of its maximum value.

4.5 Multiple time scales

In this section we discuss the multiple time scales that characterize the Hemo-Electro-Metabolic model and propose a numerical scheme in order to compute the model predictions.

As in the Electro-Metabolic Model described in Chapter 3, we consider a time step $\Delta\tau$ corresponding to the electrophysiological model, which is of the order of milliseconds and is adaptively selected by the built-in Matlab function ode15s, and a metabolic time step, denoted by Δt, which is set to $\Delta t = 0.05$ sec. In addition, we account for the slower changes in the blood flow response by considering a third time step ΔT which is set to $\Delta T = 1$ second.

Here we describe the numerical procedure developed in order to compute the predictions of the three-feedback Hemo-Electro-Metabolic model:

Algorithm 2 Hemo-electro-metabolic coupling

Given: The arterial concentrations $C_{\text{art,X}}$ of glucose, lactate and oxygen and a neuronal activation function $\xi(t)$

Initialize: $T_i = 0,\ t = 0,\ \alpha > 0$ and $\chi > 0$.

Repeat: At each iteration i:

1. Take a step in the time units of the hemodynamic model: Update

$$T_i = T_{i-1} + \Delta t.$$

2. Take 20 steps of length Δt, the time units of the metabolic model: For $j = 0, \ldots 20$,

   a. Update $t_j = t_{j-1} + \Delta t$

   b. Compute the model predictions for the electrophysiology model and generate the extracellular potassium curve $K_j(\tau)$, where $\tau \in I_j = [t_j, t_j + \Delta t]$.

   c. Compute the model predictions for the metabolic model: Compute the average potassium concentration over I_j such that

$$\sigma_j = \int_{I_j} (K_j(\tau) - K_j^{\text{base,max}}) d\tau.$$

3. Compute the model predictions for the hemodynamic model:

   a. Define the vasodilatory stimulus value at time T_i as a scaled and weighted sum of the potassium values,

$$s_i = \alpha < w, \sigma_i >,$$

   where σ is the three seconds window of the potassium values at each time $t \in [T_i, T_i + \Delta T]$ such that $\sigma = [\sigma_{i-2}\ \sigma_{i-1}\ \sigma_i]$ and w is the weight function defined in equation (4.18).

   b. Compute the cerebral blood flow at the current time T

$$\text{CBF}_i = \text{CBF}(T_i)$$

4.6 Results

In this section we present the results obtained when computing the predictions of the Hemo-Electro-Metabolic model described throughout this chapter. First, we consider a protocol where we discuss the case of the system transitioning from an awake resting state to a three minutes neuronal activation characterized by a 90 Hz frequency, followed by a recovery to the awake resting state. In this

case, we analyze the changes that occur not only in the electrophysiology and metabolism, as in Chapter 3, but also in the blood flow response. The second case is a simulation of two neuronal activations, between which we have an 11 minutes period of awake resting state. As in Chapter 3, we analyze the recovery of the main concentrations.

4.6.1 Neuronal activation

In the first computed example, the system is transitioning from an awake resting state of 8Hz corresponding to a stimulus $\xi = 0.05$ to a neuronal activation characterized by a frequency of 90 Hz, for which the activation function was set, as usual, to $\xi = 2.5$. The neuronal stimulation starts at $t = 1$ minute and lasts 3 minutes. Figure 4.5 shows the electrophysiologic and hemodynamic response.

Our model [76] predicts an initial CBF increase of 77% over baseline value, lasting approximately 15 seconds, after which the relative cerebral blood flow settles at 26% above baseline for the activation period, in agreement with recent literature [78]. A similar spike is observed also in the firing frequency showed in the second panel of Figure 4.5, which briefly tops at 107Hz before stabilizing at 90Hz throughout the neuronal activation period. As expected, during the neuronal stimulation the amplitude of the action potential decreases and is accompanied by an increase in the ionic concentrations of both intracellular sodium and extracellular potassium. As in Chapter 3, we observe the slow after-hyperpolarization effect, characterized by a 16 seconds neuronal silencing once the activation has ended.

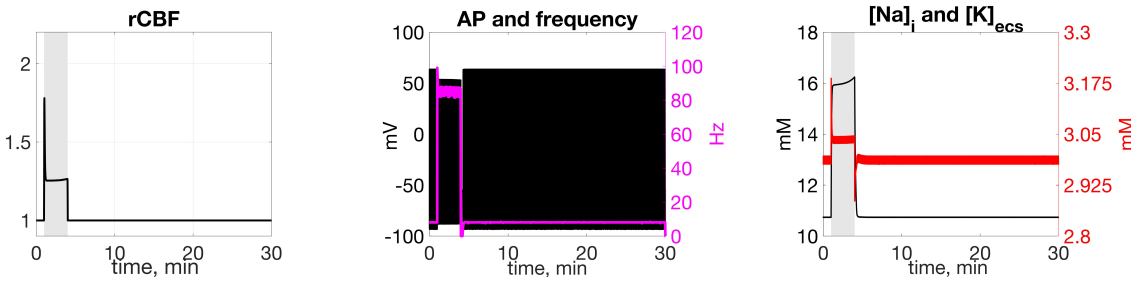

Figure 4.5: Dynamical model predictions of the changes in the electrophysiology and hemodynamic response as the system switches from resting state to high firing for a three minutes period: In each panel, the neuronal activation is indicated by a gray shadow. Left to right: Relative cerebral blood flow, action potential (black) and its associated frequency (magenta), time course of the intracellular sodium concentration (black) and extracellular potassium concentration (red).

The top row of Figure 4.6 shows the metabolic response in the blood compartment. Note that the initial spike in the relative cerebral blood flow is concomitant to the initial increase in the concentrations of glucose and oxygen. After this brief increase, glucose slowly decreases and continues its descent for 20 seconds after the activation is over. At the same time, we observe a large production of lactate in the blood compartment, which reaches a 37% increase over the baseline level. The oxygen shown in Figure 4.6 refers to the total concentration of oxygen which, as explained in Chapter 2, is composed of the oxygen which is freely dissolved in plasma and the oxygen that bounds to hemoglobin. After the initial increase at the beginning of the activation, oxygen concentration stabilizes at a value that is 3% over the baseline. Once the activation had ended, there is a dip of 5% in oxygen concentration in blood, followed by a fast recovery to the baseline value.

The time courses of the metabolites corresponding to the cellular compartments and extracellular space are shown on the two bottom rows of Figure 4.6, where we see that during neuronal activation glucose concentration falls to only 35% of its resting state value in the neuron and extracellular space, while in the astrocyte, where there is a higher glucose consumption, it drops to 13% of its baseline value. As expected, there is a significant lactate production in the neuron, astrocyte and the extracellular space, where lactate concentration increases by 66% of its baseline value. Not surprisingly, there is a much higher consumption of oxygen during neuronal stimulation, with a 90% decay in concentration in neuron, 76% in astrocyte and 50% in extracellular space. The phosphorylation states

in the cellular compartments are almost depleted at the end of the activation, suggesting that all the ATP produced is used to satisfy the energetic requirement [76], while redox states exhibit a very large increase during activation, 8 fold in neuron and 4 fold in astrocyte.

The high pyruvate consumption in the cellular compartments during the neuronal activation period is shown in the first panel of the bottom row of Figure 4.6, as well as by the large increase in the TCA flux shown in Figure 4.7: 83% in the neuron and 59% in the astrocyte.

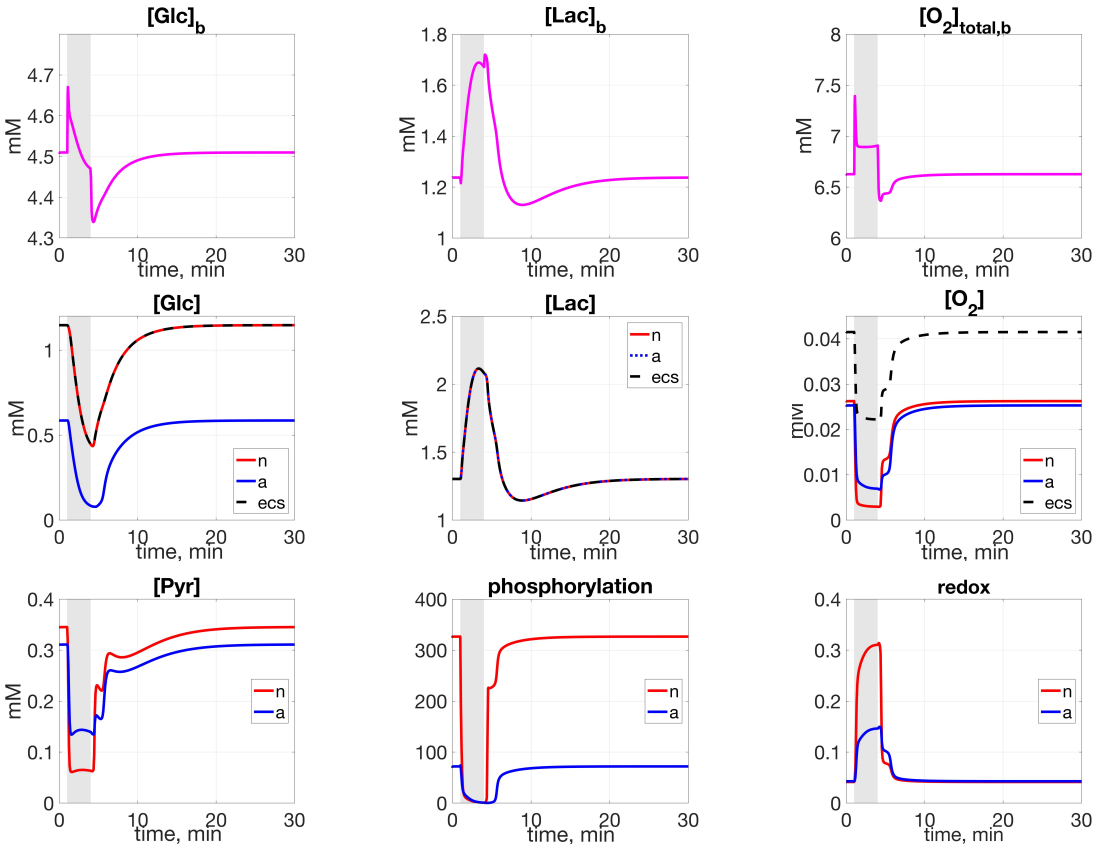

Figure 4.6: Time course of metabolites concentrations as the system switches from resting state to high frequency firing for a three minutes period: In each panel, the neuronal activation period is indicated by a gray shadow. Top row: Blood compartment. Left to right: glucose, lactate and oxygen. Second row: glucose, lactate and oxygen in the neuron (red), astrocyte (blue) and extracellular space (black). Bottom row: pyruvate, phosphorylation and redox in neuron (red) and astrocyte (blue).

The transport fluxes for glucose, lactate and oxygen between extracellular space and cellular compartments, and between blood and extracellular space are displayed in Figure 4.7. The flux of glucose from blood to extracellular space shows an increase of 39% above resting state value, while the flux of oxygen

between the same compartments increases by 15%, passing from 1.49 mM/min during resting state to 1.71mM/min during neuronal activation, in agreement with experimental literature [53, 79]. From these fluxes, we calculate from equation (2.89) the oxygen glucose index (OGI), shown in the last panel of the third row of Figure 4.7. Notice that at the start of the activation, the OGI index exhibits a brief increase of 10% over baseline, which occurs simultaneously with the initial increase in blood flow, followed by a fast decrease of 18% below the resting state. Our model predicts an OGI value of around 5.15 during resting state and 4.2 during neuronal activation, in agreement with recent literature [51, 53, 47, 52].

Lactate flux from the blood to extracellular space shows a very significant 6 fold drop during neuronal activation. Additionally, the lactate transport between extracellular space and neuron, shown in the first panel of Figure 4.7, exhibits a shift in direction during neuronal activation, with lactate moving from the neuron back to the extracellular space. A similar behavior can be observed for the lactate dehydrogenase flux in neuron: during resting state, the prevailing direction is towards pyruvate production, while during activation it shifts towards lactate production. Astrocyte exhibits a different pattern: the prevailing direction is towards lactate production during resting state, followed by a brief switch to pyruvate production at the beginning of the activation and followed by a return to lactate production.

The glycolysis and oxidative phosphorylation fluxes presented in the first two panels of Figure 4.7 show large increases during neuronal activation in neuron. In astrocyte, the glycolysis flux increases during the first seconds of the activation and is followed by a fast drop, which continues for a couple of seconds after the activation ends. The oxidative phosphorylation flux in astrocyte has a very small decrease during activation, and it is followed by a sudden increase at the end of the activation.

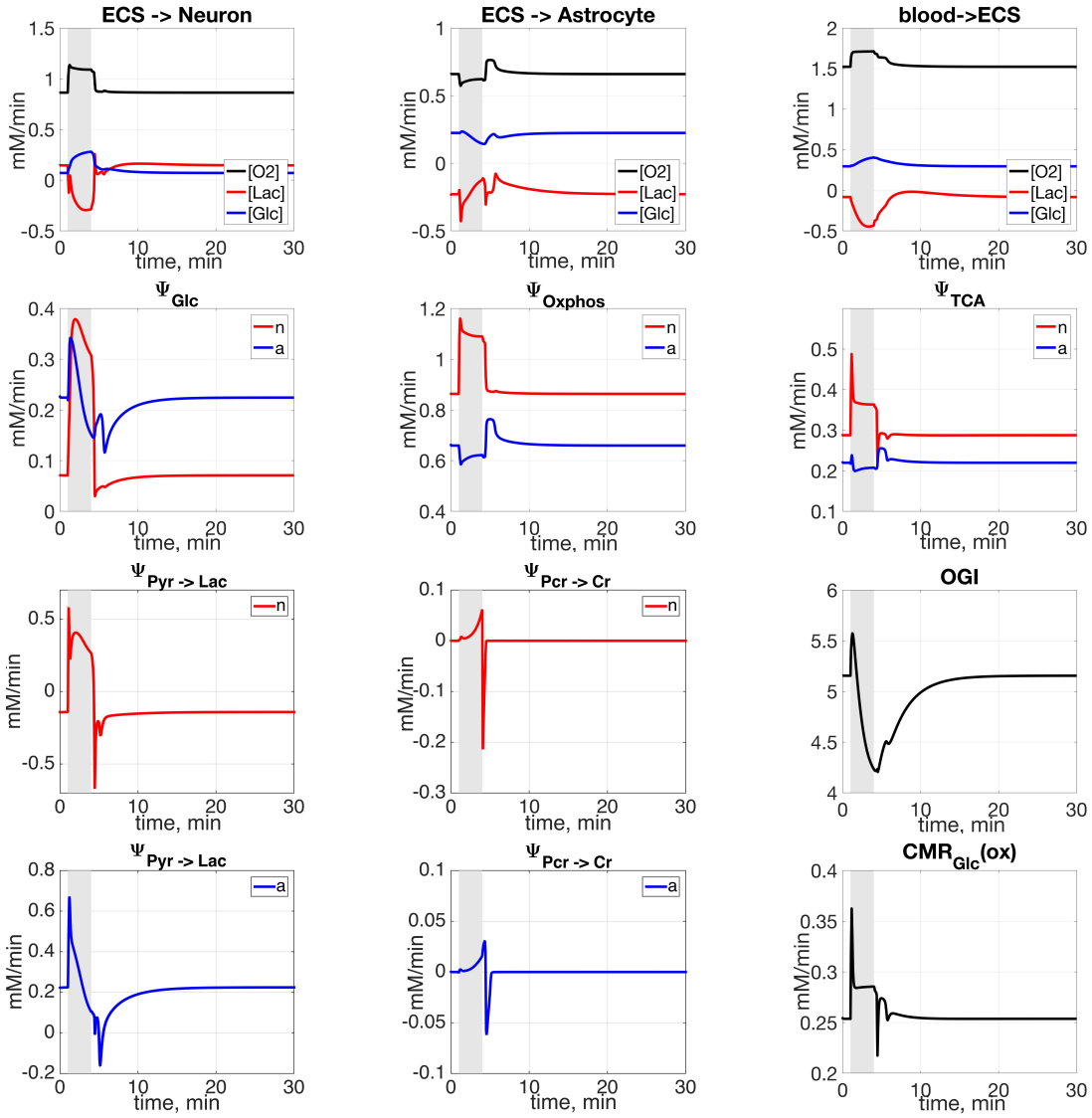

Figure 4.7: Time course of the transport and reaction fluxes as the system switches from resting state to high frequency firing for a three minutes period: In each panel, the neuronal activation period is indicated by a gray shadow. Left to right. Top row: Transport fluxes for oxygen (black), lactate (blue) and oxygen (red) from the extracellular space to the neuron, from the extracellular space to the astrocyte and from the blood to the extracellular space. Second row: Glycolysis, oxidative phosphorylation and tricarboxylic acid cycle in the neuron (red) and in the astrocyte (blue). Third row: lactate dehydrogenase balance flux in the neuron, creatine phosphorylation balance flux in the neuron and the OGI index. Last row: Lactate dehydrogenase balance flux in the astrocyte, creatine phosphorylation balance flux in the astrocyte and the oxidative cerebral metabolic rate of glucose.

4.6.2 Consecutive neuronal activations

In the previous section we described the behaviour of the cerebral blood flow, ionic concentrations and metabolites when the system transitions from an awake

resting state to neuronal activation. In this section of the thesis we discuss the recovery time needed for the metabolites and ionic concentrations to return to their baseline value after activation. As observed in Section 3.4.1 and Section 3.4.2, each metabolite has its own characteristic time required for reaching its normal state, once the activation has ended. Not allowing a sufficient period of resting state in between the activations, can lead to problems in sustaining the second neuronal activation, as described in Section 3.4.2, Figure 3.10.

The computed experiment that we present here consists of two consecutive neuronal activations of three minutes duration each, separated by a period of 11 minutes of awake resting state. More specifically, the first activation starts at $t = 1$ minute and it ends at $t = 4$ minutes, while the second activation starts at $t = 15$ minutes and it ends at $t = 18$ minutes.

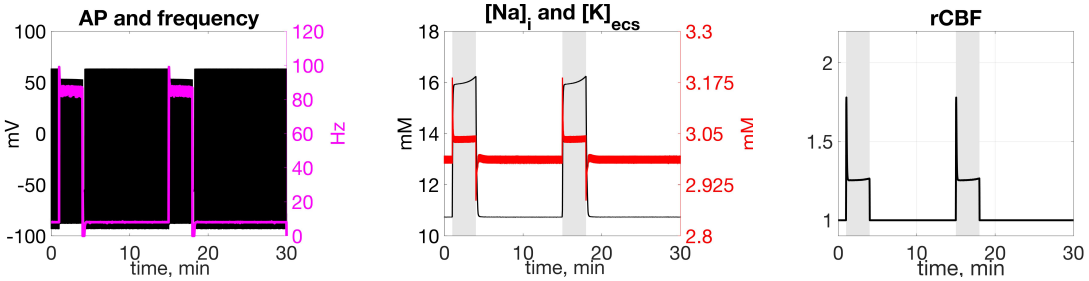

Figure 4.8: Dynamical model predictions of the changes in the electrophysiology and hemodynamic response as the system switches from resting state to high firing for a three minutes period for two neuronal activations, each having a duration of 3 minutes with a resting period of 11 minutes in between: In each panel, the neuronal activation is indicated by a gray shadow. Left to right: Relative cerebral blood flow, action potential (black) and its associated frequency (magenta), time course of the intracellular sodium concentration (black) and extracellular potassium concentration (red).

Figure 4.8 shows the electrophysiologic and hemodynamic response during the transition to neuronal activation, followed by the 11 minutes awake resting state, after which a second neuronal activation starts. The neuronal activations are identical to those described in the previous section. After each neuronal activation period there is a slow after-hyperpolarization effect lasting approximately 16 seconds, after which the normal firing rate is resumed. Accordingly, at the end of each activation the potassium value exhibits a 16 seconds period during which it falls below the normal firing rate, coinciding with the slow after-hyperpolarization effect period, after which potassium recovers back to its resting state. Sodium

concentration reaches its normal concentration immediately after the activation is over. The cerebral blood flow fully recovers by the time start of the second activation and therefore provides an appropriate supply of metabolites.

The metabolic response to the consecutive neuronal activations is captured in Figure 4.9. The eleven minutes of resting period between the two activations, were enough for most of the metabolites to reach their initial state. However, for example, while the concentration of glucose in neuron, extracellular space and blood compartment reaches its normal value before the start of the second activation, the concentration of glucose is the astrocyte is slower, reaching 98% of its initial value. Lactate recovers up to 95% of its resting state value in neuron, astrocyte and extracellular space and a recovery to 97% in the blood compartment. Compared to glucose and lactate, oxygen requires a much shorter period in order to fully reach its baseline value. In in the case of pyruvate and the phosphorylation state, we observe a recovery to 99% of their initial value. Owing to the full recovery of the cerebral metabolic flow and the fact that the metabolites are almost entirely replenished at $t = 15$ minutes, the second neuronal activation can be sustained.

The fluxes considered in our model are showed in Figure 4.10, where we observe full recovery to the baseline value before the start of the second activation.

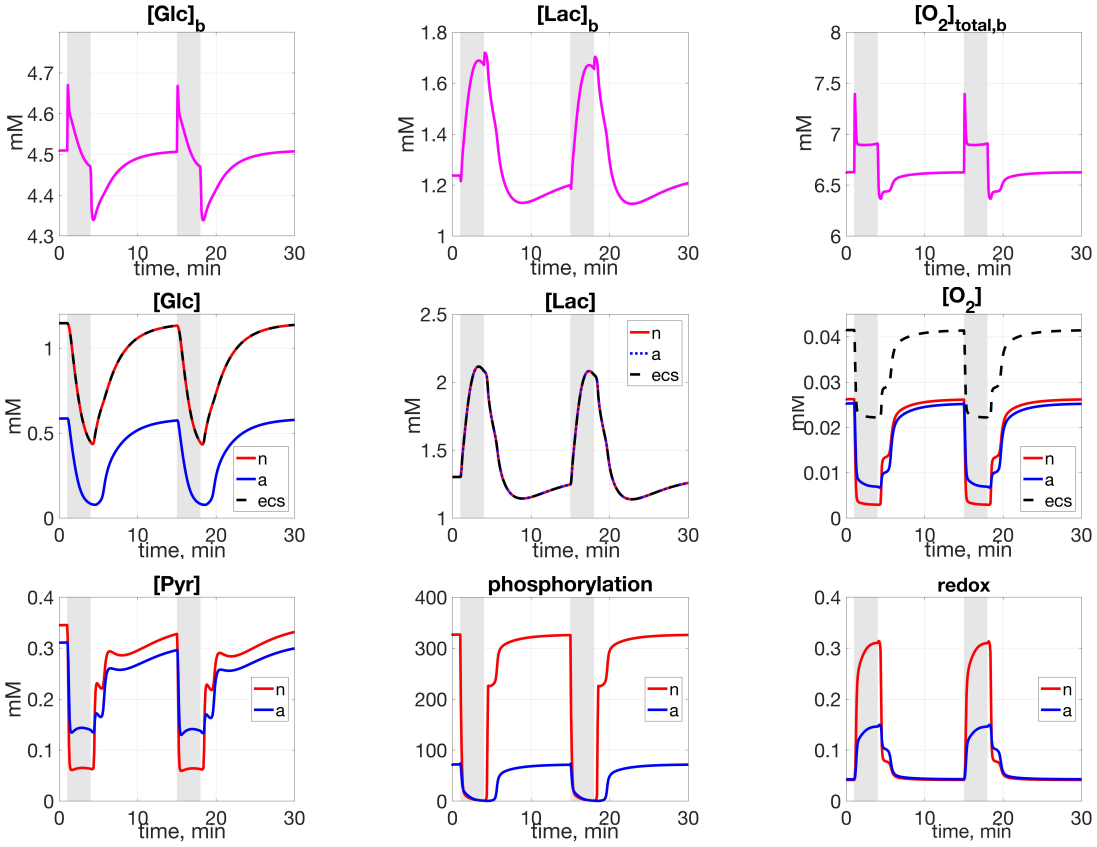

Figure 4.9: Time course of metabolites concentrations as the system switches from resting state to high frequency firing for two consecutive neuronal activations, each having a duration of three minutes with a resting period of 11 minutes in between: In each panel, the neuronal activation periods are indicated by a gray shadow. Top row: Blood compartment. Left to right: glucose, lactate and oxygen. Second row: glucose, lactate and oxygen in the neuron (red), astrocyte (blue) and extracellular space (black). Bottom row: pyruvate, phosphorylation and redox in neuron (red) and astrocyte (blue)

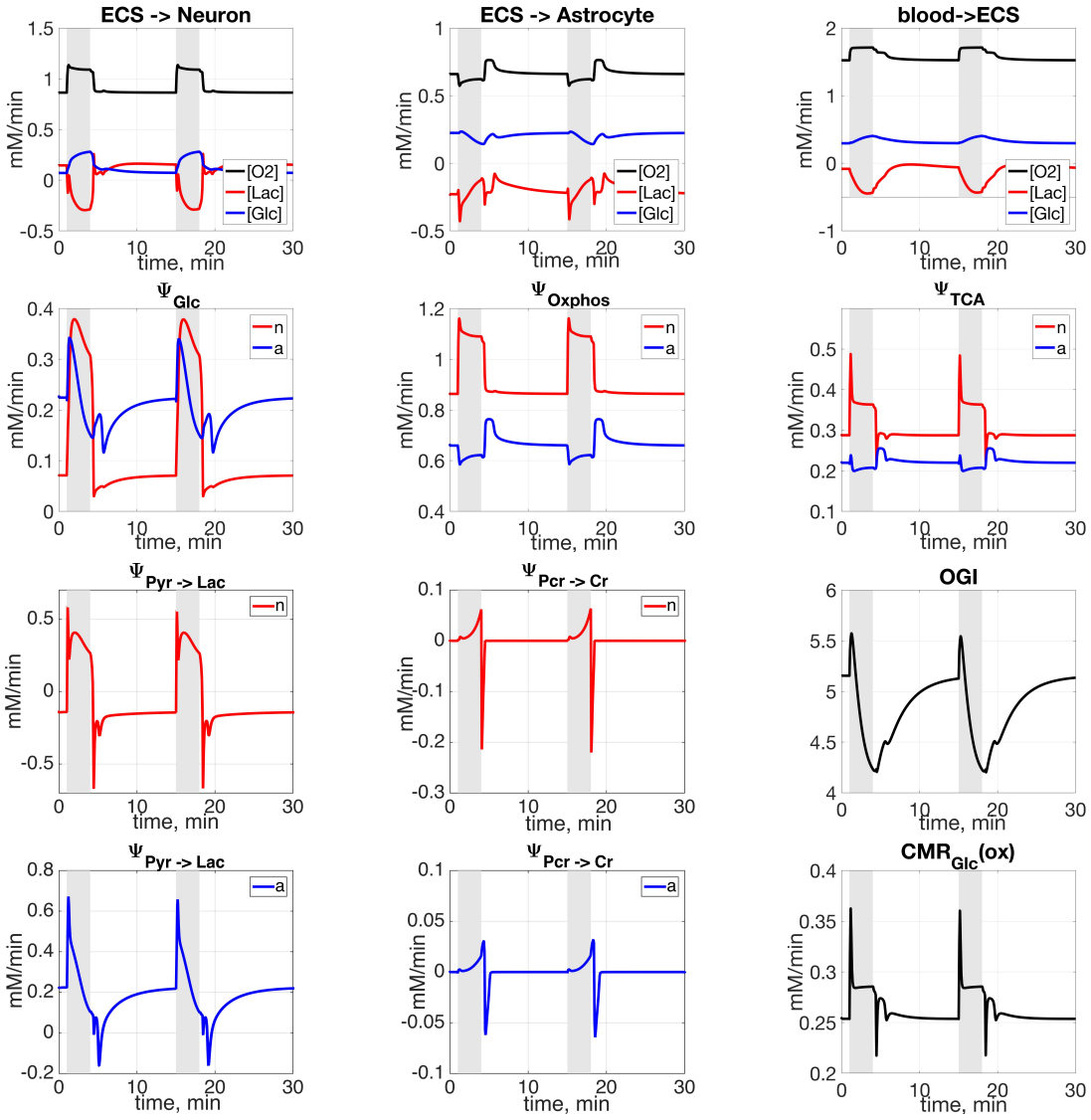

Figure 4.10: Time course of the transport and reaction fluxes as the system switches from resting state to high frequency firing for two consecutive neuronal activations, each having a duration of three minutes with a resting period of 11 minutes in between: In each panel, the neuronal activation period is indicated by a gray shadow. Left to right. Top row: Transport fluxes for oxygen (black), lactate (blue) and oxygen (red) from the extracellular space to the neuron, from the extracellular space to the astrocyte and from the blood to the extracellular space. Second row: Glycolysis, oxidative phosphorylation and tricarboxylic acid cycle in the neuron (red) and in the astrocyte (blue). Third row: lactate dehydrogenase balance flux in the neuron, creatine phosphorylation balance flux in the neuron and the OGI index. Last row: Lactate dehydrogenase balance flux in the astrocyte, creatine phosphorylation balance flux in the astrocyte and the oxidative cerebral metabolic rate of glucose.

Chapter 5

Cortical Spreading Depression

Cortical spreading depression (CSD) are very slow propagating waves of intense cellular depolarizations, accompanied by a period of suppressed neuronal activity and an extreme alteration of the ionic homeostasis [80, 81]. This phenomenon has been studied intensively in recent years, as it was observed to occur spontaneously in various neurologic pathologies like stroke, traumatic brain injury or subarachnoid hemorrhage, where it can provoke additional brain damage or severely slows down the patients' recovery process [82, 81, 83, 84, 85]. On the other hand, in healthy brain CSD is a reversible process that does not cause brain damage [5, 86, 87, 88], and in fact its beneficial properties against future ischemic episodes are currently under investigation [89, 90, 91, 88, 89].

In this chapter we propose a new unified electro-metabolic model that accurately describes the processes underlying brain electrophysiological activity and metabolism during the passing of multiple cortical spreading depression waves. We begin with a short introduction outlining the consequences of CSD waves in human brain: utmost changes in ionic homeostasis, extreme energetic demand, morphologic changes and altered vascular response. We then provide an overview of the published mathematical models that can capture the essential features of CSD. In Section 5.3 we describe a novel electrophysiologic model specifically designed for modeling CSD waves, while in Section 5.4 we provide details about the computational challenges of our coupled electro-metabolic model and we present computed experiments.

5.1 Introduction

Cortical spreading depression waves have been observed to appear spontaneous after head trauma and in ischemic, hypoglycemic or hypoxic brain tissue [82]. These waves can also be triggered in the healthy brain by means of electrical, chemical or mechanical stimuli, by inhibiting the sodium potassium pump's activity or simply as a result of an insufficient energy supply [92, 93]. Among the chemical agents that can initiate a CSD event in experimental settings, the most common are potassium ions, glutamate and the acetylcholine [93]. In general, a potassium bath concentration of at least 10-12 mM [88, 94, 85, 81] is known to trigger a self propagating wave moving slowly across the cortex, although a much lower potassium bath concentration is needed in the case of Familial Hemiplegic Migraine (FHM) patients, who exhibit a particular mutation in the calcium channel [88, 92].

CSD detection: neurophysiologic techniques

The short duration of cortical spreading depression events and the small cortical volume affected make its detection extremely difficult when using the traditional noninvasive electroencephalography (EEG) [82]. Therefore, the typical neurophysiologic technique used for investigating CSD is **electrocorticography (ECOG)**, which records the electrical activity of the cerebral cortex through electrodes placed directly on the surface of the brain. Among other procedures used for studying this phenomenon, we mention the classical **microdialysis technique**, which requires individual samples to be collected hourly. This approach, although unsuited to distinguish between the different spreading depression waves, follows the behavior of the main metabolites during CSD characterized by a dip in the concentration of glucose and an increase in the concentration of lactate. Various researchers investigate CSD with **two-photon imaging** [94], which makes it possible to monitor not only changes in redox states but also changes in capillary perfusion and in cell morphology during the passing of cortical spreading depression waves.

CSD electrophysiologic and metabolic signature

Cortical spreading depression induces very large increases in extracellular potassium concentration, reported to rise from the baseline value of 3-4 mM

to more than 80 mM, matched by large decreases in the concentrations of extracellular sodium and extracellular chloride. Restoring the ionic homeostasis comes with one of the biggest energetic costs ever observed in brain [81, 5], which in turn, cause large increases in both aerobic and anaerobic metabolism [81] with a significant 50% depletion of ATP concentration [95, 96]. CSD waves induce a large decrease in extracellular glucose concentration and a very large increase in extracellular lactate concentration [83, 97, 80, 81, 96]. In order to shed light on the changes in metabolites concentrations during spreading depolarizations, *Lourenćo et al.* [80] recently developed a dual biosensor capable of simultaneously monitoring changes in the concentrations of glucose and lactate and brain electric activity [80]. Experiments on rats under urethane anesthesia where spreading depolarizations were induced mechanically through the insertion of a needle prick, show a 51% decrease in glucose concentration and a 66% increase in lactate concentrations with respect to their initial values [80]. Higher oxidative phosphorylation rates and increased oxygen demand during CSD waves were confirmed by many authors [98, 99] and, as expected, the spreading depolarizations lead to substantial increases in the cerebral metabolic rates of glucose and oxygen [81, 83, 97, 100, 5].

Moreover, multiple CSD episodes were shown to cause cumulative changes in metabolite concentrations [101, 97]: more specifically, glucose in extracellular space exhibits a stepwise decay with each passing CSD wave [97], and a similar behavior was observed for oxygen concentration [102, 103].

Morphology during CSD

Cortical spreading depression waves are known to produce an extreme shrinkage of the extracellular space, whose volume was reported to decrease from 50 to 78% below its resting state value [104, 105, 106, 81, 107]. While it is widely accepted that the neuronal cells swell and that there is a pronounced loss of dendritic spines [88, 94], there is an ongoing debate in the literature regarding the changes in astrocyte morphology: some authors suggest that the astrocyte also swells during CSD episodes [105, 104, 106], while others report that the increase in the astrocytic volume is negligible [94].

Hemodynamic response during CSD

In normoxic brain, once a cortical spreading depolarization is initiated, the

cerebral blood flow tries to match the very high energetic demand through an extreme hyperemia, often reported to be in the range of 100 to 250% above the baseline value [80, 83, 81, 82]. This vasodilation, attributed to nitric oxid and arachidonic acid metabolites [108], can be sustained only for 1-2 minutes [81, 82, 80], after which the blood flow is reported to exhibit either a mild 20-30% decay or to return to its baseline value [81]. It has been remarked that blood flow measurements vary substantially with respect to the species considered [90, 109, 110], the anesthetic agent used [71, 111], the baseline cerebral blood flow value and the CSD triggering mechanism [90].

The hyperemic response is significantly lower or even absent when CSDs occur in injured brain, most likely due to the fact that the nitric oxide concentration is not optimal and the potassium concentration is very high [108].

The alterations in the electrophysiology, metabolism, morphology and hemodynamics associated with CSD are presented schematically in Figure 5.1.

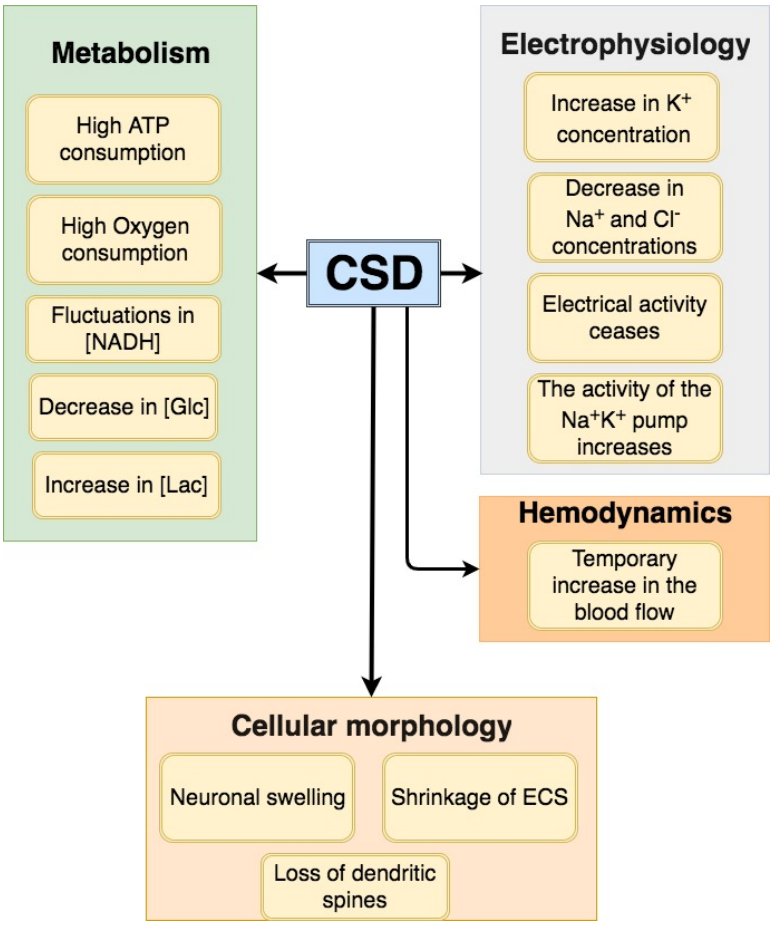

Figure 5.1: A schematics of the changes that occur during CSD from four perspectives: the metabolism, the electrophysiology, the hemodynamics and the cellular morphology.

Role of astrocytes in CSD

While most research done in the last century has regarded neuronal cells as the main players in human brain, in the recent years multiple authors have shifted their attention to the study of astrocytes, their interaction with neurons [4, 3, 7] and the their role in various neurological pathologies [112, 113, 114, 115, 116, 117, 6]. In CSD in particular, glial cells are responsible for clearing extracellular potassium and glutamate [118, 5, 119], regulating the ionic composition of the extracellular space, its size and geometry [120, 121], as well as mediating the cerebral blood flow response [1, 5, 122].

It was recently observed that regions of the brain characterized by a larger number of glial cells, in particular astrocytes, are less susceptible to CSD [81, 5, 123, 106, 124, 125]. Factors that were reported to contribute greatly to the spreading of the waves are high density of neuronal cell bodies and small extracellular space, and the propagation speed of cortical spreading depression was observed to take place at a much lower pace in regions with large number of astrocytes [119].

While most CSD studies concentrate on the cerebral cortex, *Karunasinghe et al.*[124] studied the appearance of these waves in Substantia Nigra (SN), a basal ganglia structure found in the midbrain, responsible for eye movement, learning, motor planning and reward [124]. This region's utmost importance comes from the fact that the death of the dopaminergic neurons is responsible for Parkinson's disease. In their study *Karunasinghe et al.* analyzed individually the two components of Substantia Nigra: Substantia Nigra pars compacta (SNc) and Substantia Nigra pars reticulata (SNr) and they observed that SNc has a remarkable resistance to SD waves. This is believed to be due to the larger number of astrocytes, the lower density of neurons and the larger extracellular space present in this region of the brain.

5.2 Review of mathematical CSD models

The increased attention granted in the recent years to the study of the mechanisms underlying cortical spreading depression, created the need for complex mathematic models able to capture this phenomenon [126, 127, 23, 21, 128]. In

this section we describe two such models: a mathematical model developed by *Wei et al.* in [11], able to capture different firing patterns, among which also CSD waves, and another model proposed by *Huguet et al.* in [21] which focuses specifically on CSD.

5.2.1 Wei model

The model developed by *Wei et al.* in [11] is based on the Cressman model, described in Chapter 1, to which it adds chloride and oxygen dynamics. Moreover, the exterior concentration of sodium and the interior concentration of potassium, previously defined as algebraic equations, are now modeled as differential equations.

The differential equation governing the membrane potential is given by:

$$c_m \frac{dV}{dt} = -I_{\mathrm{Na}^+} - I_{\mathrm{K}^+} - I_{\mathrm{Cl}^-} - \frac{J_{\mathrm{pump,Na}^+}}{\gamma}, \tag{5.1}$$

where c_m is the membrane capacitance, I_{Na^+}, I_{K^+} and I_{Cl^-} are the sodium, potassium and chloride currents defined through (1.13), (1.14), (1.15), $J_{\mathrm{pump,Na}^+}$ the current induced by the sodium potassium pump and γ a factor used in order convert the current given in $\mu\mathrm{A/cm}^2$ into mM/s.

As in the Hodgkin-Huxley model, the dynamics of the gating variables n, m and h follows:

$$\frac{dw}{dt} = \alpha_w(V)(1-w) - \beta_w(V)w, \quad w \in \{m, n, h\}, \tag{5.2}$$

where α_w and β_w are the corresponding saturation functions for each gating variable $w \in \{m, n, h\}$ and are given in Table 5.1.

w	m	h	n
$\alpha_w(V)$	$0.32\dfrac{V+54}{1-\exp(-(V+54)/4)}$	$0.128\exp(-(V+50)/18)$	$0.032\dfrac{V+52}{1-\exp(-(V+52)/5)}$
$\beta_w(V)$	$0.28\dfrac{V+27}{\exp((V+27)/5)-1}$	$\dfrac{4}{1+\exp(-(V+27)/5)}$	$0.5\exp(-(V+57)/40)$

Table 5.1: Gating variables: voltage-dependent saturation functions for the Wei model.

The reversal potentials V_{Na^+}, V_{K^+} and V_{Cl^-} are obtained through the Nernst equations,

$$V_{\mathrm{X}} = \frac{26.64}{z_X} \ln\left(\frac{[\mathrm{X}]_{\mathrm{ecs}}}{[\mathrm{X}]_{\mathrm{i}}}\right), \quad \mathrm{X} \in \{\mathrm{Na}^+, \mathrm{K}^+, \mathrm{Cl}^-\}, \tag{5.3}$$

where z is the valence corresponding to the ion X.

The differential equations governing the intracellular $[\mathrm{X}]_i$ and extracellular $[\mathrm{X}]_{\mathrm{ecs}}$ concentration of sodium, potassium and chloride are given by:

$$\begin{aligned}
\tau\frac{d[\mathrm{Na}^+]_{\mathrm{i}}}{dt} &= \left(-\gamma I_{\mathrm{Na}^+} - 3J_{\mathrm{pump,Na}^+} - J_{\mathrm{nkcc}l}\right) v_i,\\
\tau\frac{d[\mathrm{Na}^+]_{\mathrm{ecs}}}{dt} &= \left(\gamma\beta I_{\mathrm{Na}^+} + 3\beta J_{\mathrm{pump,Na}^+} + \beta J_{\mathrm{nkcc}l}\right) v_{\mathrm{ecs}},\\
\tau\frac{d[\mathrm{K}^+]_{\mathrm{i}}}{dt} &= \left(-\gamma I_{\mathrm{K}^+} + 2J_{\mathrm{pump,Na}^+} - J_{\mathrm{kcc2}} - J_{\mathrm{nkccl}}\right) v_i,\\
\tau\frac{d[\mathrm{K}^+]_{\mathrm{ecs}}}{dt} &= \left(\gamma\beta I_{\mathrm{K}^+} - 2\beta J_{\mathrm{pump,Na}^+} - J_{\mathrm{diff}} - J_{\mathrm{glia}} - 2J_{\mathrm{g,p}} + \beta\left(J_{\mathrm{kcc2}} + J_{\mathrm{nkccl}}\right)\right) v_i,\\
\tau\frac{d[\mathrm{Cl}^+]_{\mathrm{i}}}{dt} &= \left(\gamma I_{\mathrm{Cl}} - J_{\mathrm{kcc2}} - 2J_{\mathrm{nkccl}}\right) v_i,\\
\tau\frac{d[\mathrm{Cl}^+]_{\mathrm{ecs}}}{dt} &= \left(-\gamma\beta I_{\mathrm{Cl}} + \beta J_{\mathrm{kcc2}} + 2\beta J_{\mathrm{nkcc}l}\right) v_{\mathrm{ecs}},
\end{aligned} \tag{5.4}$$

where $\tau = 1000$ is a conversion factor used for transforming seconds into milliseconds and β the ratio between the intracellular volume v_i and the extracellular volume v_{ecs}, which will be discussed later on. The scalar γ is a conversion factor for the transformation of current $\mu\mathrm{A/cm}^2$ into concentration in mM/s defined as:

$$\gamma = \frac{1}{100}\frac{S}{F \cdot v_i} \tag{5.5}$$

where the Faraday constant F is the product of the Avogadro constant $N_A = 6.023 \cdot 10^{-23}$ mol^{-1} and the elementary charge $e = 1.602 \cdot 10^{-19}$ C. The surface area S depends on the intracellular volume according to

$$S = 4\pi\left(\frac{3v_i}{4\pi}\right)^{\frac{2}{3}}. \tag{5.6}$$

Chloride, the main permeant anion, has an important role in various physiological processes. In [11] its dynamics is accounted for in the model, through two cotransporters: $\mathrm{Na}^+/\mathrm{K}^+/2\mathrm{Cl}^-$ denoted by NKCC1, and $\mathrm{K}^+/\mathrm{Cl}^-$ denoted by

KCC2, whose fluxes are of the form

$$\begin{aligned} \mathrm{J_{kcc2}} &= U_{\mathrm{kcc2}} \ln\left(\frac{[\mathrm{K^+}]_\mathrm{i}[\mathrm{Cl^-}]_\mathrm{i}}{[\mathrm{K^+}]_\mathrm{ecs}[\mathrm{Cl^-}]_\mathrm{ecs}}\right) \\ \mathrm{J_{nkcc1}} &= \frac{U_{\mathrm{nkcc1}}}{1+\exp\left(16-[\mathrm{K^+}]_\mathrm{ecs}\right)}\left(\ln\left(\frac{[\mathrm{K^+}]_\mathrm{i}[\mathrm{Cl^-}]_\mathrm{i}}{[\mathrm{K^+}]_\mathrm{ecs}[\mathrm{Cl^-}]_\mathrm{ecs}}\right)+\ln\left(\frac{[\mathrm{Na^+}]_\mathrm{i}[\mathrm{Cl^-}]_\mathrm{i}}{[\mathrm{Na^+}]_\mathrm{ecs}[\mathrm{Cl^-}]_\mathrm{ecs}}\right)\right) \end{aligned} \tag{5.7}$$

where U_{kcc2} and U_{nkcc1} are the strengths given to the cotransporters (see Table 5.2). The NKCC1 cotransporter is modeled in (5.7) as a function of extracellular potassium concentration, in line with experimental results suggesting that high concentration of $[\mathrm{K}]_\mathrm{ecs}$ leads to activation of NKCC1 [11].

The model also includes the dynamics of the extracellular concentration of oxygen, governed by the differential equation:

$$\tau\frac{d[\mathrm{O_2}]_\mathrm{ecs}}{dt} = -\alpha\gamma(J_{\mathrm{pump,Na^+}}-J_{\mathrm{g,p}})+\varepsilon_o([\mathrm{O_2}]_\infty-[\mathrm{O_2}]_\mathrm{ecs}), \tag{5.8}$$

where α is a conversion factor between pump current expressed in mM/s and change in the concentration of oxygen expressed in $\mathrm{mgL^{-1}s^{-1}}$, ε_0 is a diffusion coefficient obtained from Fick's law and $[\mathrm{O_2}]_\infty$ is the bath concentration of oxygen.

The current induced by the sodium potassium pump $J_{\mathrm{pump,Na^+}}$, the current induced by the glial potassium cleaning $J_{\mathrm{glia,K^+}}$ and the current corresponding to the sodium potassium pump on glia $J_{\mathrm{g,p}}$ have the following expressions:

$$\begin{aligned} J_{\mathrm{pump,Na^+}} &= \left(\frac{\rho}{1+\exp(25-[\mathrm{Na^+}]_\mathrm{i})/3)}\right)\times\left(\frac{1}{1+\exp(3.5-[\mathrm{K^+}]_\mathrm{ecs})}\right), \\ J_{\mathrm{g,p}} &= \frac{1}{3}\left(\frac{\rho}{1+\exp(25-[\mathrm{Na^+}]_\mathrm{gli})/3)}\right)\times\left(\frac{1}{1+\exp(3.5-[\mathrm{K^+}]_\mathrm{ecs})}\right), \\ J_{\mathrm{glia}} &= \frac{G_{\mathrm{glia}}}{1+\exp((18-[\mathrm{K^+}]_\mathrm{ecs})/25)}, \end{aligned} \tag{5.9}$$

where ρ is the strength of the sodium potassium pump and G_{glia} is the strength of the glial uptake. Following [12, 13], the diffusion of the potassium away from the extracellular space is modeled as

$$J_{\mathrm{diff,K^+}} = \varepsilon([\mathrm{K^+}]_\mathrm{ecs}-k_\infty), \tag{5.10}$$

where ε is the diffusion coefficient and k_∞ is the concentration of potassium in the bathing solution.

To describe the dependency of the sodium potassium pump on the oxygen supply, the strength of the pump ρ is modeled as a sigmoid function of the oxygen concentration:

$$\rho = \frac{\rho_{\max}}{1 + \exp((20 - [\mathrm{O_2}]_{\mathrm{ecs}})/3)}, \tag{5.11}$$

while G_{glia} and ε, previously considered constant in the Cressman model [12], are now written with respect to the bath oxygen concentration:

$$G_{glia} = \frac{G_{\mathrm{glia,max}}}{1 + \exp((2.5 - [\mathrm{O_2}]_{\infty})/0.2)}, \tag{5.12}$$

$$\varepsilon_{\mathrm{k}} = \left(\frac{1}{1 + \exp((\beta - 20)/2)}\right)\left(\frac{\varepsilon_{\mathrm{k},max}}{1 + \exp((-[\mathrm{O_2}]_{\infty} - 2.5)/0.2)}\right), \tag{5.13}$$

where $\rho_{\max}$, $G_{\mathrm{glia,max}}$ and $\varepsilon_{\mathrm{k,max}}$ represent the maximal strength of the sodium potassium pump, glial uptake and respectively the potassium diffusion and are given in Table 5.2. Note that the expression of the diffusion of potassium depends on β, which represents the ratio between the intracellular and extracellular volume. In this manner, the diffusion of potassium outside the cell, will be limited by the ratio of the two volumes.

In equations (5.4), v_i and v_{ecs} denote the intracellular and extracellular volume. In the Wei model [11], the dynamics of the volume of the cell was modified such that the sum between the intracellular and the extracellular volume of the cell is constant at 114.29% of its initial neuronal volume:

$$\bar{v}_i = v_i^0 \left(1.1029 - 0.029 \exp\left(\frac{\pi_{\mathrm{ecs}} - \pi_i}{20}\right)\right),$$

where $\bar{v}_i$ denotes the expected intracellular volume calculated with respect the extracellular (π_{ecs}) and intracellular osmotic pressure (π_i), which are given by the sum of all the ions in the extracellular, and intracellular space:

$$\begin{aligned} \pi_i &= [\mathrm{Na^+}]_i + [\mathrm{K^+}]_i + [\mathrm{Cl^-}]_i + r_1 \cdot [A^-]_i, \\ \pi_{\mathrm{ecs}} &= [\mathrm{Na^+}]_{\mathrm{ecs}} + [\mathrm{K^+}]_{\mathrm{ecs}} + [\mathrm{Cl^-}]_{\mathrm{ecs}} + r_2 \cdot [A^-]_{\mathrm{ecs}}. \end{aligned} \tag{5.14}$$

The concentration of intracellular and extracellular anions was set to: $[\mathrm{A^-}]_i = 132$

mM and $[A^-]_{ecs} = 18$ mM and r_1 and r_2 have the following expression:

$$r_1 = \frac{v_i^0}{v_i}, \quad r_2 = \frac{1}{\beta_0} \frac{v_i^0}{\left(1 + \frac{1}{\beta_0}\right) v_i^0 - v_i},$$

The change in the volume of the cell as is modeled as

$$\frac{\mathrm{d}v_i}{\mathrm{d}t} = \frac{\bar{v}_i - v_i}{250}, \tag{5.15}$$

where 250 is a time constant expressed in milliseconds, and the extracellular volume was calculated as:

$$v_{ecs} = \left(1 + \frac{1}{\beta_0}\right) v_i^0 - v_i, \tag{5.16}$$

where β_0 is the initial ratio of the intracellular and extracellular volume and v_i^0 is the initial volume of the cell. The ratio β is updated with respect to the intracellular volume obtained from equation (5.15):

$$\beta = \frac{v_i}{v_{ecs}}. \tag{5.17}$$

Name	Symbol	Value	Units
Capacitance	c_m	1	μF/cm^2
Time constant	φ	3	1/msec
Sodium conductance	g_{Na^+}	30	mS/cm^2
Potasium conductance	g_{K^+}	25	mS/cm^2
Sodium leak conductance	$g_{Na^+,leak}$	0.0247	mS/cm^2
Potassium leak conductance	$g_{K^+,leak}$	0.05	mS/cm^2
Chloride conductance	g_{Cl}	0.1	mS/cm^2
Oxygen diffusion coefficient	ε_0	0.17	s^{-1}
Conversion factor	α	5.3	g/mol
Maximum strength of the Na/K pump	ρ_{max}	2.32	mM/s
Maximum strength of the glial uptake	$G_{glia,max}$	3.48	mM/s
Maximum potassium diffusion coefficient	$\varepsilon_{k,max}$	0.25	s^{-1}
Intracellular concentration of sodium of glia	$[Na^+]_{gli}$	18	mM
NKCC1 cotransporter strength	U_{nkcc1}	0.1	mM/s
KCC2 cotransporter strength	U_{kcc2}	0.3	mM/s
Ratio of intra/extracellular volume	β_0	7	
Initial volume of the cell	v_i^0	$1.436e^{-15}$	

Table 5.2: Parameter values for the Wei model

Using the parameters listed in Table 5.2 and the initial conditions in Table 5.3, we performed multiple simulations with the Wei model using an explicit forward Euler method. We have varied the parameters k_∞ and O_∞ and we have obtained various firing patterns. For each pair of parameters, we considered a 60 seconds burn-in period and a final time of 100 seconds.

V	-60.74	$[K]_{ecs}$	$2e^{-15}$	$[Cl^+]_{ecs}$	$2.3e^{-14}$
m	0.049	$[K]_i$	$2.08e^{-13}$	$[Cl^+]_i$	$1.3e^{-14}$
h	0.981	$[Na]_{ecs}$	$3.2e^{-14}$	$[v]_i$	e^{-15}
n	0.096	$[Na]_i$	$2.3e^{-14}$	$[O_2]_{ecs}$	26.96

Table 5.3: Initial conditions for the Wei model.

In Figure 5.2 we show that depending on the choice of k_∞ and O_∞ we can distinguish 5 different neuronal firing patterns: wave of death (dark blue), no firing (blue), tonic firing (green), bursts (orange) and spreading depression (yellow). Since we are particularly interested in describing the last three situations, we choose one case for each particular region to illustrate in Figures 5.4, 5.3, 5.6 respectively.

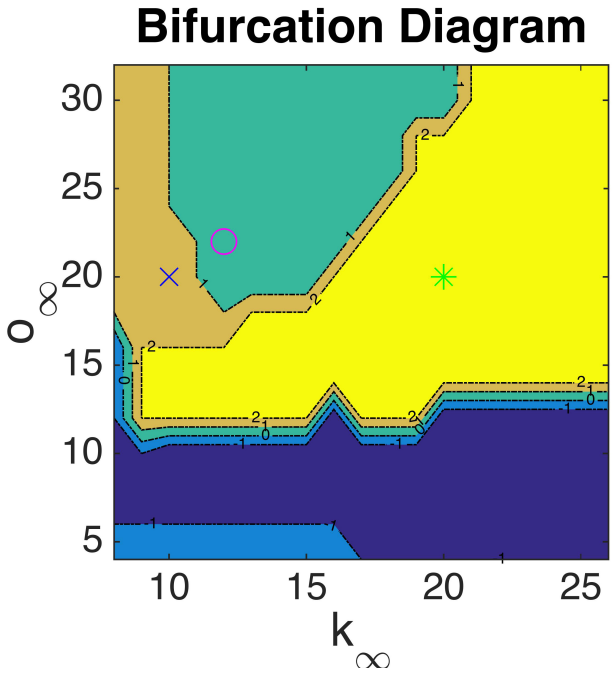

Figure 5.2: Bifurcation diagram for the Wei model with the parameters defined in Table 5.2. The colour coding gives five different neuronal firing patterns: the dark blue indicates the wave of death described in [129], the blue shows no firing, in green we see regions characterized by tonic firing, in orange we get a bursting pattern, while the pairs (k_∞, O_∞) corresponding to the yellow region indicate the formation of CSD waves.

To illustrate the tonic firing we set $k_\infty = 12$ mM and $O_\infty = 22$ mg/L, marked in Figure 5.2 with a circle, while the bursting patterns were obtained by setting $k_\infty = 10$ mM, $O_\infty = 20$ mg/L marked by the blue cross. The mixed spreading depression for the case $k_\infty = 20$ mM and $O_\infty = 20$ mg/L, is represented in Figure 5.2 by the green star in yellow region.

Figures 5.3, 5.4 and 5.6 capture these different firing patterns by showing the membrane potential and the ionic concentrations for the three situations: bursting pattern, tonic firing and mixed spreading depression.

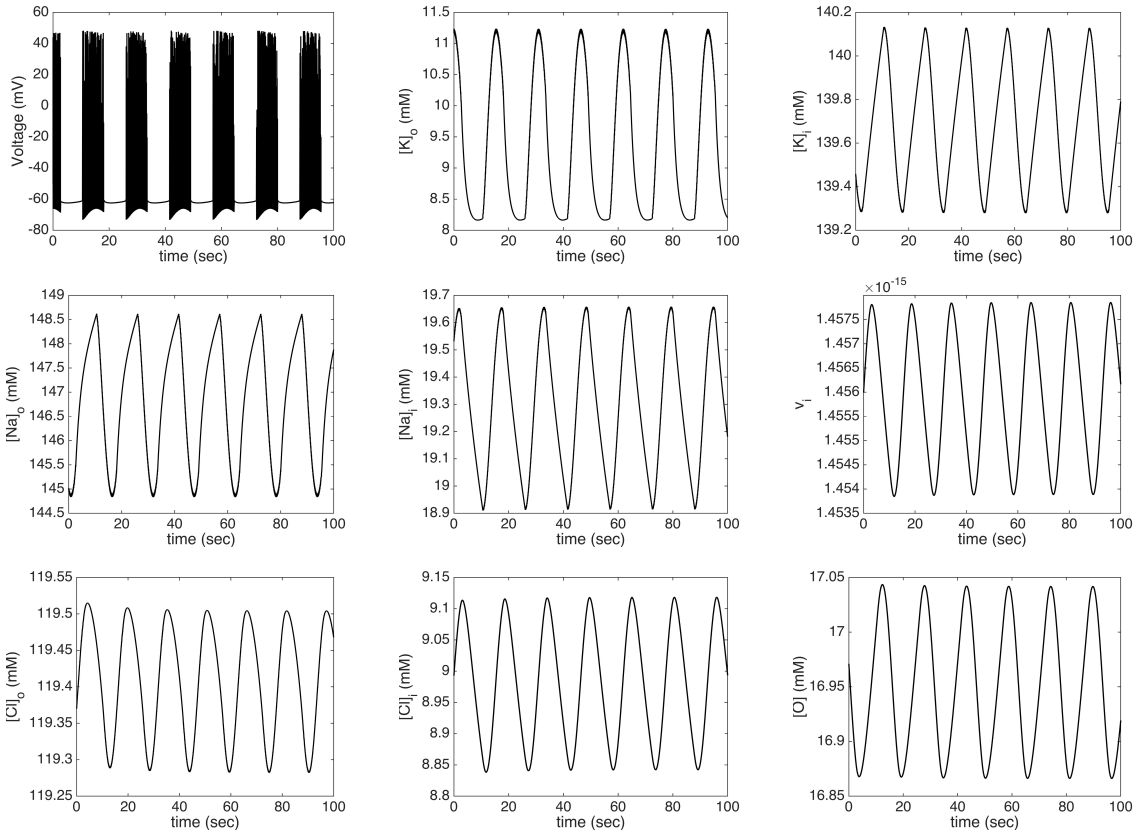

Figure 5.3: Bursting pattern from the Wei model with $k_\infty = 10$ and $O_\infty = 20$.

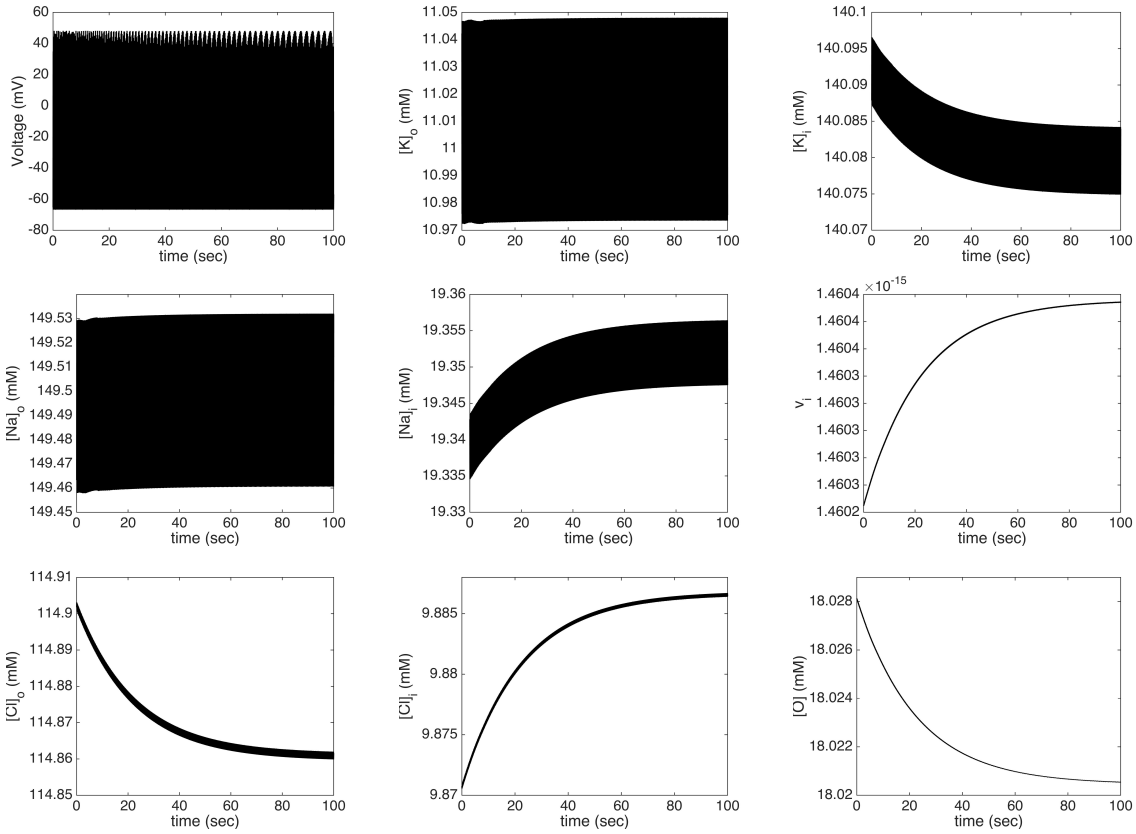

Figure 5.4: Tonic firing pattern from Wei model with $k_\infty = 12$ and $O_\infty = 22$.

Figure 5.5 zooms inside of the membrane potential for an interval of one second. Notice that the amplitude of the spikes differs, unlike in the other electrophysiological models considered. This is because the Nernst potential depends on both exterior and interior ionic concentrations, which in this case are modelled through differential equations.

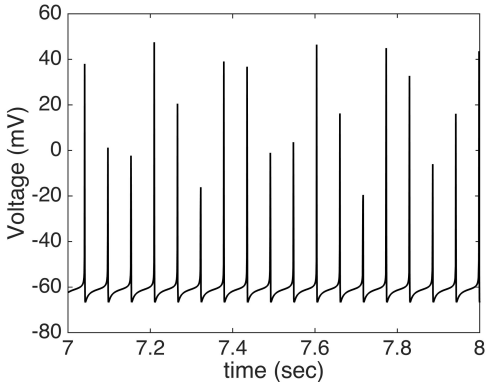

Figure 5.5: Magnification of the action potential in the Wei model for $k_\infty = 12$ and $O_\infty = 22$.

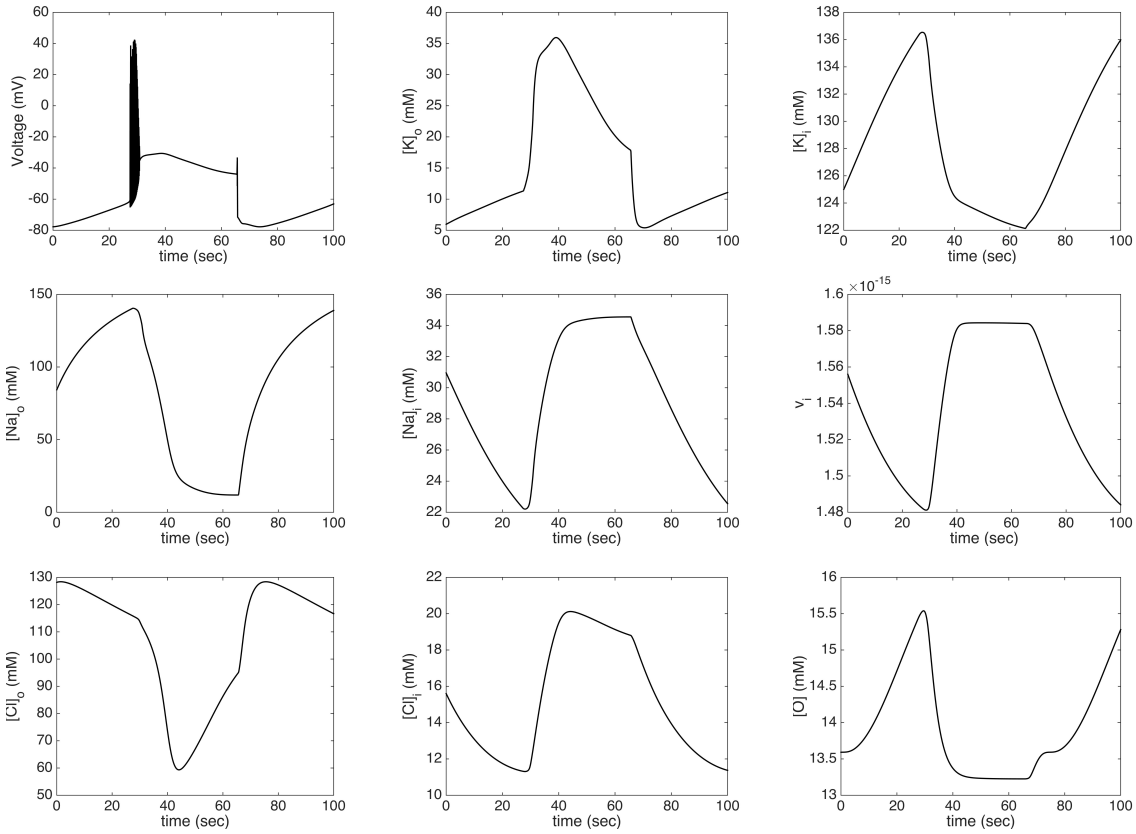

Figure 5.6: Mixed spreading depression from the Wei model with $k_\infty = 20$ and $O_\infty = 20$.

5.2.2 Huguet model

The model developed by *Huguet et al.* [21] is based on Hodgkin Huxley type models like the Wei model described in the previous section, or the Cressman model reviewed in Chapter 1. Unlike in the other models, where the only role of the astrocyte is an extracellular potassium buffer, *Huguet et al.* include a detailed biophysical description of astrocytes based on experimental results. This is in full agreement with the most recent literature acknowledging that astrocytes have been severely overlooked and their role in the brain is much more significant than initially thought [4, 3, 7].

Huguet et al. investigate whether astrocytes have a role in preventing or assisting the propagation of cortical spreading depression waves. More specifically, they study the role of the gap junctions connecting neighboring astrocytes. It has been previously shown that in the rat hippocampus, each astrocyte is connected on average to 11 of its neighbors and these connections are realized mostly

through Cx43 , which is the main connexin that forms gap junctions between astrocytes [130]. Interestingly, in the experimental literature, these gap junctions have proven to be both beneficial and detrimental during CSD, depending on the gravity of the injury [21, 130]. On one hand, during an initial stage of ischemic injury, the gap junctions seem to enhance neuron viability [130], while on the other hand, if the injury is moderate or severe they can increase the spread of the ischemic brain injury [131].

In [21], the authors consider a network consisting of fifty pairs of neuron-astrocyte cells. The ignition of the cortical spreading depression wave is done by injecting potassium inside of the extracellular space, for the middle cells $\mathcal{M} = \{24, 25, 26, 27\}$. Mathematically, this is achieved by adding a constant in the right hand side of the differential equation of the extracellular potassium. This mathematical model is built specially to simulate CSD and it consists of the basic mechanisms required to induce such a depolarization wave, i.e. for the neuron model there is a sodium current which is voltage dependent (as in [12] and [11]), a slow inactivating sodium current, a fixed leak current, while for the astrocytic model there is a potassium current and a small leak current.

Huguet et al. suggest that the initiation of a CSD wave can be successfully prevented if the maximum conductance of the gap junction, the number of connections with the neighboring astrocytes and the strength of the pump are all sufficiently large. Their computer experiments, which agree with the experimental work, confirm that once a cortical spreading depression wave has been initiated, the gap junctions can contribute to its amplification [21]. One limitation of the Huguet model is that it does not include cell swelling, as explained in the previous section, neuronal swelling and extracellular space shrinking can gravely affect the ionic homeostasis.

5.3 CSD electrophysiologic model

5.3.1 Description

For describing the massive changes that occur in the ionic concentrations and membrane potential during cortical spreading depression, we used an electrophys-

iologic model based on the work of *Hubel et al.* in [23]. In the previous section we described the Wei model which, like many other models [12, 13, 22, 126, 127] focuses on capturing transitions between different neuronal firing patterns: tonic firing, bursts and SD. Below, we present a model specifically tailored for characterizing cortical spreading depression, that follows electroneutrality, mass conservation principle and osmotic equilibrium. In addition, it accounts for the large morphologic changes characteristic to CSD waves and it also includes glutamate dynamics.

The rate equations corresponding to membrane potential and gate dynamics are built on the classic Hodgkin-Huxley model:

$$\tau c_m \frac{\mathrm{d}V}{\mathrm{d}t} = -I_{\mathrm{Na}^+} - I_{\mathrm{K}^+} - I_{\mathrm{Cl}^-} - J_{\mathrm{pump,Na}^+}, \tag{5.18}$$

$$\tau \frac{\mathrm{d}w}{\mathrm{d}t} = \varphi(\alpha_w(V)(1-w) - \beta_w(V)w), \quad w \in \{h, n\}, \tag{5.19}$$

where c_m is the membrane capacitance, V represents the membrane potential, n is the activation gate corresponding to potassium activation while h is the gating variable attributed to sodium activation.

As in [12, 13], the gate for sodium inactivation m is modelled through an adiabatic approximation of the form:

$$m = \frac{\alpha_m}{\alpha_m + \beta_m},$$

where $\alpha_{m/n/h}$ and $\beta_{m/n/h}$ are the Hodgkin-Huxley voltage saturated functions given in the Table 5.4.

w	m	h	n
$\alpha_w(V)$	$0.1\dfrac{V+30}{1-\exp(-(V+30)/10)}$	$0.07\exp(-(V+44)/20)$	$0.01\dfrac{V+34}{1-\exp(-(V+34)/10)}$
$\beta_w(V)$	$4\exp(-(V+55)/18)$	$\dfrac{1}{1+\exp(-(V+14)/10)}$	$0.125\exp(-(V+44)/80)$

Table 5.4: Gating variables: voltage-dependent saturation functions in the CSD model [23].

The ionic currents of sodium (Na^+), potassium (K^+) and the leak current of chloride, are a slightly modified version of those proposed by Hodgkin and

Huxley:

$$
\begin{aligned}
I_{\mathrm{Na}^+} &= g_{\mathrm{Na}^+} m^3 h (V - V_{\mathrm{Na}^+}) + g_{\mathrm{Na}^+,\mathrm{leak}} (V - V_{\mathrm{Na}^+}) + I^{\mathrm{NMDA}}_{\mathrm{Na}^+} + I^{\mathrm{AMPA}}_{\mathrm{Na}^+} + I^{\mathrm{co}}_{\mathrm{Na}^+}, \\
I_{\mathrm{K}^+} &= g_{\mathrm{K}^+} n^4 (V - V_{\mathrm{K}^+}) + g_{\mathrm{K}^+,\mathrm{leak}} (V - V_{\mathrm{K}^+}) + I^{\mathrm{NMDA}}_{\mathrm{K}^+} + I^{\mathrm{AMPA}}_{\mathrm{K}^+} + I^{\mathrm{co}}_{\mathrm{K}^+}, \\
I_{\mathrm{Cl}^-} &= g_{\mathrm{Cl}^-} (V - V_{\mathrm{Cl}^-}) + I^{\mathrm{co}}_{\mathrm{K}^+},
\end{aligned}
$$

where g_{Na^+}, $g_{\mathrm{Na}^+,\mathrm{leak}}$, g_{K^+} and $g_{\mathrm{K}^+,\mathrm{leak}}$ are the conductances and leak conductances of sodium and potassium respectively, g_{Cl^-} the conductance of chloride and are listed in Table 5.5. $I^{\mathrm{NMDA}}_{\mathrm{Na}^+/\mathrm{K}^+}$ and $I^{\mathrm{AMPA}}_{\mathrm{Na}^+/\mathrm{K}^+}$ are the currents induced by the NMDA and AMPA channels and will be discussed later on. $V_{\mathrm{Na}^+}, V_{\mathrm{K}^+}$ and V_{Cl^-} are the Nernst potentials for sodium, potassium and chloride:

$$
V_x = \frac{26.64}{z_x} \ln\left(\frac{x_e}{x_i}\right), \text{where } \; x = \{\mathrm{Na}^+, \mathrm{K}^+, \mathrm{Cl}^-\} \tag{5.20}
$$

where z_x is the valence of each ion x.

Parameter description	Symbol	Value	Unit
Sodium conductance	g_{Na^+}	100	$\mathrm{mS/cm}^2$
Potassium conductance	g_{K^+}	40	$\mathrm{mS/cm}^2$
Chloride conductance	g_{Cl^-}	0.05	$\mathrm{mS/cm}^2$
Sodium leak conductance	$g^0_{\mathrm{Na}^+,\mathrm{leak}}$	0.0135	$\mathrm{mS/cm}^2$
Potassium leak conductance	$g^0_{\mathrm{K}^+,\mathrm{leak}}$	0.05	$\mathrm{mS/cm}^2$
Capacitance	C	1	$\mu\mathrm{F/cm}^2$
Faraday's constant	F	97485	C/mol
Time constant	φ	3	1/msec
Sodium valence	z_{Na}	+1	-
Potassium valence	z_{K}	+1	-
Sodium valence	z_{Cl}	-1	-

Table 5.5: Ionic conductances, membrane capacitance, ionic valences and time constants in the CSD model [23].

The changes in the ionic concentrations over time are tracked both inside (i) and outside the cell (ecs). In addition, *Hubel et al.* [23] consider three compartments: soma (i), glia (g) and extracellular space (ecs). However, the ionic concentrations in the glia are not explicitly modeled but set to mantain the balance between glia and extracellular space. Each of the three compartments is attributed its own volume denoted by ω_j ($j = \{\mathrm{ecs}, i, g\}$), which will change over

time.

The rate of the sodium potassium pump is defined as

$$J_{\text{pump,Na}^+} = \left(\frac{\rho}{1+\exp(15-[\text{Na}^+]_\text{i})/3)}\right) \times \left(\frac{1}{1+\exp(5.5-[\text{K}^+]_\text{ecs})}\right), \quad (5.21)$$

where ρ is the strength of the sodium potassium pump.

The differential equations describing the dynamics of potassium and chloride in the soma are given by:

$$\tau\frac{d[\text{K}^+]_i}{dt} = -\gamma(I_{\text{K}^+} - 2J_{\text{pump,Na}^+}). \quad (5.22)$$

$$\tau\frac{d[\text{Cl}^-]_i}{dt} = \gamma I_{\text{Cl}^-}. \quad (5.23)$$

where $\tau = 10^3$ is a conversion factor and γ is used for converting the current from μA/cm^2 to mM:

$$\gamma = \frac{A_m}{F \cdot 10}, \quad (5.24)$$

F is the Faraday constant and A_m is the membrane surface area and are listed in Table 5.6.

Parameter description	Symbol	Value	Unit
Membrane surface	A_m	18000	μm^2
Intracellular volume	ω_i^0	7500	μm^3
Extracellular volume	ω_{ecs}^0	2500	μm^3
Glial volume	ω_g^0	7500	μm^3

Table 5.6: Membrane surface and the initial volumes of the soma, extracellular and glial compartments in the CSD model [23]

In this model, the electroneutrality of the fluxes across the membrane is insured: the sum of the ionic concentrations in the soma is constant and equals the sum of the initial ionic concentrations: $[\text{Na}^+]_i + [\text{K}^+]_i + [\text{Cl}^-]_i = \text{Na}_i^0 + \text{K}_i^0 + \text{Cl}_i^0$.

The intracellular concentration of sodium is thus

$$[\text{Na}^+]_i = \text{Na}_i^0 + \text{K}_i^0 - \text{Cl}_i^0 - [\text{K}^+]_i + [\text{Cl}^-]_i \quad (5.25)$$

The extracellular concentrations of sodium, potassium and chloride are expressed

such that the mass conservation and electroneutrality principles hold:

$$[\mathrm{Na}^+]_{\mathrm{ecs}} = \mathrm{Na}^0_{\mathrm{ecs}} + \mathrm{Na}^0_i - [\mathrm{Na}^+]_i - \Delta\mathrm{Na}_{\mathrm{glia}}, \tag{5.26}$$

$$[\mathrm{K}^+]_{\mathrm{ecs}} = \mathrm{K}^0_{\mathrm{ecs}} + \mathrm{K}^0_i - [\mathrm{K}^+]_i - \Delta\mathrm{K}_{\mathrm{glia}} - \Delta K_{\mathrm{bath}}, \tag{5.27}$$

$$[\mathrm{Cl}^-]_{\mathrm{ecs}} = \mathrm{Cl}^0_{\mathrm{ecs}} + \mathrm{Cl}^0_i - [\mathrm{Cl}^-]_i - \Delta\mathrm{Cl}_{\mathrm{glia}}. \tag{5.28}$$

The terms ΔK_{glia} and ΔK_{bath} in (5.26)-(5.28) represent the ion exchange with the glia cells, respectively, an external potassium bath, while the fluxes of sodium and chloride to the glia are approximated by:

$$\Delta\mathrm{Na}_{\mathrm{glia}} = -0.2\Delta\mathrm{K}_{\mathrm{glia}} \tag{5.29}$$

$$\Delta\mathrm{Cl}_{\mathrm{glia}} = 0.8\Delta\mathrm{K}_{\mathrm{glia}} \tag{5.30}$$

The astrocyte's crucial role in clearing the potassium and the glutamate released in huge quantities into the extracellular space during cortical spreading depression has been largely studied in the recent years [5, 118, 119]. The potassium regulation schemes proposed in this model [23] are given by a coupling to an extracellular potassium bath and a glial buffering. These two schemes were analyzed first in a separate manner in previous published work of *Hubel et al.*: the mechanisms underlying extracellular potassium bath were investigated in [126], while glial buffering was studied in detail in [127]. In the current model, the buffering of the glial potassium is modeled as [23]:

$$\tau^2 \frac{d\Delta K_{\mathrm{glia}}}{dt} = J_{\mathrm{glia},\mathrm{K}^+}, \tag{5.31}$$

where

$$J_{\mathrm{glia},\mathrm{K}^+} = -\left[\lambda_{\mathrm{rel}} - \lambda_1 \left(1 + \exp\left(\frac{5.5 - [\mathrm{K}^+]_{\mathrm{ecs}}}{2.5}\right)\right)^{-1}\right] \frac{\Delta K^{\max}_{\mathrm{glia}} - \Delta K_{\mathrm{glia}}}{\Delta K^{\max}_{\mathrm{glia}}} \tag{5.32}$$

with $K^{\max}_{\mathrm{glia}}$ being the upper bound of the potassium uptake, λ_{rel} the constant release rate, listed in Table 5.7.

The diffusive coupling to the bath is written as:

$$\tau^2 \frac{d\Delta K_{\mathrm{bath}}}{dt} = J_{\mathrm{diff}}, \tag{5.33}$$

where the diffusion current is defined as:

$$J_{\text{diff}} = \lambda([K]_{\text{ecs}} - K_{\text{bath}}),$$

with λ the diffusion coefficient listed in Table 5.7.

Parameter description	Symbol	Value	Unit
Strength of the sodium potassium pump	ρ	6.46	μA/cm^2
Diffusion coefficient	λ	1e − 4	1/msec
Glial potassium uptake parameter	λ_1	1.44e − 2	mM/msec
Glial potassium release rate	λ_{rel}	5.1e − 3	mM/msec
Potassium bath concentration	K_{bath}	4	mM
Maximum uptake glial capacity	$\Delta K_{\text{glia}}^{\max}$	350	fmol

Table 5.7: **Parameters in the CSD model:** Strength of the sodium potassium pump, diffusion coefficient, potassium bath concentration, the uptake and release glial parameters.

It is well known in the documented literature [121, 105, 5, 81] that cortical spreading depression waves induce swelling in neurons and glia and a very large shrinkage of the extracellular space. This is believed to be an osmosis driven phenomenon, in which the volumes change in order to maintain the equilibrium between soma, glia and extracellular space. We denote the volumes of these three compartments by ω_i, ω_g, ω_{ecs} respectively.

The total matter in the intracellular and extracellular space $N_{i/\text{ecs}}$ is the sum of all the ionic concentrations, the impermeable anions $A_{i/\text{ecs}}$ and neutral matter $X_{i/\text{ecs}}$:

$$N_i = [\text{Na}^+]_i + [\text{K}^+]_i + [\text{Cl}^-]_i + A_i + X_i \tag{5.34}$$

$$N_{\text{ecs}} = [\text{Na}^+]_{\text{ecs}} + [\text{K}^+]_{\text{ecs}} + [\text{Cl}^-]_{\text{ecs}} + A_{\text{ecs}} + X_{\text{ecs}} \tag{5.35}$$

Ion	Initial concentration (mM)	
	Intracellular (i)	Extracellular (ecs)
Na^0	15	144
K^0	140	4
Cl^0	9	130
A	146	18
X	5	19
total	315	315

Table 5.8: Initial concentration of ions, impermeable anions and neutral matter in the intracellular and extracellular space. The initial glial content N_g^0 was chosen such that the glia is in equilibrium with the extracellular space, and therefore $N_g^0 = 315$.

The total glial content is modeled as:

$$N_{\text{glia}} = N_g^0 + \Delta\text{Na}_{\text{glia}} + \Delta\text{K}_{\text{glia}} + \Delta\text{Cl}_{\text{glia}}, \tag{5.36}$$

where N_g^0 is the initial glial content, chosen such that the glial cell is in balance with the extracellular space.

The osmotic equilibrium equations are

$$\frac{N_i}{\omega_i} = \frac{N_{\text{ecs}}}{\omega_{\text{ecs}}} = \frac{N_g}{\omega_g} = \frac{N_{\text{tot}}}{\omega_{\text{tot}}}, \tag{5.37}$$

and therefore, the volume changes in the three compartments are given by:

$$\omega_j = N_j \frac{\omega_{\text{tot}}}{N_{\text{tot}}} \text{ with } j = \{i,\ \text{ecs},\ g\}, \tag{5.38}$$

where $N_{\text{tot}} = N_i + N_{\text{ecs}} + N_g$ is the total number of ions and $\omega_{\text{tot}} = \omega_i + \omega_{\text{ecs}} + \omega_g$ is the total volume.

In the electrophysiologic model, *Hubel et al.* included also glutamate dynamics, the brain's main excitatory neutrotransmitter, known to be released in large amounts during cortical spreading depression [132]. When glutamate concentration is high, glutamate binds to the AMPA and NMDA receptors, which activate and trigger the release of additional glutamate and potassium, that later on diffuse in the nearby cells, contributing to the propagation of the CSD waves. In this model, it is assumed that all synapses are involved in the CSD event due to the high synchronous neuronal activity. Additionally, the neuronal connections

are split equally between presynaptic and postsynaptic, as it is assumed that each neuron experiences both presynaptic and postsynaptic activity.

The glutamate release mechanism depends on the membrane potential and it gradually increases for depolarizations which exceed a critical potential $V_{\rm cr}$:

$$I_{\rm rel}(V) = \begin{cases} N_{\rm syn} R_{\rm max} \left(\dfrac{V - V_{\rm cr}}{V_{\rm hi} - V_{\rm cr}} \right)^2 \dfrac{[{\rm Glu}]_i}{[{\rm Glu}]_{\rm max}} & \text{for} \quad V \geq V_{\rm cr}, \\ 0 & \text{for} \quad V < V_{\rm cr}, \end{cases} \tag{5.39}$$

where $[{\rm Glu}]_i$ is the intracellular amount of glutamate and is expressed as the difference between the total amount of glutamate $[{\rm Glu}]_{\rm max}$ and the currently released glutamate $[{\rm Glu}]_{\rm rel}$:

$$[{\rm Glu}]_i = [{\rm Glu}]_{\rm max} - [{\rm Glu}]_{\rm rel}, \tag{5.40}$$

while $R_{\rm max}$ is the maximal release late of glutamate and $V_{\rm hi}$ is the highest membrane potential value.

Parameter description	Symbol	Value	Unit
Maximal release rate	$R_{\rm max}$	1.4e-5	fmol/msec
Critical membrane potential	$V_{\rm cr}$	-50	mV
Highest membrane potential	$V_{\rm hi}$	50	mV
Number of activated synapses during SD	$N_{\rm syn}$	5000	-
Available glutamate for signaling	$[{\rm Glu}]_{\rm max}$	10	fmol

Table 5.9: Parameters associated to glutamate release in the CSD model

We denote the averaged values of the concentrations of glutamate in extracellular space and cleft by $[{\rm Glu}]_{\rm ecs}$, respectively $[{\rm Glu}]_c$. The release of glutamate molecules gives an extracellular concentration of:

$$[{\rm Gl}]_{\rm ecs} = \frac{[{\rm Glu}]_{\rm ecs}}{\omega_{\rm ecs}} \tau, \tag{5.41}$$

and a cleft concentration of:

$$[{\rm Gl}]_c = \frac{[{\rm Glu}]_c}{\omega_{\rm en} N_{\rm syn}} \tau. \tag{5.42}$$

At high concentrations, glutamate binds to the AMPA and NMDA recep-

tors causing the channels to open and therefore allowing the ions of sodium and potassium to flow through. The opening probability of the AMPA and NMDA gates is denoted by r_{AMPA}, respectively r_{NMDA}, and their dynamics is modeled in [23] by Hodgkin-Huxley formalism with added dependence on the available concentration of glutamate in the cleft $[\text{Gl}]_c$:

$$\tau \frac{dr_{\text{AMPA}}}{dt} = [\text{Gl}]_c \alpha_{\text{AMPA}}(1 - r_{\text{AMPA}}) - \beta_{\text{AMPA}} r_{\text{AMPA}}, \tag{5.43}$$

$$\tau \frac{dr_{\text{NMDA}}}{dt} = [\text{Gl}]_c \alpha_{\text{NMDA}}(1 - r_{\text{NMDA}}) - \beta_{\text{NMDA}} r_{\text{NMDA}}. \tag{5.44}$$

The AMPA currents for sodium and potassium obey:

$$I_{\text{Na}^+}^{\text{AMPA}} = g_{\text{AMPA}} r_{\text{AMPA}}(V - V_{\text{Na}^+}), \tag{5.45}$$

$$I_{\text{K}^+}^{\text{AMPA}} = g_{\text{AMPA}} r_{\text{AMPA}}(V - V_{\text{K}^+}), \tag{5.46}$$

where g_{AMPA} is the conductance of the AMPA channels given in Table 5.10, and V_{Na^+} and V_{K^+} are the Nernst potentials for sodium, potassium and chloride given in equation (5.20).

For maintaining their normal physiological function, NMDA channels require a certain magnesium concentration [132]. It was observed that when the membrane potential is at rest, there is a flow of external magnesium ions into the pore, where they bind tightly, blocking further ion permeation [133], while in state of strong depolarization, magnesium ions are repelled from the pore, permitting the flow of ions [133]. This physiological mechanism of NMDA channels is captured in the mathematical expression proposed by *Hubel et al.* for the NMDA currents:

$$I_{\text{Na}^+}^{\text{NMDA}} = g_{\text{NMDA}} r_{\text{NMDA}} \frac{V - V_{\text{Na}^+}}{1 + 0.33[\text{Mg}^{2+}] \exp(-0.07V - 0.7)}, \tag{5.47}$$

$$I_{\text{K}^+}^{\text{NMDA}} = g_{\text{NMDA}} r_{\text{NMDA}} \frac{V - V_{\text{K}^+}}{1 + 0.33[\text{Mg}^{2+}] \exp(-0.07V - 0.7)}, \tag{5.48}$$

where g_{NMDA} is the conductance of the NMDA channels, while $[\text{Mg}^{2+}]$ is the extracellular concentration of magnesium (see Table 5.10).

Glutamate present in the synaptic cleft is cleared into the extracellular space

through diffusion at a rate

$$I_{\text{Glu, diff}} = -A_\sigma N_{\text{syn}} \frac{D_G}{\Delta x} \left(\frac{[\text{Glu}]_{\text{ecs}}}{\omega_{\text{ecs}}} - \frac{[\text{Glu}]_{\text{c}}}{\omega_{en} N_{\text{syn}}^{\text{SD}}} \right), \tag{5.49}$$

where D_G is the diffusion coefficient of glutamate, A_σ the cross section area and Δx the cutoff distance from the synapse where the concentration of glutamate in the extracellular space is at steady state [23].

Parameter description	**Symbol**	**Value**	**Unit**
Gating constant for AMPA receptor	α_{AMPA}	1.1	mM· msec
Gating constant for AMPA receptor	β_{AMPA}	0.19	1/msec
Gating constant for NMDA receptor	α_{NMDA}	0.072	mM· msec
Gating constant for NMDA receptor	β_{NMDA}	0.0066	1/msec
Maximum conductance of AMPA receptor	$\bar{g}_{\text{AMPA}}$	0.486	mS/cm^2
Maximum conductance of NMDA receptor	$\bar{g}_{\text{NMDA}}$	0.139	mS/cm^2
Maximal [Glu] uptake rate from the cleft to the neuron	$\nu_{c\to i}^{\max}$	0.03	mM/msec
Extracellular magnesium concentration	$[\text{Mg}^{2+}]$	1.2	mM
Cross section area	A_σ	6.3e-3	μm^2
Glutamate diffusion coefficient	D_G	0.3	μm^2/msec
Distance from the cleft to the stationary $[\text{Glu}]_{\text{ecs}}$	Δx	20	μm

Table 5.10: Parameters associated glutamate diffusion in the CSD model.

The chemical reaction for glutamate uptake is:

$$\text{Glu} + \text{B} \underset{k_{-1}}{\overset{k_{+1}}{\rightleftharpoons}} \text{GluB} \xrightarrow{k_{\text{r}}} \text{Glu}^{\text{up}} + \text{B}$$

where Glu indicates the glutamate concentration in the extracellular space or in the cleft, B the concentration of free binding sites through which glutamate can be transported into the neurons or glia, GluB the concentration of bound glutamate, that can be released back or be taken into the cell and Glu^{up} that of buffered glutamate. Under the assumption that the reaction chain is stationary with B constant, the velocity of glutamate uptake into the cell can be expressed as [23]:

$$\nu = B k_r \frac{\text{Glu}}{\text{Glu} + K_m}, \tag{5.50}$$

where $K_m = \dfrac{k_{-1} + k_r}{k_{+1}}$.

The maximal uptake velocities from extracellular space to neuron and to glia

are expressed as:

$$\nu^{\max}_{\text{ecs}\to i} = 0.12\nu^{\max}_{c\to i}\frac{\omega^0_{\text{ecs}}}{\omega_{\text{ecs}}}, \tag{5.51}$$

$$\nu^{\max}_{\text{ecs}\to g} = 0.24\nu^{\max}_{c\to g}\frac{\omega^0_{\text{ecs}}}{\omega_{\text{ecs}}}, \tag{5.52}$$

where $\nu^{\max}_{c\to i}$ is the uptake velocity from the cleft to the neuron, assumed constant (see Table 5.10), while the maximal uptake velocity $\nu^{\max}_{c\to g}$ from cleft to glia and is

$$\nu^{\max}_{c\to g} = 4\nu^{\max}_{c\to i}. \tag{5.53}$$

The uptake velocities are expressed in Michaelis Menten form

$$v^i_c = \nu^{\max}_{c\to i}\frac{[\text{Gl}]_c}{[\text{Gl}]_c + K_m}\cdot\frac{\omega_{en}}{\tau}N_{\text{syn}}, \tag{5.54}$$

$$v^i_{\text{ecs}} = \nu^{\max}_{\text{ecs}\to i}\frac{[\text{Gl}]_{\text{ecs}}}{[\text{Gl}]_{\text{ecs}} + K_m}\cdot\frac{\omega_{\text{ecs}}}{\tau}, \tag{5.55}$$

$$v^g_c = \nu^{\max}_{c\to g}\frac{[\text{Gl}]_c}{[\text{Gl}]_c + K_m}\cdot\frac{\omega_{en}}{\tau}N_{\text{syn}}, \tag{5.56}$$

$$v^g_{\text{ecs}} = \nu^{\max}_{\text{ecs}\to g}\frac{[\text{Gl}]_{\text{ecs}}}{[\text{Gl}]_{\text{ecs}} + K_m}\cdot\frac{\omega_{\text{ecs}}}{\tau}, \tag{5.57}$$

where ω_{en} is the volume in the glial envelope and K_m is the affinity constant for the uptake system given in Table 5.11.

One molecule of glutamate is cotransported with three ions of Na^+ and one ion of Cl^-, while one ion of K^+ is released. This yields, the following cotransport currents [23]:

$$I^{\text{co}}_{\text{Na}^+} = \frac{3\tau}{\gamma}\left(v^i_c + v^i_{\text{ecs}}\right), \tag{5.58}$$

$$I^{\text{co}}_{\text{K}^+} = -\frac{\tau}{\gamma}\left(v^i_c + v^i_{\text{ecs}}\right), \tag{5.59}$$

$$I^{\text{co}}_{\text{Cl}^-} = -\frac{\tau}{\gamma}\left(v^i_c + v^i_{\text{ecs}}\right). \tag{5.60}$$

where γ is the conversion factor defined in (5.24).

The variation over time of glutamate in cleft is modeled as a function of the glutamate release flux into the synaptic cleft I_{rel}, the diffusive glutamate flux from cleft to extracellular space $I_{\text{Glu,diff}}$ and the corresponding uptake velocities

from cleft to soma ν_c^i and glia ν_c^g. Similarly, the variation over time of glutamate in extracellular space depends on the diffusive glutamate flux and the uptake velocities from extracellular space to soma ν_{ecs}^i and to glia ν_{ecs}^g:

$$\frac{d[\text{Glu}]_c}{dt} = I_{\text{rel}} - I_{\text{Glu,diff}} - \nu_c^i - \nu_c^g, \tag{5.61}$$

$$\frac{d[\text{Glu}]_{\text{ecs}}}{dt} = I_{\text{Glu,diff}} - \nu_{\text{ecs}}^i - \nu_{\text{ecs}}^g, \tag{5.62}$$

The amount of glutamate transported from cleft to the intracellular, extracellular and glial compartments is expressed with respect to the corresponding uptake velocities ν_c^i and ν_c^g and glutamate recycling rate k_{rec}:

$$\frac{d[\text{Glu}]_c^i}{dt} = \nu_c^i - k_{\text{rec}} \frac{[\text{Glu}]_c^i}{[\text{Glu}]_{\text{max}}}, \tag{5.63}$$

$$\frac{d[\text{Glu}]_c^g}{dt} = \nu_c^g - k_{\text{rec}} \frac{[\text{Glu}]_c^g}{[\text{Glu}]_{\text{max}}}, \tag{5.64}$$

$$\frac{d[\text{Glu}]_c^{\text{ecs}}}{dt} = I_{\text{Glu, diff}}, \tag{5.65}$$

where $I_{\text{Glu, diff}}$ is the glutamate diffusion current given in equation (5.49).

The change over time of glutamate in extracellular space depends on the rate at which it is transported from extracellular space to soma and glia,

$$\frac{d[\text{Glu}]_{\text{ecs}}^i}{dt} = \nu_e^i - k_{\text{rec}} \frac{[\text{Glu}]_{\text{ecs}}^i}{[\text{Glu}]_{\text{max}}}, \tag{5.66}$$

$$\frac{d[\text{Glu}]_{\text{ecs}}^g}{dt} = \nu_e^g - k_{\text{rec}} \frac{[\text{Glu}]_{\text{ecs}}^g}{[\text{Glu}]_{\text{max}}}. \tag{5.67}$$

The rate at which glutamate is released is given by:

$$\frac{d[\text{Glu}]_{\text{rel}}}{dt} = I_{\text{rel}} - \frac{k_{\text{rec}}}{[\text{Glu}]_{\text{max}}} \left([\text{Glu}]_c^i + [\text{Glu}]_c^g + [\text{Glu}]_{\text{ecs}}^i + [\text{Glu}]_{\text{ecs}}^g \right). \tag{5.68}$$

To summarize, the electrophysiologic model consists of 17 differential equations: (5.18), (5.19), (5.22), (5.23), (5.31), (5.33), (5.43), (5.44), (5.61)-(5.68).

For simplicity, we define a vector G_v containing all glutamate concentrations tracked in the CSD model, whose dynamics is given in equations (5.61)- (5.68):

$$G_v = \left[[\text{Glu}]_c \; [\text{Glu}]_{\text{ecs}} \; [\text{Glu}]_c^i \; [\text{Glu}]_c^g \; [\text{Glu}]_c^{\text{ecs}} \; [\text{Glu}]_{\text{ecs}}^i \; [\text{Glu}]_{\text{ecs}}^g \; [\text{Glu}]_{\text{rel}} \right]. \tag{5.69}$$

Parameter description	Symbol	Value	Unit
Uptake velocity from cleft to soma	$\nu_{c\to i}^{\max}$	0.03	mM· msec
Affinity constant for glutamate uptake	k_m	0.03	mM
Glutamate recycling rate	k_{rec}	0.001	fmol/msec
Maximum glutamate concentration	$[\text{Glu}]_{\max}$	10	fmol

Table 5.11: Parameters associated to glutamate uptake in the CSD model.

5.3.2 Calibration

In this section we analyze the effect of glial potassium uptake parameter λ_1, glial potassium release λ_{rel} and strength of the sodium potassium pump ρ on the duration on the cortical spreading depression waves. Using the Matlab software, we performed various computer simulations during which we recorded the duration of the CSD events for three separate cases:

a. We varied λ_{rel} while keeping λ_1 and ρ constant and equal to the values in Table 5.7. The left panel of Figure 5.7 shows that the duration of the CSD events increases with decreasing λ_{rel}.

b. We varied λ_1 while maintaining the values of ρ and λ_{rel} constant. The right panel of Figure 5.7 shows an increasing CSD duration with increasing λ_1.

c. We varied ρ while setting λ_1 and λ_{rel} equal to the constant values given in Table 5.7. Figure 5.8 shows that there is very small increase in the duration of the cortical spreading depression events with increasing strength of the pump.

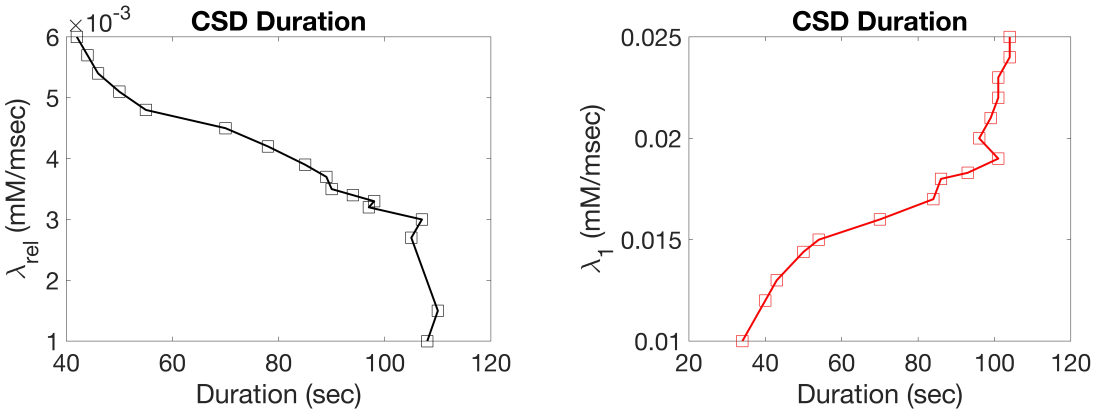

Figure 5.7: Duration (in seconds) of the cortical spreading depression waves when considering: a variable λ_{rel} (left) and variable λ_1 (right).

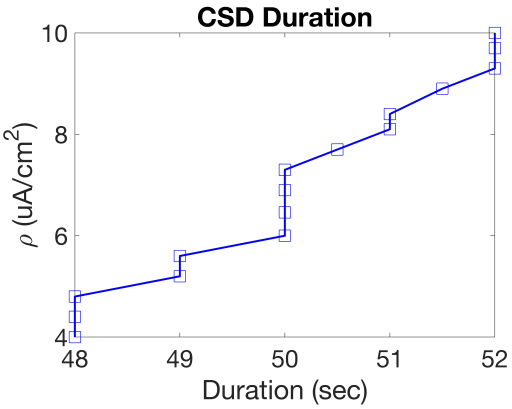

Figure 5.8: Duration (in seconds) of the cortical spreading depression waves when allowing the strength of the sodium potassium pump to variate in the interval $\rho \in [4, 10]$.

In light of the fact that the parameter controlling the strength of the sodium potassium pump had very little effect on the duration of the cortical spreading depression event, in the next simulation we set $\rho = 6.46\mu\text{A/cm}^2$ (as given in Table 5.7), and allowed both λ_1 and λ_{rel} to vary in the intervals: $\lambda_1 \in [0.014, 0.02]$ and $\lambda_{\text{rel}} \in [4.5, 5.1]$. Figure 5.9 captures through the colour maps the CSD duration, expressed in seconds, for each pair $(\lambda_1, \lambda_{\text{rel}})$.

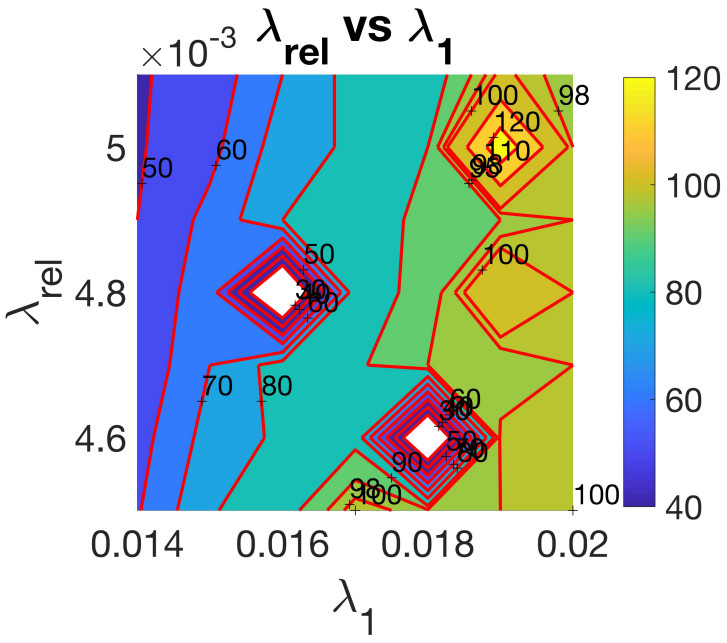

Figure 5.9: Duration of the cortical spreading depression event obtained for each pair $(\lambda_1, \lambda_{\text{rel}})$.

To be in agreement with the literature [81, 134] which place cortical spreading duration between one and three minutes, we chose the values: $\lambda_{\text{rel}} = 5 \cdot 10^{-3}$

mM/msec and $\lambda_1 = 1.6 \cdot 10^{-2}$ mM/msec for which we obtain a duration of approximatively 75 seconds.

5.3.3 Results

In this section we present the results obtained when performing a Matlab simulation of the CSD model described with parameters $\lambda_{\text{rel}} = 5 \cdot 10^{-3}$ mM/msec and $\lambda_1 = 1.6 \cdot 10^{-2}$ mM/msec. We set the final simulation time to $T = 30$ minutes and we used the Matlab built-in solver ode15s as our time integrator. The initial conditions are listed in Table 5.12, where the notation G_v^0 refers to the initial conditions of the vector G_v defined it (5.69), and $O_{6\times1}$ is a vector containing 6 zeroes.

V (mV)	n	h	$[K^+]_i$ (fmol)	$[Cl^-]_i$ (fmol)
71.1	0.07143807	0.9774849	1050	67.5
ΔK_{bath}	ΔK_{glia}	r_{NMDA}	r_{AMPA}	G_v^0
0	0	0	0	$O_{6\times1}$

Table 5.12: **Electrophysiology CSD model:** Initial conditions of membrane potential, ionic concentrations, gating variables and glutamate.

The left upper panel of Figure 5.10 shows the membrane potential, for which we observe the formation of 6.5 CSD events, each characterized by a duration of 75 seconds.

The changes in the ionic concentrations of extracellular and intracellular sodium, potassium and chloride are shown in the two right panels. In agreement with recent literature [81, 135, 89, 93], our results show very large increases in the concentration of extracellular potassium and intracellular sodium, from 4 mM to 90 mM and from 15 mM to 60 mM, while intracellular potassium decreases from 144 mM to 90 mM and extracellular sodium from 140 mM to 30 mM.

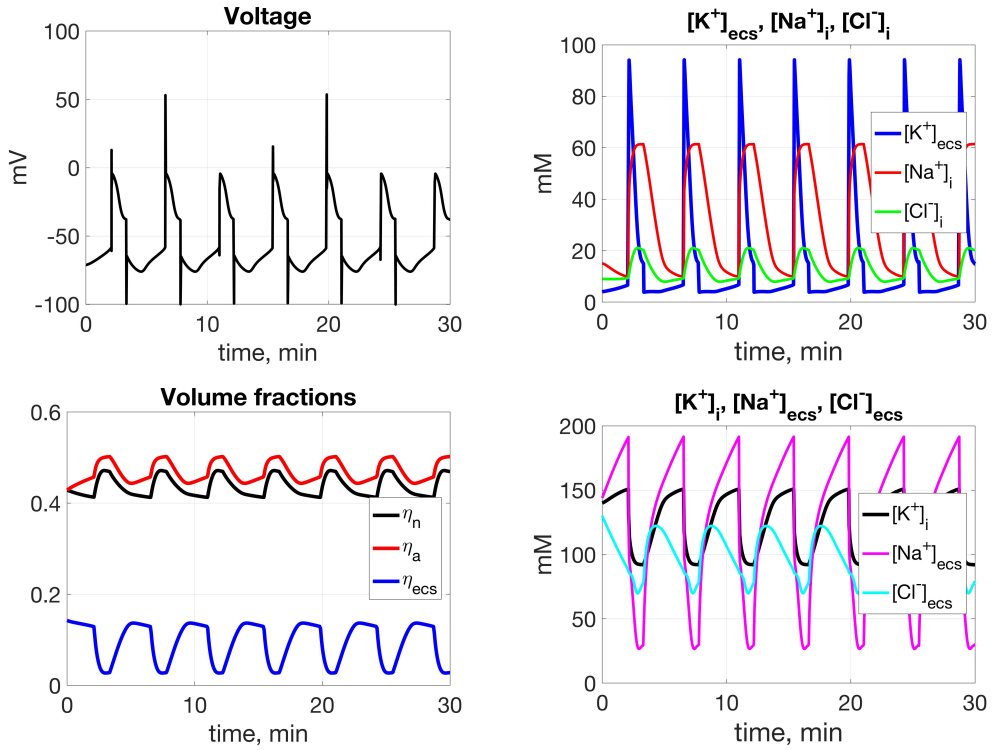

Figure 5.10: Electrophysiologic activity CSD model for $k_{\text{bath}} = 12$ mM, $\lambda_{\text{rel}} = 5 \cdot 10^{-3}$ mM/msec, $\lambda_1 = 1.6 \cdot 10^{-2}$ mM/msec, and $\rho = 6.46 \mu A/cm^2$. First row: Membrane potential (left) and ionic concentrations for extracellular potassium (blue), intracellular sodium (red) and intracellular chloride (green). Bottom row: The left panel shows the changes in the volume fractions corresponding to the three compartments: neuron (black), glia (red) and extracellular space (blue), while on the right hand side we observe the ionic concentrations of intracellular potassium (black), extracellular sodium (magenta) and extracellular chloride (cyan).

The changes in volume fractions are shown in the left bottom panel in Figure 5.10, where η_n, η_a and η_{ecs} are the ratios of the volume of each compartment and the total volume $\omega_{tot} = \omega_i + \omega_g + \omega_{\text{ecs}}$:

$$\eta_n = \frac{\omega_i}{\omega_{\text{tot}}}, \ \eta_a = \frac{\omega_g}{\omega_{\text{tot}}}, \ \eta_{\text{ecs}} = \frac{\omega_{\text{ecs}}}{\omega_{\text{tot}}}, \tag{5.70}$$

The volume of extracellular space presents a very pronounced shrinkage of 77% compared to its baseline value, while the volume of the neuron and the glia show increases of 16%, respectively 14% above baseline values. These results are in agreement with recent findings showing a shrinkage of the extracellular space between 50% to 78% [105, 104, 88, 107].

5.4 Coupled electro-metabolic CSD model

To study CSD, we developed a double-feedback mechanism [136] to couple the electrophysiology and metabolism. The novelty of this model with respect to the one described in Chapter 3 is given by the many additional details included in the electrophysiologic model, specifically tailored to simulate CSD wave.

The first step in the coupling is to insert the metabolic feed-back into the electrophysiologic model, as discussed in Chapter 3 and 4

$$\begin{aligned} J_{\text{pump,Na}^+} &= \frac{p_n}{p_n+\mu}\left(\frac{\rho}{1+\exp(15-[\text{Na}^+]_\text{i})/3)}\right)\times\left(\frac{1}{1+\exp(5.5-[\text{K}^+]_\text{ecs})}\right), \\ J_{\text{glia,K}^+} &= -\frac{p_a}{p_a+\mu}\left[\lambda_\text{rel}-\lambda_1\left(1+\exp\left(\frac{5.5-[\text{K}^+]_\text{ecs}}{2.5}\right)\right)^{-1}\frac{\Delta K^\text{max}_\text{glia}-\Delta K_\text{glia}}{\Delta K^\text{max}_\text{glia}}\right], \end{aligned}$$

where μ is an affinity constant, p_n and p_a are the phosphorylation states in neuron and astrocyte.

We emphasize the dependence of the model describing the electrophysiological activity during CSD on the phosphorylation states p_n and p_a and on the variable volume fractions, by writing it formally as:

$$\frac{du}{dt} = f(u, p_n, p_a, \eta_n, \eta_a, \eta_\text{ecs}), \tag{5.71}$$

where η_n, η_a and η_ecs are the volume fractions of neuron, astrocyte and extracellular space and and u is the vector:

$$u = [V\ n\ h\ [\text{K}^+]_i\ [\text{Cl}^-]_i\ \Delta K_\text{bath}\ \Delta K_\text{glia}\ r_\text{AMPA}\ r_\text{NMDA}\ G_v]^t,$$

The metabolic model described in Chapter 2 is summarized as

$$\frac{d[M]}{dt} = F\left([M], [M]_\text{art}, \psi^n_\text{ATPase}, \psi^a_\text{ATPase}, q, \eta_n, \eta_a, \eta_\text{ecs}\right), \tag{5.72}$$

where $[M]$ denotes the concentration of metabolite M, $[M]_\text{art}$ the arterial concentrations of glucose, lactate and oxygen while q gives the cerebral blood flow. The large energetic demand from electrophysiology during CSD enters in the

metabolic model through the ATPase fluxes ψ_{ATPase}:

$$\psi^n_{\text{ATPase}} = H_n + sI^c_{\text{pump}}, \tag{5.73}$$

$$\psi^a_{\text{ATPase}} = H_a + sI^c_{\text{glia}}, \tag{5.74}$$

where I^c_{pump} and I^c_{glia} are the values of the sodium potassium pump and potassium glial uptake taken from the electrophysiologic model and converted to mM/sec:

$$J^c_{\text{pump,Na}^+} = \frac{\gamma}{\tau\omega_i} J_{\text{pump,Na}^+}, \tag{5.75}$$

$$J^c_{\text{glia,K}^+} = \frac{1}{\tau} J_{\text{glia,Na}^+}. \tag{5.76}$$

To summarize, coupling the electrophysiologic model given by equation (5.71) with the metabolic model described by equation (5.72) results in a system of 43 differential equations. The very different time scales involved in the two models, are addressed using the algorithm developed in Chapter 3.

5.5 Results

In this section we present the results obtained for simulating our coupled electro-metabolic CSD model using the Matlab software for a time interval of 30 minutes while the potassium bath solution k_{bath} is kept constant at 12 mM, the typical threshold inducing CSD waves [88, 94, 81].

In light of recent literature pointing at the important role of astrocytes on regulating the vascular response and clearing the extracellular potassium and glutamate during cortical spreading depression [5, 81], we performed two different numerical experiments: one in which the volume of neuron equals that of astrocyte (protocol A), and another where the volume of astrocyte is twice the one of neuron (protocol B). The values corresponding to the volumes of the two cellular compartments are listed, for both protocols, in Table 5.13.

Another aspect that must be taken into account when writing a model for cortical spreading depression is related to the hemodynamic response. In normoxic brain, at the onset of a cortical spreading depression wave, there is a very large increase in cerebral blood flow, reported to be in the range from 100% [97, 95]

to 130% [83, 80, 82] up to 200% [137] above resting state value. This hyperemic response to the high energetic requirement during cortical spreading depression [81], begins with a delay of 15-20 seconds with respect to the start of the CSD wave, and it can only be sustained for short periods typically in the range of 1 to 2 minutes [82, 81]. The experimental literature reports that, at the end of the hyperemia period, the cerebral blood flow either returns to its baseline value or it displays a mild vasoconstriction of 20-30% of its value [88, 82, 138].

In line with these observations, our computed experiment considers an increase in blood flow of 130% above baseline, lasting 90 seconds, after which the blood flow decreases by 30%. The behavior of the cerebral blood flow during CSD is modeled as a piecewise continuous function given by equation (5.77) and illustrated in Figure 5.11. We denote by t_i the time at which the first CSD wave starts and as indicated in the literature, we consider that the hemodynamic response has a delay of $t_d = 20$ seconds.

$$q(t) = \begin{cases} q_0, & \text{for } t < t_1 \\ q_0\left(1 + 1.3\frac{t-t_1}{t_{r1}}\right), & \text{for } t_1 < t < t_1 + t_{r1} \\ 2.3q_0, & \text{for } t_1 + t_{r1} < t < t_1 + t_{r1} + t_h \\ q_0\left(a \cdot \mathrm{e}^{-\alpha(t-t_1-t_{r1}-t_h)} + b\right), & \text{for } t_1 + t_{r1} + t_h < t < t_1 + t_{r1} + t_h + t_{r_2} \\ 0.7q_0, & \text{for } t > t_1 + t_{r1} + t_h + t_{r2} \end{cases} \tag{5.77}$$

where $t_1 = t_i + t_d$, q_0 is the baseline value of the cerebral blood volume, t_{r1} and t_{r2} are the ramping times during which the blood flow increases, respectively, decreases, t_h is the duration of the hyperemic response and the values $a = 1.628$ and $b = 0.6701$ were chosen such that the function $f(t)$ is continuous. All the parameters regarding blood flow dynamics are listed in Table 5.13.

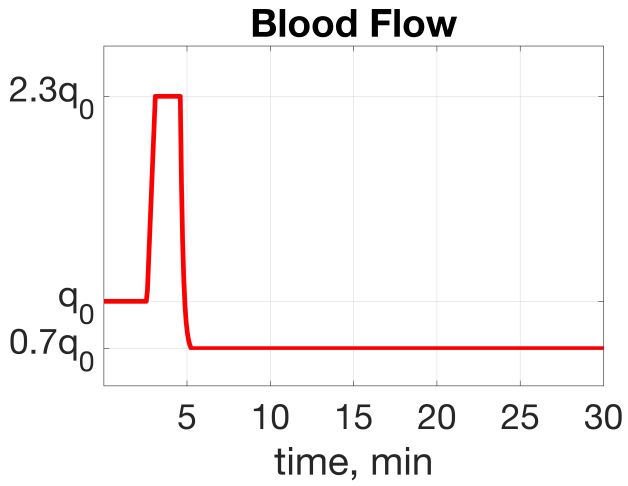

Figure 5.11: **Cerebral Blood Flow Response to Cortical Spreading Depression.** The cerebral blood flow is modeled as a piecewise continuous function starting from the initial value q_0, which increases by 130% for a period of 90 seconds and is followed by a mild 30% decrease below its resting state value.

Electro-metabolic CSD model			**Hemodynamic response**		
Parameter	Value	Units	Parameter	Value	Units
λ	1e-4	1/msec	t_i	126	sec
λ_{rel}	5e-3	mM/msec	t_d	20	sec
G_{glia}	1.6e-2	mM/msec	t_{r1}	30	sec
k_{bath}	12	mM	t_{r2}	40	sec
μ_{pump}	0.1	-	t_h	90	sec
μ_{glia}	0.1	-	α	0.1	-
s	8250	-	q_0	0.4	mL/min
Protocol A					
ω_i^0	7500	μm^3			
ω_g^0	7500	μm^3			
ω_{ecs}^0	2500	μm^3			
Protocol B					
ω_i^0	5000	μm^3			
ω_g^0	10000	μm^3			
ω_{ecs}^0	2500	μm^3			

Table 5.13: Parameters in the coupled electro-metabolic CSD model.

Figure 5.12 shows the time course of the membrane potential, the ionic concentrations of sodium, potassium and chloride in the intracellular and extracellular compartments and the alterations in the volume fractions for the two protocols considered. Under protocol A, the simulation of our double-feedback electro-metabolic CSD model for a time span of 30 minutes produces 6 cortical spreading depression waves: the first one, accompanied by a pronounced hyper-

emic response, has a duration of approximately 85 seconds, while the following waves are significantly larger, lasting about 110 seconds. Under protocol B, during the 30 minutes simulation time, we observe only 3 cortical spreading depression waves, in agreement with the recent literature reporting the propagation of the CSD waves is significantly slower in regions of the brain with a much larger number of astrocytes [119].

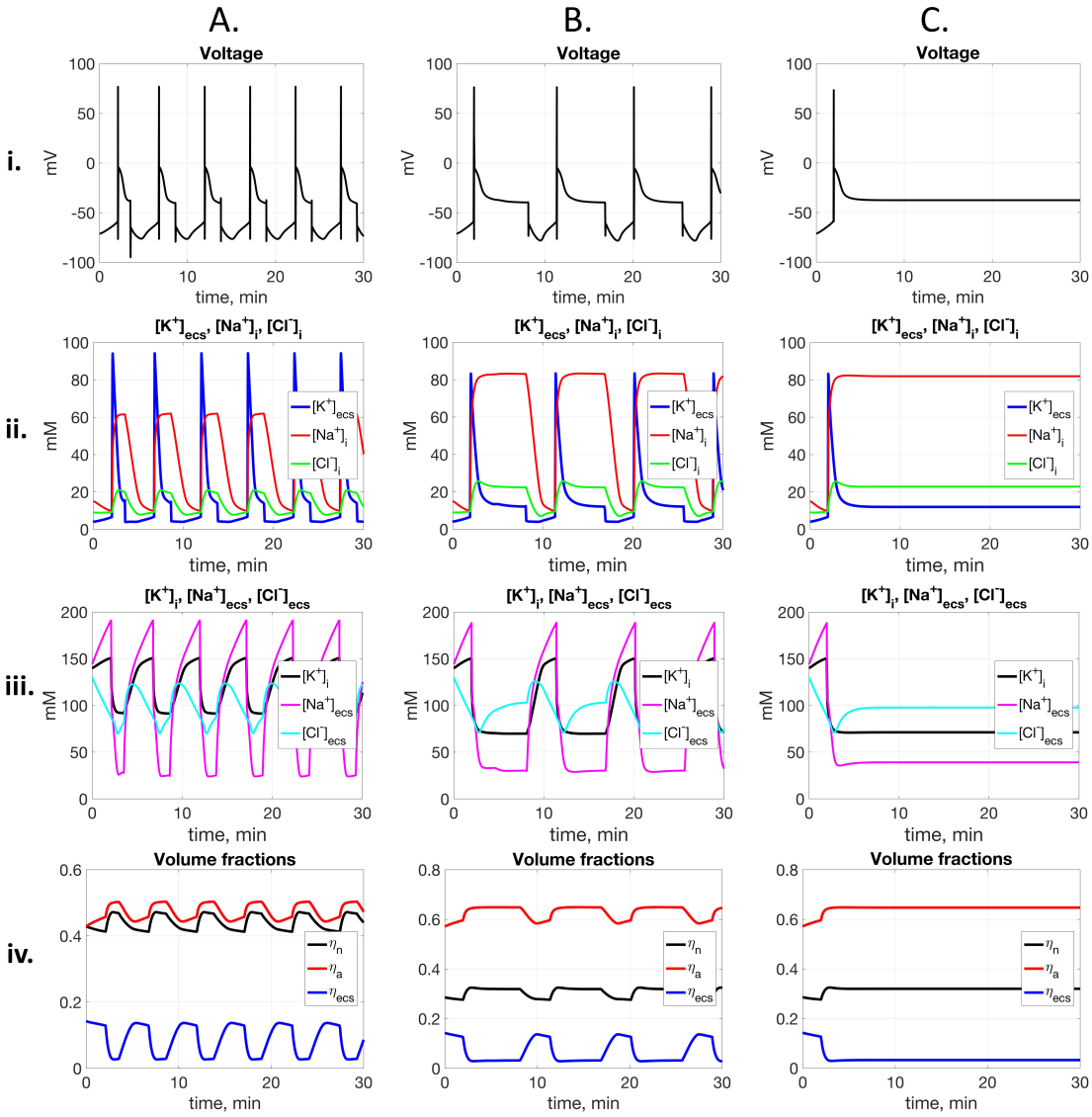

Figure 5.12: **Electrophysiological activity during cortical spreading depression.** The membrane potential (i), the ionic concentrations of intracellular and extracellular sodium, potassium and chloride (ii, iii) and the variation over time in the volume fractions (iv) during SD for the two protocols: the left column A. shows the case for which the volume of the neuron equals the one of the astrocyte (Protocol A), while the middle column B. captures the case in which the astrocytic volume is two times larger than the neuronal one (Protocol B). Column C. shows the results obtained for the uncoupled electrophysiologic model when considering the volumes as defined in Protocol B.

Under both protocols, the ionic concentrations show a large increase in the concentration of extracellular potassium and intracellular sodium and a more modest increase in intracellular chloride. The pivotal role that astrocytes play in clearing the extracellular potassium, is clear when comparing the ionic dynamics during Protocol A and Protocol B; while in Protocol A the extracellular potassium increases up to 93 mM, under Protocol B, the increase is limited to 80 mM, in agreement with recent literature [81, 89, 93].

In Figure 5.12 column C., we present the results obtained when simulating Protocol B, without considering the coupling with the metabolism. We observe how the model produces a single CSD wave and it fails to reproduce consecutive CSDs as in columns A. and B. This simulation confirms that cortical spreading depression waves are the outcome of the complex interaction between electrophysiology, metabolism and hemodynamics.

Figure 5.13 shows the time course of the main metabolites during the passing of the multiple CSD waves. Our results capture the typical metabolic response reported in recent literature [81, 83, 97, 80, 95], showing a significant decay in glucose concentration, accompanied by a massive increase in lactate concentration, a dramatic decrease in oxygen level, indication of the very large energetic need confirmed by the reduced phosphorylation and the redox.

The predictions of our model, which agree with various experimental results [81, 80, 97] show a piecewise steady decay in glucose and oxygen concentration, with each passing wave. In panel A1.i. of Figure 5.13, we note a decay of 58% below baseline for the concentration of glucose in neuron and extracellular space during the first cortical spreading depression, with further decays by another 10% in the second CSD wave. Each subsequent CSD event causes a slight decrease in glucose concentration, which is 30% of its initial value in the sixth CSD wave. The glucose consumption is even greater in the astrocytic compartment, with a decay of 65% below resting state during the first CSD, and a continuous decay up to 89% during the sixth wave.

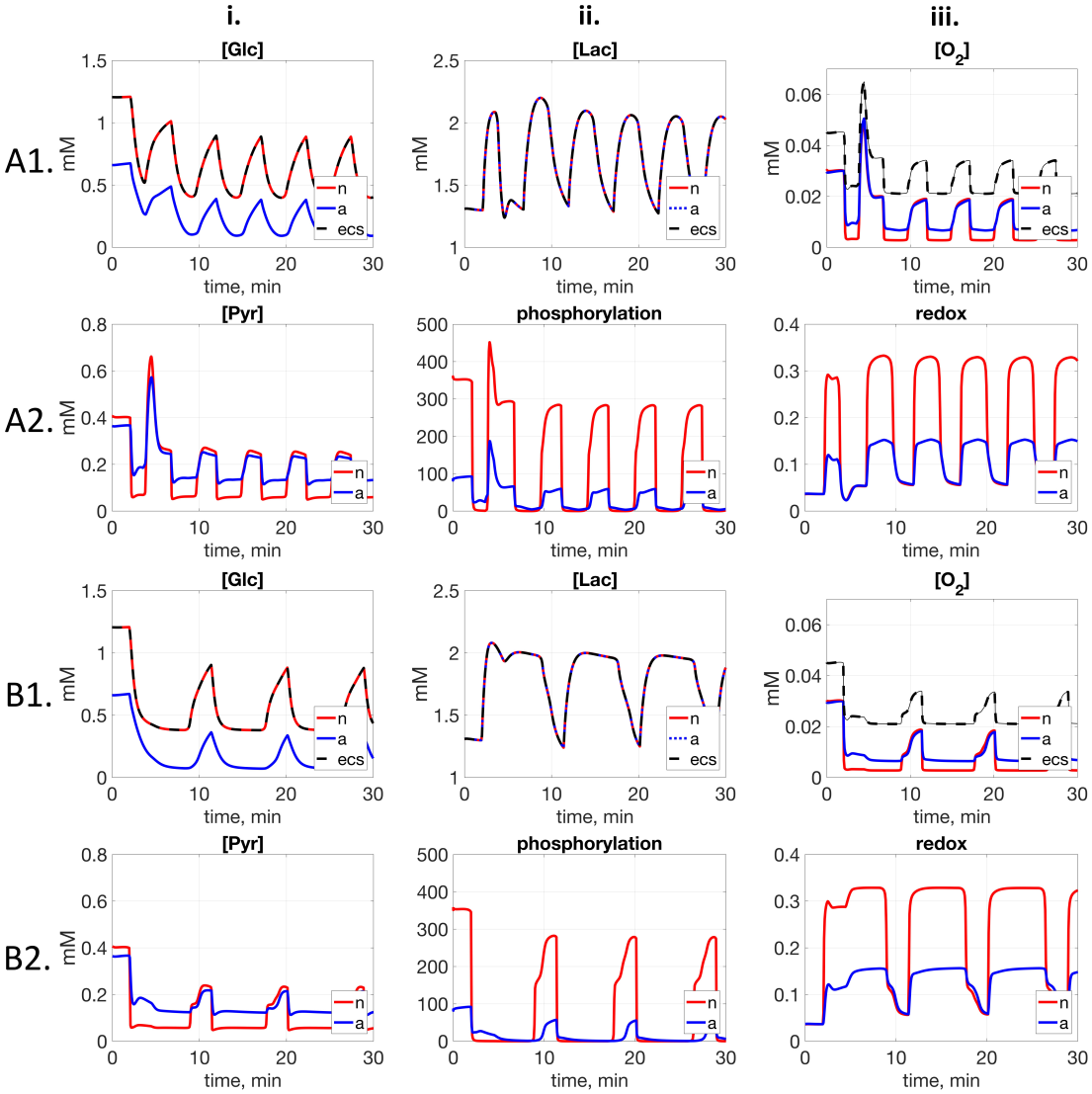

Figure 5.13: **Metabolic response to cortical spreading depression under protocol A (rows A1. and A2.) and protocol B (rows B1. and B2.).** Concentration of glucose, lactate and oxygen in neuron (red), astrocyte (blue) and extracellular space (black). Concentration of pyruvate in neuron (red) and astrocyte (blue), phosphorylation state (A2.ii. and B2.ii.) in neuron (red) and astrocyte (blue) and redox states (A2.iii. and B2.iii.) in neuron (red) and astrocyte (blue).

Our model predicts an initial increase of 65% above baseline for lactate concentration during the first CSD followed by a further rise to up to 70% above resting state value for the following passing waves, in agreement with experimental results placing lactate increase between 63% [97] and 80% [96, 95] above baseline.

The concentration of oxygen in the extracellular space exhibits a 50% decrease during the first CSD wave, after which it increases by 44% above its initial value.

The second CSD episode produces a further drop in extracellular oxygen concentration: 54% decrease with respect to its baseline, which continues to decay slightly with each passing wave. In the astrocyte, the consumption of oxygen is more significant: 69% below baseline in the case of the first CSD wave and drops to 80% below baseline in the second wave. As expected, the predicted oxygen consumption in neuron is even greater: 90% decay during the first wave, reaching a 93% drop for the last observed CSD wave, as described by various authors [81, 94, 88].

As in the case of glucose and oxygen, pyruvate concentration also undergoes a stepwise depletion with each passing CSD wave. At the end of the first wave, pyruvate concentration exhibits an overshoot, tops up at 65% above baseline in neuron and 57% above baseline in astrocyte, after which it drops to 87% of its initial value in neuron and 50% of its initial in astrocyte.

The massive energetic demand during CSD is illustrated in Figure 5.13, panel A2.ii. where we see a 99% depletion in the phosphorylation state in the neuron and a 75% depletion in astrocyte during the passing of the first wave, which becomes more pronounced during the following waves, reaching: 99.5% decay in neuron and 97.5% in astrocyte, both compared to their resting state value. The increased energetic cost can also be observed in the redox states, shown in panel A2.iii., where it increases 10 fold in neuron and 4 fold in astrocyte. Notice that due to the initial hyperemia, the increase in the redox state (see panel A2.iii.) during the first CSD wave is slightly lower than during the following waves.

Figure 5.14 shows the time course of glucose, lactate and oxygen in the blood compartment and the transport fluxes of these three species from blood to extracellular space, and from extracellular space to the two cellular compartments. In the case of the first CSD wave, due to the hyperemic response, we observe an increase above baseline for glucose and oxygen concentrations in blood compartment of 4.5% and 19% respectively. Once the hyperemia ends, for the following CSD waves, the concentrations in blood of glucose and oxygen exhibit a decay of 5%, 16% respectively. For lactate concentration in blood, we observe an initial increase of 23% above baseline during the first CSD and is rising to to 53% above resting state during the following CSD waves, when the vasoconstrictions limits the availability of oxygen during the following CSDs. The transport fluxes indi-

cated in the second and bottom row show an increase to 25% above baseline for oxygen from blood to extracellular space during the first CSD wave and a 14% increase during the following CSDs, while for glucose transport flux from blood to extracellular space we note a 43% increase above baseline. The lactate flux from blood to extracellular space shows an 8 fold decay during the first CSD, which then reduces to a 4 fold drop during the following CSD episodes. In case of oxygen, the transport fluxes from the extracellular space to neuron show an initial 40% increase above resting state for the fist CSD, after which it reaches 29% above baseline during the following CSD waves; for the transport rate of glucose we see a 4 fold increase, while for the flux of lactate between ECS and neuron there is a 3 fold decay during CSD, where we see a shift in direction, suggesting that during CSD waves, unlike during resting state, lactate is transported from neuron to extracellular space. On the other hand, the transport rate of lactate between extracellular space and astrocyte starts at a negative value, it briefly changes direction at the onset of each CSD event, showing a very short 6 fold increase over baseline, after which it drops under 0 for the remainder of each CSD wave.

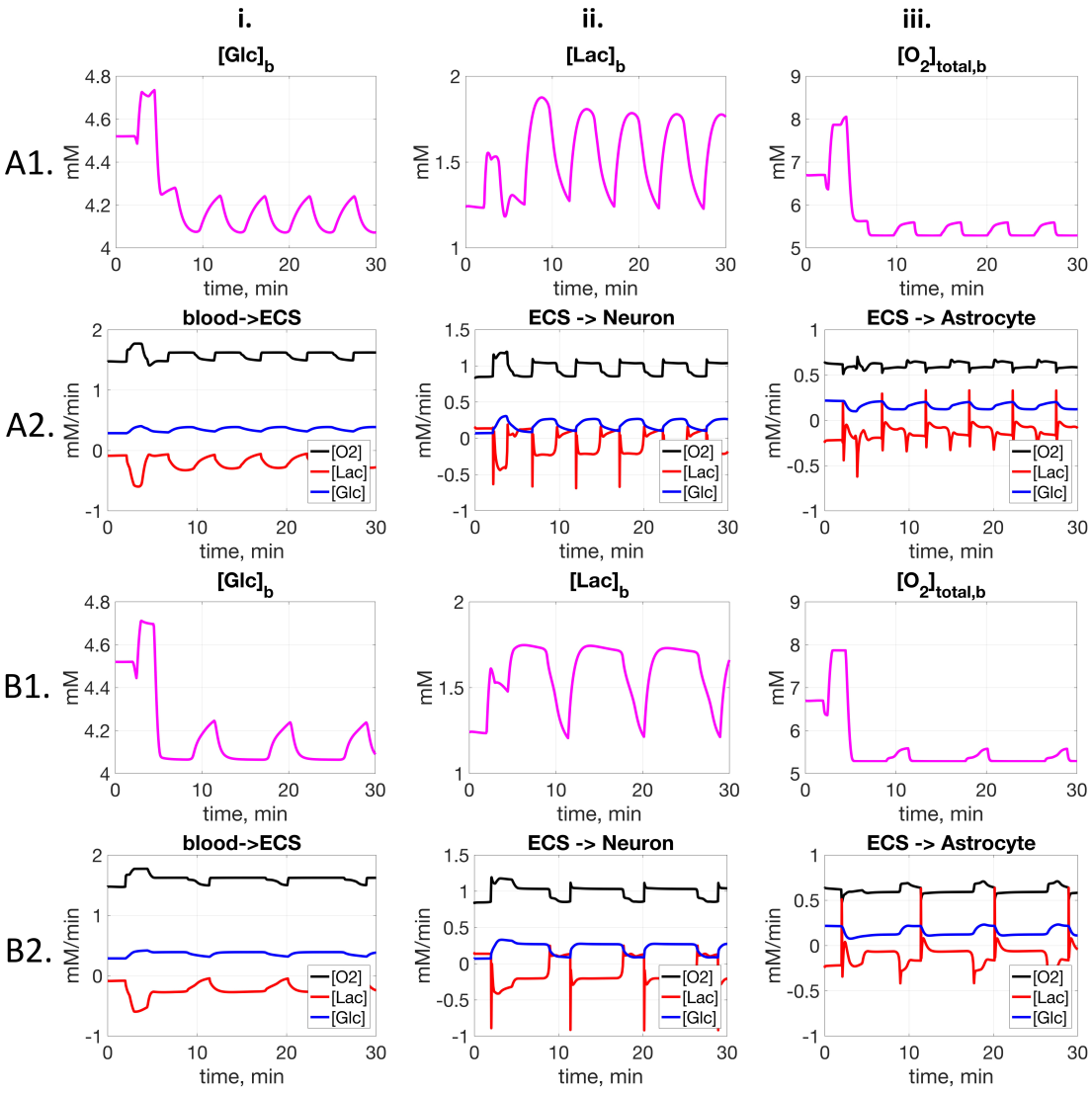

Figure 5.14: **Metabolic response in the blood compartment during the passing of multiple CSD waves.** First two rows (A1. and A2.) correspond to protocol A, for which $\eta_n = \eta_a$, while the following two rows (B1. and B2.) show the results obtained under protocol B, where the glial volume is doubled. Rows A1. and A2. show the concentrations of glucose, lactate and oxygen in the blood compartments, while rows B1. and B2. display the transport fluxes of these three metabolites between blood and extracellular space, extracellular space and neuron, and extracellular space and astrocyte, respectively.

The reaction fluxes predicted by our model are shown in Figure 5.15; we see large increase above resting state values for the glycolysis flux, which rises 7.5 fold during the first CSD and 6.7 fold during the following ones, as well as in the TCA flux, which in neuron shows a 2.4 fold increase and in astrocyte a more modest 25% increase. Similarly, the oxidative phosphorylation flux in the right upper panel presents an increase of 53% during the first wave, is followed by an increase of 39% above baseline value during the next CSD events, while in astrocyte, it

decays to 83% of its resting state. Lactate dehydrogenase flux in neuron changes its direction during the CSD events, showing that lactate is converted to pyruvate at a very large rate, while in astrocyte, the change of direction occurs for a very short period and just at the end each CSD event. Creatine phosphorylation fluxes in neuron and astrocyte increase during CSD and are followed by a large decay at the end of each event. The oxygen glucose index (OGI) starts from a resting state values of 5.15, increases briefly at the onset of each CSD, and is followed by a strong decrease to 4.

The results we obtained under Protocol B are in agreement with recent literature [119], which suggests that the duration of cortical spreading depression waves is enlarged in regions of the brain characterized by a larger number of astrocytes. Our computed experiment under Protocol B shows 3 CSD waves: the first one has a duration of 370 seconds, while the following ones last 330 seconds. The cleaning role of the astrocytes can be visualized in Figure 5.12 where we see a lower increase in the extracellular potassium concentration compared to Protocol A. From the metabolic point of view, due to the higher availability of ATP, the glycolysis and TCA fluxes are slightly lower in Protocol B, as are the LDH1 flux and creatine phosphorylation fluxes in neuron.

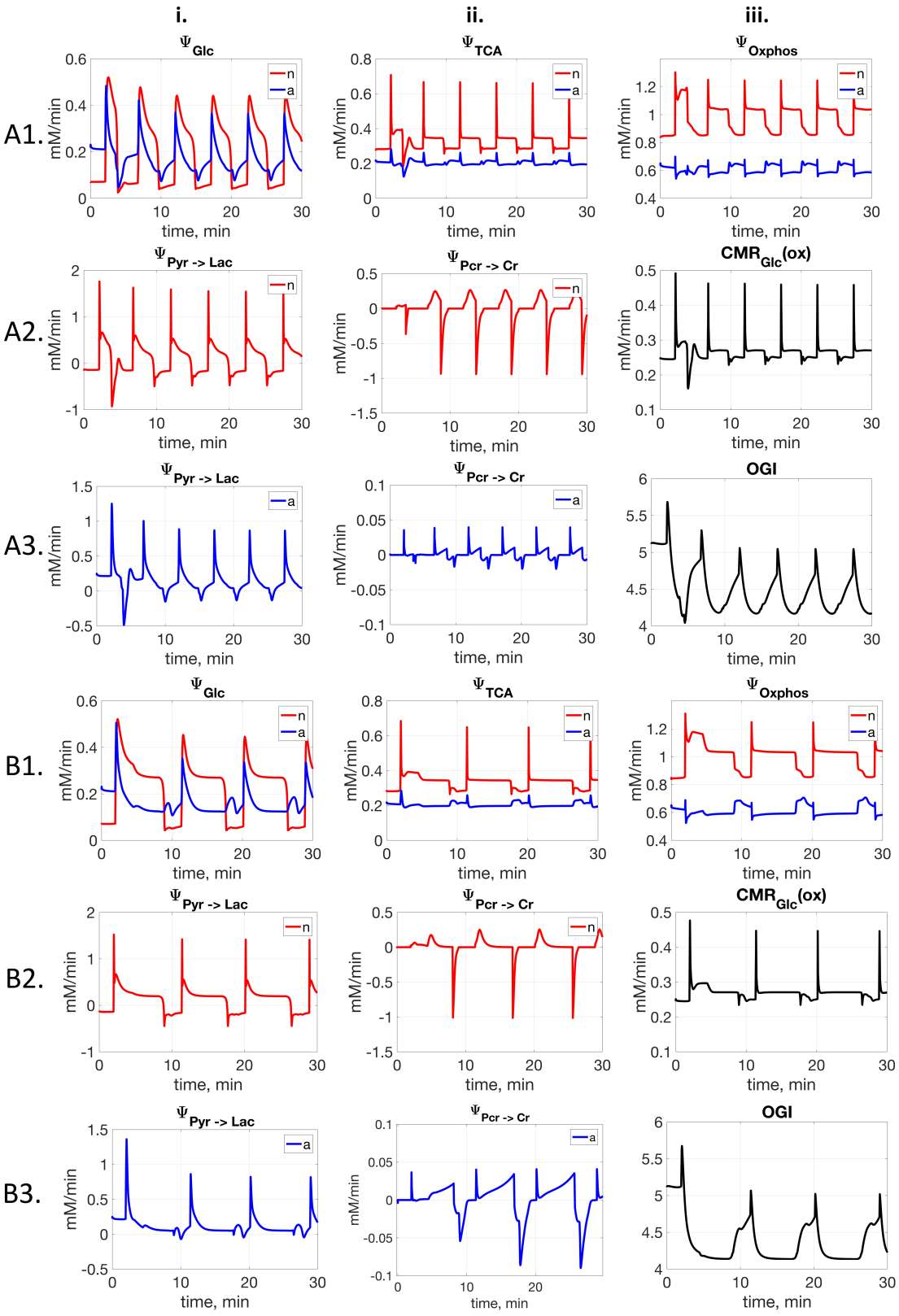

Figure 5.15: **Reaction flux for the electro-metabolic CSD model.** The panels in rows A1., A2. and A3. show the reaction fluxes corresponding to protocol A, while those in rows B1., B2. and B3. display the fluxes under protocol B. Rows A1. and B1. Left to right: glycolysis flux (i), tricarboxylic acid cycle flux (ii) and oxidative phosphorylation (iii). Rows A2. and B2. Left to right: lactate dehydrogenase balance flux for neuron (i), creatine phosphorylation flux for neuron (ii), cerebral metabolic rate of glucose oxidation (iii), Rows A3. and B3. Left to right: lactate dehydrogenase balance flux for astrocyte (i), creatine phosphorylation flux for astrocyte (ii) and oxygen glucose index (iii)

.

Conclusions

This thesis focuses on integrated computational predictive models of brain activity based on the double-feedback between electric and metabolic activity during rest and activation, based on ATP demand and consumption. The first two chapters of this thesis are dedicated to the mathematical models employed for describing the electrophysiological activity and metabolism, while the last three chapters are concerned with developing the mathematical framework and overcoming the multi-scale problems arising from the coupling of the two under different healthy and pathological situations: awake resting state, neuronal activation, ischemia and cortical spreading depression.

Electro-metabolic model

The coupling of the electrophysiologic and metabolic models is addressed in Chapter 3, where we discuss the differences in characteristic time scales: milliseconds for the electrophysiology and minutes for the metabolism; we also propose a mathematical algorithm in order to compute the solutions of the coupled model under different protocols. Our simulations show how the ion homeostasis and metabolism adjust to the transitions between resting state and neuronal activation, ischemia and a combined case of an ischemic event followed by activation.

In the first protocol, awake resting state (8 Hz) is followed by two consecutive neuronal activations corresponding to 90 Hz frequency. The model predictions, in agreement with recent literature [35] show that the membrane potential decreases in amplitude for the periods corresponding to neuronal activations. In addition, our model is able to capture also the slow after-hyperpolarization effect, characterized by the short neuronal silencing at the end of each neuronal activation, before recovering to the awake resting state and increases in the concentrations of extracellular potassium and intracellular sodium.

The metabolic response shows up in the model predictions as a significant consumption of glucose and oxygen, accompanied by a large production of lac-

tate. Moreover, due to the large energetic cost demanded by sustaining neuronal firing at a high frequency, there is a large decrease in the phosphorylation states and an increase in redox states. We remark that the phosphorylation state in astrocyte, whose decrease is not as significant as the one in the neuron, requires a much larger period to recover once the activation had stopped. This supports the hypothesis that it is the astrocyte task to clear the potassium from the extracellular space, present in large concentrations following activation, even after the sodium potassium pump has sufficient ATP to retake its normal function.

The second protocol simulates an ischemic event of 1 minute and 30 seconds, during which the blood flow is decreased by 90%. Due to the diminished supply of oxygen, we observe a more pronounced increase in lactate and larger decreases in glucose and phosphorylation states, than in the case of the neuronal activation. The inability of the metabolic system to produce enough ATP leads to the cessation of neuronal firing and to rises in the concentrations of intracellular sodium and extracellular potassium.

Hemo-Electro-Metabolic model

The fourth chapter focuses on the blood flow response during neuronal activation and the coupling of hemodynamic and Electro-Metabolic model. Here, the cerebral blood flow and cerebral blood volume are tracked in three compartments: arteries, capillaries and veins.

In our coupled Hemo-Electro-Metabolic model, the extracellular potassium concentration defines the vasodilatory stimulus which is inputed in the blood flow model. The predictions of our computed experiment agree with the experimental literature [78]; at the start of the neuronal activation we observe an initial increase of the cerebral blood flow up to 77% above its resting state, after which the blood flow stabilizes at around 26% above resting state. The initial spike in the blood flow coincides with an initial spike in the concentration of extracellular potassium: at the end of each neuronal activation, our model predicts a slow after-hyperpolarization effect of 16 seconds, which coincides with the period that the extracellular potassium concentration drops under its baseline value.

As in Chapter 3, the metabolic response to the neuronal activation is given by a large consumption of glucose and oxygen and massive production of lactate, with a significant decrease in the phosphorylation state and increase in redox state. The predictions of our model result in an oxygen glucose index of approximately 5.15 during awake resting state and around 4.2 during stimulation, in agreement with values suggested in the literature [51, 53].

CSD Electro-metabolic model

In the fifth chapter we propose a new Electro-Metabolic double feedback model for studying cortical spreading depression waves (CSDs). The electrophysiologic model employed for simulating CSD is much more complex than the one used in the previous chapters, as it tracks the concentrations of sodium, potassium and chloride in neuron, glia and extracellular space, comprises glutamate dynamics and it accounts for the changes in the volumes of the three compartments during the passing of the CSD waves [23]. The coupled Electro-Metabolic CSD model is based on ATP demand and consumption and assumes variable volume fractions. In agreement with the literature [104, 105, 106, 81, 107], the predictions of our computed experiment show a shrinkage of the extracellular space which decreases by approximately 77% from its baseline value, and swelling of the neuron and glia of approximately 16%, respectively 14% above resting state values.

As reported in the experimental literature [81, 89, 93], the predicted ionic concentrations of extracellular potassium and intracellular sodium show very large increases, while the concentrations of intracellular potassium and extracellular sodium present a significant decrease. Restoring the ionic gradients requires a very large amount of energy, which can be observed in our results in the massive consumption of the phosphorylation states and the large production of redox. The results obtained with our computed experiment outline the typical metabolic signature observed during CSD [81, 83, 97, 80, 95]: significant decays in glucose and oxygen concentrations, extreme increase in the concentration of lactate accompanied by a decrease in pyruvate concentration.

It was recently noted in the literature that the regions of the brain characterized by a larger number of astrocytes are less susceptible to CSD [81, 5, 125, 124, 106]. To test how the predictions of our model would change with an uneven ratio of neuron and astrocyte volume fractions, we performed a second computed experiment with double volume fraction for astrocyte than for neuron. Our results suggest that the speed of the cortical spreading depression waves decreases when passing brain regions with larger number of astrocytes [119]. Moreover, the number of cortical spreading depression waves observed during a 30 minutes simulation time decreases from 6 to 3. This supports the astrocytes crucial role in clearing the extracellular potassium and glutamate, present in large amount following CSD [5, 118], and in mediating the cerebral blood flow response [5, 1, 122].

Next steps

The modeling paradigm for this thesis only considered lumped models: a natural extension of our coupled Electro-Metabolic model would be adding a spatial component. The spatial variability would be particularly important when sim-

ulating cortical spreading depression waves, that travel across the cortex at a speed of a couple of millimeters per minute and can encounter barriers, for example white matter or large cerebral arteries [81]. As already discussed in Chapter 5, the propagation of the CSD waves is significantly slowed down in regions with larger astrocyte density. As the extensive experimental literature suggests [124, 123, 125], the susceptibility to CSD varies greatly between different brain regions and in some, CSD can not be triggered [124]. Understanding these aspects is of utmost importance and could guide prevention strategies, especially for patients with traumatic brain injury, in which CSD waves were proven to either provoke additional brain damage or severely slow down the recovery process.

Developing a spatially distributed Electro-Metabolic CSD model would allow us to better understand the CSD propagation by observing all the electrophysiologic and metabolic variations, depending on the onset region of the CSD waves and on the density of astrocytes. The first step towards a distributed Electro-Metabolic model is to consider a model for the diffusion of bath potassium to the neighboring cells [139]. From the mathematical point of view, the complexity of the distributed model increases substantially, as it involves using either finite differences or finite elements for our current multi-time scale problem.

In summary, developing a spatially distributed coupled Electro-Metabolic model would be very beneficial for the mechanisms underlying CSD propagation and its characteristic alterations in the ionic and metabolites concentrations.

Main Achievements

Publications

- Calvetti D, **Capo Rangel G**, Gerardo-Giorda L, Somersalo E. A computational model integrating brain electrophysiology and metabolism highlights the key role of extracellular potassium and oxygen. J Theor Biol 2018; 446: 238-258.
- **Capo Rangel G**, Prezioso J, Gerardo-Giorda L, Somersalo E and Calvetti D. Brain energetics plays a key role in the coordination of electrophysiology, metabolism and hemodynamics: evidence from an integrated computational model, Submitted 2018.
- **Capo Rangel G**, Gerardo-Giorda L, Somersalo E and Calvetti D. Metabolism plays a central role in the cortical spreading depression: evidence from a mathematical model, In Preparation 2019.

Conferences and Workshops

I presented this work at the following national and international conferences and workshops:

a. SIAM Conference on the Life Sciences, 14 July 2016, presentation included in the minisymposium "State of the Art Computational Methodologies for Mathematical Models of Human Brain, Electrophysiology, Hemodynamics and Metabolism", Boston, United States of America

b. Congreso de Jóvenes Investigadores de Ia Real Sociedad Matemática Española, 4 September 2017 - presentation (in spanish) entitled "Multiscale coupling of Electrophysiology and Metabolism in the Neuron-Astrocyte complex", Valencia, Spain.

c. The 11th European Conference on Mathematical and Theoretical Biology, 26 July 2018 - presentation entitled "A computational model integrating brain electrophysiology and metabolism", Lisbon, Portugal.

d. Second International Workshop on Neurodynamics, 26 September 2018, presentation entitled "A computational model integrating brain electrophysiology, metabolism and hemodynamics", Castro Urdiales, Spain.

Short visits

- 17 September - 16 December 2015: Case Western Reserve University, Cleveland, US. Supervisor: Prof. Dr. Daniela Calvetti.
- 15 November - 08 December 2017: Case Western Reserve University, Cleveland, US. Supervisor: Prof. Dr. Daniela Calvetti.
- 17 October - 14 November 2018: Case Western Reserve University, Cleveland, US. Supervisor: Prof. Dr. Daniela Calvetti.

List of Figures

List of Tables

Bibliography

[1] David Attwell, Alastair M Buchan, Serge Charpak, Martin Lauritzen, Brian A MacVicar, and Eric A Newman. Glial and neuronal control of brain blood flow. *Nature*, 468(7321):232, 2010.

[2] Clare Howarth, Padraig Gleeson, and David Attwell. Updated energy budgets for neural computation in the neocortex and cerebellum. *Journal of Cerebral Blood Flow & Metabolism*, 32(7):1222–1232, 2012.

[3] Maiken Nedergaard, Bruce Ransom, and Steven A Goldman. New roles for astrocytes: redefining the functional architecture of the brain. *Trends in neurosciences*, 26(10):523–530, 2003.

[4] Ross Nortley and David Attwell. Control of brain energy supply by astrocytes. *Current opinion in neurobiology*, 47:80–85, 2017.

[5] Jessica L Seidel, Carole Escartin, Cenk Ayata, Gilles Bonvento, and C William Shuttleworth. Multifaceted roles for astrocytes in spreading depolarization: A target for limiting spreading depolarization in acute brain injury? *Glia*, 64(1):5–20, 2016.

[6] Caterina Scuderi, Claudia Stecca, Aniello Iacomino, and Luca Steardo. Role of astrocytes in major neurological disorders: the evidence and implications. *IUBMB life*, 65(12):957–961, 2013.

[7] Andrea Volterra and Jacopo Meldolesi. Astrocytes, from brain glue to communication elements: the revolution continues. *Nature Reviews Neuroscience*, 6(8):626, 2005.

[8] Agnès Aubert, Robert Costalat, and Romain Valabrègue. Modelling of the coupling between brain electrical activity and metabolism. *Acta biotheoretica*, 49(4):301–326, 2001.

[9] Mathieu Cloutier, Fiachra B Bolger, John P Lowry, and Peter Wellstead. An integrative dynamic model of brain energy metabolism using in vivo neurochemical measurements. *Journal of computational neuroscience*, 27(3):391, 2009.

[10] Renaud Jolivet, Jay S Coggan, Igor Allaman, and Pierre J Magistretti. Multi-timescale modeling of activity-dependent metabolic coupling in the neuron-glia-vasculature ensemble. *PLoS computational biology*, 11(2):e1004036, 2015.

[11] Yina Wei, Ghanim Ullah, and Steven J Schiff. Unification of neuronal spikes, seizures, and spreading depression. *Journal of Neuroscience*, 34(35):11733–11743, 2014.

[12] John R Cressman, Ghanim Ullah, Jokubas Ziburkus, Steven J Schiff, and Ernest Barreto. The influence of sodium and potassium dynamics on excitability, seizures, and the stability of persistent states: I. single neuron dynamics. *Journal of computational neuroscience*, 26(2):159–170, 2009.

[13] Ernest Barreto and John R Cressman. Ion concentration dynamics as a mechanism for neuronal bursting. *Journal of biological physics*, 37(3):361–373, 2011.

[14] Brian Roland Larsen, Anca Stoica, and Nanna MacAulay. Managing brain extracellular k+ during neuronal activity: the physiological role of the na+/k+-atpase subunit isoforms. *Frontiers in physiology*, 7:141, 2016.

[15] Richard B Buxton, Eric C Wong, and Lawrence R Frank. Dynamics of blood flow and oxygenation changes during brain activation: the balloon model. *Magnetic resonance in medicine*, 39(6):855–864, 1998.

[16] Richard B Buxton, Lawrence R Frank, and Eric C Wong. Bold signal dynamics: the balloon model with viscoelastic effects. *International Society for Magnetic Resonance in Medicine*.

[17] Richard B Buxton, Kâmil Uludağ, David J Dubowitz, and Thomas T Liu. Modeling the hemodynamic response to brain activation. *Neuroimage*, 23:S220–S233, 2004.

[18] Matthew JP Barrett, Merryn H Tawhai, and Vinod Suresh. Arteries dominate volume changes during brief functional hyperemia: evidence from mathematical modelling. *Neuroimage*, 62(1):482–492, 2012.

[19] Daniela Calvetti, Jamie Prezioso, and Erkki Somersalo. Estimating hemodynamic stimulus and blood vessel compliance from cerebral blood flow data. *Journal of theoretical biology*, 460:243–261, 2019.

[20] Jamie Prezioso. *An Inverse Problem of Cerebral Hemodynamics in the Bayesian Framework*. PhD thesis, Case Western Reserve University, 2017.

[21] Gemma Huguet, Anoushka Joglekar, Leopold Matamba Messi, Richard Buckalew, Sarah Wong, and David Terman. Neuroprotective role of gap junctions in a neuron astrocyte network model. *Biophysical journal*, 111(2):452–462, 2016.

[22] Niklas Hübel and Markus A Dahlem. Dynamics from seconds to hours in hodgkin-huxley model with time-dependent ion concentrations and buffer reservoirs. *PLoS computational biology*, 10(12):e1003941, 2014.

[23] Niklas Hübel, Mahshid S Hosseini-Zare, Jokūbas Žiburkus, and Ghanim Ullah. The role of glutamate in neuronal ion homeostasis: A case study of spreading depolarization. *PLoS computational biology*, 13(10):e1005804, 2017.

[24] Stephen H Koslow and Shankar Subramaniam. *Databasing the brain: from data to knowledge (neuroinformatics)*. Hoboken, N.J.; [Great Britain]: Wiley-Liss, 2005.

[25] Alan L Hodgkin. Evidence for electrical transmission in nerve. *The Journal of physiology*, 90(2):183–210, 1937.

[26] Alan L Hodgkin and Andrew F Huxley. Action potentials recorded from inside a nerve fibre. *Nature*, 144(3651):710, 1939.

[27] Alan L Hodgkin and Andrew F Huxley. Resting and action potentials in single nerve fibres. *The Journal of physiology*, 104(2):176–195, 1945.

[28] Eugene M Izhikevich. *Dynamical systems in neuroscience*. MIT press, 2007.

[29] Richard FitzHugh. Impulses and physiological states in theoretical models of nerve membrane. *Biophysical journal*, 1(6):445–466, 1961.

[30] Jorge Duarte, Cristina Januário, and Nuno Martins. On the analytical solutions of the hindmarsh–rose neuronal model. *Nonlinear Dynamics*, 82(3):1221–1231, 2015.

[31] Giacomo Innocenti, Alice Morelli, Roberto Genesio, and Alessandro Torcini. Dynamical phases of the hindmarsh-rose neuronal model: Studies

of the transition from bursting to spiking chaos. *Chaos: An Interdisciplinary Journal of Nonlinear Science*, 17(4):043128, 2007.

[32] Roxana A Stefanescu and Viktor K Jirsa. A low dimensional description of globally coupled heterogeneous neural networks of excitatory and inhibitory neurons. *PLoS computational biology*, 4(11):e1000219, 2008.

[33] Andrey Shilnikov and Marina Kolomiets. Methods of the qualitative theory for the hindmarsh–rose model: A case study–a tutorial. *International Journal of Bifurcation and chaos*, 18(08):2141–2168, 2008.

[34] Eugene M Izhikevich. Hybrid spiking models. *Philosophical Transactions of the Royal Society of London A: Mathematical, Physical and Engineering Sciences*, 368(1930):5061–5070, 2010.

[35] Brett C Carter and Bruce P Bean. Sodium entry during action potentials of mammalian neurons: incomplete inactivation and reduced metabolic efficiency in fast-spiking neurons. *Neuron*, 64(6):898–909, 2009.

[36] Gerson Florence, Tiago Pereira, and Jürgen Kurths. Extracellular potassium dynamics in the hyperexcitable state of the neuronal ictal activity. *Communications in Nonlinear Science and Numerical Simulation*, 17(12):4700–4706, 2012.

[37] Erkki Somersalo, Yougan Cheng, and Daniela Calvetti. The metabolism of neurons and astrocytes through mathematical models. *Annals of biomedical engineering*, 40(11):2328–2344, 2012.

[38] Agnes Aubert and Robert Costalat. A model of the coupling between brain electrical activity, metabolism, and hemodynamics: application to the interpretation of functional neuroimaging. *Neuroimage*, 17(3):1162–1181, 2002.

[39] Sachin K Gujar, Sharad Maheshwari, Isabella Björkman-Burtscher, and Pia C Sundgren. Magnetic resonance spectroscopy. *Journal of neuro-ophthalmology*, 25(3):217–226, 2005.

[40] Agnes Aubert and Robert Costalat. Interaction between astrocytes and neurons studied using a mathematical model of compartmentalized energy metabolism. *Journal of Cerebral Blood Flow & Metabolism*, 25(11):1476–1490, 2005.

[41] Daniela Calvetti, Yougan Cheng, and Erkki Somersalo. A spatially distributed computational model of brain cellular metabolism. *Journal of theoretical biology*, 376:48–65, 2015.

[42] Daniela Calvetti, Yougan Cheng, and Erkki Somersalo. Uncertainty quantification in flux balance analysis of spatially lumped and distributed models of neuron–astrocyte metabolism. *Journal of mathematical biology*, 73(6-7):1823–1849, 2016.

[43] Daniela Calvetti, Gabriela Capo Rangel, Luca Gerardo Giorda, and Erkki Somersalo. A computational model integrating brain electrophysiology and metabolism highlights the key role of extracellular potassium and oxygen. *Journal of theoretical biology*, 446:238–258, 2018.

[44] James P Keener and James Sneyd. *Mathematical physiology*, volume 1. Springer, 1998.

[45] David Attwell and Simon B Laughlin. An energy budget for signaling in the grey matter of the brain. *Journal of Cerebral Blood Flow & Metabolism*, 21(10):1133–1145, 2001.

[46] Francesco A Massucci, Mauro DiNuzzo, Federico Giove, Bruno Maraviglia, Isaac Perez Castillo, Enzo Marinari, and Andrea De Martino. Energy metabolism and glutamate-glutamine cycle in the brain: a stoichiometric modeling perspective. *BMC systems biology*, 7(1):103, 2013.

[47] Robert G Shulman, Fahmeed Hyder, and Douglas L Rothman. Lactate efflux and the neuroenergetic basis of brain function. *NMR in Biomedicine: An International Journal Devoted to the Development and Application of Magnetic Resonance In Vivo*, 14(7-8):389–396, 2001.

[48] Fahmeed Hyder, Robert K Fulbright, Robert G Shulman, and Douglas L Rothman. Glutamatergic function in the resting awake human brain is supported by uniformly high oxidative energy. *Journal of Cerebral Blood Flow & Metabolism*, 33(3):339–347, 2013.

[49] Christina P Brötzner, Wolfgang Klimesch, Michael Doppelmayr, Andrea Zauner, and Hubert H Kerschbaum. Resting state alpha frequency is associated with menstrual cycle phase, estradiol and use of oral contraceptives. *Brain research*, 1577:36–44, 2014.

[50] Robin I Goldman, John M Stern, Jerome Engel Jr, and Mark S Cohen. Simultaneous eeg and fmri of the alpha rhythm. *Neuroreport*, 13(18):2487, 2002.

[51] Abel Lajtha, Guido Tettamanti, and Gianfresco Goracci. *Handbook of neurochemistry and molecular neurobiology.* Springer, 2009.

[52] Robert G Shulman, Fahmeed Hyder, and Douglas L Rothman. Insights from neuroenergetics into the interpretation of functional neuroimaging: an alternative empirical model for studying the brain's support of behavior. *Journal of Cerebral Blood Flow & Metabolism*, 34(11):1721–1735, 2014.

[53] Peter L Madsen, Rasmus Linde, Steen G Hasselbalch, Olaf B Paulson, and Niels A Lassen. Activation-induced resetting of cerebral oxygen and glucose uptake in the rat. *Journal of Cerebral Blood Flow & Metabolism*, 18(7):742–748, 1998.

[54] Nikos K Logothetis, Jon Pauls, Mark Augath, Torsten Trinath, and Axel Oeltermann. Neurophysiological investigation of the basis of the fmri signal. *Nature*, 412(6843):150, 2001.

[55] Leif Hertz, Liang Peng, and Gerald A Dienel. Energy metabolism in astrocytes: high rate of oxidative metabolism and spatiotemporal dependence on glycolysis/glycogenolysis. *Journal of Cerebral Blood Flow & Metabolism*, 27(2):219–249, 2007.

[56] Britta Göbel, Kerstin M Oltmanns, and Matthias Chung. Linking neuronal brain activity to the glucose metabolism. *Theoretical Biology and Medical Modelling*, 10(1):50, 2013.

[57] Ian A Silver and Maria Erecinska. Extracellular glucose concentration in mammalian brain: continuous monitoring of changes during increased neuronal activity and upon limitation in oxygen supply in normo-, hypo-, and hyperglycemic animals. *Journal of Neuroscience*, 14(8):5068–5076, 1994.

[58] Allan T Gulledge, Sameera Dasari, Keita Onoue, Emily K Stephens, J Michael Hasse, and Daniel Avesar. A sodium-pump-mediated afterhyperpolarization in pyramidal neurons. *Journal of Neuroscience*, 33(32):13025–13041, 2013.

[59] Brian King, Arsalan P Rizwan, Hadhimulya Asmara, Norman C Heath, Jordan DT Engbers, Steven Dykstra, Theodore M Bartoletti, Shahid Hameed, Gerald W Zamponi, and Ray W Turner. Ikca channels are a critical determinant of the slow ahp in ca1 pyramidal neurons. *Cell reports*, 11(2):175–182, 2015.

[60] Mala M Shah and Dennis G Haylett. Ca2+ channels involved in the generation of the slow afterhyperpolarization in cultured rat hippocampal pyramidal neurons. *Journal of neurophysiology*, 83(5):2554–2561, 2000.

[61] Ray W Turner, Hadhimulya Asmara, Jordan DT Engbers, Jason Miclat, Arsalan P Rizwan, Giriraj Sahu, and Gerald W Zamponi. Assessing the role of ikca channels in generating the sahp of ca1 hippocampal pyramidal cells. *Channels*, 10(4):313–319, 2016.

[62] Gunnar Krüger, Andreas Kleinschmidt, and Jens Frahm. Dynamic mri sensitized to cerebral blood oxygenation and flow during sustained activation of human visual cortex. *Magnetic resonance in medicine*, 35(6):797–800, 1996.

[63] Richard B Buxton. The physics of functional magnetic resonance imaging (fmri). *Reports on Progress in Physics*, 76(9):096601, 2013.

[64] Seiji Ogawa, David W Tank, Ravi Menon, Jutta M Ellermann, Seong G Kim, Helmut Merkle, and Kamil Ugurbil. Intrinsic signal changes accompanying sensory stimulation: functional brain mapping with magnetic resonance imaging. *Proceedings of the National Academy of Sciences*, 89(13):5951–5955, 1992.

[65] Patrick J Drew, Andy Y Shih, and David Kleinfeld. Fluctuating and sensory-induced vasodynamics in rodent cortex extend arteriole capacity. *Proceedings of the National Academy of Sciences*, 108(20):8473–8478, 2011.

[66] Jean J Chen and Bruce G Pike. Mri measurement of the bold-specific flow–volume relationship during hypercapnia and hypocapnia in humans. *Neuroimage*, 53(2):383–391, 2010.

[67] Gary H Glover. Overview of functional magnetic resonance imaging. *Neurosurgery Clinics*, 22(2):133–139, 2011.

[68] Seiji Ogawa, Tso-Ming Lee, Alan R Kay, and David W Tank. Brain magnetic resonance imaging with contrast dependent on blood oxygenation. *Proceedings of the National Academy of Sciences*, 87(24):9868–9872, 1990.

[69] Jean J Chen and Bruce G Pike. Bold-specific cerebral blood volume and blood flow changes during neuronal activation in humans. *NMR in Biomedicine: An International Journal Devoted to the Development and Application of Magnetic Resonance In vivo*, 22(10):1054–1062, 2009.

[70] Elizabeth MC Hillman, Anna Devor, Matthew B Bouchard, Andrew K Dunn, GW Krauss, Jesse Skoch, Brian J Bacskai, Anders M Dale, and David A Boas. Depth-resolved optical imaging and microscopy of vascular compartment dynamics during somatosensory stimulation. *Neuroimage*, 35(1):89–104, 2007.

[71] Kazuto Masamoto and Iwao Kanno. Anesthesia and the quantitative evaluation of neurovascular coupling. *Journal of Cerebral Blood Flow & Metabolism*, 32(7):1233–1247, 2012.

[72] Ina K Schmalbruch, Rasmus Linde, Olaf B Paulson, and Peter L Madsen. Activation-induced resetting of cerebral metabolism and flow is abolished by β-adrenergic blockade with propranolol. *Stroke*, 33(1):251–255, 2002.

[73] Mark A Mintun, Brian N Lundstrom, Abraham Z Snyder, Andrei G Vlassenko, Gordon L Shulman, and Marcus E Raichle. Blood flow and oxygen delivery to human brain during functional activity: theoretical modeling and experimental data. *Proceedings of the National Academy of Sciences*, 98(12):6859–6864, 2001.

[74] Romain Valabrègue, Agnès Aubert, Jacques Burger, Jacques Bittoun, and Robert Costalat. Relation between cerebral blood flow and metabolism explained by a model of oxygen exchange. *Journal of Cerebral Blood Flow & Metabolism*, 23(5):536–545, 2003.

[75] Takayuki Obata, Thomas T Liu, Karla L Miller, Wen-Ming Luh, Eric C Wong, Lawrence R Frank, and Richard B Buxton. Discrepancies between bold and flow dynamics in primary and supplementary motor areas: application of the balloon model to the interpretation of bold transients. *NeuroImage*, 21(1):144–153, 2004.

[76] Gabriela Capo Rangel, Jamie Prezioso, Luca Gerardo-Giorda, Erkki Somersalo, and Daniela Calvetti. Brain energetics plays a key role in the coordination of electrophysiological activity, metabolism and hemodynamics: evidence from an integrated computational model. *submitted*.

[77] Jessica A Filosa, Adrian D Bonev, Stephen V Straub, Andrea L Meredith, M Keith Wilkerson, Richard W Aldrich, and Mark T Nelson. Local potassium signaling couples neuronal activity to vasodilation in the brain. *Nature neuroscience*, 9(11):1397, 2006.

[78] Pamela Moses, Mishaela DiNino, Leanna Hernandez, and Thomas T Liu. Developmental changes in resting and functional cerebral blood flow and their relationship to the bold response. *Human brain mapping*, 35(7):3188–3198, 2014.

[79] Felix W Wehrli, Zachary B Rodgers, Varsha Jain, Michael C Langham, Cheng Li, Daniel J Licht, and Jeremy Magland. Time-resolved mri oximetry for quantifying cmro2 and vascular reactivity. *Academic radiology*, 21(2):207–214, 2014.

[80] Cátia F Lourenço, Ana Ledo, GA Gerhardt, and Rui M Barbosa. Nneurometabolic and electrophysiological changes during cortical spreading depolarization: multimodal approach based on a lactate-glucose dual microbiosensor arrays. *Scientific reports*, 7(1):6764, 2017.

[81] Cenk Ayata and Martin Lauritzen. Spreading depression, spreading depolarizations, and the cerebral vasculature. *Physiological reviews*, 95(3):953–993, 2015.

[82] Martin Lauritzen, Jens Peter Dreier, Martin Fabricius, Jed A Hartings, Rudolf Graf, and Anthony John Strong. Clinical relevance of cortical spreading depression in neurological disorders: migraine, malignant stroke, subarachnoid and intracranial hemorrhage, and traumatic brain injury. *Journal of Cerebral Blood Flow & Metabolism*, 31(1):17–35, 2011.

[83] Baptiste Balança, Anne Meiller, Laurent Bezin, Jens P Dreier, Stephane Marinesco, and Thomas Lieutaud. Altered hypermetabolic response to cortical spreading depolarizations after traumatic brain injury in rats. *Journal of Cerebral Blood Flow & Metabolism*, 37(5):1670–1686, 2017.

[84] Delphine Feuerstein, Andrew Manning, Parastoo Hashemi, Robin Bhatia, Martin Fabricius, Christos Tolias, Clemens Pahl, Max Ervine, Anthony J Strong, and Martyn G Boutelle. Dynamic metabolic response to multiple spreading depolarizations in patients with acute brain injury: an online microdialysis study. *Journal of Cerebral Blood Flow & Metabolism*, 30(7):1343–1355, 2010.

[85] Michelle L Rogers, Delphine Feuerstein, Chi Leng Leong, Masatoshi Takagaki, Xize Niu, Rudolf Graf, and Martyn G Boutelle. Continuous online microdialysis using microfluidic sensors: dynamic neurometabolic changes during spreading depolarization. *ACS chemical neuroscience*, 4(5):799–807, 2013.

[86] Maiken Nedergaard and Anker Jon Hansen. Spreading depression is not associated with neuronal injury in the normal brain. *Brain research*, 449(1-2):395–398, 1988.

[87] Xiao-Yuan Lian and Janet L Stringer. Energy failure in astrocytes increases the vulnerability of neurons to spreading depression. *European Journal of Neuroscience*, 19(9):2446–2454, 2004.

[88] Takahiro Takano and Maiken Nedergaard. Deciphering migraine. *The Journal of clinical investigation*, 119(1):16–19, 2009.

[89] Maiken Nedergaard and Anker Jon Hansen. Characterization of cortical depolarizations evoked in focal cerebral ischemia. *Journal of Cerebral Blood Flow & Metabolism*, 13(4):568–574, 1993.

[90] David W Busija, Ferenc Bari, Ferenc Domoki, Takashi Horiguchi, and Katsuyoshi Shimizu. Mechanisms involved in the cerebrovascular dilator effects of cortical spreading depression. *Progress in neurobiology*, 86(4):417–433, 2008.

[91] Takashi Horiguchi, James A Snipes, Bela Kis, Katsuyoshi Shimizu, and David W Busija. The role of nitric oxide in the development of cortical spreading depression-induced tolerance to transient focal cerebral ischemia in rats. *Brain research*, 1039(1-2):84–89, 2005.

[92] Turgay Dalkara, Nicholas T Zervas, and Michael A Moskowitz. From spreading depression to the trigeminovascular system. *Neurological sciences*, 27(2):s86–s90, 2006.

[93] George G Somjen. Mechanisms of spreading depression and hypoxic spreading depression-like depolarization. *Physiological reviews*, 81(3):1065–1096, 2001.

[94] Takahiro Takano, Guo-Feng Tian, Weiguo Peng, Nanhong Lou, Ditte Lovatt, Anker J Hansen, Karl A Kasischke, and Maiken Nedergaard. Cortical spreading depression causes and coincides with tissue hypoxia. *Nature neuroscience*, 10(6):754, 2007.

[95] Warren R Selman, W David Lust, Svetlana Pundik, Yinong Zhou, and Robert A Ratcheson. Compromised metabolic recovery following spontaneous spreading depression in the penumbra. *Brain research*, 999(2):167–174, 2004.

[96] Günter Mies and Wulf Paschen. Regional changes of blood flow, glucose, and atp content determined on brain sections during a single passage of spreading depression in rat brain cortex. *Experimental neurology*, 84(2):249–258, 1984.

[97] Delphine Feuerstein, Heiko Backes, Markus Gramer, Masatoshi Takagaki, Paula Gabel, Tetsuya Kumagai, and Rudolf Graf. Regulation of cerebral metabolism during cortical spreading depression. *Journal of Cerebral Blood Flow & Metabolism*, 36(11):1965–1977, 2016.

[98] Jonas C Fordsmann, Rebecca WY Ko, Hyun B Choi, Kirsten Thomsen, Brent M Witgen, Claus Mathiesen, Micael Lønstrup, Henning Piilgaard,

Brian A MacVicar, and Martin Lauritzen. Increased 20-hete synthesis explains reduced cerebral blood flow but not impaired neurovascular coupling after cortical spreading depression in rat cerebral cortex. *Journal of Neuroscience*, 33(6):2562–2570, 2013.

[99] Francesca Galeffi, George G Somjen, Kelley A Foster, and Dennis A Turner. Simultaneous monitoring of tissue po2 and nadh fluorescence during synaptic stimulation and spreading depression reveals a transient dissociation between oxygen utilization and mitochondrial redox state in rat hippocampal slices. *Journal of Cerebral Blood Flow & Metabolism*, 31(2):626–639, 2011.

[100] Keiji Adachi, Nancy F Cruz, Louis Sokoloff, and Gerald A Dienel. Labeling of metabolic pools by [6-14c] glucose during k+-induced stimulation of glucose utilization in rat brain. *Journal of Cerebral Blood Flow & Metabolism*, 15(1):97–110, 1995.

[101] Parastoo Hashemi, Robin Bhatia, Hajime Nakamura, Jens P Dreier, Rudolf Graf, Anthony J Strong, and Martyn G Boutelle. Persisting depletion of brain glucose following cortical spreading depression, despite apparent hyperaemia: evidence for risk of an adverse effect of leao's spreading depression. *Journal of Cerebral Blood Flow & Metabolism*, 29(1):166–175, 2009.

[102] Bert Bosche, Rudolf Graf, Ralf-Ingo Ernestus, Christian Dohmen, Thomas Reithmeier, Gerrit Brinker, Anthony J Strong, Jens P Dreier, and Johannes Woitzik. Recurrent spreading depolarizations after subarachnoid hemorrhage decreases oxygen availability in human cerebral cortex. *Annals of neurology*, 67(5):607–617, 2010.

[103] Jens P Dreier, Sebastian Major, Andrew Manning, Johannes Woitzik, Chistoph Drenckhahn, Jens Steinbrink, Christos Tolias, Ana I Oliveira-Ferreira, Martin Fabricius, Jed A Hartings, et al. Cortical spreading ischaemia is a novel process involved in ischaemic damage in patients with aneurysmal subarachnoid haemorrhage. *Brain*, 132(7):1866–1881, 2009.

[104] Tomáš Mazel, Zuzana Šimonová, and Eva Syková. Diffusion heterogeneity and anisotropy in rat hippocampus. *Neuroreport*, 9(7):1299–1304, 1998.

[105] Tomáš Mazel, Frank Richter, Lýdia Vargová, and Eva Syková. Changes in extracellular space volume and geometry induced by cortical spreading depression in immature and adult rats. *Physiological research*, 51:S85–S94, 2002.

[106] Hans Kager, Wytse J Wadman, and George G Somjen. Simulated seizures and spreading depression in a neuron model incorporating interstitial space and ion concentrations. *Journal of neurophysiology*, 84(1):495–512, 2000.

[107] Olga Cozzolino, Maria Marchese, Francesco Trovato, Enrico Pracucci, Gian Michele Ratto, Maria Gabriella Buzzi, Federico Sicca, and Filippo M Santorelli. Understanding spreading depression from headache to sudden unexpected death. *Frontiers in neurology*, 9:19, 2018.

[108] Daniel R Kramer, Tatsuhiro Fujii, Ifije Ohiorhenuan, and Charles Y Liu. Cortical spreading depolarization: pathophysiology, implications, and future directions. *Journal of Clinical Neuroscience*, 24:22–27, 2016.

[109] Cenk Ayata, Hwa Kyoung Shin, Salvatore Salomone, Yasemin Ozdemir-Gursoy, David A Boas, Andrew K Dunn, and Michael A Moskowitz. Pronounced hypoperfusion during spreading depression in mouse cortex. *Journal of Cerebral Blood Flow & Metabolism*, 24(10):1172–1182, 2004.

[110] Cenk Ayata. Spreading depression and neurovascular coupling. *Stroke*, 44(6 suppl 1):S87–S89, 2013.

[111] Chiho Kudo, Ala Nozari, Michael A Moskowitz, and Cenk Ayata. The impact of anesthetics and hyperoxia on cortical spreading depression. *Experimental neurology*, 212(1):201–206, 2008.

[112] Michelle A Bylicky, Gregory P Mueller, and Regina M Day. Mechanisms of endogenous neuroprotective effects of astrocytes in brain injury. *Oxidative medicine and cellular longevity*, 2018, 2018.

[113] Zhiyou Cai, Cheng-Qun Wan, and Zhou Liu. Astrocyte and alzheimer's disease. *Journal of neurology*, 264(10):2068–2074, 2017.

[114] Andrea Becerra-Calixto and Gloria P Cardona-Gómez. The role of astrocytes in neuroprotection after brain stroke: potential in cell therapy. *Frontiers in molecular neuroscience*, 10:88, 2017.

[115] Elena Dossi, Flora Vasile, and Nathalie Rouach. Human astrocytes in the diseased brain. *Brain research bulletin*, 136:139–156, 2018.

[116] Lizhen Li, Andrea Lundkvist, Daniel Andersson, Ulrika Wilhelmsson, Nobuo Nagai, Andrea C Pardo, Christina Nodin, Anders Ståhlberg, Karina Aprico, Kerstin Larsson, et al. Protective role of reactive astrocytes in brain ischemia. *Journal of Cerebral Blood Flow & Metabolism*, 28(3):468–481, 2008.

[117] Marta Sidoryk-Wegrzynowicz, Michal Wegrzynowicz, Eunsook Lee, Aaron B Bowman, and Michael Aschner. Role of astrocytes in brain function and disease. *Toxicologic pathology*, 39(1):115–123, 2011.

[118] Yasuhisa Tamura, Asami Eguchi, Guanghua Jin, Mustafa M Sami, and Yosky Kataoka. Cortical spreading depression shifts cell fate determination of progenitor cells in the adult cortex. *Journal of Cerebral Blood Flow & Metabolism*, 32(10):1879–1887, 2012.

[119] Satoshi Fujita, Naoko Mizoguchi, Ryuhei Aoki, Yilong Cui, Noriaki Koshikawa, and Masayuki Kobayashi. Cytoarchitecture-dependent decrease in propagation velocity of cortical spreading depression in the rat insular cortex revealed by optical imaging. *Cerebral Cortex*, 26(4):1580–1589, 2015.

[120] Maximiliano Rovegno and Juan C Saez. Role of astrocyte connexin hemichannels in cortical spreading depression. *Biochimica et Biophysica Acta (BBA)-Biomembranes*, 2017.

[121] Eva Syková and Alexandr Chvátal. Glial cells and volume transmission in the cns. *Neurochemistry international*, 36(4-5):397–409, 2000.

[122] Jessica A Filosa, Helena W Morrison, Jennifer A Iddings, Wenting Du, and Ki Jung Kim. Beyond neurovascular coupling, role of astrocytes in the regulation of vascular tone. *Neuroscience*, 323:96–109, 2016.

[123] Frank Funke, Miriam Kron, Mathias Dutschmann, and Michael Mller. Infant brain stem is prone to the generation of spreading depression during severe hypoxia. *Journal of neurophysiology*, 101(5):2395–2410, 2009.

[124] Rashika N Karunasinghe and Janusz Lipski. Oxygen and glucose deprivation (ogd)-induced spreading depression in the substantia nigra. *Brain research*, 1527:209–221, 2013.

[125] Jrn K Pomper, Stephan Haack, Gabor C Petzold, Katharina Buchheim, Siegrun Gabriel, Ulrike Hoffmann, and Uwe Heinemann. Repetitive spreading depression-like events result in cell damage in juvenile hippocampal slice cultures maintained in normoxia. *Journal of neurophysiology*, 95(1):355–368, 2006.

[126] Niklas Hübel and Ghanim Ullah. Anions govern cell volume: a case study of relative astrocytic and neuronal swelling in spreading depolarization. *PloS one*, 11(3):e0147060, 2016.

[127] Niklas Hübel, R David Andrew, and Ghanim Ullah. Large extracellular space leads to neuronal susceptibility to ischemic injury in a na+/k+ pumps–dependent manner. *Journal of computational neuroscience*, 40(2):177–192, 2016.

[128] Ghanim Ullah, Yina Wei, Markus A Dahlem, Martin Wechselberger, and Steven J Schiff. The role of cell volume in the dynamics of seizure, spreading depression, and anoxic depolarization. *PLoS computational biology*, 11(8):e1004414, 2015.

[129] Bas-Jan Zandt, Bennie ten Haken, J Gert van Dijk, and Michel JAM van Putten. Neural dynamics during anoxia and the 'wave of death". *PLoS One*, 6(7):e22127, 2011.

[130] Keith B Moore and John O'Brien. Connexins in neurons and glia: targets for intervention in disease and injury. *Neural regeneration research*, 10(7):1013, 2015.

[131] Shenton SL Chew, Cameron S Johnson, Colin R Green, and Helen V Danesh-Meyer. Role of connexin43 in central nervous system injury. *Experimental neurology*, 225(2):250–261, 2010.

[132] Ning Zhou, Ravi L Rungta, Aqsa Malik, Huili Han, Dong Chuan Wu, and Brian A MacVicar. Regenerative glutamate release by presynaptic nmda receptors contributes to spreading depression. *Journal of Cerebral Blood Flow & Metabolism*, 33(10):1582–1594, 2013.

[133] Antonius M VanDongen. *Biology of the NMDA Receptor*. CRC Press, 2008.

[134] Anthony Charles and KC Brennan. Cortical spreading depression?new insights and persistent questions. *Cephalalgia*, 29(10):1115–1124, 2009.

[135] Michael F James, Justin M Smith, Simon J Boniface, Christopher LH Huang, and Ronald A Leslie. Cortical spreading depression and migraine: new insights from imaging? *Trends in neurosciences*, 24(5):266–271, 2001.

[136] Gabriela Capo Rangel, Luca Gerardo-Giorda, Erkki Somersalo, and Daniela Calvetti. Metabolism plays a central role in the cortical spreading depression: evidence from a mathematical model. *submitted*.

[137] Henning Piilgaard and Martin Lauritzen. Persistent increase in oxygen consumption and impaired neurovascular coupling after spreading depression in rat neocortex. *Journal of Cerebral Blood Flow & Metabolism*, 29(9):1517–1527, 2009.

[138] Nouchine Hadjikhani, Margarita Sanchez Del Rio, Ona Wu, Denis Schwartz, Dick Bakker, Bruce Fischl, Kenneth K Kwong, F Michael Cutrer, Bruce R Rosen, Roger BH Tootell, et al. Mechanisms of migraine aura revealed by functional mri in human visual cortex. *Proceedings of the National Academy of Sciences*, 98(8):4687–4692, 2001.

[139] Luca Gerardo-Giorda and Julia M Kroos. A computational multiscale model of cortical spreading depression propagation. *Computers & Mathematics with Applications*, 74(5):1076–1090, 2017.